In Vivo Activity of Rhodium Metalloinsertors and Exploration of Drug Delivery Systems

Thesis by

Stephanie Denise Threatt

In Partial Fulfillment of the Requirements for the Degree of
Doctor of Philosophy in Biochemistry and Molecular Biophysics

CALIFORNIA INSTITUTE OF TECHNOLOGY

Pasadena, California

2020
Defended June 16, 2020

Stephanie Denise Threatt
ORCID: 0000-0002-2303-2166

ACKNOWLEDGEMENTS

I must begin by thanking my advisor, Professor Jacqueline Barton, for being an incredible mentor who has been essential to my development as a scientist and researcher. Throughout my doctorate, she has given me autonomy to pursue research projects of interest with continual support and assistance. As an incredibly successful female scientist, she has been a role model and her mentorship created a productive and supportive research environment for our entire lab. Furthermore, she has remained supportive of my numerous efforts towards science outreach and creating a more diverse and inclusive Caltech. I feel truly humbled to be her final doctoral student.

Additionally, my thesis committee has been instrumental towards my scientific, professional, and personal development. To Harry Gray, thank you for being my committee chair and always being available and willing to meet and give research advice, as well as mental and emotional support. To Dennis Dougherty, thank you for welcoming me into your lab during my first year. That initial experience of a supportive, motivated, and dynamic lab environment set an important example that I aspired to throughout graduate school. To Doug Rees, thank you for always being genuine, kind, and insightful. During my most trying times as a doctoral student, you have been an empathetic listener and consistent supporter. Furthermore, you have always supported my passions for science and outreach, and I very much look forward to working with you as a postdoctoral scholar. To Tim Synold, thank you for your patience, wisdom, and guidance. You have taught me so much about animal model research, and I am incredibly thankful for the time and energy you have invested towards my development as a researcher. You have each had a tremendous professional and personal influence, and I am sincerely grateful for everything you've done for me during my time at Caltech.

Next, I would like to acknowledge the many scientific collaborators who were instrumental to my research journey at Caltech. Much of my doctoral work involved animal studies that would not have been possible without my collaborators at City of Hope. In particular, thank you to Dr. Jun Wu for your involvement in planning and executing the various mouse studies. To Yuming Guo and Valerie Valenzuela, thank you for your patience and commitment to conducting thorough and complicated mouse studies. With your guidance, I became increasingly comfortable and confident working with mice and sincerely enjoyed working alongside both of you. To Dr. Steven Vonderfecht and Lori Saganek, thank you for your input on the animal study designs and teaching me how to conduct necropsies. I still remember how mesmerized I was by the ease, precision, and finesse with which Dr. Vonderfecht collected mouse tissues the very first time I observed the procedure. To Scott Virgil, you have such an incredible knowledge base and willingness to teach. Thank you for your scientific guidance; it was incredibly important for when I was synthesizing and purifying metal complexes. To Nathan Dalleska, thank you for helping to really optimize the tissue digestion procedure and your continual patience while I tried to learn how to conduct ICP-MS experiments. To Jens Kaiser, I have learned so very much from you about crystallography and structural techniques. You have a unique way of passionately explaining incredibly complicated concepts, while remaining relatable and easy to talk to, and I am so grateful that I've had you as a resource and colleague at Caltech. To Byung-kuk Yoo, I have very much enjoyed learning about electron microscopy while working with you, and I thank you for your dedication to the metalloinsertor structural project. I have sincerely appreciated that our working relationship has always been founded upon mutual respect. Also, to Julie Bailis and her team at Amgen, thank you for continuing to explore

metalloinsertors from a biological perspective and contributing findings that will be instrumental for these compound's further development.

In additional to my research experiences, I have also had the pleasure of developing my own knowledge base and pedological skills as a teaching assistant. To Ellen Rothenberg, it was such a pleasure to teach introductory biology alongside you, so thank you. I personally learned a lot during the courses and your commitment to teaching constantly pushed me to understand more and support the learning of my students. To Peter Devan, thank you for giving me the opportunity to assist in exposing first year Caltech undergraduates to the rewarding world of chemistry and chemical engineering research.

To the countless essential BBE, CCE, and BMB community members – Courtney Cechini, Lauriane Quenne, Alison Ross, Mo Renta, Elisha Okawa, Joe Drew, Agnes Tong, Amy Woodall-Ojeda, Silva Virgil, Haick Issaian, Anne Penney, Lauren Breeyear, Steve Guold, Mona Shahgholi, Dave VanderVeld, Nate Siladke, Armando Villasenor, Gregory Rolette, and the custodial staff- I want to thank each of you for your dedication to keeping the CCE and BBE divisions running smoothly, which has allowed research to be my biggest concern while at Caltech. Within the Barton lab, I would like to thank the current administrative coordinator, Elizabeth Garcia, for always being willing to listen and helping me to develop a game plan when I needed it most. You've been a good friend who has introduced me to such awesome (and weird) food and constantly brightened my days with laughter.

Furthermore, I am exceedingly grateful for the past and present members of the Barton group who have helped to create a productive, fun, and supportive work environment. I would like to begin by thanking my metalloinsertor research mentors. To Kelsey Boyle, thank you for teaching me practically everything I know about metalloinsertors! You've been such a patient,

supportive, and effective teacher from the very beginning, and I know my graduate school years would've been considerably more arduous without you around. We have had so many wonderful conversations as friends about science and the world around us that have truly pushed me to be introspective and helped me to stay balanced and motivated, so thank you. To Alyson Weidmann, thank you for giving me a strong foundation in chemical techniques when I first joined the lab. To Adam Boynton, you brought such positive energy and impressive structure and commitment to our little nook on the south side of the lab every day- thank you for all the helpful and fun discussions. To Adela Nano, thank you for the countless discussions about troubleshooting experiments and developing hypotheses and study designs. You've been a great colleague, mentor, and friend. To Yingxin Deng, thank you for the many conversations about career options outside of academia. Even now, you continue to show an interest in my future by helping to keep me informed about career development events. And thanks for the many delicious meals and fun conversations! To Rebekah Silva, thank you for being such a great lab mate from the start. I have always enjoy our life and science talks, and I love all of the adorable animal videos you send to bring a smile to my face! To Levi Ekanger, thank you for showing me how to prepare liposomes and helping to give my project direction at a time when I was really struggling with my research. To the other Barton postdocs that I have crossed paths with, including Lionel Marcelis , Edmund Tse, Natalie Muren, Katie Schaefer, Sandra König, Miguel Pinto, and Kausar Raza, thank you for your patience, insights, and advice throughout graduate school. To the rest of the lab- Ariel Furst, Anna Arnold, Michael Grodick, Ted Zwang, Liz O'Brien, Phil Bartels, Siobhán MacArdle, Aoshu Zhong, and Nirit Kantor- thank you for creating a supportive and fun work environment. You each helped me to grow as a scientist during graduate school. Lastly, I would like to thank my undergraduate mentee Daniel Peng for

being an engaged and inquisitive learner. The questions that you asked helped to solidify my own understanding of chemical principles and techniques, and I am certain you will have a long and fruitful career.

I have always had a passion for mentoring and tutoring, and during my time at Caltech, I have explored a number of Caltech resources for developing those skills and conducting outreach in the Pasadena community at large. The Caltech Y has been a vital part of my Caltech experience. Outdoor trips with the Y, including to Anza Borrego State Desert Park, were some of my first experiences with camping, and the five years I tutored Pasadena Unified School District students, including Alondra and Gracie, were important breaks from research that allowed me to recharge my enthusiasm for teaching and education. I want to thank Liz Jackman and Camila Fernandez for running the Caltech Y Rise tutoring program and helping me to create so many fond and fun memories. Additionally, the Caltech Y Social Activism Speaker Series nurtured the cultivation of my ever growing passion for science policy. I was exposed to so many interesting and stimulating topics through these seminars and so many other events hosted by the Caltech Y staff, so thank you Athen Castro, Greg Fletcher, and Agnes Tong.

Next, I would like to acknowledge the Caltech Center for Inclusion and Diversity (CCID). Starting from my very first week on campus, the CCID became my campus home outside of lab. As a black woman at Caltech, the CCID was one of the only places where I felt my complete self and range of personal identities was accepted and celebrated. Through my CCID engagement, I became increasingly involved with the Black Scientists and Engineers of Caltech (BSEC) and Black Ladies Association of Caltech (BLAC), which each served to develop my organizational skills while also allowing me to cultivate a supportive and tight-knit Caltech community. I will forever be grateful for the many ways in which Monique Thomas, Taso

Dimitriadis, Erin-Kate Escobar, Marlene Moncada, and Hanna Song contributed to my Caltech experience. I consider you each true friends, and I will forever cherish the many memories I've shared with you from the 2015 FSRI LA metro food tour to the annual and infamous HoliGay Parties. I would also like to thank past staff members at the CCID, including Megan Scott, Azani Pinkney and Eva Graham, who I also worked closely with. Also, thank you to the CCID resident puppies Banksy and Hadley for the many times of much needed doggy love and cuddles.
In connection with my CCID engagement, I spent much time and effort cultivating community among Black Techers and Alumni, as well as conducting STEM community outreach, through BLAC and BSEC. To Kyle Virgil, Sarah Sam, Matt Gethers, and Ottman Tertuliano, thank you for your support and leadership related to these clubs. Our discussion with Rep. John Lewis about education and civil rights at the 2018 Caltech commencement and the science demonstrations (STEMonstrations) we performed for PUSD students were some of the highlights of my time at Caltech.

I would also like to thank members of BSEC and BLAC for truly creating a welcoming and supportive network of Black Techers and Alumni. To Karina Edmonds, thank you for being a great mentor and role model for having a successful, balanced, and fulfilling life and career. To Chantal D'Apuzzo, thank you for all of your career advice and insights, as well as allowing us to host events at your beautiful home. To Monique Thomas, thank you for your commitment to befriending and supporting the few black students at Caltech. It has been a pleasure to work and laugh with you these past few years. To Kate McAnulty, thank you for always being open to drop-in conversations about life, research, and career struggles and being a great tennis partner! You've been such a great supporter for The Big 3. To Judy Nelson and Tom Wolfe, thank you for helping me establish a West Coast family that truly makes California feel like home. I've

made so many great memories with you both full of Monday Night Dinners and Pasadena Playhouse dates. I would also like to thank Prof. Bil Clemons for giving me advice on my career and continually investing time and energy into my success.

The friends I have made during my PhD have been incredibly important to my happiness and sanity at Caltech! I feel so fortunate to have made some truly amazing lifelong friends. Manuel Razo, I am so grateful that I made another best friend during my Caltech journey. Starting from our first days in BMB, you've always had my back. Our friendship has been full of some of my favorite grad school moments, including concerts, ramen and HOIs. You are such a kind, thoughtful, and passionate person, and I want you to know how much your presence has helped me to stay balanced and positive through this crazy journey. Porfirio Quintero, thank you for always welcoming me into your home. HOIs full of Thai Iced tea and ramen wouldn't have been the same without you. Tonia, I love your sense of humor, and I can never thank you enough for introducing me to New Moon (love that place!). Our tennis matches helped to keep me active and always left me smiling. Jeong Hoon Ko, I was so happy to find a new tennis partner once Tonia left. Thanks for listening to my Bachelor updates and keeping me up to date on the latest chemistry news. Lauren Breeyear, thanks for all the awesome Bachelor nights with you, me, Sunny, and Teddy. The Drake concert and our HOIs are just a couple of fun moments I will always cherish. Kelsey Boyle, you were so much more than my lab mate. I really consider you a friend, and we had such interesting conversations that were really stimulating about education, science, and economic inequality; topics we're both really passionate about. Rebekah Silva, thank you for always being a supportive and empathetic ear. As Jackie's last couple of graduate students, we've gotten much closer, and I appreciate you helping me to think through some of my career and personal goals (Hawaii!). Kyle Virgil, having you as a friend has been really

awesome. From our SACNAS recruiting trip in Oahu to seeing J. Cole in concert and the El Portal annual Tequila Tasting, it's been great having life experiences with you. Meaghan Sullivan, thank you for showing me how fun it can be to live with a friend! Alessandro Maggi, thank you for truly welcoming me to Caltech starting with the BMB recruitment weekend. I am so happy you, Obi, and I became the Three Musketeers. We have had so many fun and memorable nights in WeHO and all over LA.

To the many other friends who have made graduate school enjoyable – Yackar Mauzole, Andres Ortiz, Adam Gomez, Alejandra Olvera, Michael Anaya, Weslee Glenn, Ottman Tertuliano, Matthew Gethers, Siobhán MacArdle, Sarah Sam, Rachel Cummings – thank you. To my blockmates from Harvard, I always look forward to our Memorial Day weekend trips, and I'm really happy we've made an effort to stay connected. Katrina Malakhoff, thanks for being a great best friend and blockie. Even if I'm resistant at the start, I usually end up enjoying our hikes (lol), and mini vacations to visit you in Santa Barbra have always been trips that I look forward to.

I have been incredibly fortunate throughout my career to have mentors who have supported and believed in me. To my many scientific mentors over the years, Ms. Magdalene McClain, Dr. Jacob Hooker, Dr. Gregg Tucci, Dr. Natalia Jura, and Dr. Jun-Tao Guo, thank you so much for believing in me and pushing me to pursue my passion for science. Thank you to the countless family and friends who have provided guidance and encouragement over the years.

To my extended family including my aunts, uncles, cousins, and grandparents, thank you for all of the love and support. I'm incredibly grateful to have you all in my life. To my Nana, I wish you could've seen me complete my doctorate. You have been one of my main supporters and role models throughout my life, and I miss you so very much. To Meredith, Patrick, and

William, it has been amazing having family a short car drive away. Thank you for extending an open invitation for me to visit you in Encinitas. It has been such an honor and pleasure to see William grow. To Travis, thank you for being a great brother-in-law. We've had so many conversations that have shown me a different and important perspective on the world. To Jennifer, you are a great example of a strong and empowered woman. I'm so thankful to have a sister like you who is supportive and always willing to give advice. To my mom Cathy, I aspire to be as strong, thoughtful, and generous as you have always been. You have taught me so much about standing up for myself and pursuing my dreams, and I know I wouldn't be the person I am today without your awesome influence. To my dad Melvin, thank you for always listening and giving me thoughtful feedback about the complexities of research and life. I am grateful to have a loving and supportive father like you. To my niece Aria, I love you so very much. You motivate me to continue working towards making this country and world a better place. Thank you to all of my family for the endless love and support.

And lastly, to my California family, Teddy, Logic, and Chance – you've been such an important part of my graduate school experience. I never imagined that such beautiful relationships could grow from a night out dancing in West Hollywood. Logic and Chance, it has been great having a couple of turtle friends. Taking care of you has been an important and sometimes needed reminder to take care of myself. Teddy, you are such a great friend and partner. In the most difficult times during graduate school, you have always supported me and reminded me of my potential. Your ability to make me smile, laugh, and feel that I can completely be myself is truly unique, and I can't imagine having gone through the last few years without you by my side. I love you, and I can't wait to see what the future holds for us.

ABSTRACT

Rhodium metalloinsertors are octahedral complexes developed to selectively target the mismatches and insertions/deletions (indels) that result from mismatch repair (MMR) deficient cancers. By incorporating particularly wide, aromatic, inserting ligands, these complexes are able to detect thermodynamically destabilized mismatch sites via a binding mode known as metalloinsertion, in which the inserting ligand binds DNA via the minor groove and results in ejection of the destabilized mismatched base pair. *In vitro* analyses of metalloinsertors have found that these complexes are selectively cytotoxic towards MMR-deficient cancer cells compared to MMR-proficient cells. Furthermore, the newest family of Rh-O metalloinsertors, which includes $[Rh(phen)(chrysi)(PPO)]^{2+}$ (Rh-PPO), displays preferential cytotoxicities in the *nano*molar range, which is significantly more potent than first generation metalloinsertors and many standard of care chemotherapeutics. Given the high level of potency and selectivity of Rh-O metalloinsertors, further clinical development of these complexes has been pursued.

Here, we present the first preclinical mouse evaluation of a rhodium metalloinsertor as an anticancer agent. The Rh-O metalloinsertor Rh-PPO was evaluated in the HCT116 colorectal cancer xenograft tumor model alongside saline and oxaliplatin controls. Intraperitoneal studies with Rh-PPO showed significant decreases in tumor volumes over time and final tumor weights, indicating Rh-PPO has notable anticancer activity. Additionally, Rh-PPO treatment resulted in a noteworthy increase in the length of mouse survival that was on par with the FDA approved chemotherapeutic oxaliplatin. Pharmacokinetic analyses revealed rapid absorption of Rh-PPO in plasma with notable accumulation in the liver compared to tumors. Importantly, intratumoral metalloinsertor administration resulted in enhanced anticancer effects, which points to a need for more selective delivery methods in order to further metalloinsertor development.

In order to target cancerous cells with still higher selectivity, routes to metalloinsertor antibody drug conjugate (ADC) designs were explored. By attaching Rh-O metalloinsertors to an antibody specific to cancer-associated antigens, our complexes may become even more specifically directed to induce selective cytotoxicity in diseased cells. Three ADC drug linkers that incorporate maleimide groups into the N^O coordinating ligand of a Rh-O metalloinsertor were designed, synthesized, and characterized. These complexes were evaluated for their cellular potency and selectivity toward MMR-deficient cancer cells. Studies revealed that functionalization of the hydroxyl-containing ancillary ligand resulted in decreased potency and abolished preferential cytotoxicity, contrary to previous studies that assessed modifications of this ligand.

Liposomal formulations of Rh-PPO were also explored to further target metalloinsertors to malignant cells. Liposomal drug encapsulations have a demonstrated ability to decrease systemic toxicity and increase tumor drug uptake; therefore, the biological activity of Rh-PPO liposomal formulations was explored. Four distinct Rh-PPO liposome formation methods were developed and the resulting liposomes were assessed for their encapsulation efficiency, cellular toxicity, and stability. Remote loaded Rh-PPO liposomes were found to display the most promising chemical and biological characteristics, although additional optimization of encapsulation procedures is necessary for further preclinical evaluation of this metalloinsertor drug delivery approach.

As metalloinsertors continue preclinical assessment and development, a greater understanding of their mechanism of action is imperative. Biological studies with Rh-PPO and the fluorescent analogue RhPPO-Cy3 have shown that DNA damage from metalloinsertor treatment involves the formation of DNA double strand breaks near metalloinsertor-mismatch

binding sites. Furthermore, the DNA damage response, including recruitment of pH2AX and Rad51 proteins, becomes activated in response to Rh-PPO treatment. In order to further elucidate the unique mechanism of action of Rh-O metalloinsertors, which involves both metalloinsertor enantiomers binding to DNA mismatches and displaying biological activity, structural studies are ongoing. X-ray crystallography and microelectron diffraction (microED) techniques have been used in attempts to obtain a high resolution structure of Rh-O metalloinsertors bound to DNA mismatch sites. Gaining these structural insights will be critical to understanding the increased cytotoxic selectivity and uniquely high potency of these second generation metalloinsertor complexes.

The experiments detailed in this thesis have advanced the preclinical development of rhodium metalloinsertors. The ability of Rh-O metalloinsertors to decrease tumor growth *in vivo* has been established. Additionally, liposomal and ADC metalloinsertor drug formulations have been pursued as drug delivery systems, and the biological mechanisms relevant to metalloinsertor activity have been analyzed. Additional efforts to study rhodium metalloinsertors will continue to advance these promising chemotherapeutics as novel, targeted treatments for MMR-deficient cancers.

PUBLISHED CONTENT AND CONTRIBUTIONS

Rienzo, M., Rocchi, A. R., Threatt, S. D., Dougherty, D. A. & Lummis, S. C. R. Perturbation of Critical Prolines in Gloeobacter violaceus Ligand-gated Ion Channel (GLIC) Supports Conserved Gating Motions among Cys-loop Receptors. *J. Biol. Chem.* **2016,** *291*, 6272–80. DOI: 10.1074/jbc.M115.694372

S.D.T. assisted in designing, performing, and analyzing experiments.

Nano, A.; Bailis, J. M.; Mariano, N. F.; Pham, E. D.; Threatt, S. D.; Barton, J. K. Cell-Selective Cytotoxicity of a Fluorescent Rhodium Metalloinsertor Conjugate Results from Irreversible DNA Damage at Base Pair Mismatches. *Biochemistry* **2020**, *59*, 717–726. DOI: 10.1021/acs.biochem.9b01037

S.D.T. assisted in designing experiments and provided compound for biological studies.

Threatt, S. D.; Synold, T. W.; Wu, J.; Barton, J.K. In Vivo Anticancer Activity of a Rhodium Metalloinsertor in the HCT116 Xenograft Tumor Model. *Proc. Natl. Acad. Sci. USA*. **2020**, 117, 17535-17542. DOI: 10.1073/pnas.2006569117.

S.D.T. synthesized and purified compound for the study, assisted in designing, performing, and analyzing experiments, and participated in writing the manuscript.

TABLE OF CONTENTS

LIST OF FIGURES, TABLES, AND SCHEMES

Chapter 1

INTRODUCTION

1.1 Overview of Chemotherapeutics Targeting DNA

1.1.1 Role of DNA Repair in Maintaining Genome Fidelity

Cancer remains the second leading cause of death in the United States with approximately 600,000 deaths and 1.7 million new cases each year. With a 20 percent increase in the number of new cases annually, cancer is expected to soon surpass heart disease as the most fatal illness.[1] Cancerous cells result from the uncontrolled replication and division of cells. Research has revealed that a combination of mutational events, both exogenous and endogenous, alongside downregulation of DNA damage surveillance and repair mechanisms, results in the progression of this deadly disease.[2] Multiple DNA repair pathways are responsible for maintaining the integrity of the genome. For example, nucleotide excision repair (NER) includes proteins responsible for removing bulky DNA lesions, such as those formed by UV light damage and environmental mutagens.[2,3] Additionally DNA mismatch repair (MMR) proteins, such as MLH1 and MSH2, are responsible for identifying and repairing the DNA mismatches that result from improper pairing of DNA base pairs during replication.[4,5] While healthy cells typically utilize these DNA damage response (DDR) processes to maintain genomic integrity and stability, they can become malignant when oncogenes are activated and cells proliferate in an uncontrolled manner.

1.1.2 Cancer Types Associated with Malfunctions in DNA Repair

Numerous studies have revealed the role of mutations, especially those involving DNA damage response proteins, in the development of cancer. Studies show that mutations in

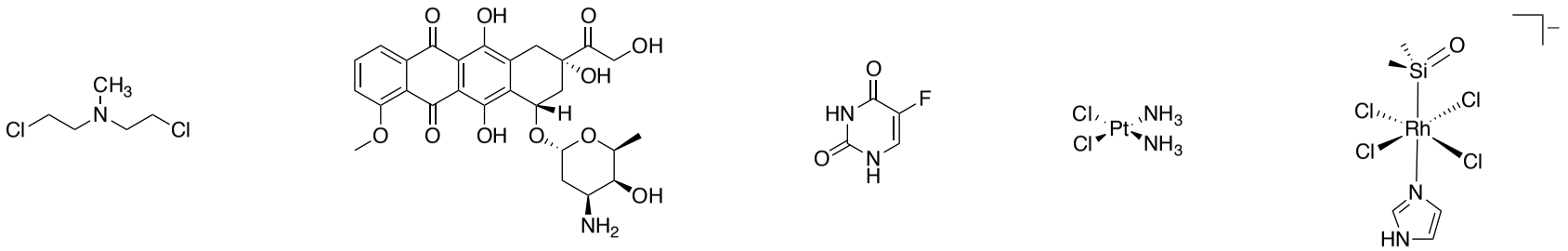

Chlormethine Doxorubicin 5-fluorouracil Cisplatin NAMI-A

Figure 1.1 Chemical structures of organic and metal chemotherapeutic compounds that target DNA. (Left to right) Chemical structures of nitrogen mustard Chlormethine, topoisomerase II inhibitor Doxorubicin, nucleotide analogue 5-fluorouracil, platinum drug Cisplatin, and ruthenium complex NAMI-A.

components of the NER pathway result in an inability to remove UV-induced, helix-distorting photodimers from DNA, ultimately causing predisposition to a very specific type of skin cancer, xeroderma pigmentosum (XP).[6] Similarly, patients with Lynch syndrome (also called hereditary non-polyposis colorectal cancer; HNPCC) were found to possess mutations in MLH1, MSH2, MSH6, or PMS2, which are proteins involved in the MMR pathway responsible for processing DNA mismatch errors.[7,8] This particular genetic disease, as well as MMR deficiencies generally, are reported to account for 15% of all colorectal cancer cases, which is the second most deadly form of cancer.[9,10] Ultimately, mutations within DNA repair proteins can result in persistent point mutations within DNA that eventually lead to the activation of oncogenes or disruption of tumor suppressors and the eventual development of cancer. Altogether, these findings support the hypothesis that patients with a hereditary predisposition for mutated DNA repair genes can be highly susceptible to the development of cancer, and our understanding of the connection between carcinogenesis and mutagenesis has continued to grow as research of DNA and DNA repair pathways has advanced.[2]

1.1.3 Development of Chemotherapeutics Targeted to DNA

1.1.3.1 Non-metal Therapeutics

Given the established relationship between genomic instability and carcinogenesis, DNA has remained a key target for chemotherapeutic drugs. Discovered in the 1940s, the first DNA-targeting compounds were nitrogen mustards and antifolate drugs (**Figure 1.1**), which were found to effectively treat Hodgkin's disease, leukemia, and lymphosarcoma. These compounds are still prescribed to cancer patients,[11,12] and studies with these molecules have shown that they induce the formation of DNA crosslinks that prevent DNA replication and cellular proliferation. In particular, nitrogen mustards form reactive cyclic aminium ions via intramolecular

displacement of the chloride by the amine nitrogen, and then alkylation of the N7 nucleophilic center of guanine DNA bases can occur; this covalent DNA binding eventually results in cell death.[13]

Doxorubicin is another common, small molecule, anticancer agent used for a variety of cancer types ranging from breast cancer to neuroblastomas (**Figure 1.1**). It has been found to be especially effective against solid tumors. This anthracycline antibiotic is believed to induce cytotoxicity by topoisomerase II inhibition and free radical generation.[14,15] Topoisomerase II is a nuclear enzyme that makes transient strand breaks within DNA in order to manage its topological state during replication and transcription.[15,16] Doxorubicin in particular is proposed to affect cancerous cells by intercalating into DNA and stabilizing the DNA-topoisomerase II complex, which inhibits the enzyme from catalyzing re-ligation reactions that are essential to DNA replication.[17] DNA double strand breaks occur as a consequence and ultimately cell death via apoptosis or mitotic catastrophe is induced.[18]

Another important DNA-targeting strategy involves the use of nucleobase analogues. The fluoropyrimidine 5-fluorouracil (5-FU) has remained a standard of care chemotherapy for patients with various types of cancer, especially advanced colorectal cancer, since its discovery in 1957.[19,20] This nucleobase analogue, shown in **Figure 1.1**, is a genotoxic agent that achieves cytotoxicity through a few known mechanisms. First, 5-FU inhibits thymidylate synthase (TS), an essential enzyme for nucleotide synthesis, which is believed to obstruct DNA replication and ultimately cause the formation of abasic sites that require repair by base excision repair (BER) proteins.[21] Additionally, the depletion of thymidine triphosphates (TPP) that is caused by TS inhibition results in the misincorporation of UTP and FdUTP into DNA creating base pair mismatches that must be recognized and repaired by the MMR pathway, particularly the hMutSα

complex (hMSH2–hMSH6).[22,23,24] Additionally, 5-FU treatment results in the misincorporation of nucleotides into RNA. Altogether, these disruptions of DNA replication and transcription result in significant genotoxicity that induces apoptosis. Furthermore, due to the broad effectiveness of 5-FU, a number of 5-FU prodrugs and other nucleoside analogues with similar mechanisms of action, including capecitabine and 5'-deoxy-5-fluorouridine (5'DFUR), have become clinically approved chemotherapeutics.[19,21,24]

1.1.3.2 Metal-based Therapeutics

Metallodrugs are a significant chemotherapeutic treatment option, and many of these complexes target and bind DNA. Metal complexes have unique photophysical and photochemical properties, as well as high modularity and relatively facile syntheses, which make them ideal scaffolds for therapeutic applications. Cisplatin, also called *cis*-diamminedichloroplatinum (II), is one of the most widely prescribed chemotherapy medications (**Figure 1.1**). It first gained recognition as a potent cytotoxic compound in the 1960s when electrolysis experiments showed that the complex had the ability to inhibit cell division within *Escherichia coli* cells. Clinical studies with cisplatin have shown that it can effectively treat a range of cancers including soft tissue, blood, muscle, and bone cancers.[25] The wide-ranging effectiveness of cisplatin has prompted countless studies that have led to a detailed understanding of this platinum drug's mechanism of action.[26] Studies have found that cisplatin uptake is mediated by the copper transporter Ctr1 in yeast and mammals. Upon entrance into the cell, the chloride atoms on cisplatin become replaced by water molecules. The hydrolyzed cisplatin product is a strong electrophile that can readily react with nucleophilic compounds within the cell, including nitrogen atoms within nucleic acids and thiols within proteins. Within DNA, cisplatin binds to the N7 nucleophilic groups of guanines and adenosines creating intra-

strand and inter-strand crosslinks to DNA. Mono-functional adducts and protein-DNA crosslinks have also been associated with cisplatin toxicity.[27] Importantly, as displayed in **Figure 1.2**, structural studies with cisplatin revealed that the formation of major cisplatin-DNA adducts results in a widened minor grove, as well as kinking of the DNA helix, ultimately causing significant distortions to the local DNA structure.[28,29] In cells, this DNA damage blocks cell division and results in apoptotic cell death.

While cisplatin has proven very effective at killing a variety of cancer cells, it also has a number of clinical side effects, including nephrotoxicity, cardiotoxicity, and hepatotoxicity, and its long-term efficacy can be hindered due to the development of drug resistance pathways. Due to these limitations, thousands of platinum analogues, including oxaliplatin, carboplatin, and ormaplatin, have been synthesized and assessed for their biological and clinical properties. Carboplatin is among these platinum-based compounds and it differs from cisplatin in that it contains a bidentate dicarboxylate (CBDCA) ligand instead of two chloride groups. This exchange of leaving groups reduces the reactivity and slows the DNA binding kinetics of the complex, and clinically results in a decrease in the number of overall side effects. Importantly, carboplatin generates the same reaction products *in vitro* as cisplatin, but appears to result in cytotoxicity through unique mechanisms.[26] The approach of using platinum-based drugs that target DNA in cancer treatment remains essential, with up to half of all cancer patients receiving platinum-based antineoplastic drugs.[27,30]

While platinum compounds have been the focus of the bulk of inorganic medicinal chemistry research, ruthenium complexes, such as NAMI-A (**Figure 1.1**) and KP1019, have also been transition metal drugs of interest.[31] Ruthenium compounds have been found to bind DNA

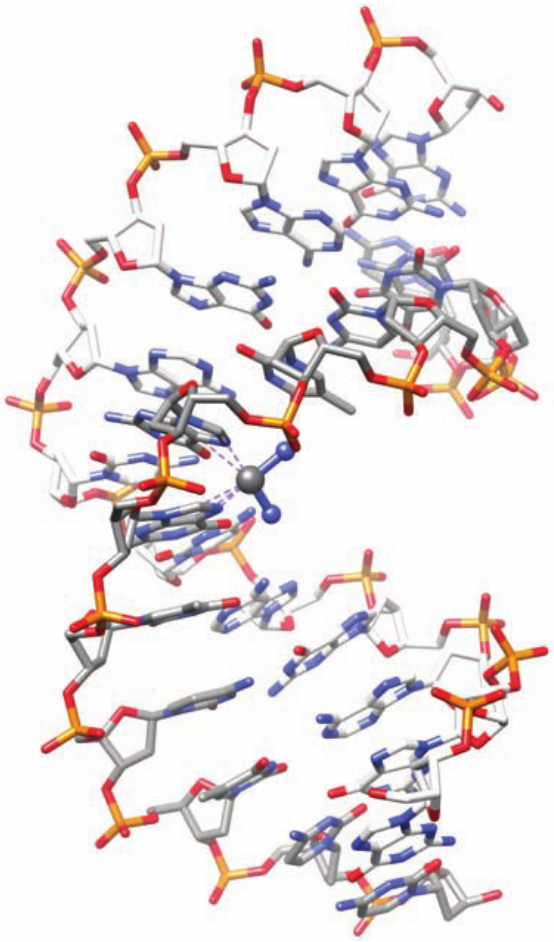

Figure 1.2 Structure of DNA-cisplatin complex showing the kink and distortions of DNA that result from cisplatin intra-strand crosslink formation. Adapted from Reference 29.[29]

with high selectivity and induce cellular toxicity within cancerous cells, though the clinical viability of these ruthenium complexes has yet to be established.

Importantly, while DNA targeting chemotherapeutics are among some of the first discovered and most effective cancer drugs, due to their low degree of selectivity and general targeting of rapidly dividing and proliferating cells, healthy cells also experience notable damage and death as a result of treatment with these complexes. As described with cisplatin, this results in a litany of side effects and dose limitations with these therapies; therefore, more recent research efforts have focused on developing chemotherapeutics targeted to bind cancer-specific biomarkers.

1.2 Mismatch Repair Protein Pathway

The human genome is approximately three billion base pairs in length. During the essential process of DNA replication, DNA polymerases efficiently copy nascent DNA strands with high but imperfect fidelity. The mismatch repair (MMR) machinery is a crucial protein network, shown in **Figure 1.3**, that maintains genomic stability by repairing DNA base pair mismatches, as well as insertion/deletion mispairs (IDLs), that are generated during DNA replication and recombination.[32] These MMR corrections result in 100- to 1000-fold increases in DNA fidelity, ultimately decreasing the overall genetic mutation frequency to one error per 10^{10} bases.

MMR corrections follow a multistep process that is initiated by MutSα (MSH2-MSH6 complex) or MutSβ (MSH2-MSH3 complex) binding to the DNA site of interest that contains the mismatch or IDL.[32] Importantly, MutSα is capable of identifying any of the eight possible DNA base pair mismatches, as well as small IDLs (1-2 bases), while MutSβ is only effective at identifying IDLs.[33,34] Subsequent to mispair recognition, MutSα is believed to participate in an

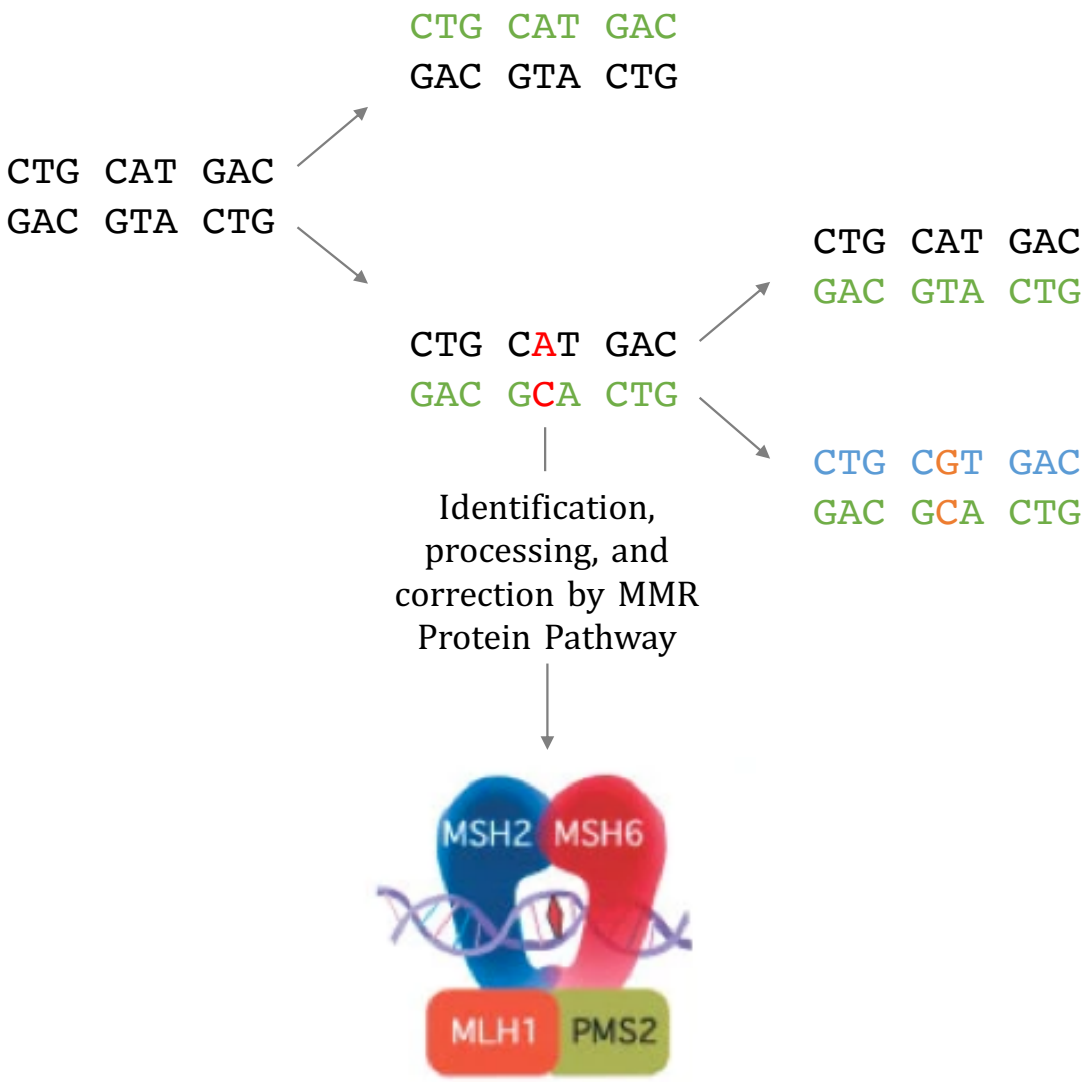

Figure 1.3 Graphic representing the role of eukaryotic mismatch repair (MMR) machinery in identifying and correcting DNA mismatches. The first iteration of replication (green) results in the formation of an AC mismatch (red). This error can be processed and repaired by MMR proteins, including MSH2, MSH6, MLH1, and PMS2. However, if the mismatch remains unchanged, upon the second iteration of replication (blue), a mutation (orange) will result. In this case, an AT base pair becomes GC mutation. Adapted from Reference 30.[30]

ATP-dependent conformational change that promotes MutLα (MLH1-PMS2 complex) binding. Studies have indicated that MutLα, when activated by PCNA, recognizes and nicks the nascent DNA strand, which commences the removal of the mismatch or IDL site; the exact mechanism of mispair removal remains to be elucidated, however, numerous models exist.[35] Lastly, synthesis of complimentary DNA followed by ligation allows for the completion of the MMR correction.[32–34]

MMR proteins represent an essential DNA repair pathway that prevents the propagation of DNA mismatches into mutations (**Figure 1.3**). Lack of function within one or multiple MMR proteins, especially MutSα and MutLα, can result in MMR deficiencies. Without the ability to properly survey recently synthesized DNA for mismatches and IDLs, there is a sharp decrease in DNA fidelity that can result in genomic instability and eventually cancer. In particular, Hereditary Nonpolyposis Colorectal Cancer (HNPCC), also known as Lynch Syndrome, is a disease commonly associated with MMR deficiencies, and 90% of HNPCC exhibit high microsatellite instability or MMR deficiencies.[36] Furthermore, MMR deficiencies are associated with 15-20% of all solid tumors and approximately 15% of colorectal cancer cases, and importantly, MMR-deficient cancer cells are often resistant to standard of care chemotherapeutics.

For example, several studies have shown MMR-deficient tumors to be less responsive to 5-FU and nucleobase analogue treatments generally. Specifically, a study conducted by Carethers *et. al.* showed that cellular proliferation is significantly reduced in MMR-proficient cells incubated with varying concentrations of 5-FU, while MMR deficient cell lines display minimal response to 5-FU treatment, as shown in **Figure 1.4**.[23] Moreover, analyses of clinical

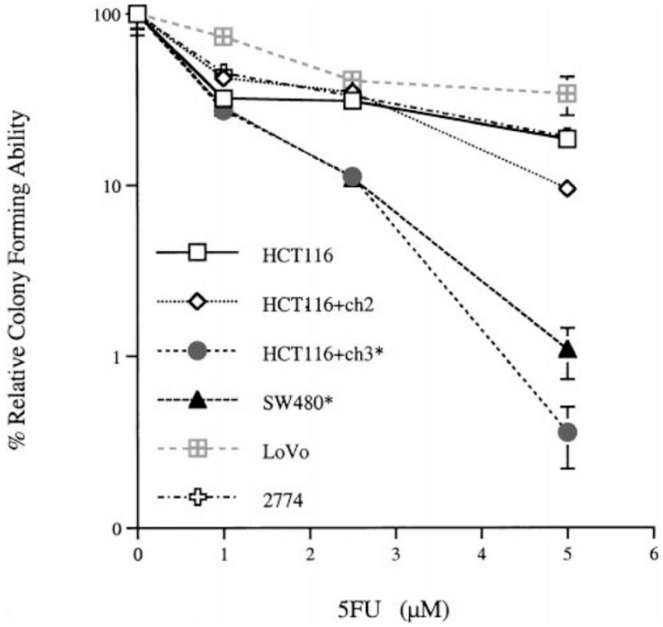

Figure 1.4 Colony forming assays in MMR-proficient and deficient colon and ovarian cancer cell lines treated with 5-fluorouracil (5-FU). The MMR-proficient cells tested, HCT116+ch3 and SW480, show reduced clonal survival with 5-FU treatment. Conversely, the results from the MMR-deficient cell lines, HCT116, HCT116+ch2, LoVo, and 2774, display 5-FU does not significantly reduce cellular proliferation in these cells. Adapted from Reference 23.[23]

trials with 5-FU have shown that advanced CRC patients with MMR deficiencies do not display improved survival when given the nucleobase as adjuvant chemotherapy.[23,37] This insensitivity to standard chemotherapies also applies to cisplatin and other alkylating agents,[38] which ultimately creates a significant need for novel, targeted therapeutics for MMR-deficient cancers.

1.2.1 FDA-Approved MMR-Deficient Targeted Chemotherapeutics

Two main strategies for selectively targeting MMR-deficient cancers have been developed. First, therapeutics have been designed to take advantage of the neoantigens that result from the high mutational load of MMR-deficient cancer cells.[39] These mutated biomolecules are presented on the surface of malignant cells and typically recognized by immune regulatory T-cells. Within non-cancerous tissues, the identification of neoantigens on foreign or diseased cells results in the secretion of cytokines and activation of the immune response. [40] This type of immune surveillance, as well as prevention of auto-immune responses against healthy cells, is tightly regulated by various mechanisms, including interactions between programmed cell death protein 1 (PD-1) and its ligands, programed cell death ligand 1 (PD-L1) and 2 (PD-L2). However, many cancerous cells upregulate the PD-L1 and PD-L2 inhibitory ligands in order to prevent immune response activation.[41] Understanding of this cancer immune evasion pathway has resulted in the development of therapeutics that target the PD-1 receptor, such as the FDA-approved Pembrolizumab.

Pembrolizumab is a highly selective, humanized monoclonal IgG_4-kappa isotype antibody against PD-1. Initial clinical studies with advanced melanoma and non-small cell lung cancer patients have shown that Pembrolizumab has high tumor response rates with long lasting effects. Clinical trials with this antibody treatment in other MMR-deficient patient populations are ongoing.[42] While the development of PD-1 inhibitors has significantly advanced efforts to

treat MMR-deficient cancers, these therapies can be prohibitively expensive and the overall response rate is still only approximately 50%.[40] Therefore, alternative approaches to selectively target MMR-deficient cancers are still needed; in particular, small molecule therapeutics designed to target the DNA base pair mismatches and IDLs that result from MMR deficiencies. Currently, there are no clinically approved drugs with this mechanism of action, and the development of such therapeutics will be essential to advancing treatment of MMR-deficient cancers.

1.3 Rhodium Metalloinsertors: Development of DNA Mismatch Targeted Therapeutics

1.3.1 Metalloinsertor Design: Targeting Thermodynamically Destabilized DNA Sites

Our laboratory has worked for several years to develop rhodium metalloinsertors, octahedral complexes designed to specifically locate and bind mismatched DNA sites.[43] These complexes capitalize on the thermodynamic instability of DNA mismatch sites compared to well-matched base pairs, which results from imperfect hydrogen bonding and π-stacking of improperly paired DNA bases.[44,45] Metalloinsertors are distinct from DNA binding intercalators and achieve selective binding to thermodynamically destabilized sites by incorporating particularly wide, aromatic, inserting ligands, such as chrysi (5,6-chrysenequinone diimine) and phzi (benzo[a] phenazine-5,6-quinone diimine). These ligands are designed to be slightly larger than Watson-Crick paired DNA bases. For example, the chrysi ligand is 0.45 Å larger than a well-matched base pair (11.3 Å compared to 10.85 Å, respectively; see **Figure 1.5**); this design is intended to significantly reduce the ligand's ability to indiscriminately intercalate between well-matched bases.[46] In addition to a wide inserting ligand, metalloinsertors coordinate bulky ancillary ligands, including phen (1,10-phenanthroline) and HDPA (2,2′- dipyridylamine), that are also intended to limit complex intercalation through steric clashes. Importantly, a rhodium

metal center was chosen due to its photophysical properties, as DNA binding rhodium complexes are known to cleave DNA strands upon photoactivation.[47] Additionally, rhodium is known to be chemically inert to ligand substitution; therefore, the complex should remain intact under physiologically relevant conditions.

1.3.2 Selective Binding of Rhodium Metalloinsertors to DNA Lesions

Initial studies of metalloinsertors explored their ability to specifically bind to mismatch sites over well-matched sites by utilizing photocleavage studies with first generation metalloinsertor $[Rh(bpy)_2(chrysi)]^{3+}$ (**Figure 1.5**). This complex was found to selectively bind to DNA base pair mismatches and cleave DNA binding sites upon photoactivation. In particular, studies comparing photocleavage within 2725 base pair linearized plasmids containing either a single CC mismatch or completely well-matched DNA found that cleavage from $[Rh(bpy)_2(chrysi)]^{3+}$ was observed specifically at the lone CC mismatch site (**Figure 1.5**). No photocleavage was detected in the Watson-Crick paired control plasmid.[48] These experiments indicated over 1000-fold selective binding to mismatches over well-matched sites.[49,48] Additionally, this first generation metalloinsertor displayed the ability to target 80% of all DNA mismatches.[49,48]

Additional studies found that $[Rh(bpy)_2(chrysi)]^{3+}$ binds to abasic sites (1- 4 x 10^6 M^{-1}) and single base bulges (10^5 M^{-1}) with high affinity and selectivity, similar to mismatch sites (3 x 10^5 M^{-1}), showcasing the versatility of these complexes to bind common DNA replication defects that are thermodynamically unstable.[50] Importantly, complex binding affinity to DNA sites correlated with the thermodynamic destabilization of each DNA lesion (K_B: abasic sites > mismatched base pair > single base bulge >> well matched base pair) regardless of sequence

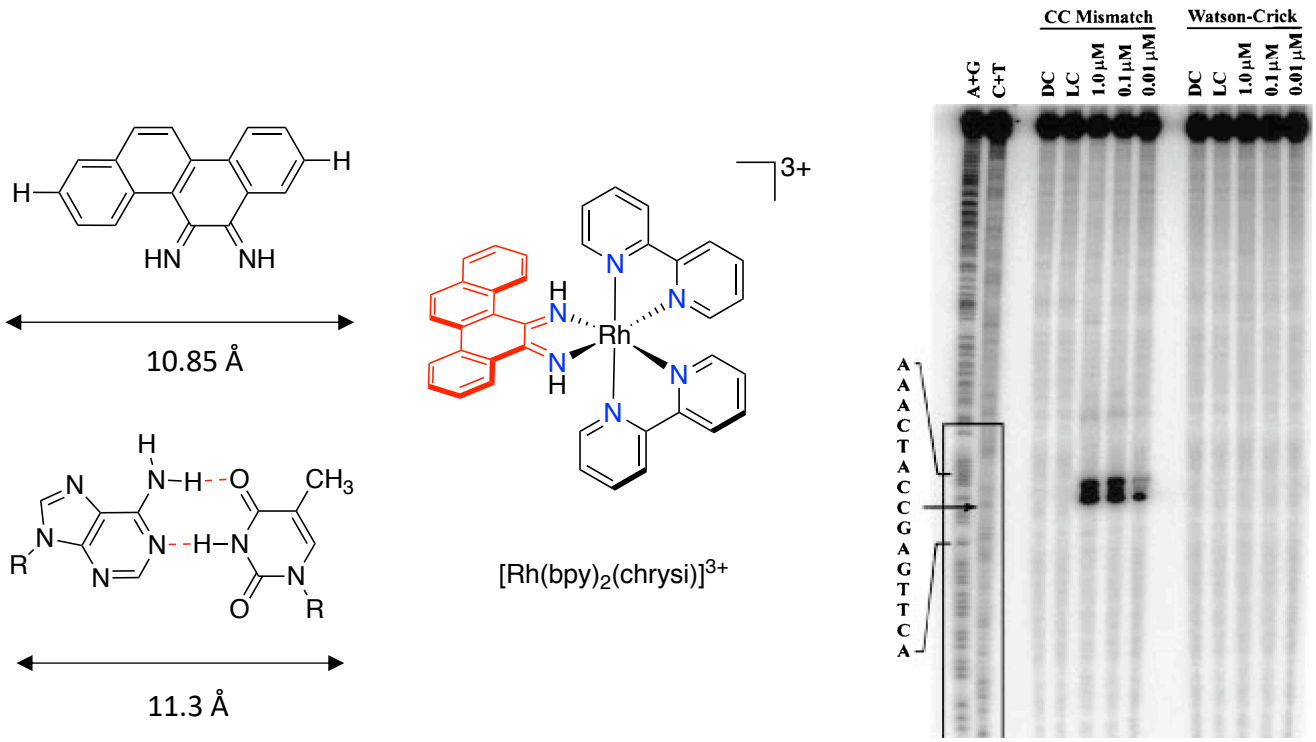

Figure 1.5 Rhodium metalloinsertor design and DNA mismatch binding specificity. (Left) Chrysi ligand (10.85 Å) is approximately 0.45 Å wider than a well matched AT base pair (11.3 Å), which decreases the favorability of complex intercalation. (Middle) Structure of first generation metalloinsertor $[Rh(bpy)_2(chrysi)]^{3+}$. The inserting chrysi ligand is shown in red. (Right) Photocleavage experiment with $[Rh(bpy)_2(chrysi)]^{3+}$ and a 2725-base pair linearized plasmid containing one CC mismatch. The arrow identifies site-selective DNA cleavage at the mismatch site. The Watson-Crick base paired equivalent plasmid does not experience cleavage, indicating a lack of complex binding to well-matched DNA sites.

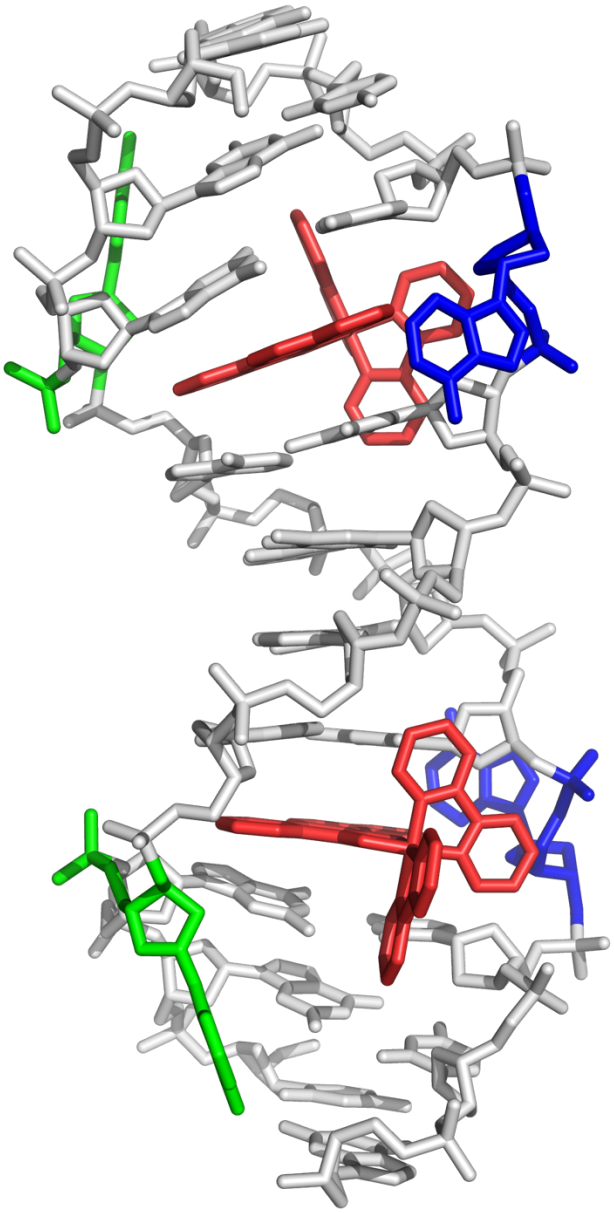

Figure 1.6 Crystal structure of first generation metalloinsertor Δ-Rh(bpy)$_2$(chrysi)$^{3+}$ bound to DNA mismatch. X-ray crystallography structure of Δ-Rh(bpy)$_2$(chrysi)$^{3+}$ (red) bound via metalloinsertion to two AA mismatches (blue and green) in the oligonucleotide 5′-CGGAAATTACCG-3′ (gray), where the mismatch site is underlined. Importantly, the mismatched bases are ejected from the DNA helix. Structure from Reference 53.[53]

context.[50–52] Notably, only the right-handed enantiomer of these metalloinsertors was found to bind to DNA.

1.3.3 Structural Studies of Rhodium Metalloinsertors Bound to DNA Mismatches

In order to further understand the activity of first generation metalloinsertors, structural studies were conducted with these complexes. In particular, X-ray crystallography and NMR experiments involving $[Rh(bpy)_2(chrysi)]^{3+}$ and DNA oligomers containing various mismatches revealed that metalloinsertor complexes interact with DNA via a completely novel binding mode called metalloinsertion (**Figure 1.6**).[53] The NMR study utilized NOESEY and COSY techniques to investigate Δ-$Rh(bpy)_2(chrysi)^{3+}$ binding to a nine base pair oligonucleotide containing one CC mismatch. This analysis found that Δ-$Rh(bpy)_2(chrysi)^{3+}$ deeply inserts into the DNA helix at the mismatch site from the minor grove side and ejects both mismatched cytosine DNA base pairs from the helix.[54] This ejection of bases allows the chrysi inserting ligand to form favorable pi stacking interactions within the helix. The complex is further stabilized by its bpy ligands interactions with the DNA backbone. Importantly, insertion of the complex at the binding site does not significantly distort the local DNA conformation and no increase in base pair rise was observed. The metalloinsertor binding mode was also observed in X-ray crystallography experiments, in which high resolution (ex. 1.1-Å) crystal structures of Δ-$Rh(bpy)_2(chrysi)^{3+}$ bound to AA and AC mismatches via the metalloinsertion binding mode were solved.[46,53,55] Note that similar to photocleavage binding experiments, only the Δ-$Rh(bpy)_2(chrysi)^{3+}$ enantiomer was found to display metalloinsertion binding. Lastly, the ejection of base pairs from the DNA helix that is characteristic of metalloinsertor binding supports the hypothesis that the rhodium complexes may not be able to target guanine containing mismatches due to their high thermodynamic stability.

1.3.4 Biological Activity of Rhodium Metalloinsertors

Given the ability of first generation metalloinsertors, particularly Δ- $Rh(bpy)_2(chrysi)]^{3+}$, to selectively bind DNA mismatches, the biological activity of these complexes was explored. In order to determine the selective cytotoxicity of the complexes towards MMR-deficient cancer cells, isogenic cell lines were used. The parent cell line HCT116, which is deficient in the MMR protein MLH1, was used to generate two daughter cell lines. HCT116O cells were transfected with human chromosome 2, which leaves the cell line MMR deficient, and HCT116N cells were transfected with human chromosome 3, which encodes for a functional MLH1 protein, ultimately making the cell line MMR proficient.[56] ELISA cellular proliferation assays were used to assess the ability of metalloinsertors $[Rh(bpy)_2(chrysi)]^{3+}$ and $[Rh(bpy)_2(phzi)]^{3+}$ to selectively inhibit cellular proliferation, and the study found that both complexes display preferential biological effects towards the HCT116O MMR-deficient cell line. Notably, the selective inhibition of cell growth was specific to the right handed enantiomer, which is consistent with structural and photocleavage studies of Δ-$Rh(bpy)_2(chrysi)^{3+}$ selectively binding to DNA mismatches.[57,58]

The impact of metalloinsertor ancillary ligands on biological activity was also explored. $[Rh(DPAE)_2(chrysi)]^{3+}$ and $[Rh(PrDPA)_2(chrysi)]^{3+}$ (DPAE = 2-(di(pyridin-2-yl)amino)ethanol, PrDPA =N-propyl-N- (pyridin-2-yl)pyridin-2-amine) are metalloinsertors with similar binding affinities ($K_B = 6.8 \times 10^6\ M^{-1}$ and $2.5 \times 10^6\ M^{-1}$, respectively). In order to better understand the mechanism for metalloinsertors generally displaying preferential potency towards MMR-deficient cells, these complexes were analyzed for their cellular uptake and subcellular localization.[59] This study revealed that $[Rh(DPAE)_2(chrysi)]^{3+}$ selectively inhibits cellular proliferation, while $[Rh(PrDPA)_2(chrysi)]^{3+}$ indiscriminately hinders cell growth in both HCT116N and HCT116O cells (**Figure 1.7**). Substitution of the terminal alcohol group on the

ancillary group with methyl groups resulted in elimination of differential biological activity. Further analysis revealed that differences in subcellular localization are critical to preferential potency in MMR-deficient cells. Specifically, $[Rh(DPAE)_2(chrysi)]^{3+}$ was found to be mainly localized to the nucleus, while $[Rh(PrDPA)_2(chrysi)]^{3+}$ displayed enhanced whole cell uptake with significant mitochondrial accumulation relative to the nucleus.[59] Ultimately, evaluation of ancillary ligands in first generation metalloinsertors suggests that complexes with enhanced lipophilicity are likely to accumulate in the mitochondria and lack biological selectivity.[58–60]

1.4 Current Rh-O Metalloinsertor Design and Activity

The most recent family of rhodium metalloinsertors is based on $[Rh(DPE)(chrysi)(phen)]^{2+}$ (DPE=1,1-di(pyridine-2-yl)ethan-1-ol) and contains an unexpected Rh-O axial coordination (**Figure 1.8**). Assessment of the biological activity of these Rh-O metalloinsertors has shown that they display enhanced potency, as much as two orders of magnitude greater than first generation complexes, within colorectal cancer (CRC) cell lines. For instance, the most promising metalloinsertor to date, $[Rh(chrysi)(phen)(PPO)]^{2+}$ (Rh-PPO), was found to be on average five times more potent than the FDA-approved chemotherapeutic cisplatin with mean IC_{50} values (50% inhibitory concentration) of 2.9 μM and 13.2 μM, respectively, across 27 CRC cell lines.[61] Furthermore, Rh-O metalloinsertors display preferential cytotoxicity towards MMR-deficient HCT116O CRC cells compared to the isogenically matched MMR-proficient HCT116N cell line.[62] In addition to showing enhanced potency and selectivity, these Rh-O metalloinsertors have displayed high tolerance to functionalization of the N^O coordinating ligand. Unlike the previous generation of metalloinsertors, which was sensitive to ancillary ligand lipophilicity, studies with Rh-O metalloinsertors have shown that chemical

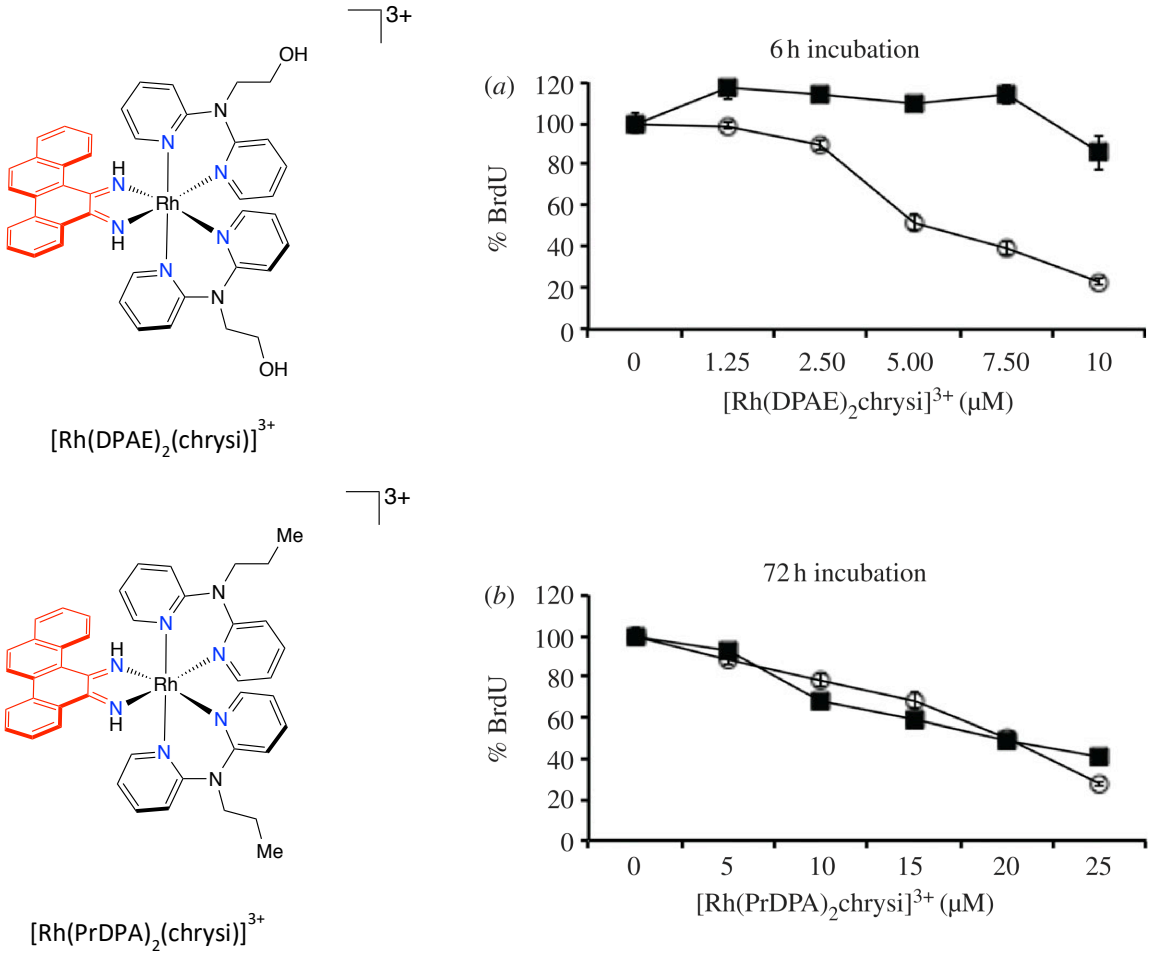

Figure 1.7 Biological activity of structurally similar first generation metalloinsertors with distinct lipophilicities. (Left) Structures of the metalloinsertors $[Rh(DPAE)_2(chrysi)]^{3+}$ and $[Rh(PrDPA)_2(chrysi)]^{3+}$, which contain slight differences in their ancillary ligands. (Right) Cellular proliferation studies of each metalloinsertor. HCT116N (MMR-proficient, closed squares) and HCT116O (MMR-deficient, open circles) cells were used in the displayed ELISA experiments. The hydrophilic complex $[Rh(DPAE)_2(chrysi)]^{3+}$ displays selective inhibition of cell growth toward MMR-deficient cells, while the lipophilic complex $[Rh(PrDPA)_2(chrysi)]^{3+}$exhibits non-selective inhibition of cellular proliferation, despite higher cellular uptake. Subcellular localization studies reveal that the lack of selectivity observed from $[Rh(PrDPA)_2(chrysi)]^{3+}$ is a result of significant complex accumulation in the mitochondria.

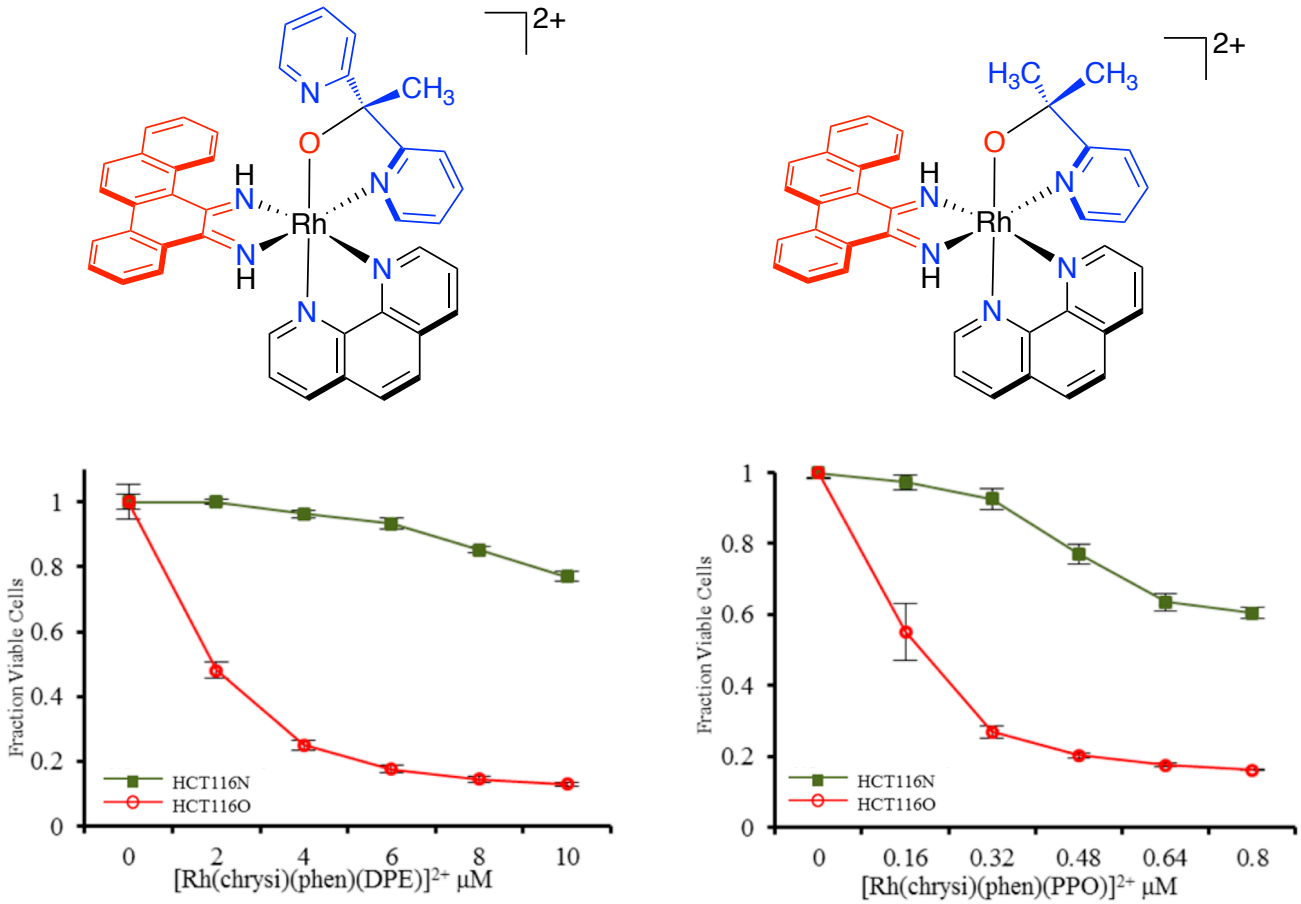

Figure 1.8 Chemical structures and cytotoxic selectivity of Rh-O metalloinsertors. Chemical structure of (top left) $[Rh(chrysi)(phen)(DPE)]^{2+}$ (Rh-DPE) and (top right) $[Rh(chrysi)(phen)(PPO)]^{2+}$ (Rh-PPO), second generation Rh-O metalloinsertors. MTT cell viability assays of cells treated with (bottom left) Rh-DPE and (bottom right) Rh-PPO. HCT116N (MMR-proficient, green squares) and HCT116O (MMR-deficient, red circles) cells were used to determine preferential toxicity of complexes towards MMR-deficient cells.

groups ranging from hydrophilic pyridines to hydrophobic hexyl chains can been incorporated into the N^O ligand, and the selective cytotoxic properties of these metalloinsertors have remained intact. Importantly, both enantiomers of Rh-O metalloinsertors display selective mismatch binding ($K_B \sim 10^6\ M^{-1}$) and preferential toxicity towards MMR-deficient cancer cells.

Notable differences between Rh-O metalloinsertors and previous complex designs involve the 2+ charge that results from the N^O coordination and the significant changes in pKa of the chrysi imine protons. Due to the higher pKa of complexes like Rh-PPO, the chrysi ligand is protonated at physiological pH, which results in a buckled ligand conformation.[62] While the exact impact of this conformational change on DNA binding remains unknown, metalloinsertion at mismatch sites is still believed to be the binding mode that affords differential toxicity toward MMR-deficient cancer cells in these complexes. Importantly, the DNA lesion generated by Rh-O metalloinsertors must be unique from first generation complexes because both the Δ and Λ enantiomers are able to selectively kill MMR-deficient cells at *nano*molar concentrations.[62,63] Structural and mechanistic studies will be essential to clarifying the unique biological activity of Rh-O metalloinsertors.

1.5 Conclusions

Development of chemotherapeutics has shifted towards designing compounds with specific biological targets that are characteristic of cancer cells. This approach aims to minimize the side effects and dose limitations associated with traditional chemotherapeutics, such as cisplatin and doxorubicin, by limiting cytotoxicity within healthy cells. Metal compounds have particular promise for targeted therapeutic development due to their distinct photophysical properties, unique reactivity, and tunable coordination geometries. Here, we present

advancements in the preclinical development of rhodium metalloinsertors, octahedral complexes targeted toward the DNA mismatches that result from MMR-deficient cancers.

1.6 References

(1) Siegel, R. L.; Miller, K. D.; Jemal, A. Cancer Statistics, 2015. *CA. Cancer J. Clin.* **2015**, *65* (1), 5–29. https://doi.org/10.3322/caac.21254.

(2) Jeggo, P. A.; Pearl, L. H.; Carr, A. M. DNA Repair, Genome Stability, and Cancer: A Historical Perspective. *Nat. Rev. Cancer* **2016**, *16* (1), 35–42. https://doi.org/10.1038/nrc.2015.4.

(3) Schärer, O. D. Nucleotide Excision Repair in Eukaryotes. *Cold Spring Harb. Perspect. Biol.* **2013**, *5* (10), 1–19. https://doi.org/10.1101/cshperspect.a012609.

(4) Wheeler, J. M. D.; Bodmer, W. F.; McC Mortensen, N. J. DNA Mismatch Repair Genes and Colorectal Cancer. *Gut* **2000**, *47* (1), 148–153. https://doi.org/10.1136/gut.47.1.148.

(5) Toft, N. J.; Arends, M. J. DNA Mismatch Repair and Colorectal Cancer. *J. Pathol.* **1998**, *185*, 123–129.

(6) Cleaver, J. E. Xeroderma Pigmentosum: A Human Disease in Which an Initial Stage of DNA Repair Is Defective. *Proc. Natl. Acad. Sci. U. S. A.* **1969**, *63* (2), 428–435. https://doi.org/10.1073/pnas.63.2.428.

(7) Duraturo, F.; Liccardo, R.; De Rosa, M.; Izzo, P. Genetics, Diagnosis, and Treatment of Lynch Syndrome: Old Lessons and Current Challenges (Review). *Oncol. Lett.* **2019**, *17* (3), 3048–3054. https://doi.org/10.3892/ol.2019.9945.

(8) Sehgal, R.; Sheahan, K.; O'Connell, P. R.; Hanly, A. M.; Martin, S. T.; Winter, D. C. Lynch Syndrome: An Updated Review. *Genes (Basel).* **2014**, *5* (3), 497–507. https://doi.org/10.3390/genes5030497.

(9) Arzimanoglou, I. I.; Gilbert, F.; Barber, H. R. Microsatellite Instability in Human Solid Tumors. *Cancer* **1998**, *82*, 1808–1820. https://doi.org/10.1016/S1357-4310(96)10055-1.

(10) Hatch, S. B.; Lightfoot, H. M.; Garwacki, C. P.; Moore, D. T.; Calvo, B. F.; Woosley, J. T.; Sciarrotta, J.; Funkhouser, W. K.; Farber, R. A. Microsatellite Instability Testing in Colorectal Carcinoma: Choice of Markers Affects Sensitivity of Detection of Mismatch Repair-Deficient Tumors. *Clin. Cancer Res.* **2005**, *11* (6), 2180–2187. https://doi.org/10.1158/1078-0432.CCR-04-0234.

(11) Louis S Goodman; Maxwell M Wintrobe; William Dameshek; Morton J Goodman; Alfred Gilman; Margaret T McLennan. Nitrogen Mustard Therapy: Use of Methyl-Bis (Beta-Chloroethyl) Amine Hydrochloride and Tris (Beta-Chloroethyl) Amine. *J. Am. Med. Assoc.* **1946**, *132* (3), 126–132. https://doi.org/10.1001/jama.1946.02870380008004.

(12) Farber, S.; Cutler, E. C.; Hawkins, J. W.; Harrison, J. H.; Peirce, E. C.; Lenz, G. G. The Action of Pteroylglutamic Conjugates on Man. *Science (80-.).* **1947**, *106* (2764), 619–621. https://doi.org/10.1126/science.106.2764.619.

(13) Chen, Y.; Jia, Y.; Song, W.; Zhang, L. Therapeutic Potential of Nitrogen Mustard Based Hybrid Molecules. *Front. Pharmacol.* **2018**, *9* (1453), 1–12. https://doi.org/10.3389/fphar.2018.01453.

(14) Mizutani, H.; Tada-Oikawa, S.; Hiraku, Y.; Kojima, M.; Kawanishi, S. Mechanism of Apoptosis Induced by Doxorubicin through the Generation of Hydrogen Peroxide. *Life Sci.* **2005**, *76* (13), 1439–1453. https://doi.org/10.1016/j.lfs.2004.05.040.

(15) Bodley, A.; Liu, L. F.; Israel, M.; Seshadri, R.; Koseki, Y.; Giuliani, F. C.; Kirschenbaum, S.; Silber, R.; Potmesil, M. DNA Topoisomerase II-Mediated Interaction of Doxorubicin and Daunorubicin Congeners with DNA. *Cancer Res.* **1989**, *49* (21), 5969–5978.

(16) McClendon, A. K.; Osheroff, N. DNA Topoisomerase II, Genotoxicity, and Cancer. *Mutat Res.* **2007**, *623* (1–2), 83–97. https://doi.org/10.1038/jid.2014.371.

(17) Zhu, H.; Sarkar, S.; Scott, L.; Danielisen, I.; Trush, M. A.; Jia, Z.; Li, Y. R. Doxorubicin Redox Biology: Redox Cycling, Topoisomerase Inhibition, and Oxidative Stress. *React Oxyg Species* **2016**, *1* (3), 189–198. https://doi.org/10.1016/j.physbeh.2017.03.040.

(18) Eom, Y. W.; Kim, M. A.; Park, S. S.; Goo, M. J.; Kwon, H. J.; Sohn, S.; Kim, W. H.; Yoon, G.; Choi, K. S. Two Distinct Modes of Cell Death Induced by Doxorubicin: Apoptosis and Cell Death through Mitotic Catastrophe Accompanied by Senescence-like Phenotype. *Oncogene* **2005**, *24* (30), 4765–4777. https://doi.org/10.1038/sj.onc.1208627.

(19) Gustavsson, B.; Carlsson, G.; MacHover, D.; Petrelli, N.; Roth, A.; Schmoll, H. J.; Tveit, K. M.; Gibson, F. A Review of the Evolution of Systemic Chemotherapy in the Management of Colorectal Cancer. *Clin. Colorectal Cancer* **2015**, *14* (1), 1–10. https://doi.org/10.1016/j.clcc.2014.11.002.

(20) Longley, D. B.; Harkin, D. P.; Johnston, P. G. 5-Fluorouracil: Mechanisms of Action and Clinical Strategies. *Nat. Rev. Cancer* **2003**, *3* (5), 330–338. https://doi.org/10.1038/nrc1074.

(21) Reilly, N. M.; Novara, L.; Di Nicolantonio, F.; Bardelli, A. Exploiting DNA Repair Defects in Colorectal Cancer. *Mol. Oncol.* **2019**, *13* (4), 681–700. https://doi.org/10.1002/1878-0261.12467.

(22) Iwaizumi, M.; Tseng-Rogenski, S.; T. R.; Carethers, J. M. DNA Mismatch Repair Proficiency Executing 5-Fluorouracil Cytotoxicity in Colorectal Cancer Cells. *Cancer Biol. Ther.* **2011**, *12* (8), 756–764. https://doi.org/10.4161/cbt.12.8.17169.

(23) Carethers, J. M.; Chauhan, D. P.; Fink, D.; Nebel, S.; Bresalier, R. S.; Howell, S. B.; Boland, C. R. Mismatch Repair Proficiency and in Vitro Response to 5-Fluorouracil. *Gastroenterology* **1999**, *117* (1), 123–131. https://doi.org/10.1016/S0016-5085(99)70558-

5.

(24) Huehls, A. M.; Huntoon, C. J.; Joshi, P. M.; Baehr, C. A.; Wagner, J. M.; Wang, X.; Lee, M. Y.; Karnitz, L. M. Genomically Incorporated 5-Fluorouracil That Escapes Ung-Initiated Base Excision Repair Blocks DNA Replication and Activates Homologous Recombination. *Mol. Pharmacol.* **2016**, *89* (1), 53–62. https://doi.org/10.1124/mol.115.100164.

(25) Zamble, D. B.; Lippard, S. J. Cisplatin and DNA Repair in Cancer Chemotherapy. *Trends Biochem. Sci.* **1995**, *20* (10), 435–439. https://doi.org/10.1016/S0968-0004(00)89095-7.

(26) Shaloam, D.; Tchounwou, P. B. Cisplatin in Cancer Therapy: Molecular Mechanisms of Action. *Eur. J. Pharmacol.* **2014**, *0*, 364–378. https://doi.org/10.1016/j.ejphar.2014.07.025.Cisplatin.

(27) Fichtinger-Schepman, A. M. J.; Lohman, P. H. M.; van der Veer, J. L.; den Hartog, J. H. J.; Reedijk, J. Adducts of the Antitumor Drug Cis-Diamminedichloroplatinum(II) with DNA: Formation, Identification, and Quantitation. *Biochemistry* **1985**, *24* (3), 707–713. https://doi.org/10.1021/bi00324a025.

(28) Takahara, P. M.; Frederick, C. a.; Lippard, S. J. Crystal Structure of the Anticancer Drug Cisplatin Bound to Duplex DNA. *J. Am. Chem. Soc.* **1996**, *118* (10), 12309–12321. https://doi.org/10.1021/ja9625079.

(29) Gelasco, A.; Lippard, S. J. NMR Solution Structure of a DNA Dodecamer Duplex Containing a Cis- Diammineplatinum(II) d(GpG) Intrastrand Cross-Link, the Major Adduct of the Anticancer Drug Cisplatin. *Biochemistry* **1998**, *37* (26), 9230–9239. https://doi.org/10.1021/bi973176v.

(30) Zaki, M.; Arjmand, F.; Tabassum, S. Current and Future Potential of Metallo Drugs:

Revisiting DNA-Binding of Metal Containing Molecules and Their Diverse Mechanism of Action. *Inorganica Chim. Acta* **2016**, *444*, 1–22. https://doi.org/10.1016/j.ica.2016.01.006.

(31) Alessio, E.; Messori, L. NAMI-A and KP1019/1339, Two Iconic Ruthenium Anticancer Drug Candidates Face-to-Face: A Case Story in Medicinal Inorganic Chemistry. *Molecules* **2019**, *24* (1995), 1–20. https://doi.org/10.3390/molecules24101995.

(32) Bellacosa, A. Functional Interactions and Signaling Properties of Mammalian DNA Mismatch Repair Proteins. *Cell Death Differ.* **2001**, *8* (11), 1076–1092. https://doi.org/10.1038/sj.cdd.4400948.

(33) Modrich, P. Mechanisms in Eukaryotic Mismatch Repair. *J. Biol. Chem.* **2006**, *281* (41), 30305–30309. https://doi.org/10.1074/jbc.R600022200.

(34) Kunkel, T. A.; Erie, D. A. Eukaryotic Mismatch Repair in Relation to DNA Replication. *Annu. Rev. Genet.* **2015**, *49* (1), 291–313. https://doi.org/10.1146/annurev-genet-112414-054722.

(35) Li, G. M. Mechanisms and Functions of DNA Mismatch Repair. *Cell Res.* **2008**, *18* (1), 85–98. https://doi.org/10.1038/cr.2007.115.

(36) Hsieh, P.; Yamane, K. DNA Mismatch Repair: Molecular Mechanism, Cancer, and Ageing. *Mech. Ageing Dev.* **2008**, *129* (7), 391–407. https://doi.org/10.1016/j.mad.2008.02.012.DNA.

(37) Bracht, K.; Nicholls, A. M.; Liu, Y.; Bodmer, W. F. 5-Fluorouracil Response in a Large Panel of Colorectal Cancer Cell Lines Is Associated with Mismatch Repair Deficiency. *Br. J. Cancer* **2010**, *103* (3), 340–346. https://doi.org/10.1038/sj.bjc.6605780.

(38) Fink, D.; Aebi, S.; Howell, S. B. The Role of DNA Mismatch Repair in Drug Resistance. *Clin. Cancer Res.* **1998**, *4* (1), 1–6. https://doi.org/10.3929/ethz-a-001915508.

(39) Le, D. T.; Uram, J. N.; Wang, H.; Bartlett, B. R.; Kemberling, H.; Eyring, A. D.; Skora, A. D.; Luber, B. S.; Azad, N. S.; Laheru, D.; et al. PD-1 Blockade in Tumors with Mismatch-Repair Deficiency. *N. Engl. J. Med.* **2015**, *372* (26), 2509–2520. https://doi.org/10.1056/NEJMoa1500596.

(40) Zhao, P.; Li, L.; Jiang, X.; Li, Q. Mismatch Repair Deficiency/Microsatellite Instability-High as a Predictor for Anti-PD-1/PD-L1 Immunotherapy Efficacy. *J. Hematol. Oncol.* **2019**, *12* (1), 1–14. https://doi.org/10.1186/s13045-019-0738-1.

(41) Alsaab, H. O.; Sau, S.; Alzhrani, R.; Tatiparti, K.; Bhise, K.; Kashaw, S. K.; Iyer, A. K. PD-1 and PD-L1 Checkpoint Signaling Inhibition for Cancer Immunotherapy: Mechanism, Combinations, and Clinical Outcome. *Front. Pharmacol.* **2017**, *8* (AUG), 1–15. https://doi.org/10.3389/fphar.2017.00561.

(42) McDermott, J; Jimeno, A. Pembrolizumab: PD-1 Inhibition as a Therapeutic Strategy in Cancer. *Drugs of Today* **2015**, *51* (1), 7–20.

(43) Boyle, K. M.; Barton, J. K. Targeting DNA Mismaches with Rhodium Metalloinsertors. *Inorganica Chim. Acta* **2016**, *452*, 3–11. https://doi.org/110.1016/j.bbi.2017.04.008.

(44) Allawi, H. T.; Santalucia, J. Thermodynamics and NMR of Internal G·T Mismatches in DNA. *Biochemistry* **1997**, *36* (34), 10581–10594. https://doi.org/10.1021/bi962590c.

(45) Allawi, H. T.; SantaLucia, J. Nearest-Neighbor Thermodynamics of Internal A·C Mismatches in DNA: Sequence Dependence and PH Effects. *Biochemistry* **1998**, *37* (26), 9435–9444. https://doi.org/10.1021/bi9803729.

(46) Zeglis, B. M.; Pierre, V. C.; Kaiser, J. T.; Barton, J. K. A Bulky Rhodium Complex Bound to an Adenosine-Adenosine DNA Mismatch: General Architecture of the Metalloinsertion Binding Mode. *Biochemistry* **2009**, *48* (20), 4247–4253.

https://doi.org/10.1021/bi900194e.

(47) Sitlani, A.; Long, E. C.; Pyle, A. M.; Barton, J. K. DNA Photocleavage by Phenanthrenequinone Diimine Complexes of Rhodium(III): Shape-Selective Recognition and Reaction. *J. Am. Chem. Soc.* **1992**, *114* (7), 2303–2312. https://doi.org/10.1021/ja00033a003.

(48) Jackson, B. A.; Alekseyev, V. Y.; Barton, J. K. A Versatile Mismatch Recognition Agent: Specific Cleavage of a Plasmid DNA at a Single Base Mispair. *Biochemistry* **1999**, *38* (15), 4655–4662. https://doi.org/10.1021/bi990255t.

(49) Jackson, B. A.; Barton, J. K. Recognition of Base Mismatches in DNA by 5,6-Chrysenequinone Diimine Complexes of Rhodium(III): A Proposed Mechanism for Preferential Binding in Destabilized Regions of the Double Helix. *Biochemistry* **2000**, *39* (20), 6176–6182. https://doi.org/10.1021/bi9927033.

(50) Zeglis, B. M.; Boland, J. A.; Barton, J. K. Recognition of Abasic Sites and Single Base Bulges in DNA by a Metalloinsertor. *Biochemistry* **2009**, *48* (5), 839–849. https://doi.org/10.1038/jid.2014.371.

(51) Zeglis, B. M.; Boland, J. A.; Barton, J. K. Targeting Abasic Sites and Single Base Bulges in DNA with Metalloinsertors. *J Am Chem Soc* **2008**, *130* (24), 7530–7531. https://doi.org/10.1038/jid.2014.371.

(52) Brunner, J.; Barton, J. K. Site-Specific DNA Photocleavage by Rhodium Intercalators Analyzed by MALDI-TOF Mass Spectrometry. *J. Am. Chem. Soc.* **2006**, *128* (21), 6772–6773. https://doi.org/10.1021/ja0612753.

(53) Zeglis, B. M.; Pierre, V. C.; Kaiser, J. T.; Barton, J. K. A Bulky Rhodium Complex Bound to an Adenosine-Adenosine DNA Mismatch: General Architecture of the Metalloinsertion

Binding Mode. *Biochemistry* **2009**, *48* (20), 4247–4253. https://doi.org/10.1021/bi900194e.A.

(54) Cordier, C.; Pierre, C.; Barton, J. K. Insertion of a Bulky Rhodium Complex into a DNA Cytosine - Cytosine Mismatch : An NMR Solution Study. *J. Am. Chem. Soc.* **2007**, *129* (2), 12287–12295.

(55) Pierre, C.; Kaiser, J. T.; Barton, J. K. Insights into Finding a Mismatch through the Structure of a Mispaired DNA Bound by a Rhodium Intercalator. *Proc. Natl. Acad. Sci.* **2007**, *104* (2), 429–434.

(56) De Las Alas, M. M.; Aebi, S.; Fink, D.; Howell, S. B.; Los, G. Loss of DNA Mismatch Repair: Effects on the Rate of Mutation to Drug Resistance. *J. Natl. Cancer Inst.* **1997**, *89* (20), 1537–1541. https://doi.org/10.1093/jnci/89.20.1537.

(57) Hart, J. R.; Glebov, O.; Ernst, R. J.; Kirsch, I. R.; Barton, J. K. DNA Mismatch-Specific Targeting and Hypersensitivity of Mismatch-Repair-Deficient Cells to Bulky Rhodium(III) Intercalators. *Proc. Natl. Acad. Sci.* **2006**, *103* (42), 15359–15363. https://doi.org/10.1073/pnas.0607576103.

(58) Komor, A. C.; Schneider, C. J.; Weidmann, A. G.; Barton, J. K. Cell-Selective Biological Activity of Rhodium Metalloinsertors Correlates with Subcellular Localization. *J. Am. Chem. Soc.* **2012**, *134* (46), 19223–19233. https://doi.org/10.1021/ja3090687.

(59) Weidmann, A. G.; Komor, A. C.; Barton, J. K. Biological Effects of Simple Changes in Functionality on Rhodium Metalloinsertors. *Philos. Trans. R. Soc. A Math. Phys. Eng. Sci.* **2013**, *371* (1995). https://doi.org/10.1098/rsta.2012.0117.

(60) Modica-Napolitano, J. S.; Aprille, J. R. Delocalized Lipophilic Cations Selectively Target the Mitochondria of Carcinoma Cells. *Adv. Drug Deliv. Rev.* **2001**, *49* (1–2), 63–70.

https://doi.org/10.1016/S0169-409X(01)00125-9.

(61) Boyle, K. M.; Nano, A.; Day, C.; Barton, J. K. Cellular Target of a Rhodium Metalloinsertor Is the DNA Base Pair Mismatch. *Chem. Eur. J.* **2019**, *25*, 1–7. https://doi.org/10.1002/chem.201900042.

(62) Komor, A. C.; Barton, J. K. An Unusual Ligand Coordination Gives Rise to a New Family of Rhodium Metalloinsertors with Improved Selectivity and Potency. *J. Am. Chem. Soc.* **2014**, *136* (40), 14160–14172. https://doi.org/10.1021/ja5072064.

(63) Boyle, K. M.; Barton, J. K. A Family of Rhodium Complexes with Selective Toxicity toward Mismatch Repair-Deficient Cancers. *J. Am. Chem. Soc.* **2018**, *140* (16), 5612–5624. https://doi.org/10.1021/jacs.8b02271.

Chapter 2

IN VIVO ANTICANCER ACTIVITY OF A RHODIUM METALLOINSERTOR IN THE HCT116 XENOGRAFT TUMOR MODEL*

S.D.T. participated in designing the project, synthesized complex for the studies, performed and analyzed experiments, and participated in composing the manuscript.

2.1 Introduction

Metal complexes have long been used to target DNA in order to achieve efficient cytotoxicity in cancerous cells.[1–4] Several of the leading chemotherapeutic drugs, such as cisplatin and oxaliplatin, are metal complexes that irreversibly bind DNA and inhibit DNA replication. Due to the efficacy of these therapeutics, 10-20% of all cancer patients are prescribed platinum-based drugs.[5] While these platinum complexes successfully cause cell death within cancerous tissues, they also result in toxicity towards healthy, often rapidly dividing cells, leading to side effects that include gastrointestinal toxicity and nephrotoxicity. [6,7] Additionally, the majority of patients treated with these classic DNA-targeted chemotherapeutics develop resistance, which causes these therapies to lose effectiveness.[8,9,10] As a result, much research has shifted focus towards developing chemotherapeutics with improved selectivity for killing tumor cells.[11]

Our laboratory has designed transition metal complexes that specifically target DNA base pair mismatches, such as those that result from polymerase errors during DNA replication. While in healthy, normal cells these mismatches are repaired by the mismatch repair (MMR) protein machinery, certain cancerous tissues have malfunctioning MMR, which causes mismatch sites

---

*Adapted from Threatt, S. D.; Synold, T. W.; Wu, J.; Barton, J.K. In Vivo Anticancer Activity of a Rhodium Metalloinsertor in the HCT116 Xenograft Tumor Model. *Proc. Natl. Acad. Sci. USA*. **2020**, 117, 17535-17542. DOI: 10.1073/pnas.2006569117
Dr. Nathan Dalleska assisted in optimizing the ICP-MS experiments to detect rhodium and platinum content in tissues.

to persist, ultimately yielding increased mutations and enhanced cancerous transformations.[12] MMR deficiencies are a hallmark for approximately 15% of colorectal cancer cases and up to 20% of all solid tumors. Colorectal cancer patients often undergo genetic screens, including for MMR mutations and microsatellite instability, which help to guide clinical treatment decisions.[13,14] Low responsiveness is often apparent with traditional chemotherapeutics, such as fluoropyrimidines and platinum therapy, particularly leading to the build-up of resistance. Recent reports have found that microsatellite instability high (MSI-H) and MMR-deficient patients have been particularly responsive to anti-PD-1/PD-L1 immunotherapies with overall response rates of 40%. While developments with immunotherapies have been promising for treating MMR-deficient cancers, there is still a strong need for additional therapeutic options. [15]

Designing metal complexes capable of selectively targeting the DNA mismatches that are associated with MMR-deficient cancers and exploring their biological activity has been an objective of our group and others.[16,17] We have developed transition metal complexes, specifically rhodium compounds, that bind to thermodynamically destabilized DNA mismatch sites via a binding mode termed metalloinsertion. In this binding mode, the metal complex inserts at the site of the mismatched base pair via its planar and sterically expansive inserting ligand, chrysi (5,6-chrysenequinone diimine), resulting in the ejection of the destabilized mismatch base pair from the DNA helix.[18 19]

Early generation metalloinsertor complexes, such as $[Rh(bpy)_2(chrysi)]^{3+}$ were characterized by an all N^N coordination environment and initial studies with these metalloinsertors revealed highly selective binding to mismatch sites. Remarkably, the *in vitro* mismatch binding of metalloinsertors translated into selective cellular properties, in which preferential inhibition of cellular proliferation was observed for MMR-deficient cells over

MMR-proficient cells. However, observing selective cellular inhibition required micromolar concentrations of these first-generation compounds. Additionally, complexes studied that contained lipophilic ligands to enhance cellular uptake showed a loss of selective cellular toxicity.[20,21] Second generation complexes containing an N^O coordination and lower overall charge yielded compounds that are selectively cytotoxic towards MMR-deficient cells at nanomolar concentrations. Currently, our leading rhodium metalloinsertor complex, $[Rh(chrysi)(phen)(PPO)]Cl_2$ (Rh-PPO), where phen = 1,10-phenanthroline and PPO = 2-(pyridine-2-yl)propan-2-ol, displays highly potent and selective cytotoxicity towards the MMR-deficient human colorectal cancer (CRC) cell line HCT116O compared to HCT116N cells, the matched MMR-proficient cell line.[22]

Furthermore, a study assessing the cytotoxicity of Rh-PPO in 27 CRC cell lines spanning the four subtypes of CRC, as well as both MMR-deficient and MMR-proficient phenotypes, provided additional support to the hypothesis that the targets of Rh-PPO are DNA base pair mismatches.[23,24] Rh-PPO was found to be on average five times more potent than the FDA-approved chemotherapeutic cisplatin with mean IC_{50} values (50% inhibitory concentration) of 2.9 μM and 13.2 μM, respectively across CRC cell lines. Specifically for HCT116O MMR-deficient cells, Rh-PPO displays a half maximal inhibitory concentration (IC_{50}) of 250 nM compared to 27.5 μM for oxaliplatin, the comparator used in this study. **Figure 2.1** shows structures from both generations of metalloinsertors along with oxaliplatin.

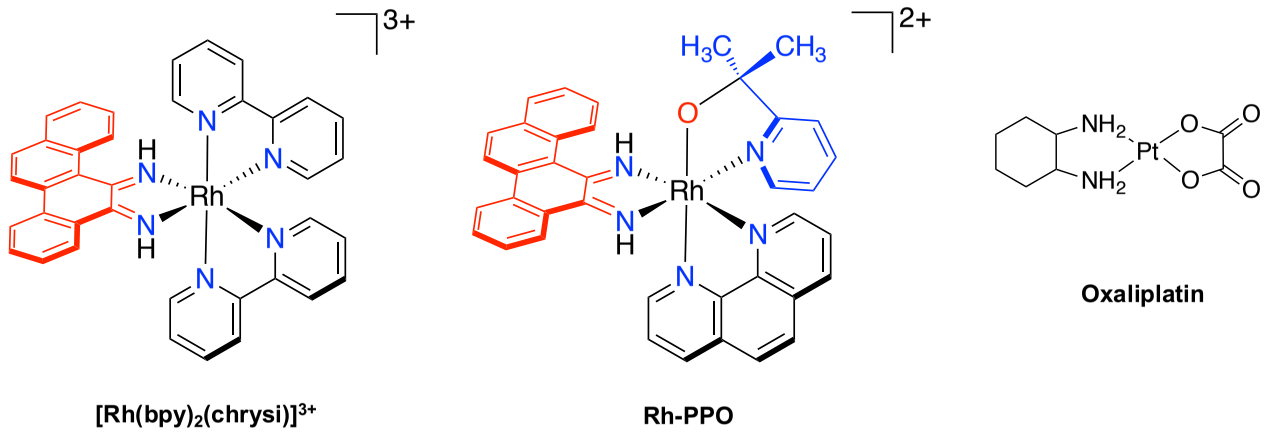

Figure 2.1 Chemical structures of compounds relevant to this *in vivo* study. Chemical structure of (left) $[Rh(bpy)_2(chrysi)]^{3+}$, a first generation metalloinsertor, (middle) $[Rh(chrysi)(phen)(PPO)]^{2+}$ (Rh-PPO), a second generation metalloinsertor, and (right) oxaliplatin, a widely used FDA-approved chemotherapeutic. The inserting chrysi ligand is shown in red and the axial PPO ligand is displayed in blue.

Given the demonstrated significant and selective toxicity towards MMR-deficient cancer cells, and the high cellular potency observed with Rh-PPO, we have continued to explore the potential application of this rhodium metalloinsertor as a targeted chemotherapeutic. Here, we report *in vivo* pharmacokinetic and efficacy studies evaluating Rh-PPO in an HCT116 xenograft tumor model. The results presented demonstrate that Rh-PPO displays significant anticancer effects and potency *in vivo*, highlighting the therapeutic potential of this class of metal complexes targeted to bind DNA mismatches.

2.2 Experimental Methods

2.2.1 Materials

All chemicals, reagents, and solvents used for synthesis were commercially available, unless otherwise noted, and used as received. Organic solvents were purchased from Sigma Aldrich unless otherwise noted (St. Louis, MO). Water was purified using the Millipore Milli-Q system (Milford, MA, USA). Oxaliplatin was purchased from Alfa Aesar (Haverhill, MA). HPLC-grade acetonitrile (ACN) and methanol were purchased from Fisher Scientific (Fair Lawn, NJ, USA). Formic acid (99% pure) was purchased from Acros organic (New Jersey, USA). Analytical standards for Rh, Pt, and transition metals were purchased from Analytical West, Ultra Scientific, and Sigma Aldrich. Redistillation purified nitric acid was purchased from Sigma Aldrich and used for all ICP-MS experiments.

Sep-Pak C18 solid-phase extraction (SPE) cartridges were acquired from Waters Chemical Co (Milford, MA). All HPLC metal complex purifications were carried out on a Hewlett-Packard 1100 HPLC. All UV-Visible spectroscopic experiments were performed on a Cary 100 spectrometer. Cell culture media and supplements were purchased from Life

Technologies (Carlsbad, CA). Cell lines used in the experiment were purchased from ATCC (Manassas, VA). Tissue culture flasks and plates were obtained from Corning (Corning, NY).

2.2.2 Synthesis and Purification of Rhodium Metalloinsertor Compounds

[Rh(chrysi)(phen)(2-(pyridine-2-yl)propan-2-ol]Cl_2 (Rh-PPO) and [Rh(chrysi)(phen)(1-Phenyl-1-(pyridine-2-yl)ethan-1-ol]Cl_2 (Rh-PPE) were synthesized following published methodology.[22] The purification of Rh-PPO and Rh-PPE was modified from the literature preparations as follows: the crude reaction mixture of Rh-PPO or Rh-PPE was loaded onto a C18 SPE cartridge equilibrated with 15% acetonitrile in 0.1% TFA(aq). The concentration of acetonitrile was gradually increased and the complex eluted from the SPE cartridge with 25% acetonitrile in 0.1% TFA(aq), then dried *in vacuo*. The SPE purified complex was then dissolved in minimal acetonitrile before HPLC purification and filtered. Rh-PPO was purified by HPLC using an isocratic method of 25:75 MeCN:H_2O + 0.1% TFA over 60 min. Rh-PPE was purified by HPLC using a gradient elution from 85:15 to 5:95 H_2O + 0.1% TFA:ACN over 30 minutes. Peaks corresponding to the desired products were verified using ESI-MS and were collected using an automatic fraction collector or by hand. The chloride salts were obtained from a Sephadex QAE anion exchange column equilibrated with 0.1 M $MgCl_2$ and complex structure was verified using NMR. Before drug solution preparation, Rh-PPO was precipitated by dissolving in minimal EtOH, then generous addition of diethyl either. The resulting red precipitate was filtered using a fine glass frit and thoroughly dried on the lyophilizer.

2.2.3 Concentration Determination of Rhodium Complexes

A stock solution of each rhodium metalloinsertor was made in MilliQ water and a UV-Vis trace was recorded. The concentration of stock solution was then determined by using the Cary UV-Vis instrument, as well as molar absorptivity values from the literature.[21] The

following molar absorptivity values were used to estimate the concentration of Rh-PPO in water: UV−vis (H_2O, pH 7.0): 270 nm (122,400 M^{-1} cm^{-1}), 300 nm (41,600 M^{-1} cm^{-1}), 430 nm (12,300 M^{-1} cm^{-1}). The following molar absorptivity values were used to estimate the concentration of Rh-PPE in water: UV−vis (H_2O, pH 7.0): 270 nm (165,800 M^{-1} cm^{-1}), 300 nm (56,300 M^{-1} cm^{-1}), 430 nm (16,100 M^{-1} cm^{-1}).

2.2.4 Cell Culture

HCT116 cells were grown and maintained using McCoy's 5A (modified) media supplemented with 10% fetal bovine serum (FBS) and 100 units/mL penicillin and streptomycin. The cells were incubated in tissue culture flasks at 37°C in a 5% CO_2 atmosphere. Standard procedures for entering and exiting cryostorage were followed, as well as methods for subculturing HCT116 cells. Cell solutions of 2.5 x 10^6 cells/100 µL media were made for tumor inoculation using only McCoy's 5A (modified) media supplemented with 10% FBS.

2.2.5 Mice Preclinical Assessment Studies

All animal experiments were done in accordance with protocols approved by the Institutional Animal Care and Use Committees at City of Hope. All experiments were performed in accordance with the City of Hope policies on the care, welfare, and treatment of laboratory animals. For all experiments, strain NOD-*scid* IL2Rgamma^{null} (NSG) mice from City of Hope Animal Resources Center were used (Duarte, CA). Each cage contained up to four mice and animals were offered standard diet and water. All animal studies were performed with the chloride salt of the metalloinsertor. Rh-PPO and Rh-PPE concentrations were determined by UV-Vis using the extinction coefficients of the complex.[22]

2.2.6 Maximum Tolerated Dose (MTD) Studies

NSG mice were weighed then received intraperitoneal injections of Rh-PPO dissolved in saline at concentrations of 1, 2, 5, or 15 mg drug per kg mouse (mpk). Intraperitoneal injections were administered once daily for 10 consecutive days. Clinical observations were made daily and mouse body weights were recorded. At the end of the study, surviving animals were euthanized using carbon dioxide.

2.2.7 *In Vivo* Tumor Growth Inhibition and Survival Rate

NSG mice, weighing 23-34 g, were injected subcutaneously in the right flank with 100 µL HCT116 cells (2.5 x 10^6 cells) suspended in McCoy's media. Tumors were allowed to grow until they reached ~100 mm^3, 11-12 days after tumor inoculation. Tumor volumes (TV) were estimated by measuring the width (W) and length (L) of the tumor using a digital caliper and calculated based on the following formula: $TV = W^2L/2$.[25]

2.2.8 *In vivo* Intraperitoneal Efficacy Experiments

Mice were randomly assigned to each treatment group, such that each group had 10-13 mice and an average tumor volume of ~100 mm^3. Mice were allocated to the following treatment groups: vehicle (0.9% NaCl), Rh-PPO at 0.5 mpk, Rh-PPO at 1 mpk, and oxaliplatin at 7.5 mpk. Rh-PPO was dissolved in saline at the MTD (1 mpk) and MTD/2 (0.5 mpk) and administered intraperitoneally 3-4 times per week. Saline was administered intraperitoneally to the control group 3-4 times per week. Clinical grade oxaliplatin (Alfa Aesar) was dissolved in 5% dextrose using sonication and administered intraperitoneally two times per week, as reported in previous studies.[26] Two *in vivo*, intraperitoneal efficacy experiments were conducted, and the specific dosing schedules for each study and treatment group are outlined in **Figure 2.2**. Mouse body weights and tumor volumes were measured twice per week over the course of each study.

2.2.8.1 Efficacy Experiment #1

This study contained the following number of mice per dosing group: saline (n=13), Rh-PPO at 0.5 mpk (n=10), Rh-PPO at 1 mpk (n=10), and oxaliplatin at 7.5 mpk (n=11). As described in **Figure 2.2**, mice in all treatment groups in Efficacy Experiment #1 received 2 mL bolus, subcutaneous injections of saline twice per week in order to increase drug tolerability (Day 18, 20, 25, 27, and 32). The specific dosing schedule for each treatment group in Efficacy Experiment #1 is outlined in **Figure 2.2**.

2.2.8.2 Efficacy Experiment #2

This study contained 10 mice in each treatment group. The specific dosing schedule for each treatment group in Efficacy Experiment #2 is outlined in **Figure 2.2**. Note that the drug dosing schedule was altered after Day 14 to increase tolerability of Rh-PPO.

2.2.8.3 Survival Rate Studies

Survival rate was determined by comparing the number of animals alive at different time points during the study to the total number of animals at the start of the study. Mice were removed from the study if: found dead in their cage, declining health necessitated euthanasia, or tumor diameter exceeded 15 mm. These parameters were used to construct a Kaplan-Meier survival curve. Increase in life span (ILS) was calculated based on the following equation: $ILS = (Days_T - Days_C) / Days_C$, where $Days_C$ = days survived by control group mice and $Days_T$ = days survived by treatment group mice.

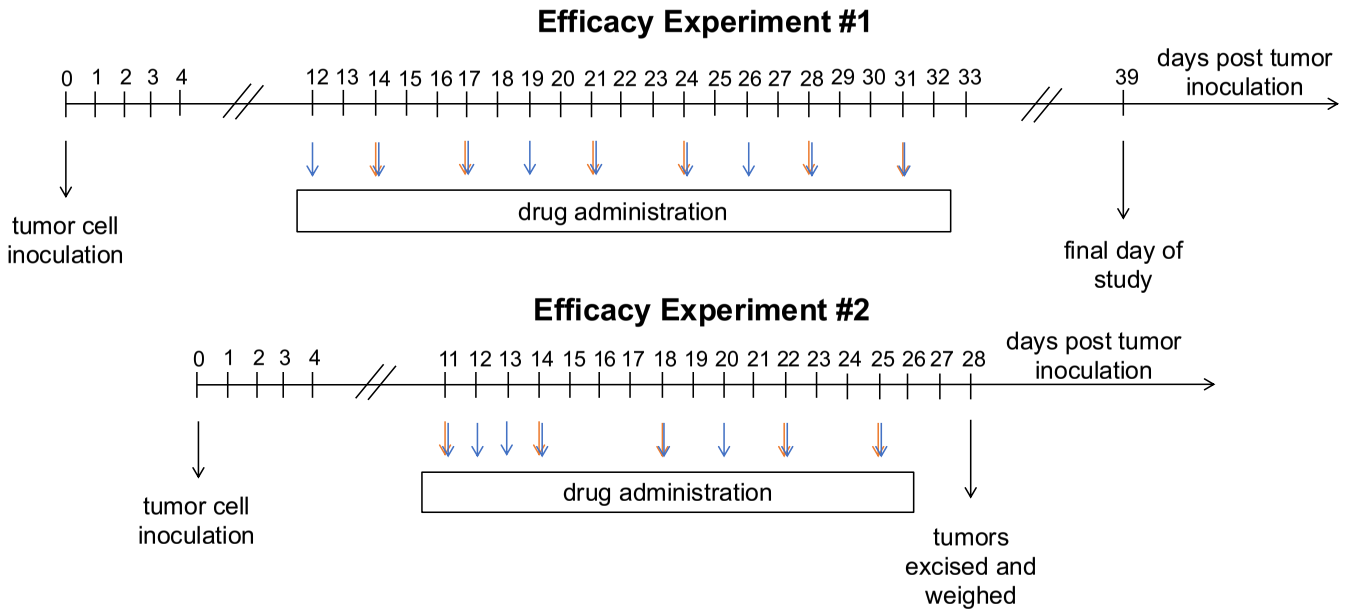

Figure 2.2 Drug treatment schedules for Rh-PPO *in vivo* efficacy experiments with intraperitoneal drug administration. (Top) Efficacy Experiment #1 treatment schedule for the *in vivo* study monitoring tumor volume and survival rate over time of mice treated intraperitoneally. Mice in all treatment groups received 2 mL bolus, subcutaneous, hydrating doses of saline on Day 18, 20, 25, 27, and 32. (Bottom) Efficacy Experiment #2 treatment schedule for the *in vivo* study assessing final tumor weight of mice receiving intraperitoneal drug treatment. Blue arrow indicates when mice in the saline and Rh-PPO at 0.5 mpk and 1 mpk treatment groups were administered drug doses. Orange/blue double arrow denotes when mice in the saline, oxaliplatin at 7.5 mpk, and Rh-PPO at 0.5 mpk and 1 mpk treatment groups were administered drug doses.

ILS was determined to compare the survival rates of the different treatment groups. Each treatment group started with 10-13 mice. After treatment completion, mice were euthanized using carbon dioxide, and tumors were dissected and weighed. In three mice per treatment group in Efficacy Experiment #1, major organs (spleen, kidneys, liver, heart, skeletal muscle, lungs, small intestine, colon, stomach, cecum, testes, epididymis, tumor, tibia/femur and brain) were harvested, cut in half, and one half fixed in 10% formalin and the other half frozen on dry ice for further analysis.

2.2.8.4 Tumor Weight Analysis

In Efficacy Experiment #2, 18 days after starting treatment, all mice were euthanized using carbon dioxide and HCT116 xenograft tumors were dissected, weighed, and frozen on dry ice. Tumor weights were analyzed using the Anova test to determine the significance of the results. In three mice per treatment group in Efficacy Experiment #2, major organs (spleen, kidneys, liver, heart, skeletal muscle, lungs, small intestine, colon, stomach, cecum, testes, epididymis, tumor, Tibia/Femur and brain) were harvested, cut in half, and one half fixed in 10% formalin and the other half frozen on dry ice for further analysis.

2.2.9 Tumor Volume and Final Tumor Weights Analysis for Intratumoral Efficacy Experiment

Female NSG mice (28-37 g) were injected subcutaneously with HCT116 cells (2.5×10^6) suspended in McCoy's media; 100 µL injections into the right flank. Tumors were allowed to grow until they reached ~90 mm^3 (11 days). Mice were then randomly assigned to each treatment group with 5 or 10 mice in each, so each group had an average tumor volume of 80-90 mm^3. Mice were assigned to the following treatment groups: saline (n=5) and Rh-PPO at 1 mpk (n=10). Rh-PPO was dissolved in saline at the MTD (1 mpk) and administered intratumorally

based on the schedule outlined in **Figure 2.9**. Saline was administered intratumorally to the control group based on the same schedule. Mouse body weights and tumor volumes were measured twice per week over the course of the study, and tumors were excised and weighed on day 18 of the study. Tumor volumes (TV) were estimated by measuring the width (W) and length (L) of the tumor using a digital caliper and calculated based on the following formula: $TV = W^2L/2$.

2.2.10 Pharmacokinetic Studies for Intraperitoneal Mouse Experiments

2.2.10.1 Determination of Rh-PPO *in vivo* Biodistribution

In Efficacy Experiment #1, after the final Rh-PPO drug dose was administered, blood was collected via cardiac puncture using a syringe and immediately transferred to heparinized blood collection vials on ice at time intervals of 0.5, 1, 2, 4, and 8 hr post administration (three mice per Rh-PPO treatment group per time point). The blood samples were centrifuged at 15,000 g at RT for 5 min, and the supernatant plasma was transferred to 1.5 mL microcentrifuge tubes and maintained at -80^{o}C until analysis. Plasma samples were prepared for LC-MS/MS analysis by mixing 20 µl mouse plasma sample with 10 µl 50% acetonitrile in water in a 0.5 mL low retention microcentrifuge tube. Then, 100 µl of 500ng/mL Rh-PPE internal standard (INS) in acetonitrile was added to the sample tube and the solution was vortexed for 3 min. The sample was then centrifuged at 14,800 g for 5 min at 4°C and 20 µl of the resulting supernatant was mixed with 180 µl 25% acetonitrile in 10mM NH_4OAC buffer (pH 3.2). Finally, 2 µl of the resulting sample was analyzed via LC-MS/MS.

2.2.10.1.1 LC-MS/MS Analysis of Plasma Samples

Standard Rh-PPO and internal standard (INS) Rh-PPE solutions were made as needed and concentration determined via UV-Vis. Mouse plasma for preparation of standards and

quality controls (QC) were obtained from BioChemed Services. LC-MS/MS analysis was performed using a Waters Acquity UPLC system (Milford, MA, USA) interfaced with a Waters Quattro Premier XE Mass Spectrometer. HPLC separation was achieved using a Luna 3µ Phenyl-Hexyl 100 x 2 mm column (Phenomenex, Torrance, CA, USA) proceeded by a Phenomenex Phenyl guard column (Torrance, CA, USA). The column temperature was maintained at 40°C. The mobile phase consisted of A (0.1% formic acid, 10% ACN in water) and B (0.1% formic acid in acetonitrile). The following gradient program was used: 0% B (0min, 0.3 ml/min), 8% B (3.2 min, 0.3ml/min), 60% B (4.0 min, 0.3ml/min), 85% B (5.5 min, 0.3 ml/min), 0% B (5.6 min, 0.3ml/min), 0% B (8.5 min, 0.3ml/min). The total run time was 8.5 minutes. The auto-injector temperature was maintained at 5°C. The strong needle wash solution was 0.1% formic acid in 50% ACN and 50% water and the weak needle wash solution was 0.1 % formic acid and 10% ACN in water. The electrospray ionization source of the mass spectrometer was operated in positive ion mode with a cone gas flow of 25 L/hr and a desolvation gas flow of 900 L/hr. The capillary voltage was set to 0.7 kV for both Rh-PPO and INS (Rh-PPE), and the cone voltages were optimized to 45 V for Rh-PPO and 51 V for INS, respectively. The collision voltages were set to 48 V for both Rh-PPO and Rh-PPE. The source temperature was 125°C and the desolvation temperature was 480°C. A solvent delay program was used from 0 to 3.8 minutes and from 5.2 to 8.5 minutes for Rh-PPO and INS, to minimize mobile phase to flow to the source. MassLynx version 4.1 software was used for data acquiring and processing.

2.2.10.2 Chicken Liver Test Digestion

A Rh/Pt solution with 100 ppm rhodium and 100 ppb platinum was made using 2% nitric acid and ICP-MS standards. Approximately 1 gram of purchased chicken liver was manually homogenized. Then, chicken liver was separated into three 50 mL digitubes. 3 mL conc. HNO_3

(aq) was added to each tube. Each digitube sample underwent a digestion protocol in which tubes were covered with a watch glass and heated to 100ºC on a DigiPREP block digestion system for 1.75 hr (Champlain, N.Y.). Tube A had no metal standard added. Tube B had 100 µL Rh/Pt solution added before the digestion procedure. Tube C had the Rh/Pt solution added after the digestion procedure. After digestion was complete, samples were evaporated using gentle heating at 63ºC for ~2hr. Next, 2% HNO_3 (aq) was added to make a final volume of 25 mL, then samples were analyzed by ICP-MS for Rh^{103} and Pt^{195} content. Experiment was performed in quadruplicate.

2.2.10.3 Tissue Digestion Analysis

Mice from Efficacy Experiment #2 bearing HCT116 xenografts that were treated with Rh-PPO and oxaliplatin were used for the following analyses. The chicken liver test described above was performed to assess the accuracy of the nitric acid digestion protocol in detecting rhodium and platinum using ICP-MS.

2.2.10.3.1 Tumor digestion analysis

Tumors were collected, weighed, frozen at -80°C overnight, then dried using the lyophilizer for over 3 days. Lyophilized tumor samples were then immediately manually homogenized using a metal spatula, and reweighed. The homogenized tumors were transferred to 50 mL Digitubes and 2 mL of 25% HNO_3 was added to each sample. The sample was then covered with a watch glass and heated to 100ºC on a DigiPREP block digestion system for 24 hr (Champlain, N.Y.). The digested tumor samples were centrifuged for 5 min at 1,000 rpm. Supernatant (200 µL) was transferred to new 15 mL falcon tubes containing 4.8 mL H_2O. The diluted sample (1% HNO_3) was centrifuged for 5 min at 1,500 rpm and analyzed by ICP-MS for Rh^{103} and Pt^{195}.

2.2.10.3.2 Organ Digestion Analysis

The collected organs were weighed and transferred to 50 mL Digitubes, to which 2-5 mL of concentrated HNO_3 (68%) was added. The tubes were then covered with a watch glass and heated to 100°C on a DigiPREP block until the sample was fully digested (2-8 hr). The digested tissue samples were evaporated using gentle heating at 65 °C until ~1 mL of sample remained. Then a 2% HNO_3 (aq) solution was added to each sample to reach a final volume of 25 mL. The resulting samples were analyzed by ICP-MS for Rh^{103} and Pt^{195}.

2.2.11 Rh-PPO Continuous Infusion Pharmacokinetic Studies

Initial *in vivo* studies with Rh-PPO utilized Alzet osmotic pumps (Cupertino, CA) to achieve continuous infusion of the drug. In these studies, osmotic pumps were filled with Rh-PPO at 1 mpk and implanted subcutaneously in four mice. Importantly, Mouse#1 and Mouse#2 received 2 mL, daily, subcutaneous infusions of saline for hydration. Mice were assessed for Rh-PPO plasma concentration by performing tail vein blood draws every 24 hr. After blood was collected, it was immediately transferred to heparinized blood collection vials on ice at time intervals of 24, 48, and 72 hr. The blood samples were centrifuged at 15,000 g at RT for 5 min, and the plasma supernatant was transferred to 1.5 mL microcentrifuge tubes and maintained at -80°C until analysis. Plasma samples were analyzed for Rh-PPO concentration using LC-MS/MS.

2.2.12 Immunohistochemistry Analysis of Tissues and Tumors Treated with Rh-PPO

At the completion of the intraperitoneal study, all major organs were collected (spleen, kidneys, liver, heart, skeletal muscle, lungs, small intestine, colon, stomach, cecum, testes, epididymis, tumor, tibia/femur and brain) via necropsy, then fixed in 10% formalin for more than

48 hrs. Tissues were then trimmed and embedded in paraffin. Tissues were then examined using hematoxylin and eosin staining and immunohistochemistry experiments.

2.2.12.1 Immunohistochemistry Procedures

Embedded tissues were deparaffinized using xylene and rehydrated in a series of descending concentrations of ethanol. Then, antigens were retrieved using a Decloaker (DC2012-220V) for 15 min at 110ºC. Endogenous peroxidase was blocked for 15 min at room temperature (RT), then protein blocking was performed for 10 min at RT, and finally the primary antibody (anti-BrdU (BU1/75 (ICR, RatIgG2a); cleaved caspase-3(Asp175); anti-pH2AX (Ser139) (20E3) (RbIgG); anti-HMGB1 ([EPR3507], RbIgG) or isotype control antibody (Rat IgG2a, κ Isotype Ctrl Antibody, Biolegend, Cat B242904; Rabbit IgG(EPR25A), Abcam, Cat ab172730) was applied for 60 minutes at RT. Wash buffer was used on tissues for 3 min (3x). Then, secondary antibody (Rabbit Anti-Rat IgG H&L (HRP), Abcam, Cat ab6734, EnVision+System-HRP Labelled polymer anti-Rabbit, Dako, Cat K4003) used for 30 minutes at RT. Then, Wash buffer was applied for 3 min (3x). Tissues were visualized with Chromogen, washed with Wash buffer for 3 min (3x), then CounterStained, dehydrated, and mounted with mounting medium**.** Stained slides were scanned at 20x using an Aperio Scanscope AT2 scanner. Image quantification was done by using Halo image analysis software. Data analysis was performed using GraphPad Prism 7.04. Note that the above procedures were performed by Barton lab collaborators at Amgen.

2.3 Results

2.3.1 Evaluation of the Maximum Tolerated Dose (MTD) for Metalloinsertor Rh-PPO

In order to determine the *in vivo* anticancer effects of Rh-PPO, the MTD of Rh-PPO was assessed in NOD-*scid* IL2Rgamma^{null} (NSG) mice. Mice were treated intraperitoneally with Rh-PPO at 1, 2, 5, and 15 mg drug per kg mouse body weight for up to 10 consecutive days and observed for adverse clinical side effects. During this experiment, the highest dose evaluated, 15 mg/kg/day (mpk), was found to be lethal within minutes of administration. Mice in the saline group maintained their activity throughout the 10-day study. Mice receiving Rh-PPO at 2 mpk and 5 mpk began displaying notable symptoms of distress and inactivity, such as becoming lethargic, scruffy, and hunched, starting on day 4 and day 2 of the study, respectively; these mice had to be euthanized before the 10-day study ended. Conversely, mice receiving Rh-PPO at 1 mpk displayed only mild symptoms of distress, including becoming slightly hunched after 6 days of consecutive treatment. Throughout the MTD study, mice in all treatment groups lost body weight in a dose dependent manner. The MTD for Rh-PPO was determined to be 1 mpk (1.34 micromol/kg); the mice in this dosing group displayed minimal symptoms of distress or inactivity and survived until the end of the study (10 consecutive days of treatment). Given the results of the MTD study, we chose the Rh-PPO dose of 1 mpk given three to four times per week to conduct the subsequent *in vivo* trial. Rh-PPO is compared to oxaliplatin at 7.5 mpk given twice per week, which is a treatment that has been shown to have notable anti-cancer effects in HCT116 xenograft tumors.[26]

2.3.2 Impact of Rh-PPO on *in vivo* Tumor Growth Rate

Two distinct intraperitoneal efficacy experiments with HCT116 xenograft tumors were performed. As outlined in **Figure 2.2**, mice in Efficacy Experiment #1 and #2 received intraperitoneal doses of metalloinsertor treatments with or without additional saline hydration to assist with drug tolerability, respectively.

First, mice were inoculated with HCT116 human colorectal carcinoma cells. Once tumors were palpable at ~100 mm^3 in volume, mice were randomly assigned to each treatment group and drug administration commenced. Mice in Efficacy Experiment #1 and #2 received the following treatment doses intraperitoneally (i.p.): Rh-PPO at 0.5 mpk and 1 mpk, oxaliplatin at 7.5 mpk, and vehicle (0.9% NaCl). The doses were administered based on the schedule outlined in **Figure 2.2**. In Efficacy Experiment #1 mice, subcutaneous administration of 2 mL saline was initiated on the off-treatment days to mitigate the weight loss observed in the first several days of treatment.

As can be seen in **Figure 2.3**, treatment with Rh-PPO yielded a significant decrease in tumor size. In the groups treated with Rh-PPO in Efficacy Experiment #1, we observed a significant decrease in tumor growth rate compared to the vehicle control group. By day 21 of the study, the Rh-PPO treatment groups exhibited a 25 ± 2.7 % reduction in tumor volume relative to the vehicle treatment group (**Figure 2.3**). This statistically significant reduction in tumor growth rate occurred after mice received 4 doses of Rh-PPO.

Similar decreases in tumor growth were observed in both Rh-PPO treatment groups. Notably this decrease in tumor volume compared to the control group was sustained for the duration of the study. By the conclusion of the study on day 28, the Rh-PPO and oxaliplatin

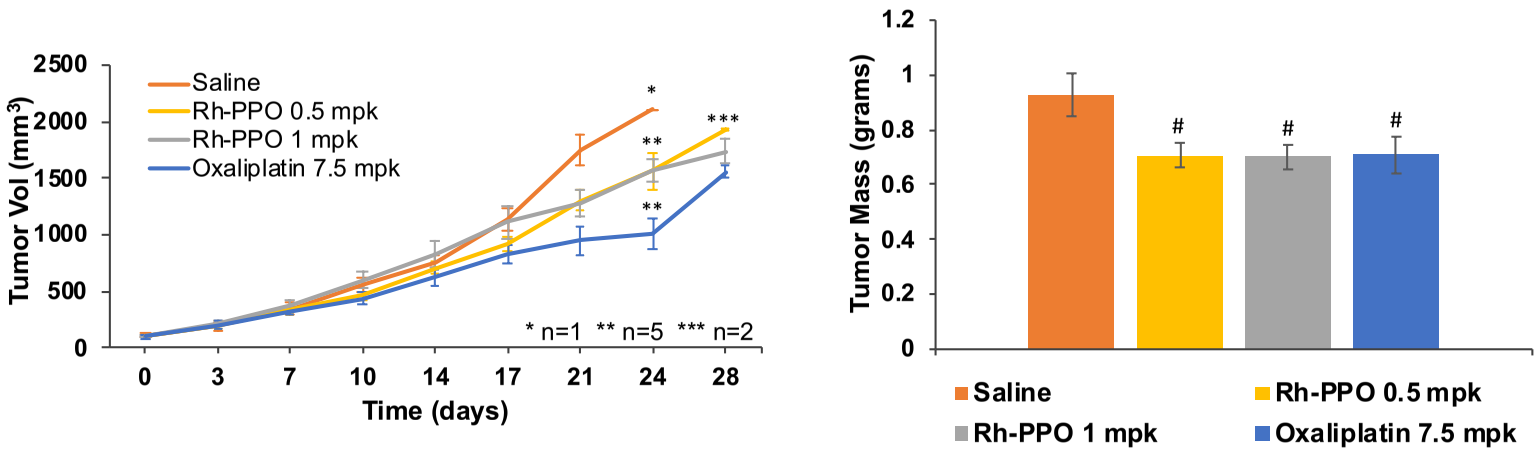

Figure 2.3 Rh-PPO impact on *in vivo* tumor growth rate. (Left) Average tumor volumes of Efficacy Experiment #1 mice receiving intraperitoneal doses throughout the dosing period. *Number of mice (n=1), **number of mice (n=5), ***number of mice (n=2). (Right) Average final tumor weights for Efficacy Experiment #2 mice. Tumors were excised after 18 days of treatment with 8 to 10 tumors collected and analyzed per treatment group. Statistically significant difference between treatment groups and saline control was found based on Anova analysis; $^{\#}P<0.05$ ($^{\#}P=0.03$)**.** All error bars represent standard error of the mean.

treated groups had statistically similar tumor volumes with oxaliplatin being administered at a 7.5-fold higher dose than Rh-PPO.

Additionally, in the Efficacy Experiment #2 study, where tumors from each treatment group were all excised on day 28, significant reduction in the final tumor weights was observed (**Figure 2.3**). Specifically, the average tumor weight of the Rh-PPO treatment groups was 24 ± 9.7% lower than the vehicle group, and Anova analyses of the final tumor weights showed that the reduction was statistically significant (p-value = 0.03); this decrease in tumor weight was on par with the reduction observed in oxaliplatin treated animals. Importantly, neither treatment schedule resulted in significant mouse weight loss (more than 15% of original body weight lost) in the Rh-PPO treatment groups, as shown in **Figure 2.4**, which indicates that the metalloinsertor was minimally toxic over the duration of treatment.[27]

2.3.3 Rh-PPO Treatment Influence on Survival Rate of Mice Bearing HCT116 Xenograft Tumors

In order to investigate further the *in vivo* anticancer efficacy and tolerability of Rh-PPO, we analyzed the survival rates and classified the reason for death of mice in Efficacy Experiment #1 (**Figure 2.5**). As described, Efficacy Experiment #2 instead focused on a tumor weight analysis. Each Efficacy Experiment #1 treatment group began with 10-13 NSG mice bearing HCT116 xenograft tumors. Over the course of the 39-day study, their level of activity and overall health status was monitored. Based on these data, a Kaplan Meier survival curve (**Figure 2.5**) was constructed for each treatment group from the study (vehicle with 0.9% NaCl, Rh-PPO at 0.5 mpk and 1 mpk, and oxaliplatin at 7.5 mpk). Note the difference in doses for Rh-PPO versus oxaliplatin based on their distinct tolerability and potency.

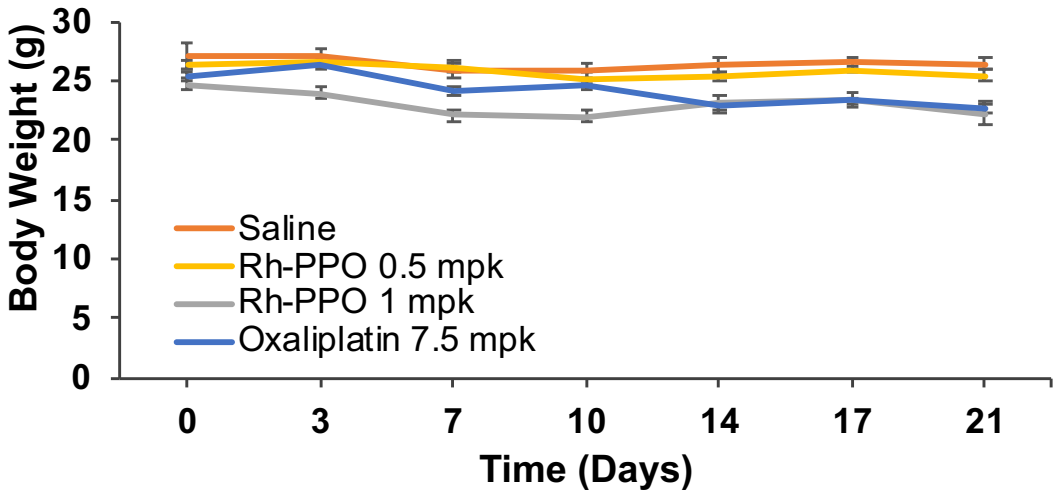

Figure 2.4 Rh-PPO tolerability *in vivo* throughout intraperitoneal efficacy study. Efficacy Experiment #1 average mouse body weights over time after drug treatment commenced (n=8 to 11 mice). Error bars represent standard error of the mean.

Mice receiving the Rh-PPO treatment displayed an increase in life span (ILS) of 12% relative to the vehicle control groups (**Figure 2.5**). Additionally, mice in the control group began dying 7 days before those in the Rh-PPO group with three mice in the vehicle group found dead on day 13 after tumor inoculation, as shown in **Figure 2.5**. Furthermore, classification of the cause of death revealed that 45.5% of saline mouse deaths resulted from mice either being found dead in their cages or euthanized due to poor health and inactivity (**Figure 2.5**). Conversely, 90% of mice in both Rh-PPO treatment groups died due to their tumors reaching the maximum allowable size (15 mm in diameter). Note that mice in the vehicle group found dead in their cage are assumed to have succumbed to the physical stress of their HCT116 xenograft tumors, while mice in the Rh-PPO and oxaliplatin groups found dead are assumed to have perished due to the combined physical stress of their HCT116 xenograft tumors and the drug treatment. Also, mice euthanized due to poor health displayed signs of distress, such as having scruffy fur or being hunched, for multiple consecutive days before they were sacrificed.

Importantly, the FDA-approved chemotherapeutic oxaliplatin displayed the same increase in life span of 12% as Rh-PPO, but was associated with more toxicity; 45.5% and 18.2% of oxaliplatin mouse deaths resulted from mice being found dead in their cages and mice being euthanized due to poor health and inactivity, respectively. It should be noted that the death classification analysis was conducted based on mice from Efficacy Experiment #1 only. Overall, these findings show that Rh-PPO prolongs the survival of mice bearing HCT116 xenograft tumors to a similar extent as oxaliplatin, while also being better tolerated than the platinum complex at their respective MTDs.

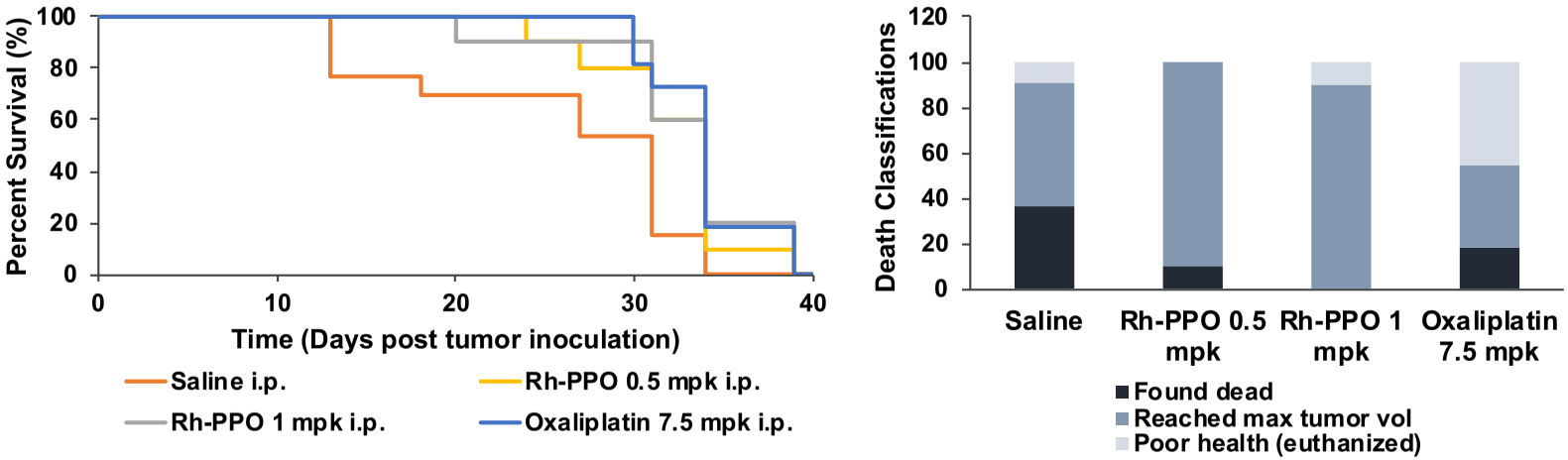

Figure 2.5 Rh-PPO treatment increases mouse survival rate. (Left) Kaplan Meier survival curve for Efficacy Experiment # 1 mice. Mice were considered dead if found dead in their cage, mouse health warranted euthanasia, or tumor diameter surpassed 15 mm. (Right) Classification of reason for mouse deaths. Black indicates mice were found dead. Blue-gray represents mice that were euthanized due to their tumor reaching the maximum allowable size (15 mm in diameter). Light gray denotes mice had to be euthanized due to poor health. Bar graph displays percentage of mice that died for each outlined reason.

2.3.4 Pharmacokinetic Profile of Rh-PPO

Mice from Efficacy Experiment #1 were further examined to assess the pharmacokinetic profile of Rh-PPO in NSG mice. **Figure 2.6** summarizes the plasma concentration of the metalloinsertor drug over time during this *in vivo* analysis. This experiment reveals that the average plasma concentration and bioavailability of Rh-PPO is very similar for both doses tested, which may explain the comparable anti-tumor effects observed at 0.5 and 1 mpk Rh-PPO. The variation in compound detected at the first time point could indicate the need to take earlier time points in future studies or potentially reflects the variability in clearance rates or drug administration of the different animals evaluated. As shown in the graph, the peak plasma concentration was reached within 30 min of dosing and Rh-PPO was eliminated quickly with elimination half-lives ($t_{1/2}$) of 1.79 hr and 1.11 hr for the Rh-PPO 1 mpk and Rh-PPO 0.5 mpk dosing groups, respectively. For comparison, the half-life of oxaliplatin is 14.1 minutes.[28] A maximum plasma concentration (C_{max}) of 650 nM for the Rh-PPO 1 mpk cohort was observed, which indicates that the exposure level of Rh-PPO *in vivo* for this dose is ~2.5-fold greater than the *in vitro* cell IC_{50} value of 250 nM for HCT116 cells.[23] Additionally, the area under the curve ($AUC_{0\text{-}8\ hr}$) value was calculated based on the plasma concentration curve as summarized in Table 2.1. Importantly, Rh-PPO concentration was determined by LC-MS/MS; therefore, the measured drug levels represent detection of the intact Rh-PPO complex.

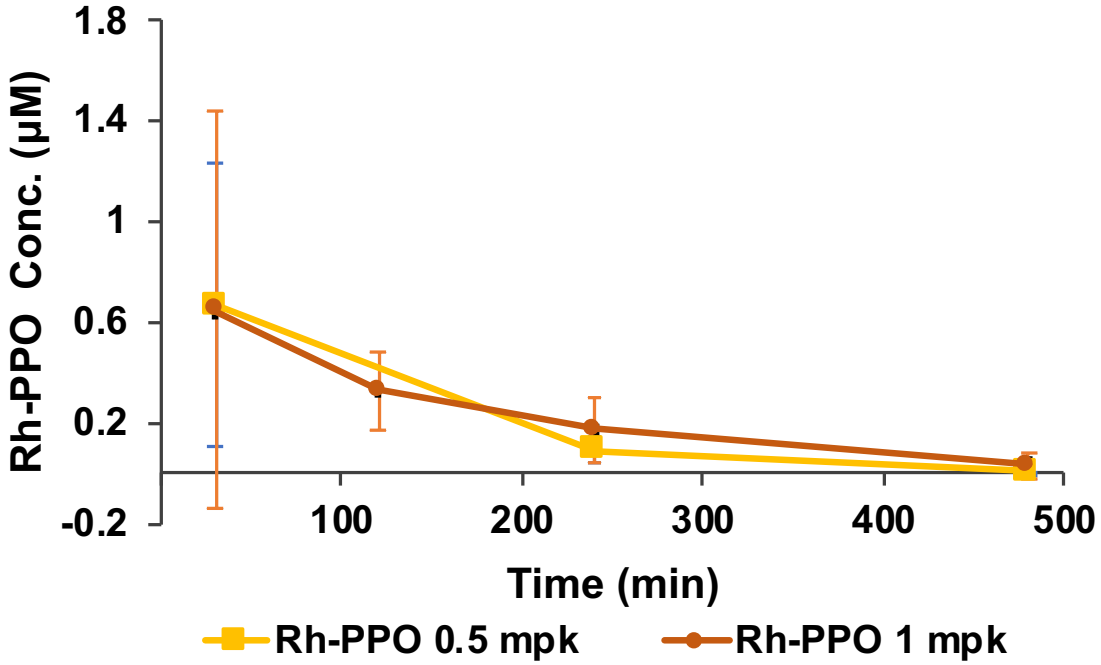

Figure 2.6 Pharmacokinetic profile of Rh-PPO after intraperitoneal drug administration. Concentration of Rh-PPO in mouse plasma of Efficacy Experiment #1 animals (n=2 to 3) dosed intraperitoneal with Rh-PPO at 0.5 mpk and 1 mpk. Amount of intact Rh-PPO detected in mouse plasma was analyzed via LC-MS/MS at various time points up to 4 hours after a single, intraperitoneal bolus dose was administered.

At the conclusion of each efficacy study, the tumors along with various organs were collected and analyzed for rhodium and platinum content (**Figure 2.7**) using inductively coupled plasma mass spectrometry (ICP-MS); this high sensitivity technique allows for the detection of low concentrations of metal-based drugs (less than 1 ng/ml) and as a result, background levels of rhodium and platinum can be detected in the saline treatment group. [29]

In order to assess the ability of the nitric acid digestion protocol to accurately determine rhodium and platinum concentrations within tissues, initial tests were performed using chicken liver. Within these experiments, diluted ICP-MS standards were added to the chicken liver digestion tubes before and after the nitric acid digestion, and the samples were analyzed by ICP-MS. Because a known concentration of rhodium and platinum was added to each sample, the detected metal concentrations were compared to the known concentration of metal added (400 ppb Rh and 0.4 ppb Pt). The results of these chicken liver experiments confirmed that the outlined nitric acid digestion protocols allowed for accurate and precise detection of Rh^{103} and Pt^{195} concentrations.

Importantly, the tumor and organ samples underwent distinct nitric acid digestion protocols (see Experimental Section), and therefore metal content in the tumors and organs cannot be directly compared. Nonetheless, the results collected from ICP-MS studies indicate that a significant amount of both drugs, Rh-PPO and oxaliplatin, became distributed to various organs as opposed to being directed selectively to the site of the tumors. Notably, when comparing the tumor to normal tissue ratio for both drugs, a higher proportion of platinum was localized to tumors in the oxaliplatin treated mice. Additionally, dose-dependent accumulation of rhodium was detected in the analyzed intraperitoneal treated tumors. It should be noted that for the intraperitoneal efficacy studies, 9-fold less rhodium was present in Rh-PPO tumors compared

Table 2.1 Pharmacokinetic parameters of Rh-PPO after intraperitoneal drug administration.

Pharmacokinetic parameter	Rh-PPO 0.5 mpk	Rh-PPO 1 mpk
C_{max} (μM)	0.45	0.65
$t_{1/2}$ (hr)	1.11	1.79
$AUC_{0\text{-}8\ hr}$ (μM x hr)	1.31	1.52

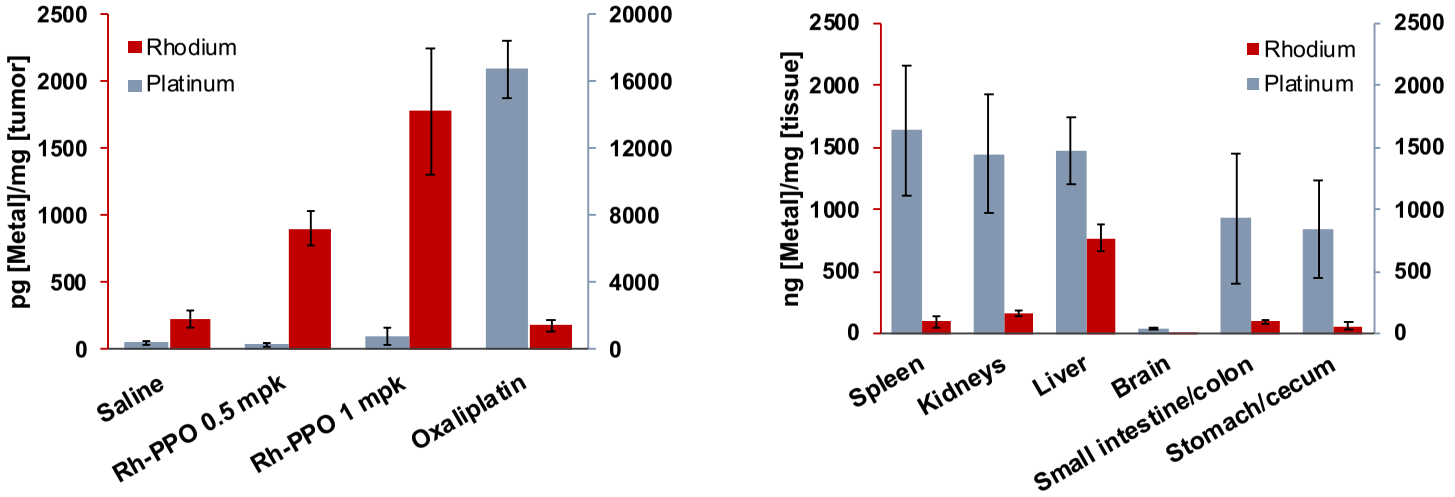

Figure 2.7 Accumulation of Rh and Pt in tissues after intraperitoneal drug treatment. (Left) Rhodium and platinum uptake in HCT116 xenograft tumors of Efficacy Experiment #2 mice. Rhodium and platinum accumulation in tumors was determined using ICP-MS analysis of tumors digested in nitric acid and normalized to initial tumor weight. The rhodium and platinum concentrations detected in tumors from each treatment group (n=9 or n=10) were averaged. (B) Rhodium and platinum uptake in various tissues collected from Efficacy Experiment #1 mice. Rhodium accumulation was determined using ICP-MS analysis of digested tissue samples collected from mice treated with Rh-PPO at 1 mpk. Platinum accumulation was determined using ICP-MS analysis of digested tissue samples collected from mice treated with oxaliplatin at 7.5mpk. Metal concentrations were normalized to initial tissue weight. The metal concentrations detected in organs from each treatment group were averaged (n=2 to 4). Error shown as the standard error of the mean.

to platinum levels in oxaliplatin treated mice, despite similar anticancer effects being observed for the two drugs; this result reflects the higher potency of the rhodium complex. Furthermore, the tissue analysis of oxaliplatin-treated animals showed that platinum was distributed evenly (within the standard error) for all organs analyzed.

Additionally, Rh content (**Figure 2.7**) and histological analyses of the tissues collected showed normal organ morphology in Rh-PPO treated mice with accumulation of rhodium most significantly in the liver (1 ng [Rh]/mg tissue = 9.718×10^{-9} mol [Rh]/kg tissue). This tissue analysis gives insight into the potential mechanisms of Rh-PPO clearance and currently suggests that Rh-PPO is most readily cleared through the liver and the incorporation of saline hydrating doses likely decreased the overall rhodium concentration in the kidneys. Additionally, the histopathology evaluations using hematoxylin and eosin (H&E) staining of collected tissues revealed slight single cell necrosis/apoptosis of the cryptical epithelial cells within multiple oxaliplatin treated mice. Furthermore, immunohistochemistry experiments showed slight decreases in cleaved caspase-3 protein expression, which is an indication of apoptosis, in Rh-PPO treated tumors, and minor increases in phosphorylated H2AX (**Figure 2.8**), a marker for DNA double strand breaks, were detected in all drug treated tumors; though importantly none of the observed trends were statistically significant. Overall, these findings support our analysis that Rh-PPO was sufficiently tolerated throughout the study and displays an expected pharmacokinetic profile.[30] However, increased efficacy will require more selective delivery of Rh-PPO to the tumor versus healthy organs.

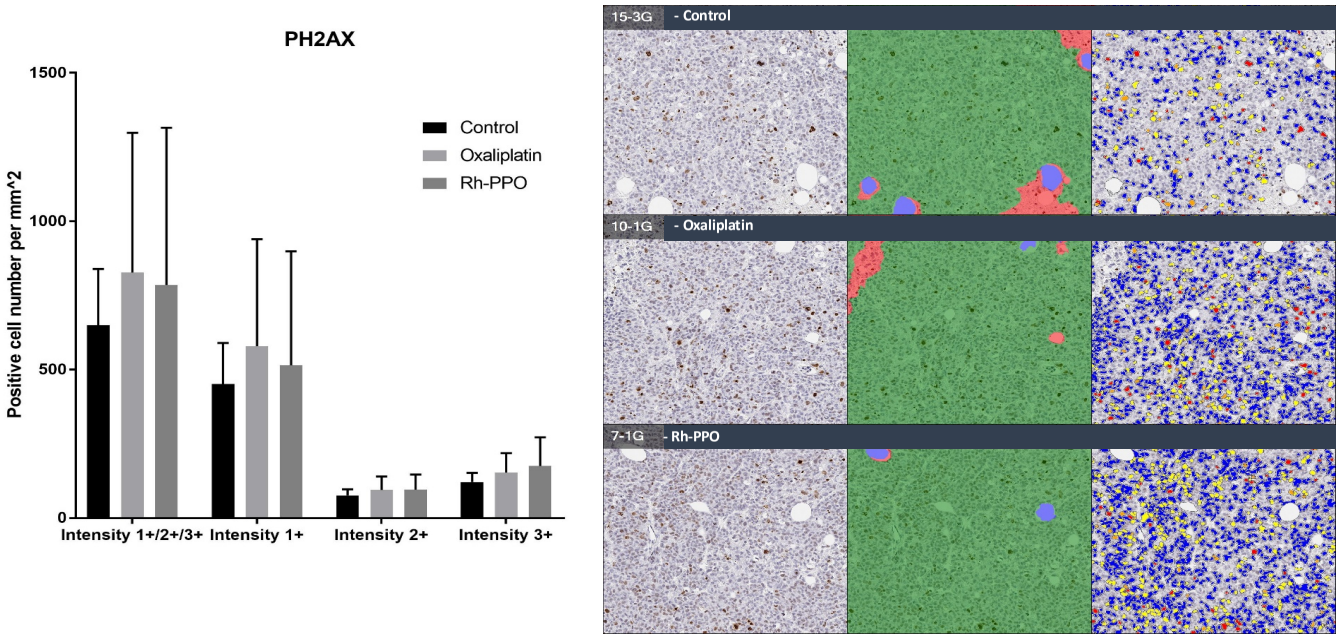

Figure 2.8 Immunohistochemistry of tumor samples from intraperitoneal treatment groups. (Left) Quantitative representation of phospho-H2AX (PH2AX) staining for different treatment groups. Also, divided based on signal intensity. Plot shows mean positive cell number with error bars representing standard deviation. (Right) Representative immunohistochemistry images of PH2AX staining. Left panel shows haematoxylin/eosin staining, middle panel displays identification of normal (green) and necrotic tumor tissues (red), and right panel showcases PH2AX staining with positive cells of intensity 1+ (yellow), intensity 2+ (orange), and intensity 3+ (red).

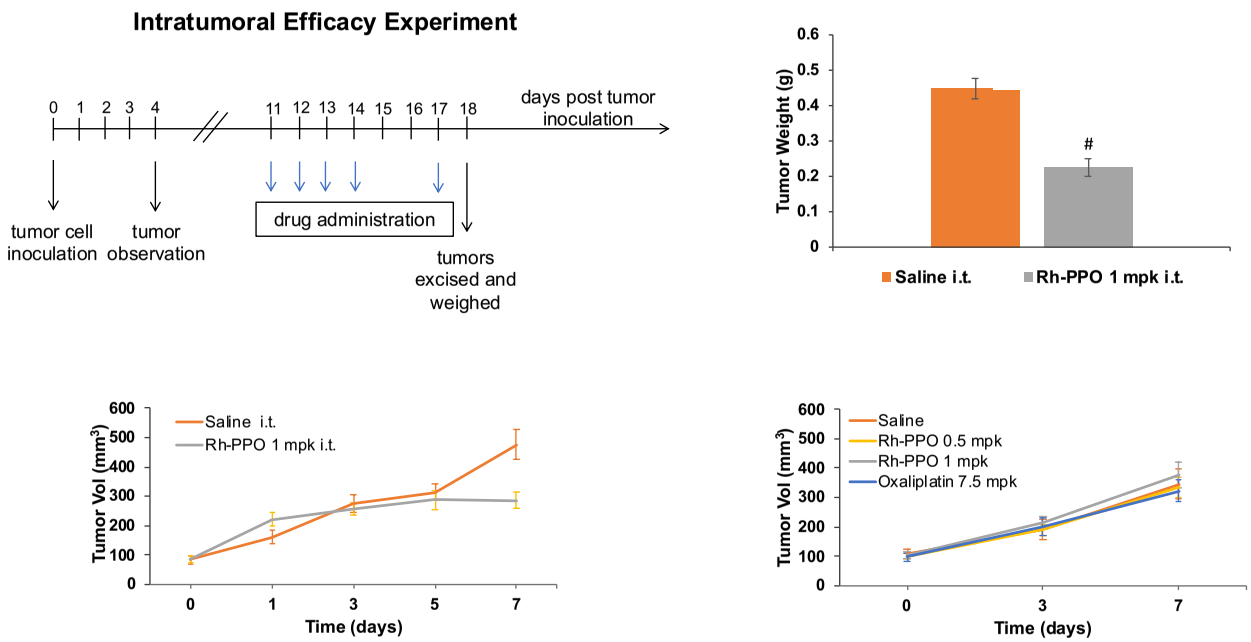

Figure 2.9 Intratumoral Rh-PPO treatment causes *in vivo* tumor growth rate to decrease rapidly. (Top left) Intratumoral Efficacy Experiment treatment schedule for study monitoring tumor volume and final tumor weight in mice treated intratumorally. Blue arrow indicates that mice received intratumoral drug doses of saline and Rh-PPO at 1 mpk. (Top right) Average final tumor weights for intratumoral treated mice. Tumors were collected after 7 days of treatment. (Bottom left) Evaluation of the average tumor volume over first seven days of treatment in cohorts receiving intratumoral and (bottom right) intraperitoneal drug doses. Error bars represent standard error of the mean. Statistically significant difference between the final tumor weights of Rh-PPO and saline treatment groups was found using Anova test; $^{\#}P<0.005$ ($P=0.002$).

2.3.5 Impact of Intratumoral Rh-PPO Treatment on *in vivo* Tumor Growth

In addition to the two efficacy studies detailed above, in which Rh-PPO was administered intraperitoneally, we also explored the anti-tumor effects observed with Rh-PPO intratumoral treatment. The Intratumoral Efficacy Experiment gave insight into the antiproliferative potential of Rh-PPO if the complex is specifically targeted to the site of the tumor. As shown in **Figure 2.9**, intratumoral doses of Rh-PPO at 1 mpk resulted in a 40% reduction in tumor volume, as well as 49% lower average tumor weights (P=0.002), compared to the saline control after only 7 days of treatment (0.142 mg Rh-PPO total administered). These results indicate that reductions to tumor growth can be doubled in one-third of the time frame when the treatment is administered directly to the tumor compared to intraperitoneal injections. Additionally, this increased level of anticancer activity was strongly correlated with enhanced levels of rhodium in tumors detected by ICP-MS, specifically tumors from intratumorally treated mice had 50-fold higher rhodium concentrations at the tumor site compared to the intraperitoneal treatment groups (**Figure 2.10**). It should be noted that intratumoral doses were only given for 7 days because this administration route resulted in significant systemic toxicity, including mouse inactivity and notable weight loss.

2.4 Discussion

Platinum complexes have been extensively studied and utilized as chemotherapeutics,[31] where these compounds aim to target DNA within rapidly dividing malignant cells. However, these complexes are associated with adverse effects and patients frequently develop resistance to these treatments.[8,9,10] As a result, we have focused on the development of targeted chemotherapeutics for DNA with improved selectivity for cancerous cells, specifically for MMR-deficient cancers, which have underdeveloped treatment options currently.

We have designed and characterized rhodium metalloinsertors which bind specifically to DNA mismatches, and as a result, induce selective toxicity within MMR-deficient cancer cell lines.[16,22,23,32–34] In addition, various ruthenium complexes have been designed and synthesized as chemotherapeutics, although with different biological targets.[21,35–37] The high potency and demonstrated biological selectivity of Rh-PPO for DNA mismatches and MMR-deficient cells distinguish it from most other metal chemotherapeutics.

2.4.1 Preliminary Experiments Support the Preclinical Analysis of Rh-PPO *in Vivo*

Given the cell-selective cytotoxicity and potency of the Rh-PPO metalloinsertor, the *in vivo* anticancer activity of the complex was evaluated in NSG mice with human colorectal carcinoma HCT116 xenograft tumors. Initial experiments showcased the high aqueous solubility of the complex and stability of Rh-PPO in rat plasma and rat liver microsomes for up to four hours. Furthermore, plasma protein binding studies indicated 1-3% free Rh-PPO with the remainder of the compound bound to plasma or inactive. Additionally, screenings of Rh-PPO in the Ambit kinase and CEREP receptor panels to assess selectivity of the compound showed that Rh-PPO did not inhibit any of the kinases tested and only had moderate activity against a few of the CEREP receptors, including the muscarinic M1 receptor and Serotonin 5-HT1a receptor. Altogether, these initial studies supported the transition toward preclinical evaluation of Rh-PPO as a chemotherapeutic drug.

Our first mouse experiments aimed to explore the administration route (oral, intravenous, subcutaneous, intraperitoneal, etc.) best suited for achieving tolerable, systemic chemotherapeutic effects with the metalloinsertor complex. These studies showed that Rh-PPO

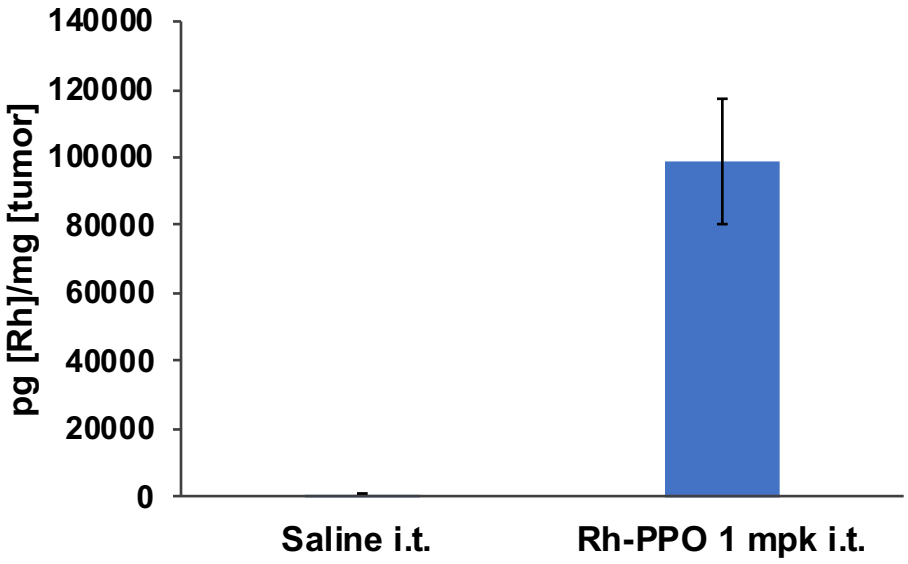

Figure 2.10 Significant accumulation of rhodium in tumors occurs after intratumoral Rh-PPO treatment. Rhodium uptake in HCT116 xenograft tumors from Efficacy Experiment # 3 mice receiving intratumoral injections. Rhodium accumulation in tumors was determined using ICP-MS analysis of tumors digested in nitric acid and normalized to initial tumor weight. The rhodium concentration of tumors from saline (n=5) and Rh-PPO at 1 mpk (n=10) treated mice was averaged with error shown as the standard error of the mean. Statistically significant difference between Rh-PPO and saline treatment group detected rhodium content was found using Anova test; $^{\#}P<0.005$.

effectively had zero oral bioavailability and intravenous administration of the metalloinsertor at 20 mpk was not well tolerated; therefore, alternative administration routes and drug concentrations were explored. The MTD study described in this work revealed that bolus, intraperitoneal injections of Rh-PPO at 1 mpk are tolerated over a 10-day period with minor indications of systemic toxicity. Additionally, initial pharmacokinetic studies using continuous subcutaneous infusions (**Figure 2.11**) suggested that supplemental injections of saline promoted the clearance of Rh-PPO and increased overall tolerability of the drug; therefore, supplemental saline hydration was incorporated into the *in vivo* study design, as described in **Figure 2.2**. With the MTD and dose administration conditions for Rh-PPO determined, we continued with the preclinical evaluation of this metalloinsertor compound as a targeted chemotherapeutic.

2.4.2 Rh-PPO *in Vivo* Preclinical Evaluation

The described study evaluates the *in vivo* tolerability, cytotoxic tumor effects, and pharmacokinetic properties of the metalloinsertor Rh-PPO. Analysis of tumor growth in the two intraperitoneal, efficacy experiments demonstrates statistically significant differences in tumor volume and final tumor mass between the intraperitoneal vehicle and Rh-PPO treatment groups. Specifically, an Anova test of the final tumor weights obtained from Efficacy Experiment #2 mice reveal a decrease in average tumor weights of 24 ± 9.7% for both Rh-PPO treatment groups (p-value = 0.03), which is comparable to the decrease in HCT116 tumor weight observed in mice treated with oxaliplatin. Importantly, while platinum complexes are generally less effective in MMR-deficient cells, our *in vivo* experiments with Rh-PPO were conducted alongside oxaliplatin because previous studies have demonstrated that this compound has anti-proliferative effects in HCT116 xenograft tumors and colon cancer cells generally.[26]

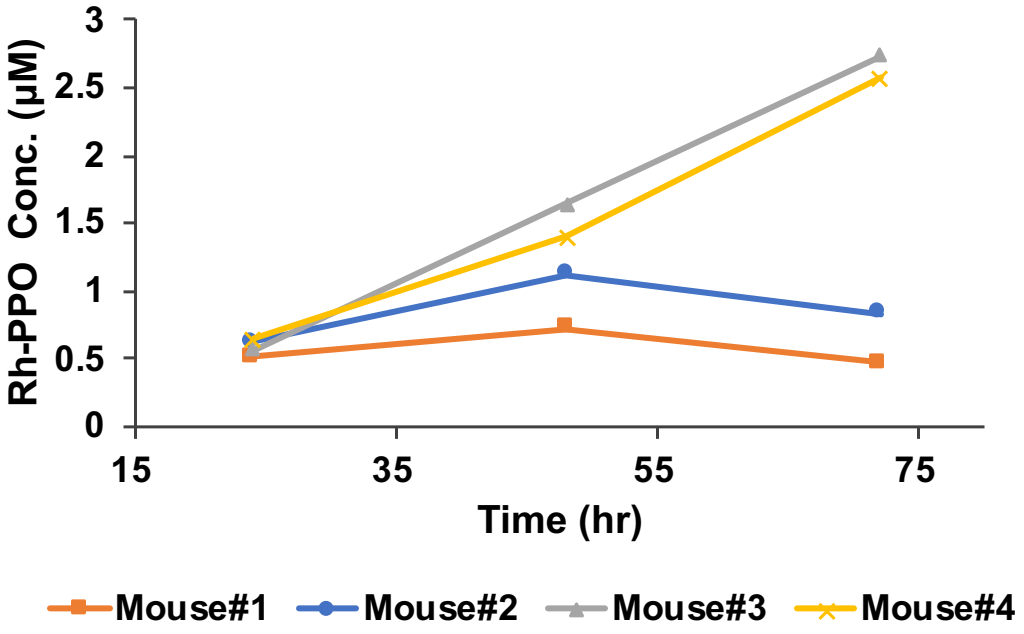

Figure 2.11 Plasma accumulation of Rh-PPO administered via continuous infusion is dependent on mouse hydration. Concentration of Rh-PPO in mouse plasma of NSG mice given continuous infusion doses of Rh-PPO at 1 mpk for 72 hr. Importantly, Mouse#1 and Mouse#2 received 2 mL, daily, subcutaneous infusions of saline. Amount of intact Rh-PPO detected in mouse plasma was analyzed via LC-MS/MS every 24 hr for 72 hr total. Continuous infusion was accomplished using an osmotic pump.

Reduction in tumor growth from Rh-PPO administration was also evident based on the tumor volume analysis conducted in Efficacy Experiment #1, which clearly showed a decrease in tumor growth rate starting on day 21 of the study. In particular, Rh-PPO treated tumors were 25 ± 2.7% smaller than the control group mean tumor volume. Additionally, analysis of the survival rates in the first efficacy experiment showed a 12% increase in life span for metalloinsertor treated animals compared to the vehicle treated group. Furthermore, Rh-PPO was found to be less systemically toxic than oxaliplatin, as 10% and 45% of Rh-PPO (1 mpk) and oxaliplatin treated animals had to be euthanized due to poor health and inactivity, respectively. Moreover, Rh-PPO was shown to be significantly more potent than oxaliplatin *in vivo*, as 9-fold lower metal concentrations were necessary, as shown by ICP-MS analysis of tumors, to cause similar anticancer effects with the two drugs (**Figure 2.7**). Additionally, we assessed the tumor growth effects when Rh-PPO was administered through intratumoral injection and found greater than 40% reductions in tumor volume and weight after only 7 days of treatment. The intratumoral route of administration was also found to be unacceptably toxic, most likely due to rapid increases in systemic Rh-PPO concentrations similar to those achieved with intravenous dosing. Importantly, this experiment clearly indicates that when more complex becomes specifically localized to the tumor site *in vivo*, significantly greater anti-cancer effects are observed.

In order to assess further the preclinical potential of Rh-PPO, pharmacokinetic analyses of plasma samples collected from mice receiving intraperitoneal doses of Rh-PPO were conducted. These experiments revealed that the half-life of the compound is in the range expected for a chemotherapeutic (1.11 hr to 1.79 hr depending on the dose). Additionally, the pharmacokinetic curve obtained demonstrates a concentration max (C_{max}) that is above the IC_{50} of Rh-PPO (250 nM in HCT116 cells) for both doses assessed, consistent with the anti-tumor

efficacy observed *in vivo*.[23] Tumor and tissue analyses revealed a dose dependent accumulation of rhodium within the tumors of Rh-PPO-treated mice; however, a higher distribution of rhodium to the liver compared to the tumor and other organs was observed. The rhodium liver accumulation detected could be indicative of Rh-PPO undergoing hepatic drug clearance. This differs greatly from oxaliplatin which showcased equal distribution of platinum in the different organs analyzed, with the exception of the brain, which is consistent with reports of oxaliplatin being cleared by a combination of tissue binding and renal clearance.[38,39] Comparing the concentrations of rhodium/platinum measured within tumors and tissues revealed that significant amounts of drug are becoming absorbed within healthy tissues, which underscores the need for Rh-PPO to be further targeted to the site of tumors for its full chemotherapeutic potential to be achieved.

In summary, we report that significant antiproliferative effects in colorectal carcinoma HCT116 xenograft tumors are observed when Rh-PPO is administered via intraperitoneal injection, and these anti-tumor effects are on par with oxaliplatin treatment. Tumor growth in Rh-PPO-treated mice is notably slowed in the described efficacy experiments. However, tumor cell proliferation is ultimately not eliminated. Furthermore, while the intraperitoneal administration route did not result in detrimental systemic toxicity during the outlined treatment period, accumulation of rhodium in organs is likely to cause long-term, toxic side effects. Results from the intratumoral Rh-PPO study indicate that higher localization of compound to the site of the tumor should result in even greater anticancer effects. In order to mitigate the systemic toxicity of Rh-PPO observed at higher concentrations and increase cytotoxic effects at the tumor site, it will be important to explore different approaches to drug delivery that may further target metalloinsertor complexes to tumors more efficiently. This study reports the first *in vivo* analysis

of DNA mismatch-targeted rhodium metalloinsertors, and the anti-cancer effects observed validate these compounds as potential chemotherapeutic agents that warrant further investigation.

2.5 Conclusions and Implications for Future Metalloinsertor Studies

In summation, we have demonstrated the potential of Rh-PPO, a water-soluble, rhodium complex that specifically binds to mismatched DNA base pairs, as an anticancer therapeutic targeted towards mismatch repair (MMR) deficient cancers. Previous work from our laboratory has demonstrated the specific binding of Rh-PPO to DNA mismatches over other cellular targets, as well as its selective cytotoxic effects in MMR-deficient cancer cell lines.[22,23] The *in vivo* pre-clinical studies presented herein showcase the efficacy of Rh-PPO on human colorectal carcinoma HCT116 xenograft tumors grown in NSG mice. Significant reductions in final tumor weight and volume compared to the saline control of 24 ± 9.7% and 25 ± 2.7 % were observed in Rh-PPO treatment groups, respectively. Also, Rh-PPO displayed a notable increase in survival of 12% compared to the saline control. Additionally, the impacts on tumor growth and survival reported for Rh-PPO are on par with the chemotherapeutic oxaliplatin and fewer health side effects were observed in mice treated with the rhodium complex. Analysis of plasma samples collected after Rh-PPO administration at 1 mpk showed that the drug is rapidly cleared with a half-life of 1.79 hr. The promising anticancer activity observed with Rh-PPO *in vivo* further supports the continued assessment of this rhodium complex and the strategy of targeting DNA mismatches. Ongoing research in our lab is aimed towards enhancing the efficacy of rhodium metalloinsertors with antibody drug conjugates and liposomal formulations, as well as better understanding of the biological mechanism of action.

2.6 References

(1) Zamble, D. B.; Lippard, S. J. Cisplatin and DNA Repair in Cancer Chemotherapy. *Trends Biochem. Sci.* **1995**, *20* (10), 435–439. https://doi.org/10.1016/S0968-0004(00)89095-7.

(2) Bruijnincx, P. C.; Sadler, P. J. New Trends for Metal Complexes with Anticancer Activity. *Curr. Opin. Chem. Biol.* **2008**, *12* (2), 197–206. https://doi.org/10.1016/j.cbpa.2007.11.013.

(3) Muhammad, N.; Guo, Z. Metal-Based Anticancer Chemotherapeutic Agents. *Curr. Opin. Chem. Biol.* **2014**, *19* (1), 144–153. https://doi.org/10.1016/j.cbpa.2014.02.003.

(4) Komor, A. C.; Barton, J. K. The Path for Metal Complexes to a DNA Target. *Chem Commun* **2013**, *49* (35), 3617–3630. https://doi.org/10.1016/j.immuni.2010.12.017.Two-stage.

(5) Kelland, L. The Resurgence of Platinum-Based Cancer Chemotherapy. *Nat. Rev. Cancer* **2007**, *7* (8), 573–584. https://doi.org/10.1038/nrc2167.

(6) Cheung-Ong, K.; Giaever, G.; Nislow, C. DNA-Damaging Agents in Cancer Chemotherapy: Serendipity and Chemical Biology. *Chem. Biol.* **2013**, *20* (5), 648–659. https://doi.org/10.1016/j.chembiol.2013.04.007.

(7) Capra, S.; Ferguson, M.; Ried, K. Cancer: Impact of Nutrition Intervention Outcome-Nutrition Issues for Patients. *Nutrition* **2001**, *17* (9), 769–772. https://doi.org/10.1016/S0899-9007(01)00632-3.

(8) Shaloam, D.; Tchounwou, P. B. Cisplatin in Cancer Therapy: Molecular Mechanisms of Action. *Eur. J. Pharmacol.* **2014**, *0*, 364–378. https://doi.org/10.1016/j.ejphar.2014.07.025.Cisplatin.

(9) Martinez-Balibrea, E.; Martínez-Cardus, A.; Gines, A.; Ruiz De Porras, V.; Moutinho, C.;

Layos, L.; Manzano, J. L.; Buges, C.; Bystrup, S.; Esteller, M.; et al. Tumor-Related Molecular Mechanisms of Oxaliplatin Resistance. *Mol. Cancer Ther.* **2015**, *14* (8), 1767–1776. https://doi.org/10.1158/1535-7163.MCT-14-0636.

(10) Shen, D. W.; Pouliot, L. M.; Hall, M. D.; Gottesman, M. M. Cisplatin Resistance: A Cellular Self-Defense Mechanism Resulting from Multiple Epigenetic and Genetic Changes. *Pharmacol. Rev.* **2012**, *64* (3), 706–721. https://doi.org/10.1124/pr.111.005637.

(11) Weidmann, A. G.; Komor, A. C.; Barton, J. K. Targeted Chemotherapy with Metal Complexes. *Comments Inorg. Chem.* **2014**, *34* (3–4), 114–123. https://doi.org/10.1080/02603594.2014.890099.

(12) Li, Z.; Pearlman, A. H.; Hsieh, P. DNA Mismatch Repair and the DNA Damage Response. *DNA Repair (Amst).* **2016**, *38*, 94–101. https://doi.org/10.1111/mec.13536.Application.

(13) Arzimanoglou, I. I.; Gilbert, F.; Barber, H. R. Microsatellite Instability in Human Solid Tumors. *Cancer* **1998**, *82*, 1808–1820. https://doi.org/10.1016/S1357-4310(96)10055-1.

(14) Hatch, S. B.; Lightfoot, H. M.; Garwacki, C. P.; Moore, D. T.; Calvo, B. F.; Woosley, J. T.; Sciarrotta, J.; Funkhouser, W. K.; Farber, R. A. Microsatellite Instability Testing in Colorectal Carcinoma: Choice of Markers Affects Sensitivity of Detection of Mismatch Repair-Deficient Tumors. *Clin. Cancer Res.* **2005**, *11* (6), 2180–2187. https://doi.org/10.1158/1078-0432.CCR-04-0234.

(15) Zhao, P.; Li, L.; Jiang, X.; Li, Q. Mismatch Repair Deficiency/Microsatellite Instability-High as a Predictor for Anti-PD-1/PD-L1 Immunotherapy Efficacy. *J. Hematol. Oncol.* **2019**, *12* (1), 1–14. https://doi.org/10.1186/s13045-019-0738-1.

(16) Boyle, K. M.; Barton, J. K. Targeting DNA Mismaches with Rhodium Metalloinsertors.

Inorganica Chim. Acta **2016**, *452*, 3–11. https://doi.org/110.1016/j.bbi.2017.04.008.

(17) Fung, S. K.; Zou, T.; Cao, B.; Chen, T.; To, W. P.; Yang, C.; Lok, C. N.; Che, C. M. Luminescent Platinum(II) Complexes with Functionalized N-Heterocyclic Carbene or Diphosphine Selectively Probe Mismatched and Abasic DNA. *Nat. Commun.* **2016**, *7* (May 2015), 1–9. https://doi.org/10.1038/ncomms10655.

(18) Zeglis, B. M.; Pierre, V. C.; Kaiser, J. T.; Barton, J. K. A Bulky Rhodium Complex Bound to an Adenosine-Adenosine DNA Mismatch: General Architecture of the Metalloinsertion Binding Mode. *Biochemistry* **2009**, *48* (20), 4247–4253. https://doi.org/10.1021/bi900194e.

(19) Zeglis, B.; Pierrea, V.; Barton, J. K. Metallointercalators and Metalloinsertorss. *Chem Commun* **2007**, *44*, 4565–4579. https://doi.org/10.1016/j.biotechadv.2011.08.021.Secreted.

(20) Ernst, R. J.; Komor, A. C.; Barton, J. K. Selective Cytotoxicity of Rhodium Metalloinsertors in Mismatch Repair-Deficient Cells. *Biochemistry* **2011**, *50* (50), 10919–10928. https://doi.org/10.1021/bi2015822.

(21) Komor, A. C.; Schneider, C. J.; Weidmann, A. G.; Barton, J. K. Cell-Selective Biological Activity of Rhodium Metalloinsertors Correlates with Subcellular Localization Alexis. *J Am Chem Soc* **2012**, *134* (46), 19223–19233. https://doi.org/10.1038/jid.2014.371.

(22) Komor, A. C.; Barton, J. K. An Unusual Ligand Coordination Gives Rise to a New Family of Rhodium Metalloinsertors with Improved Selectivity and Potency. *J. Am. Chem. Soc.* **2014**, *136* (40), 14160–14172. https://doi.org/10.1021/ja5072064.

(23) Boyle, K. M.; Nano, A.; Day, C.; Barton, J. K. Cellular Target of a Rhodium Metalloinsertor Is the DNA Base Pair Mismatch. *Chem. Eur. J.* **2019**, *25* (12), 3014–3019.

https://doi.org/10.1002/chem.201900042.

(24) Guinney, J.; Dienstmann, R.; Wang, X. The Consensus Molecular Subtypes of Colorectal Cancer. *Nat. Med.* **2015**, *21* (11), 1350–1356. https://doi.org/10.7303/syn2623706.

(25) Jensen, M. M.; Jørgensen, J. T.; Binderup, T.; Kjær, A. Tumor Volume in Subcutaneous Mouse Xenografts Measured by MicroCT Is More Accurate and Reproducible than Determined by 18F-FDG-MicroPET or External Caliper. *BMC Med. Imaging* **2008**, *8*, 1–9. https://doi.org/10.1186/1471-2342-8-16.

(26) Howells, L. M.; Sale, S.; Sriramareddy, S. N.; Irving, G. R. B.; Jones, D. J. L.; Ottley, C. J.; Pearson, D. G.; Mann, C. D.; Manson, M. M.; Berry, D. P.; et al. Curcumin Ameliorates Oxaliplatin-Induced Chemoresistance in HCT116 Colorectal Cancer Cells in Vitro and in Vivo. *Int. J. Cancer* **2011**, *129* (2), 476–486. https://doi.org/10.1002/ijc.25670.

(27) Aston, W. J.; Hope, D. E.; Nowak, A. K.; Robinson, B. W.; Lake, R. A.; Lesterhuis, W. J. A Systematic Investigation of the Maximum Tolerated Dose of Cytotoxic Chemotherapy with and without Supportive Care in Mice. *BMC Cancer* **2017**, *17* (1), 1–10. https://doi.org/10.1186/s12885-017-3677-7.

(28) Alcindor, T.; Beauger, N. Oxaliplatin: A Review in the Era of Molecularly Targeted Therapy. *Curr. Oncol.* **2011**, *18* (1), 18–25. https://doi.org/10.3747/co.v18i1.708.

(29) Perry, B. J.; Balazs, R. E. ICP-MS Method for the Determination of Platinum in Suspensions of Cells Exposed to Cisplatin. *Anal. Proc. Incl. Anal. Commun.* **1994**, *31* (9), 269–271. https://doi.org/10.1039/AI9943100269.

(30) Frik, M.; Martínez, A.; Elie, B. T.; Gonzalo, O.; Ramírez De Mingo, D.; Sanaú, M.; Sánchez-Delgado, R.; Sadhukha, T.; Prabha, S.; Ramos, J. W.; et al. In Vitro and in Vivo

Evaluation of Water-Soluble Iminophosphorane Ruthenium(II) Compounds. A Potential Chemotherapeutic Agent for Triple Negative Breast Cancer. *J. Med. Chem.* **2014**, *57* (23), 9995–10012. https://doi.org/10.1021/jm5012337.

(31) Jemal, A.; Bray, F.; Center, M. M.; Ferlay, J.; Ward, E.; Forman, D. Global Cancer Statistics. *CA Cancer J Clin* **2011**, *61* (1), 69–90. https://doi.org/10.3322/caac.20107.Available.

(32) Boyle, K. M.; Barton, J. K. A Family of Rhodium Complexes with Selective Toxicity toward Mismatch Repair-Deficient Cancers. *J. Am. Chem. Soc.* **2018**, *140* (16), 5612–5624. https://doi.org/10.1021/jacs.8b02271.

(33) Nano, A.; Bailis, J. M.; Mariano, N. F.; Pham, E. D.; Threatt, S. D.; Barton, J. K. Cell-Selective Cytotoxicity of a Fluorescent Rhodium Metalloinsertor Conjugate Results from Irreversible DNA Damage at Base Pair Mismatches. *Biochemistry* **2020**, *59*, 717–726. https://doi.org/10.1021/acs.biochem.9b01037.

(34) Bailis, J. M.; Weidmann, A. G.; Mariano, N. F.; Barton, J. K. Rhodium Metalloinsertor Binding Generates a Lesion with Selective Cytotoxicity for Mismatch. *Proc. Natl. Acad. Sci.* **2017**, *114* (27), 6948–6953. https://doi.org/10.1073/pnas.1706665114.

(35) Coverdale, J.; Laroiya-McCarron, T.; Romero-Canelón, I. Designing Ruthenium Anticancer Drugs: What Have We Learnt from the Key Drug Candidates? *Inorganics* **2019**, *7* (3), 1–15. https://doi.org/10.3390/inorganics7030031.

(36) Bergamo, A.; Masi, A.; Dyson, P. J.; Sava, G. Modulation of the Metastatic Progression of Breast Cancer with an Organometallic Ruthenium Compound. *Int. J. Oncol.* **2008**, *33*, 1281–1289. https://doi.org/10.3892/ijo.

(37) Gondi, C. S.; Rao, J. S. Cathepsin B as a Cancer Target. *Expert Opin Ther Targets* **2013**,

17 (3), 281–291. https://doi.org/10.4149/neo_2015_003.

(38) Graham, M. A.; Lockwood, G. F.; Greenslade, D.; Brienza, S.; Bayssas, M.; Gamelin, E. Clinical Pharmacokinetics of Oxaliplatin: A Critical Review. *Clin. Cancer Res.* **2000**, *6* (4), 1205–1218.

(39) Lévi, F.; Metzger, G.; Massari, C.; Milano, G. Oxaliplatin: Pharmacokinetics and Chronopharmacological Aspects. *Clin. Pharmacokinet.* **2000**, *38* (1), 1–21. https://doi.org/10.2165/00003088-200038010-00001.

Chapter 3

DEVELOPMENT AND CHARACTERIZATION OF LIPOSOMAL FORMULATIONS OF METALLOINSERTOR RH-PPO[§]

3.1 Introduction

Colorectal cancer (CRC) is the third most diagnosed cancer in the world with an estimated 700,000 deaths worldwide each year.[1] Most patients diagnosed with the disease still localized to the site of origin have good prognoses with 70-80% of newly diagnosed patients being eligible for curative surgical resection and adjuvant chemotherapy; however, once the cancer has metastasized, patients have much poorer prognoses with a median overall survival of 5 months.[1,2] Various therapeutics, including 5-fluorouracil, oxaliplatin, and irinotecan, are currently prescribed to metastatic colorectal cancer (mCRC) patients. While these drugs often effectively cause cytotoxicity in malignant cells by directly or indirectly inducing DNA damage, these compounds are also toxic towards healthy, often rapidly dividing cells, which results in numerous side effects ranging from gastrointestinal toxicity to nephrotoxicity. Importantly, non-selective, covalent modification is the DNA binding mode (**Figure 3.1**) common to platinum-based chemotherapeutics, which are prescribed to more than 50% of cancer patients.[27,30] Ultimately, in order to mitigate the undesired side effects, toxicity, and resistance to traditional, non-targeted chemotherapeutics, there is a need to develop therapies that specifically target biological markers unique to cancerous cells; in particular, drugs effective against cancers resistant to our current leading chemotherapeutics.

[§]Daniel Peng, a Caltech Undergraduate, assisted with assessment of the liposome lysis procedure and with attempts to optimize Rh-PPO encapsulation. Dr. Levi Ekanger participated in discussions about the Rh-PPO liposome design and advised on the manual extrusion method.

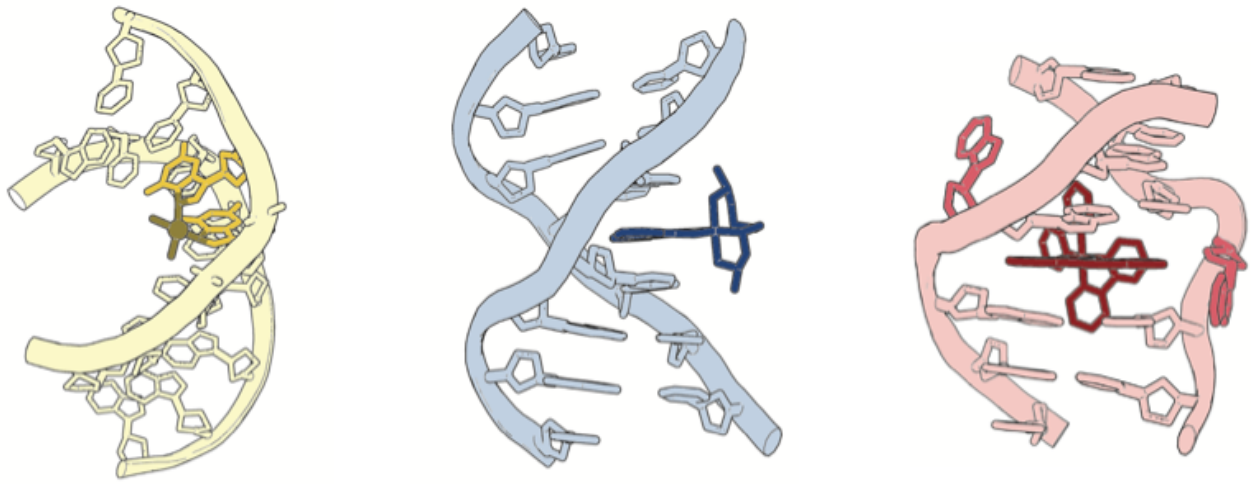

Figure 3.1 Structures of DNA binding modes represented in classic and novel chemotherapeutics. (Left) Representative covalent binding structure based on PDB 1AIO, (middle) intercalation structure based on PDB 454D, and (right) metalloinsertion structure based on data from Reference 3.[3]

Mismatch repair (MMR) deficiencies are a hallmark for 16% of all solid tumors and 80% of hereditary nonpolyposis colon (Lynch syndrome) cancers, and many patients with these types of malignancies are resistant to current oncology treatments.[4] Developing compounds able to selectively target the mismatch base pairs that result from MMR-deficient colorectal cancers has been a research objective for several years. As shown in **Figure 3.1**, research in our group has pursued the development of transition metal complexes that bind to DNA via modes of intercalation (binding between the planar bases of DNA) and metalloinsertion (insertion into the minor groove and ejection of base pairs).[3]

Rhodium metalloinsertors have been shown to selectively bind to mismatched over well-matched DNA sites. Through the incorporation of planar, sterically expansive inserting ligands, such as chrysi (5,6-chrysenequinone diamine) and phzi (benzo[a] phenazine-5,6-quinone diimine), our rhodium metalloinsertor complexes are able to detect and bind to thermodynamically destabilized mismatches. We attribute the selective binding of these complexes to the incorporation of these expansive inserting ligands; for example, the chrysi ligand is slightly larger than a well-matched base pair (11.3 Å compared to 10.85 Å, respectively), which significantly reduces the ligand's ability to indiscriminately intercalate between well-matched bases.[3] Once mismatch sites are identified, the rhodium molecules insert from the minor groove and eject the mismatched bases from the DNA pi stack (**Figure 3.1**).[3]

The latest family of metalloinsertors (Rh-O metalloinsertors) are octahedral complexes that contain an N^O coordinating ligand and chrysi as the inserting ligand. These complexes display high selectivity and potency (ranging from 300 nm to 3 μM) towards MMR-deficient cancer cell lines based on cell viability and cellular proliferation activity assays.[5] Studies have found that alterations to the hydroxyl-containing ancillary ligand of these metalloinsertor has

little effect on the biological activity of these complexes. Additionally, the formation of the N^O coordination resulted in these metalloinsertors having higher pKa values than previous generations, which caused a buckling of the inserting chrysi ligand at physiological pH.[5] Recent studies have supported our hypothesis that Rh-O metalloinsertors induce necrotic cell death by generating lesions and DNA double strand breaks that are recognized by DNA repair machinery.[6]

These new Rh-O metalloinsertor complexes have significant potential as chemotherapeutics, and our most potent and selective compound, $[Rh(chrysi)(phen)(PPO]Cl_2$ (Rh-PPO), where phen = 1,10-phenanthroline, and PPO = 2-(pyridine-2-yl)propan-2-ol), has undergone preclinical evaluation in mice studies to assess its efficacy, pharmacokinetic characteristics, and systemic toxicity. As detailed in Chapter 2, Rh-PPO shows significant promise as a chemotherapeutic for MMR-deficient cancers. Xenograft studies with HCT116 colorectal carcinoma cells showed significant reductions in tumor weight and volume after Rh-PPO was administered intraperitoneally, as well as an increase in overall survival as a result of treatment. However, pharmacokinetic studies revealed notable accumulation of rhodium in a number of the collected organs, especially the liver, which indicates that systemic toxicity is likely to occur after prolonged treatment with the metalloinsertor. Additionally, intratumoral studies with Rh-PPO found that even greater anti-tumor effects can be achieved if the drug is administered directly to the tumor site. Altogether, these findings suggest that increased targeting of Rh-PPO to the tumor site will be necessary to maximize the drug's cancer killing abilities, while minimizing systemic toxicity.

In particular, liposomes have been explored as a therapeutic carrier for Rh-PPO to reduce the systemic toxicity of the metalloinsertor and increase targeting to the tumor site. Liposomes

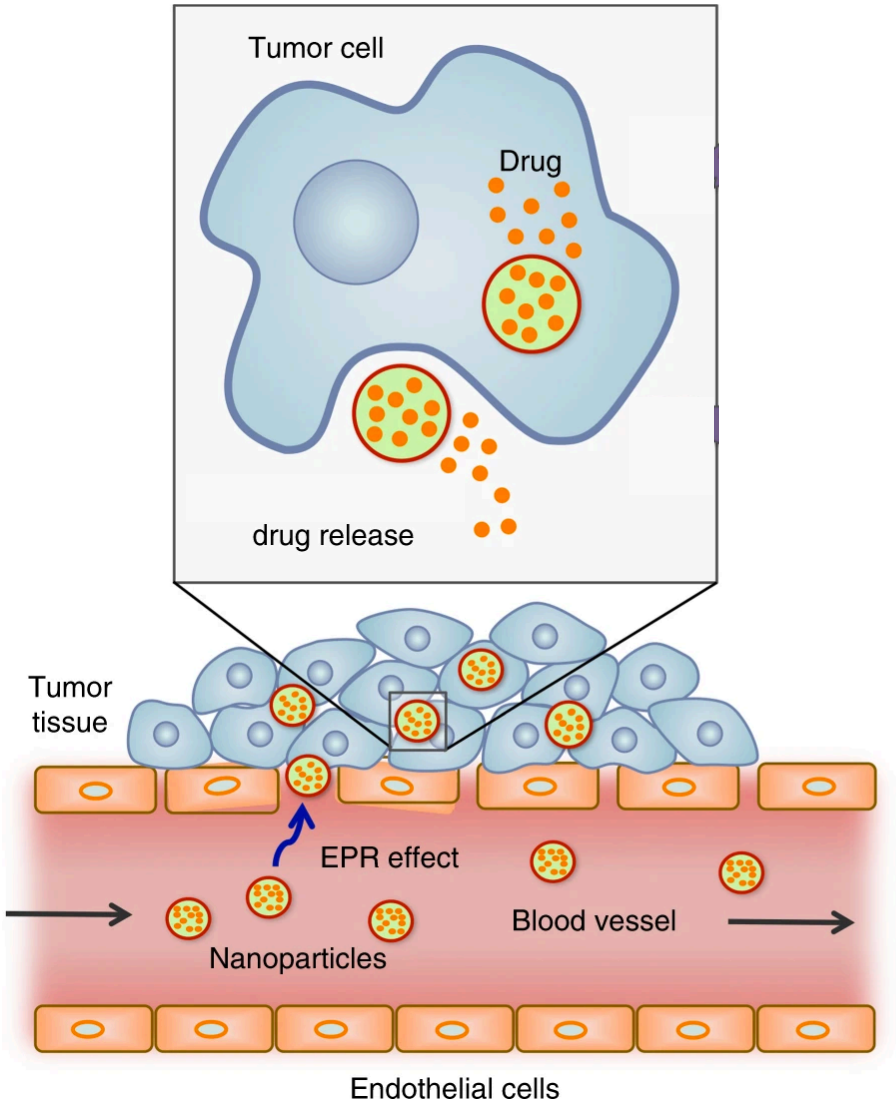

Figure 3.2 The EPR effect and passive targeting of nanoparticles, including liposomes, to the tumor microenvironment. Briefly, due to uncontrolled angiogenesis at the site of tumors, endothelial vasculature produced from tumors is "leaky." This results in nanoparticles between 100 and 700 nm in diameter being accumulated at the site of tumors, allowing for passive targeting of nanoparticles to the tumor microenvironment. Adapted from Reference 31.

are nanoparticles that consist of a phospholipid bilayer. These biocompatible, low-toxicity drug delivery systems can enclose hydrophilic and hydrophobic compounds either inside or within their lipid bilayer.[8] In the case of chemotherapeutics, liposomes, especially small unilamellar vesicles (SUVs), are thought to achieve increased drug efficacy and exhibit lower systemic toxicity compared with the free drug by utilizing the enhanced permeability and retention (EPR) effect. Specifically, the EPR effect allows for accumulation of nanoparticles in the tumor microenvironment through leaky tumor-associated blood vessels (**Figure 3.2**).[7,31] Several promising chemotherapeutic liposomal drug formulations have been developed and undergone clinical trials. For instance, Lipoplatin is a cisplatin-loaded liposomal formulation with PEGylated phospholipids that has shown substantially reduced renal toxicity, myelotoxicity, and other dose limiting side effects compared to the free platinum drug.[8,9,10]

Due to the systemic toxicity of the free drug, a Rh-PPO liposomal formulation was designed, generated, and assessed *in vitro.* The procedures for synthesizing and characterizing the nanoparticle were optimized, and ultimately resulted in the establishment of procedures for a liposomal formulation of metalloinsertors that may allow for these compounds to continue preclinical development as chemotherapeutic treatments for MMR-deficient cancers.

3.2 Experimental Methods

3.2.1 Materials

All materials were commercially available and used as received, unless otherwise noted. Organic solvents were purchased from Sigma Aldrich unless otherwise noted. Sep-Pak C18 solid-phase extraction (SPE) cartridges were acquired from Waters Chemical Co (Milford, MA). Water was purified using the Millipore Milli-Q system (Milford, MA, USA). All HPLC metal

complex purifications were carried out on a Hewlett-Packard 1100 HPLC. All UV-Visible experiments were performed on a Cary 100 spectrometer. NMR experiments were carried out on Varian 300 and 500MHz instruments, as indicated. 18:0 PC (DSPC) 1,2-distearoyl-sn-glycero-3-phosphocholine, DSPE-PEG(2000) Maleimide 1,2-distearoyl-sn-glycero-3-phosphoethanolamine-N-[maleimide(polyethylene glycol)-2000] (ammonium salt), and cholesterol were ordered from Avanti Polar Lipids (Alabaster, AL).

3.2.2 Synthesis and Purification of Rhodium Metalloinsertor Compounds

[Rh(chrysi)(phen)(2-(pyridine-2-yl)propan-2-ol]Cl_2 (Rh-PPO) was synthesized following published methodology.[5] The purification of Rh-PPO was modified from the literature as described in Chapter 2.

3.2.3 Literature Analysis to Determine Liposome Lipid Composition

In order to determine which lipids should be used to compose the Rh-PPO liposomes, a thorough literature analysis was conducted. A number of FDA approved liposomal drugs, as well as ones undergoing clinical trials, were researched, and the identity and molar percentage of each lipid was evaluated.[9,11,12] This information was utilized to determine the lipids and molar percentages of each that were evaluated in the Rh-PPO liposome studies.

3.2.4 Liposome Preparation Procedures

3.2.4.1 Passive Loading

Lipid thin films were generated in 4 mL glass vials by measuring lipids (ex. 30 mg total Cholesterol:DSPE-PEG:DSPC; 40:5:55 mol%), dissolving the lipids in chloroform (1-2 mL), then evaporating *in vacuo* (chloroform lipid solution was first cooled in an ice bath to prevent bumping on the rotovap). Lipids were further dried under vacuum overnight. A solution of [Rh(phen)(chrysi)(PPO)]Cl_2 (Rh-PPO) in MilliQ water was generated (0.1 to 2 mM Rh-PPO)

and transferred to the vial containing dried lipids. The vial was sonicated for 1 min, then the Rh-lipid solution was mixed at 60ºC for 1 hr. The resulting mixture was then extruded as described in detail below with 200 nm, then 100 nm filters, and free Rh-PPO was removed by following the centrifugation procedure.

3.2.4.2 Thin film

Lipids were weighed out (ex. 30 mg total lipid with Cholesterol:DSPE-PEG:DSPC; 40:5:55 mol%), and dissolved the lipids in 1 – 2 mL chloroform (30 mg lipid per mL $CHCl_3$). Rh-PPO was weighed out (ex. ~ 0.75 mg), then dissolved in 1mL solvent, either methanol, isopropanol, or acetonitrile. Metalloinsertor solution was heated and sonicated if necessary. Then, made 1:1 solution by mixing lipid solution and Rh-PPO solution and subsequently evaporated *in vacuo*. Mixture was further dried under vacuum overnight. 1 mL aqueous solvent was added to the Rh-lipid thin film, then the mixture was stirred at 60ºC for 1-6 hr. The resulting mixture was then extruded as described below with 200 nm, then 100 nm filters, and free Rh-PPO was removed by following the centrifugation procedure.

3.2.4.3 Remote Loading

Lipid thin films were generated in 4 mL glass vials by measuring lipids (ex. Cholesterol:DSPE-PEG:DSPC; 40:5:55 mol%), dissolving the lipids in 1-2 mL chloroform (30 mg lipid per mL $CHCl_3$), then evaporating *in vacuo*. Lipids were further dried under vacuum overnight. The lipid thin film was then hydrated with 1 mL of 250 mM ammonium sulfate (pH ~5.5) and mixed at 60ºC for 1 hr – 6 hr. The resulting liposome mixture was then extruded as described below with 200 nm, then 100 nm filters. Buffer exchange, removal of unencapsulated ammonium sulfate, and concentration of liposomes were performed using Amicon Ultra Centrifugal filters. Note that the filters can only hold a volume of 450 μL, so the liposome

solution was iteratively added to the filters to concentrate all of the liposomes. Briefly, the liposomes were spun down in the filter for 30 min at 16.1 rfc at RT. Then, 450 μL MilliQ water was used to resuspend the liposome pellet and the buffer procedure was repeated twice more. Next, the concentrated liposome solution was transferred to a new tube. A Rh-PPO solution was made using MilliQ water or saline (0.1 to 2 mM Rh-PPO) and the concentration was determined by UV-Visible spectrum analysis. The pH of the rhodium metalloinsertor solution was adjusted to ~pH 8 using dilute NaOH. The Rh-PPO solution was then added to the tube containing concentrated liposome, then transferred to a 4 mL glass vial and mixed for 1 hr at 65ºC, subsequently the resulting mixture was extruded as described below with 200 nm, followed by the 100 nm filters, and lastly free Rh-PPO was removed by following the centrifugation procedure. Because the Rh-PPO complex is bright red in color, additional loading of the compound with this method was visually detectable based on the darkness of the resulting liposome pellet. The above remote loading procedure was adapted from Reference 13.[13]

3.2.4.4 Freeze Thaw

Lipid thin films were generated in 4 mL glass vials by measuring lipids (ex. Cholesterol:DSPE-PEG:DSPC; 40:5:55 mol%), dissolving the lipids in chloroform (1-2 mL), then evaporating in vacuo. Lipids were further dried under vacuum overnight. Thin film was then hydrated with 1 mL of Phosphate Buffered Saline (PBS, 1X, pH 7.4) and mixed at 60ºC for 2 hr. The resulting liposome mixture was then extruded as described below with 200 nm, then 100 nm filters and concentrated using Amicon Ultra Centrifugal filters. Note that the filters can only hold a volume of 450 μL, so the liposome solution was iteratively added to the filters to concentrate all of the liposomes. Briefly, the liposomes were spun down in the filter for 30 min at 16.1 rfc at RT. Then, the concentrated liposome solution was transferred to a new tube. A Rh-PPO solution

was made using MilliQ water or saline (0.1 to 2 mM Rh-PPO) and the concentration was determined by UV-Visible spectrum analysis. The Rh-PPO solution was then added to the tube containing liposomes. The Eppendorf tube cap was secured, then the Rh-PPO/liposome mixture was frozen using LN2 (−196°C) for 5 min. The mixture was then thawed in water bath at 63°C (above the phase transition temperature of the lipids) for 5 min. This freeze-thaw procedure was repeated 5 to 8 times total (more cycles result in more uniform liposome particles). The physical characteristics of the liposomes were then analyzed by DLS as described below. If the polydispersity index was found to be above 0.4, the extrusion procedure was repeated on the Rh-PPO liposomes. Free Rh-PPO was removed via centrifugation as described, and the resulting Rh-PPO liposome pellets were combined and resuspended.

3.2.4.5 Extrusion Procedure

Extruder holder and heating block were set up using filter supports and a 200 nm filter, and maintained at a temperature of 55-60ºC on a hot plate. The Rh-PPO/lipid mixture was transferred to the extrusion syringe and inserted into the holder. The lipid mixture was allowed to equilibrate for 5 minutes. The solution was then extruded through the 200 nm filter at least 7 times, then switched to 100 nm filter and extruded 11+ times. Extrusion should be performed an odd number of times such that final extruded lipid solution is not in the syringe that was initially loaded. Note that a wrench should be used for slight additional tightening of the metal component of the extruder to ensure minimal leakage during the extrusion procedure, and additional care should be taken not to touch the middle of filter when positioning it in the metal component. Additionally, syringes should be washed with warmed buffer between extrusion procedures and immediately following the final extrusion. The syringes and metal component of the extruder should be disassembled and washed with warmed MilliQ water, then isopropyl

alcohol and allowed to dry before reassembling. Generally 20 - 30 mg total of lipid was used in each liposome procedure.

3.2.4.6 Removal of Free Rh-PPO via Centrifugation

Following extrusion, Rh-PPO liposome mixtures were spun down in a cold room at ~21K rcf for 90 min, then the supernatant was removed and transferred to a labeled Eppendorf tube. Aqueous solvent (ex. MilliQ water, buffer, or saline) was added to the liposome pellet to resuspend the mixture, and then was spun down again. This procedure was repeated at least 3 times until the supernatant was light orange or clear. The resulting liposome pellet was then resuspended in aqueous media to achieve the desired final liposome/Rh-PPO concentration. Note that the supernatant was also centrifuged multiple times and all of the resulting Rh-PPO liposome pellets were ultimately combined.

3.2.5 Liposome Stability Studies

Three solutions were made by mixing 250 μL of concentrated Rh-PPO liposome solution with 5 mL HCT116N/O media in a falcon tube. Tube A was placed at 4ºC, Tube B was placed at 25ºC, and Tube C was placed at 37ºC. 500 μL of the liposome/media solution was removed immediately from each tube, and transferred to labeled Eppendorf tubes. Additional 250 μL samples were taken at the following time points: 20 min, 40 min. 1 hr, 20 hr, 45 hr, 72 hr, 120 hr, 31 days. Immediately after each sample was collected, the tube was centrifuged at 20k+ rcf for 30 min at 4ºC, then 200 μL supernatant was removed and transferred to labeled tubes. Samples were stored at 4ºC until analyzed. Once all samples were collected, each 200 μL sample was mixed with 200 μL 10% HNO_3 (aq.) and vortexed for 5 min in order to lyse the liposomes. Samples were diluted to 1% HNO_3(aq) by mixing 1.8 mL H_2O and 200 μL lysed sample. The 1% HNO_3 samples were then centrifuged for 5 min at 2K rcf. The resulting solutions were

analyzed via ICP-MS for rhodium content. Percent Rh-PPO retained was calculated with the following equation:

$$\textit{Rh-PPO retained (\%)} = Rh_X / Rh_{initial} \times 100$$

where Rh_x is the detected rhodium content at any given timepoint and $Rh_{initial}$ is the detected rhodium content at timepoint 0 min. These stability experiments were repeated in triplicate with newly generated remote loaded Rh-PPO liposomes for each study.

3.2.6 Lipid concentration assay

3.2.6.1 Standard Curve Determination

A standard curve of liposomal lipids was made to quantify the amount of lipids based on OD_{560} values. Cholesterol:DSPE-PEG:DSPC lipid solution with 40:5:55 mol% (20 mg lipid/ml in 250 mM ammonium sulfate) was generated following the passive loading procedures described above. Then, serial dilutions of extruded lipid were made in order to have the following concentrations: 0 mg/ml, 4 mg/ml. 8 mg/ml, 12 mg/ml, 16 mg/ml, and 20 mg/ml. Dilutions were made using 250 mM ammonium sulfate. Two wells of each concentration were added to a 96-well plate. Absorbance at OD_{560} was collected and used to generate a best fit equation for determining lipid concentration. The following polynomial equation was found to best fit the lipid standard curve:

$y = 32.847x^2 + 26.441x - 0.93,$ where x is the OD_{560} values. Note that the data displayed has an R^2 value of 0.9996.

3.2.6.2 Rh-PPO Lipid Concentration determination

The Rh-PPO liposome solution was diluted to make 200 µL samples of the following approximate lipid concentrations: 1 mg/mL, 2 mg/mL, and 4 mg/mL. Two wells of each concentration were added to a 96-well plate (100 µL each). Absorbance at OD_{560} and OD_{590} was

collected and averaged for each concentration. The standard curve equation determined above was used to estimate the lipid concentration. Note that background from wells filled with buffer only were subtracted from the collected absorbances.

3.2.7 Liposome Physical Characterization Analysis

The particle size of the liposomes was characterized by dynamic light scattering (DLS). Particle size radius and polydispersity index (PDI) were determined using a DLS instrument and analyzed using Dynamics software (Santa Barbra, CA). Note, the concentrated Rh-PPO liposome solution had to be diluted at least 30-fold in order to accurately detect the liposome size and PDI. Typically duplicate 30X, 60X, and 120X dilutions were made for each liposome solution and measurements were averaged. Note that dilutions were thoroughly mixed using pipetting before the sample was analyzed.

3.2.8 Determination of Extinction Coefficients for Rh-PPO in MeOH

Two aqueous solutions of Rh-PPO with different concentrations were made, and a UV-Visible spectrum was taken for each. The concentration of Rh-PPO was determined based on molar absorptivity values reported in the literature.[5] The solutions were then transferred to Eppendorf tubes and the solvent was removed using a speed vacuum. Rh-PPO was re-dissolved in an equivalent volume of MeOH and a UV-Visible spectrum was taken. The major UV-Visible spectrum peaks from the complex were identified as 270 nm, 319 nm, and 386 nm. The molar extinction coefficients for each wavelength were then determined using Beer's law ($A = \varepsilon lc$), as the concentration of Rh-PPO (c) had been determined in water initially and the absorbance values (A) were based on the spectra collected for the MeOH Rh-PPO solutions. The calculated molar coefficients for the two Rh-PPO samples were averaged.

3.2.9 Concentration Determination of Rh-PPO

3.2.9.1 Rh-PPO H_2O UV-Visible Analysis

A solution of Rh-PPO metalloinsertor was made in MilliQ water and a UV-Vis spectrum was recorded. The concentration of Rh-PPO stock solution was then determined by using the Cary UV-Vis instrument absorbance values, as well as molar absorptivity values from the literature.[5] The following molar absorptivity values were used to estimate the concentration of Rh-PPO in water: UV−vis (H_2O, pH 7.0): 270 nm (122,400 M^{-1} cm^{-1}), 300 nm (41,600 M^{-1} cm^{-1}), 430 nm (12,300 M^{-1} cm^{-1}).

3.2.9.2 Rh-PPO MeOH UV-Visible Analysis

A solution of Rh-PPO metalloinsertor or lysed Rh-PPO liposome was made in MeOH and a UV-Vis spectrum was recorded. The concentration of Rh-PPO was then determined by using the Cary UV-Vis instrument, as well as molar absorptivity values calculated for Rh-PPO in methanol. The following molar absorptivity values were used to estimate the concentration of Rh-PPO in MeOH: UV−vis (MeOH): 270 nm (93,800 M^{-1} cm^{-1}), 319 nm (31,430 M^{-1} cm^{-1}), 386 nm (11,390 M^{-1} cm^{-1}).

3.2.10 Encapsulation Efficiency Determination

3.2.10.1 Methanol Lysis

The liposomes were lysed using methanol to determine the amount of Rh-PPO drug encapsulated. Briefly, 20 μL of Rh-PPO liposomal suspension was added to 530 μL of methanol and heated at 60^{o}C for 5 minutes, then vortexed for 5 min (cycle completed 3X) to facilitate full lysis of the liposomes. The liposome samples were then analyzed by UV-Vis to determine Rh-

PPO concentration.

3.2.10.2 Triton X-100 lysis

The liposomes were lysed using 1% Triton X-100 (10% Triton X had too large of a background UV-Vis absorption) to determine the amount of Rh-PPO encapsulated in the liposome. Briefly, 25 µL of liposomal suspension was added to 975 µL of 1% Triton X-100 (or 12.5 µL Liposome added to 487.5 µL 1% Triton-x) and heated at 60^{o}C for 3 min, then vortexed for 3 min (cycle completed 3X) to facilitate lysis of the liposomes. Sample was centrifuged for 10 min at 16.1K rcf. The supernatant was then used to make three different dilution samples (ex. 2X dilution, 3X dilution, 4X dilution) and UV-Vis analysis was conducted. Note that various concentrations of Triton-X buffer were first assessed for their UV-Vis absorption to determine which detergent concentration had low signals at the relevant wavelengths.

3.2.10.3 Encapsulation Efficiency Calculations (EE%)

3.2.10.3.1 Direct EE%

Calculations were performed to determine the total moles of Rh-PPO added to lipids to generate liposomes (Rh_{tot}), and total moles of Rh-PPO encapsulated in liposomes (Rh_{lip}) was determined by performing the MeOH lysis procedure. The following calculation was then performed:

$$Direct\ EE\% = Rh_{lip} / Rh_{tot}$$

3.2.10.3.2 Indirect EE%

The molar concentration of the initial Rh-PPO supernatant (Rh_{sup}), which resulted from the first centrifugation of Rh-PPO liposomes to remove free Rh, was determined using UV-Vis. Additionally, the molar concentration of Rh-PPO in the Rh-PPO/liposome solution (still

containing free Rh-PPO) was determined by performing the MeOH lysis procedure ($Rh_{lip+free}$) The following calculation was then performed: $Indirect\ EE\% = (Rh_{lip+free} - Rh_{sup}) / Rh_{lip+free}$

3.2.11 Cell Culture

The cells were incubated in tissue culture flasks at 37°C in a 5% CO_2 atmosphere. Standard procedures for entering and exiting cryostorage were followed, as well as methods for subculturing HCT116 cells. HCT116N and HCT116O cells were grown and maintained using RPMI (Roswell Park Memorial Institute) 1640 media supplemented with 10% FBS (fetal bovine serum), 2mM L-glutamine, 0.1 mM non-essential amino acids, 1 mM sodium pyruvate, 100 units/mL penicillin, streptomycin, and 100 μg/mL geneticin (G418).

3.2.11.1 MTT Cell Viability Assay

MTT experiments were performed in HCT116N and HCT116O cells as detailed in the literature.[5] Briefly, approximately 50,000 HCT116N or HCT116O cells in 100 μL of media were plated per well into a 96-well plate. 40 wells were filled with each cell line. Varying concentrations of free Rh-PPO or Rh-PPO liposome solutions (ex. 0-10 μM) were added to the wells and the cells were allowed to incubate at 37°C for 72 hours. After incubation, MTT (2-(4,5-dimethylthiazol-2-yl)-2,5-diphenultatrazolium bromide) was added. Metabolically active cells were given 4 hours to convert the MTT reagent to insoluble formazan. The reaction was then stopped and solubilized using a solubilizing reagent. The quantity of formazan was determined colorimetrically by absorbance at 570 nm (background subtracted at 690 nm). Viability was determined by comparing absorbance for treated and untreated cells.

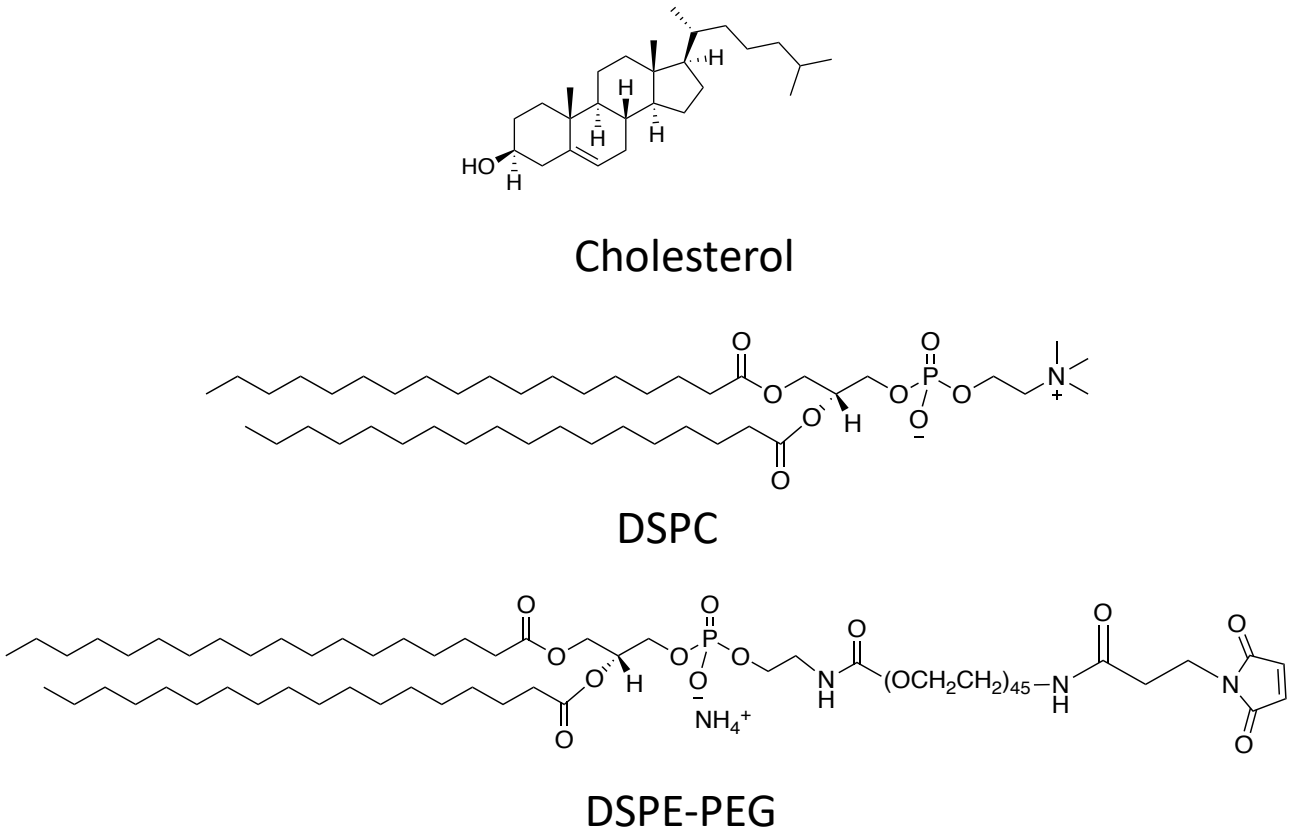

Figure 3.3 Chemical structures of lipids used in the Rh-PPO liposomal studies. Chemical structure of (top) Cholesterol (Chol), a steriod used as a structural stabilizer for liposomes, (middle) 1,2-distearoyl-sn-glycero-3-phosphocholine (DSPC), a saturated, neutral phospholipid with a high transition temperature that is used in two clinically approved liposomal chemotherapeutics, and (bottom) 1,2-distearoyl-sn-glycero-3-phosphoethanolamine-N-[maleimide(polyethylene glycol)-2000] ammonium salt (DSPE-PEG), a PEGylated lipid with a maleimide functionalization that should allow for increased circulation *in vivo* and potential chemical conjugation.

3.3 Results

3.3.1 Rh-PPO Liposome Lipid Selection

After a thorough literature analysis, 1,2-distearoyl-sn-glycero-3-phosphocholine (DSPC), 1,2-distearoyl-sn-glycero-3-phosphoethanolamine-N-[maleimide(polyethylene glycol)-2000] ammonium salt (DSPE-PEG), and cholesterol (Chol) were the lipids selected to compose the Rh-PPO liposomes (**Figure 3.3**). The DSPC lipid was chosen because it is used in at least 2 FDA approved, chemotherapeutic liposomal drugs.[12] It is a saturated, neutral phospholipid; therefore, it will be relatively stable and less prone to oxidation compared to other phospholipids. Cholesterol is expected to stabilize the local packing order of the lipid bilayer, and cholesterol content can significantly influence the phase transition temperature and liposomal membrane fluidity, elasticity, and permeability.[9,14] Ultimately, the molar content of cholesterol can be modulated to optimize drug release from the liposome once it reaches and accumulates at the site of target tumor cells. Importantly, cholesterol has also been reported to reduce drug incorporation efficiency, so the cholesterol content in a liposome must be carefully optomized.[14]

Lastly, the DSPE-PEG lipid was chosen to be incorporated into the liposome because studies have shown that non-PEGylated liposomes experience rapid clearance due to the mononuclear phagocyte system (MPS),[15] predominantly in the liver and spleen. Incorporation of PEGylated phospholipids into the liposomes allows the nanoparticle to evade MPS clearance, and ultimately have longer circulation *in vivo* and less toxicity within the liver and spleen. Additionally, the DSPE-PEG lipid is functionalized with a maleimide chemical group which can be used to conjugate peptides and other macromolecules to the liposome.

3.3.2 Initial Liposome Preparation and Characterization

Liposomes were initially generated using the standard passive loading protocol described above with MilliQ water as the hydrating solution. The procedure was developed for the selected lipids with the following molar ratio: Cholesterol:DSPE-PEG:DSPC at 40:5:55 mol%. For example, the phase transition temperature for the lipid combination is expected to be ~ 55°C, mainly due to the saturated chains of DSPC, and as a result, all hydration and extrusion procedures were performed at temperatures greater than 55°C (typically 60°C to 65°C). The 40:5:55 molar ratio was initially selected to balance liposome stability and drug release with increased *in vivo* circulation.[14] The resulting liposome underwent physical and biological characterization. Note that these liposomes with no Rh-PPO encapsulated are referred to as Chol:DSPE-PEG:DSPC liposomes.

3.3.2.1 Physical Characterization

Dynamic light scattering (DLS) was utilized to assess the radius/diameter of the Chol:DSPE-PEG:DSPC liposomes., as well as the size distribution of the nanoparticles. The liposome solution was diluted (30X) and measured in triplicate for these studies. These experiments revealed a mean liposome diameter of 146.9 nm and polydispersity index (PDI) of 0.277 (**Figure 3.4**). The PDI is lower than 0.4, which indicates that the liposome preparation and extrusion resulted in acceptable dispersion homogeneity.[16] Furthermore, the diameter measurements show that the generated liposomes are a size compatible with the EPR effect (between 100 and 700 nm), which can allow for passive accumulation of nanoparticles at tumor cell sites through leaky vasculature.[7]

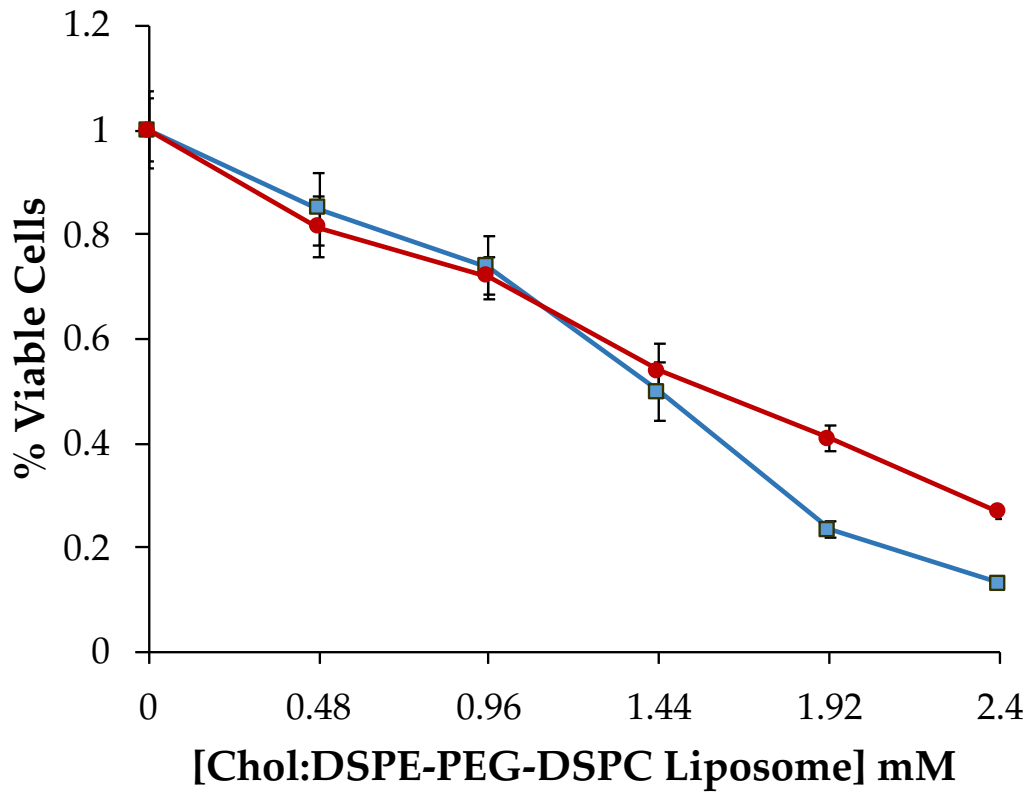

Sample Number	Mean Radius (nm)	Diameter (calculated)	Sample Standard Deviation (s)	Sample Variance (s^2)	Polydispersity Index (PDI)
1	74.499	148.9998	1.029	1.059	0.248
2	74.109	148.218	1.426	2.033	0.303
3	71.731	143.462	1.140	1.300	0.251

Figure 3.4 Biological and physical characterization of liposomes without Rh-PPO encapsulated. (Top) MTT cell viability assay of the Chol:DSPE-PEG:DSPC liposome (Cholesterol:DSPE-PEG:DSPC at 40:5:55 mol%) with HCT116N (MMR-proficient, blue) and HCT116O (MMR-deficient, red) cell lines. (Bottom) Table containing physical characterization measurements of the Chol:DSPE-PEG:DSPC liposomes including radius, diameter, standard deviation, variance, and polydispersity index (PDI).

3.3.2.2 Biological Characterization

MTT cell viability assays were used to determine the cytotoxicity of the empty Chol:DSPE-PEG:DSPC liposomes (Cholesterol:DSPE-PEG:DSPC at 40:5:55 mol%) towards the MMR-deficient human colorectal cancer cell line HCT116O, as well as HCT116N cells, the matched MMR-proficient cell line (**Figure 3.4**). These cell lines have consistently been used to characterize the potency and selectivity of rhodium metalloinsertors, including Rh-PPO, towards MMR-deficient cells; therefore, initial toxicity experiments focused on the liposomes without Rh-PPO encapsulated (Chol:DSPE-PEG:DSPC liposomes) to determine the cytotoxicity of the liposomes alone. This experiment found that the Chol:DSPE-PEG:DSPC liposomes have significant cytotoxicity at low millimolar concentrations. Furthermore, as expected, there is minimal cytotoxic selectivity based on MMR status with half maximal inhibitory concentrations (IC_{50}) of 1.44 mM and 1.55 mM for HCT116N and HCT116O cells, respectively. These findings indicate that achieving high encapsulation efficiency of Rh-PPO will be important for limiting the cytotoxicity of the liposome lipids alone and ensuring that toxicity mainly occurs as a result of metalloinsertor cellular activity.

3.3.3 Optimization of Rh-PPO Liposome Preparation

Rh-PPO liposomes were first generated using the same passive loading procedure utilized to generate the empty Chol:DSPE-PEG:DSPC liposomes. During this liposomal preparation, drug loading and liposomal formation occur concurrently. Due to the cytotoxicity of the empty Chol:DSPE-PEG:DSPC liposomes at high lipid concentrations, the encapsulation of Rh-PPO into the liposomes was thoroughly examined by developing lysis procedures for the purified Rh-PPO liposomes and determining the metalloinsertor concentration using UV-Visible absorbance

measurements. Note that UV-Visible absorbance measurements are the method typically utilized to determine metalloinsertor concentration due to the complexes being hygroscopic.

3.3.3.1 Rh-PPO Liposome Lysis Protocol Development

Initial Rh-PPO liposome lysis protocols used the nonionic detergent Triton X-100, which is known to disrupt the phospholipid bilayer and cause release of encapsulated molecules.[17] The background UV-Vis spectrum of Triton X-100 was taken for concentrations ranging from 1% to 10% Triton X-100. Higher concentrations of Triton-X-100 had absorbance at wavelengths of 350 nm and lower; therefore, 1% Triton X-100 was used for the lysis studies with this detergent. The 1% Triton X-100 solution did not efficiently lyse the liposomes (as determined by DLS) and the background absorbance of the detergent made it difficult to accurately determine low Rh-PPO concentrations in liposomes. As a result, the use of methanol to lyse the Rh-PPO liposomes was explored.

First, the molar absorptivity values for Rh-PPO in methanol were determined to be as follows: UV−vis (MeOH): 270 nm (93,800 M^{-1} cm^{-1}), 319 nm (31,430 M^{-1} cm^{-1}), 386 nm (11,390 M^{-1} cm^{-1}). **Figure 3.5** shows the structure of Rh-PPO alongside the data used to determine the molar absorptivity values, specifically the UV-Visible spectra for Rh-PPO in water compared to methanol. Next, the methanol lysis procedure was developed. First, the ratio of methanol-to-liposome necessary to efficiently lyse the liposomes was determined to be greater than 25:1; then a series of vortexing and heating steps were incorporated to further promote liposome lysis. Full lysis was confirmed by lack of pellet formation after centrifugation and DLS measurements. In **Figure 3.6**, the metalloinsertor sample that resulted from MeOH lysis of the Rh-PPO liposomes can be seen to have a similar UV-Visible spectra to a solution of only

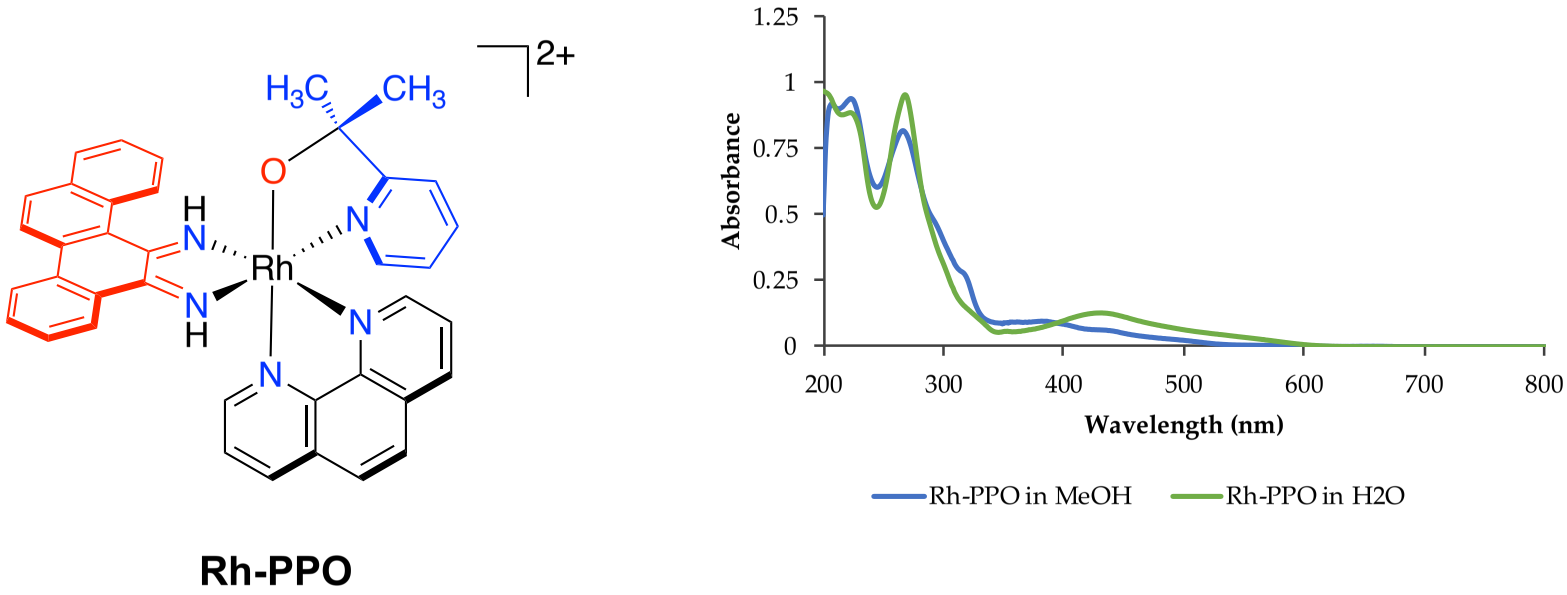

Figure 3.5 Rh-O metalloinsertor Rh-PPO structure and UV-Vis spectra. (Left) Chemical structures of [Rh(chrysi)(phen)(PPO)]$^{2+}$ (Rh-PPO) with the inserting chrysi ligand is shown in red and the axial PPO ligand is displayed in blue, and (right) the UV-Visible spectrum of Rh-PPO in H_2O at pH 7 and MeOH.

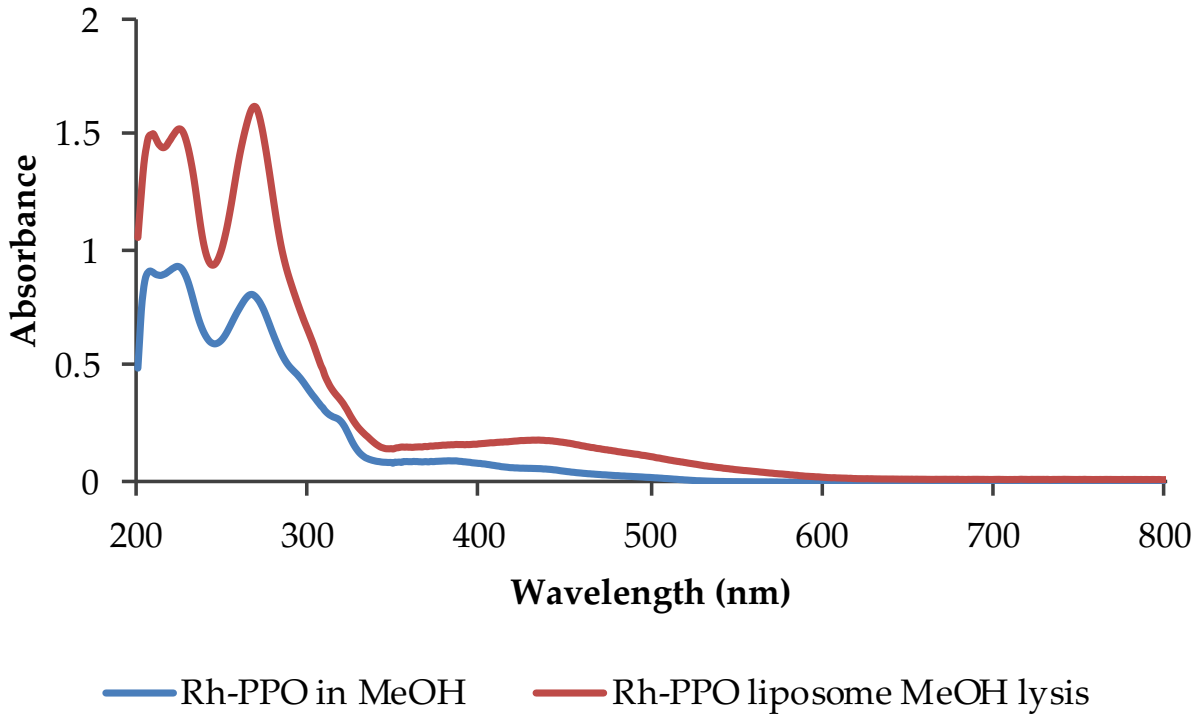

Figure 3.6 UV-Visible spectrum of $[Rh(chrysi)(phen)(PPO)]^{2+}$ (Rh-PPO) in MeOH and Rh-PPO liposome MeOH lysis sample.

Rh-PPO in MeOH; a finding that supports the use of this methanol lysis method to determine the concentration of Rh-PPO encapsulated into liposomes.

3.3.3.2 Characterization of Passively Loaded Rh-PPO Liposomes

Passively loaded Rh-PPO liposomes were generated with two lipid molar ratios: Cholesterol:DSPE-PEG:DSPC at 40:5:55 mol% (Rh-PPO Lip P40) and Cholesterol:DSPE-PEG:DSPC at 20:5:75 mol% (Rh-PPO Lip P20). Only a small percentage (ex. 5%) of PEGylated lipid is needed to achieve decreased blood clearance of the liposomes, so the molar percentage of DSPE-PEG was kept consistent. Varying the ratio of Cholesterol and DSPC lipid allows phospholipid membrane parameters such as fluidity, elasticity, and permeability to be modulated; therefore, physical and biological characterization of these liposomes was conducted. Note that the literature suggests cholesterol mol% should not surpass 50% because higher Chol molar lipid composition percentages often result in crystal formation.[18]

Both Rh-PPO liposomes were characterized using DLS. As shown in **Figure 3.7**, Rh-PPO Lip P20 was found to have a PDI of 0.43, while Rh-PPO Lip P40 samples had a PDI of 0.24. Additionally, Rh-PPO Lip P20 and Rh-PPO Lip P40 had diameters of 240 nm and 155 nm, respectively. Methanol lysis of the liposomes revealed an encapsulation efficiency (EE%) of 30.2±4% for Rh-PPO Lip P20 and 17.7±3% for Rh-PPO Lip P40.

Lastly, MTT cell viability assays tested if the passively loaded liposomes retained the high selectivity and potency of the free Rh-PPO metalloinsertor (**Figure 3.7** and **Figure 3.8**). Given the particle uniformity, cytotoxic selectivity for MMR-deficient HCT116O cells, and low PDI, Rh-PPO Lip 40 appears to have superior characteristics; however, both Rh-PPO liposome compositions have drug encapsulation efficiencies lower than 50%. As a result, alternative

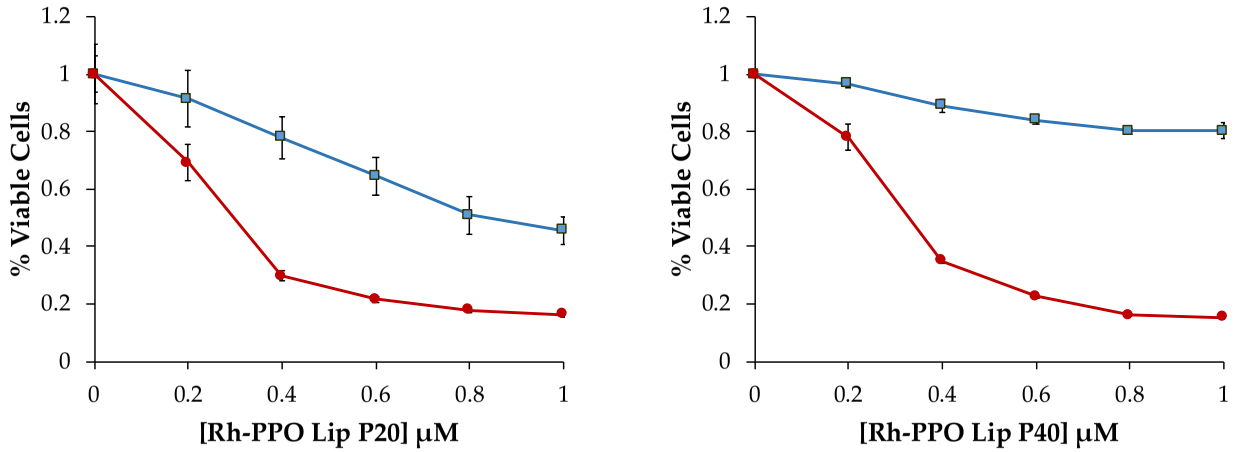

Sample Name	Encapsulation Efficiency (%)	Maximum Differential Cytotoxicity (%)	Diameter (PDI)
Rh-PPO Lip P20	30.2±4	48.2 ± 7%	240 nm (0.43)
Rh-PPO Lip P40	17.7 ±3	64.8 ± 5%	155 nm (0.24)

Figure 3.7 MTT cell viability assay of cells treated with passively loaded Rh-PPO liposomes. HCT116N (MMR-proficient, blue squares) and HCT116O (MMR-deficient, red circles) cells were treated with (left) passively loaded Rh-PPO liposomes with Cholesterol:DSPE-PEG:DSPC at 20:5:75 mol% (Rh-PPO Lip P20) and (right) passively loaded Rh-PPO liposome with Cholesterol:DSPE-PEG:DSPC at 40:5:55 mol% (Rh-PPO Lip P40). Cells were incubated with each liposome solution at the Rh-PPO concentrations indicated for 72 hr, then cells were treated with the MTT reagent for 4 hr. The resulting formazan crystals were solubilized with acidified SDS. Percent viable cells is defined as the percentage of formazan normalized to that of untreated cells. Error is shown as standard deviation calculated from 5 replicates. (Bottom) Table summarizing the encapsulation efficiency, maximum differential cytotoxicity, diameter, and polydispersity index of the two passively loaded Rh-PPO liposomes.

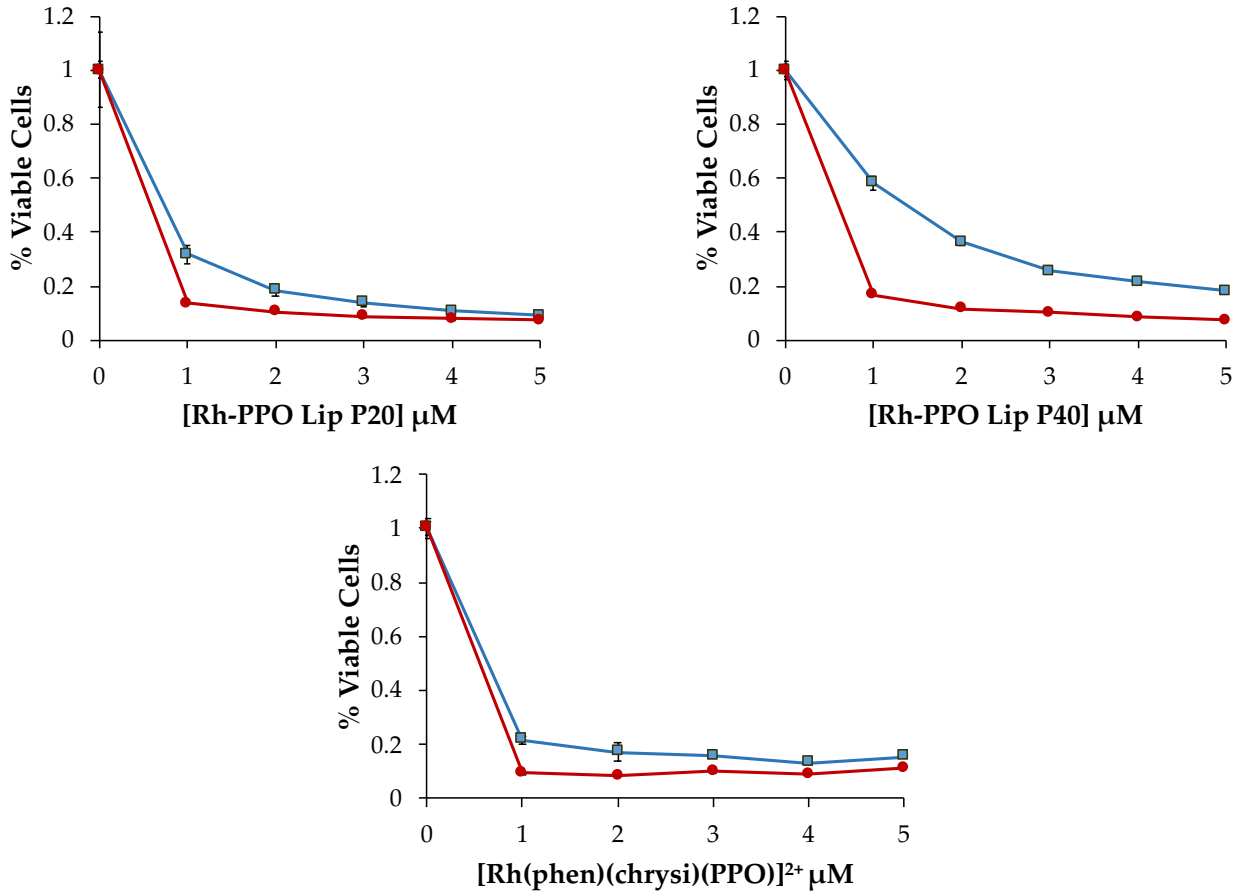

Figure 3.8 MTT cell viability assay comparing passively loaded Rh-PPO liposomes and free Rh-PPO metalloinsertor. HCT116N (MMR-proficient, blue squares) and HCT116O (MMR-deficient, red circles) cells were treated with passively loaded Rh-PPO liposomes (top left) Rh-PPO Lip P20 and (top right) Rh-PPO Lip P40, as well as (bottom) free $[Rh(phen)(chrysi)(PPO)]Cl_2$ (Rh-PPO). Cells were incubated with each liposome solution at the Rh-PPO concentrations indicated for 72 hr, then cells were treated with the MTT reagent for 4 hr. The resulting formazan crystals were solubilized with acidified SDS. Percent viable cells is defined as the percentage of formazan normalized to that of untreated cells. Error is shown as standard deviation calculated from 5 replicates.

liposome formulation and drug encapsulation methods were explored.

3.3.3.3 Characterization of Remote Loaded Rh-PPO Liposomes

Remote loaded Rh-PPO liposomes were generated by first hydrating the lipid thin film with ammonium sulfate (pH ~5.5) and forming large, unilamellar vesicles through extrusion. The resulting liposomes were then loaded with a slightly basic solution of Rh-PPO. The pH and phosphate gradient generated is reported to result in remote loading of drugs into the liposomes.[13] Methanol lysis studies revealed that this method resulted in encapsulation efficiencies of 40% to 80% depending on the lipid composition and the pH of the Rh-PPO solution used. Encapsulation efficiency studies with remote loaded Rh-PPO Lip R20 and Rh-PPO Lip R40 samples showed an increase in Rh-PPO encapsulation most notably with Rh-PPO Lip 40 nanoparticles. Additionally, the Rh-PPO Lip R40 samples retained the selectivity and potency of the free metalloinsertor complex with optimal differential activity of 0.537 at 1 μM, as seen in **Figure 3.9**.

3.3.3.4 Characterization of Thin Film Method Rh-PPO Liposomes

Thin film liposome formation methods were assessed in which the Rh-PPO metalloinsertor and lipid components (Cholesterol:DSPE-PEG:DSPC at 40:5:55 mol%) were mixed using various solvents to generate a thin film; this allows the complex and lipids to mix thoroughly before bilayer formation. Water or buffer was then used to hydrate the mixture and generate Rh-PPO liposomes. The solvent mixture using isopropanol and chloroform to form the thin film resulted in the most promising liposomes with a Rh-PPO encapsulation efficiency of 52%. Cytotoxicity assays were used to compare the biological activity of the resulting thin film liposome (Rh-PPO Lip TF40) and the previously discussed remote loaded Rh-PPO liposomes as

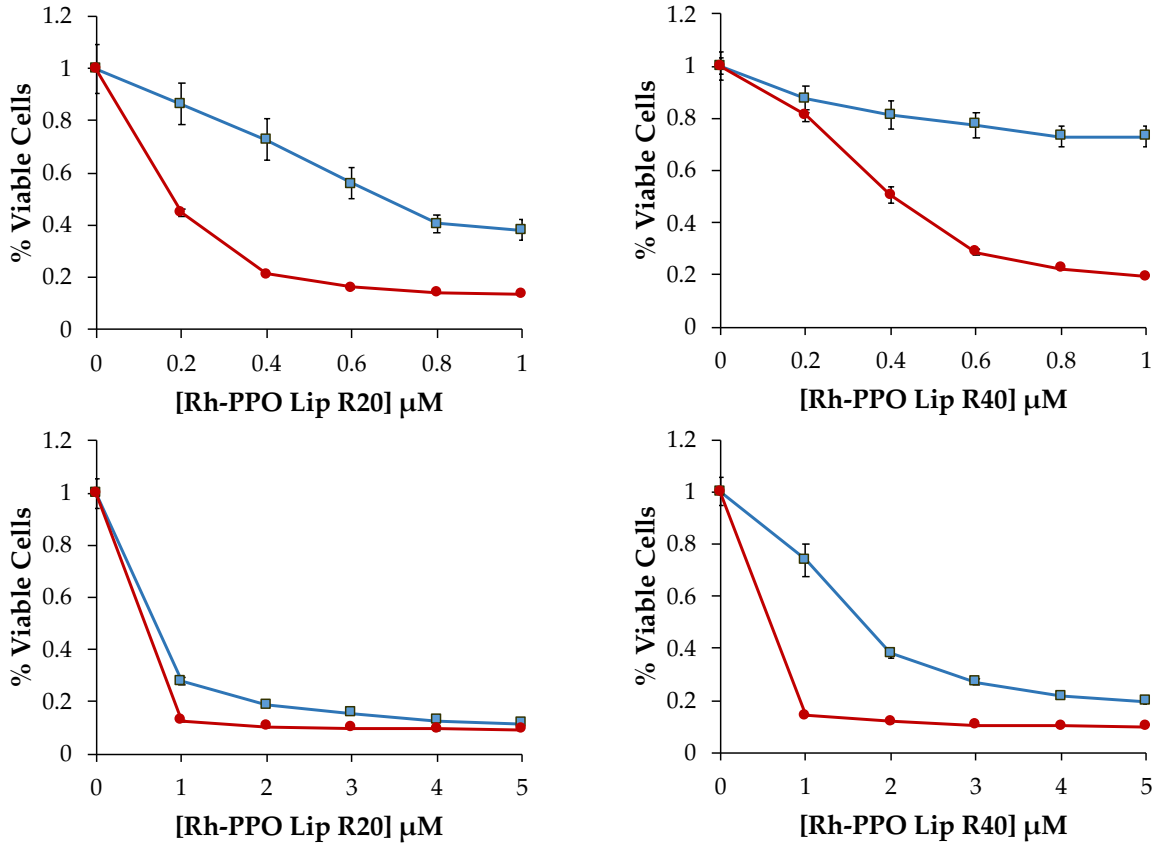

Figure 3.9 MTT cell viability assays comparing different concentration ranges of remote loaded Rh-PPO liposomes. HCT116N (MMR-proficient, blue squares) and HCT116O (MMR-deficient, red circles) cells were treated with remote loaded Rh-PPO liposomes (left) Rh-PPO Lip R20 and (right) Rh-PPO Lip R40. Cells were incubated with each liposome solution at the Rh-PPO concentrations indicated for 72 hr, then cells were treated with the MTT reagent for 4 hr. The resulting formazan crystals were solubilized with acidified SDS. Percent viable cells is defined as the percentage of formazan normalized to that of untreated cells. Error is shown as standard deviation calculated from 5 replicates.

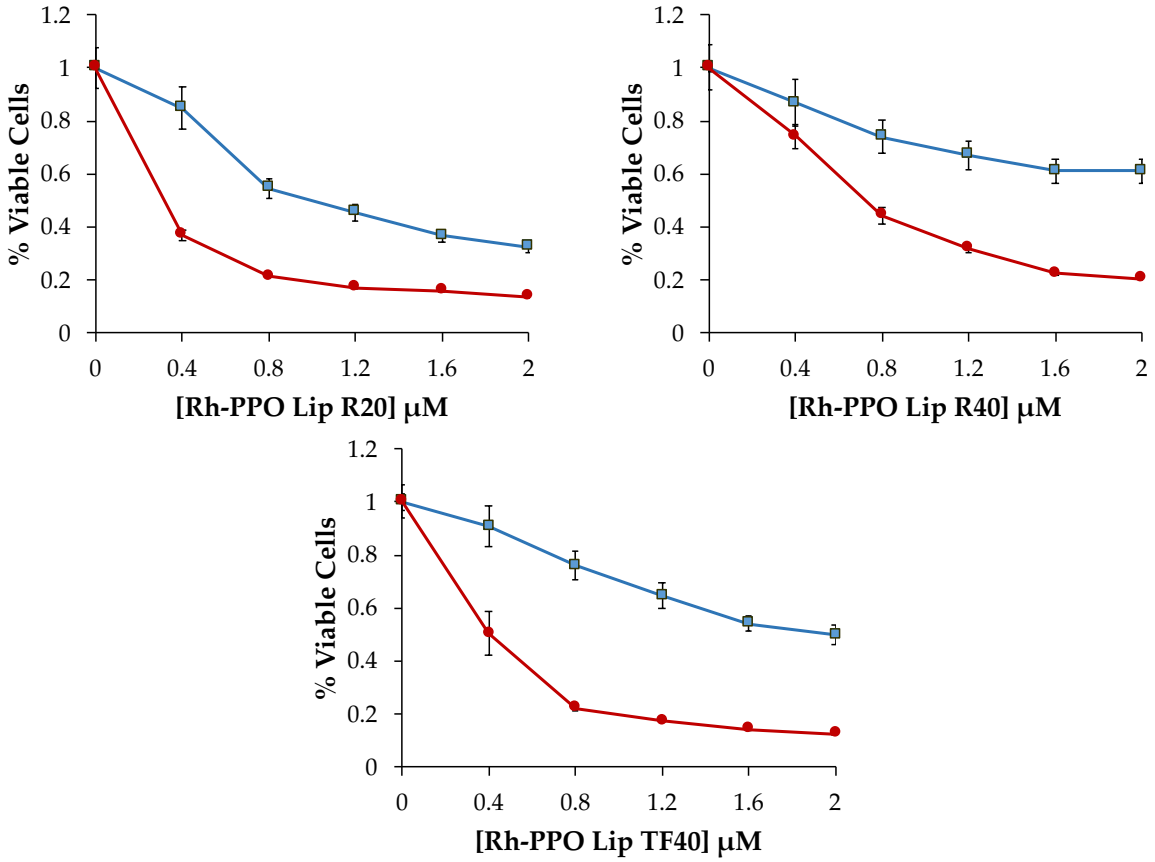

Figure 3.10 MTT cell viability assays comparing remote loaded and thin film Rh-PPO liposomes. HCT116N (MMR-proficient, blue squares) and HCT116O (MMR-deficient, red circles) cells were treated with remote loaded Rh-PPO liposomes (top left) Rh-PPO Lip R20 and (top right) Rh-PPO Lip R40, as well as thin film generated liposomes (bottom) Rh-PPO Lip TF40. Cells were incubated with each liposome solution at the Rh-PPO concentrations indicated for 72 hr, then cells were treated with the MTT reagent for 4 hr. The resulting formazan crystals were solubilized with acidified SDS. Percent viable cells is defined as the percentage of formazan normalized to that of untreated cells. Error is shown as standard deviation calculated from 5 replicates.

shown in **Figure 3.10**. These experiments revealed that the thin film Rh-PPO liposomes had promising biological selectivity; however, the remote loaded liposomes had similar selective cytotoxicity toward MMR-deficient cells with even greater encapsulation efficiency of Rh-PPO. Note that thin film liposomes made with methanol and acetonitrile solutions of Rh-PPO aggregated or did not maintain a stable phospholipid bilayer, so further studies with these samples were not pursued.

3.3.4 Rh-PPO Liposome Stability Studies

After displaying the most promising physical and biological characteristics, the remote loaded Rh-PPO liposomes with Cholesterol:DSPE-PEG:DSPC at 40:5:55 mol% underwent a final assessment to determine their long-term stability and drug leakage over time. The liposomes were diluted in HCT116N/O cell culture media, incubated at various temperatures (4°C, 25°C, and 37°C), and evaluated for drug leakage by collecting the supernatant at various timepoints over a 31-day time period. Inductively coupled plasma mass spectrometry (ICP-MS), a high sensitivity technique that allows for the detection of low concentrations of metal-based drugs (less than 1 ng/ml),[19] was used to assess the collected samples for rhodium content, and the results are displayed in **Figure 3.11**. These stability experiments indicate that minimal drug leakage occurred over 31 days. Notable Rh-PPO drug leakage was only detected in the 37°C samples with 87% of the original metalloinsertor concentration retained in the liposomes after 31 days of incubation. Based on these ICP-MS studies, the metalloinsertor appears to remain encapsulated within the remote loaded Rh-PPO liposomes at 4°C and 25°C throughout the 31-day analysis, as well as at 37°C for 120 hr, which indicates that the cytotoxic activity observed with the liposomes does not result from premature drug release.

3.4 Discussion

A range of chemotherapeutics with different mechanisms of action have been developed for the treatment of colorectal cancer (CRC). For example, cisplatin and other platinum based derivatives induce cytotoxicity through the formation of intrastrand crosslinks between purines in DNA,[20] while the anthracycline doxorubicin is believed to intercalate into DNA and cause topoisomerase II inhibition and DNA double strand break formation.[20] There have been numerous meaningful developments in treatment options for CRC patients; however, the median overall survival for advanced CRC patients remains only 5 months and MMR-deficient patients in particular have low response rates towards standard of care CRC therapeutics, such as 5-fluorouracil.[1,21]

Metalloinsertors are a promising, novel class of targeted chemotherapeutics able to specifically locate and bind mismatched DNA sites and ultimately induce cellular necrosis.[22] Initially designed to selectively target the mismatches that result from MMR-deficient CRCs, these complexes contain particularly wide, aromatic, ancillary ligands that allow the rhodium compounds to detect thermodynamically destabilized DNA mismatch sites. These transition metal complexes are capable of a unique binding mode known as metalloinsertion, in which the inserting ligand binds DNA via the minor groove resulting in ejection of the destabilized mismatched base pairs (**Figure 3.1**).[23] The newest family of metalloinsertors, which contain rhodium-oxygen bond coordinations, consistently displays increased potency in the *nanomolar* range, and notable selective cytotoxicity towards MMR-deficient cell lines.[5] Recent studies into the mechanism of action of the most potent metalloinsertor, Rh-PPO, have shown enhanced

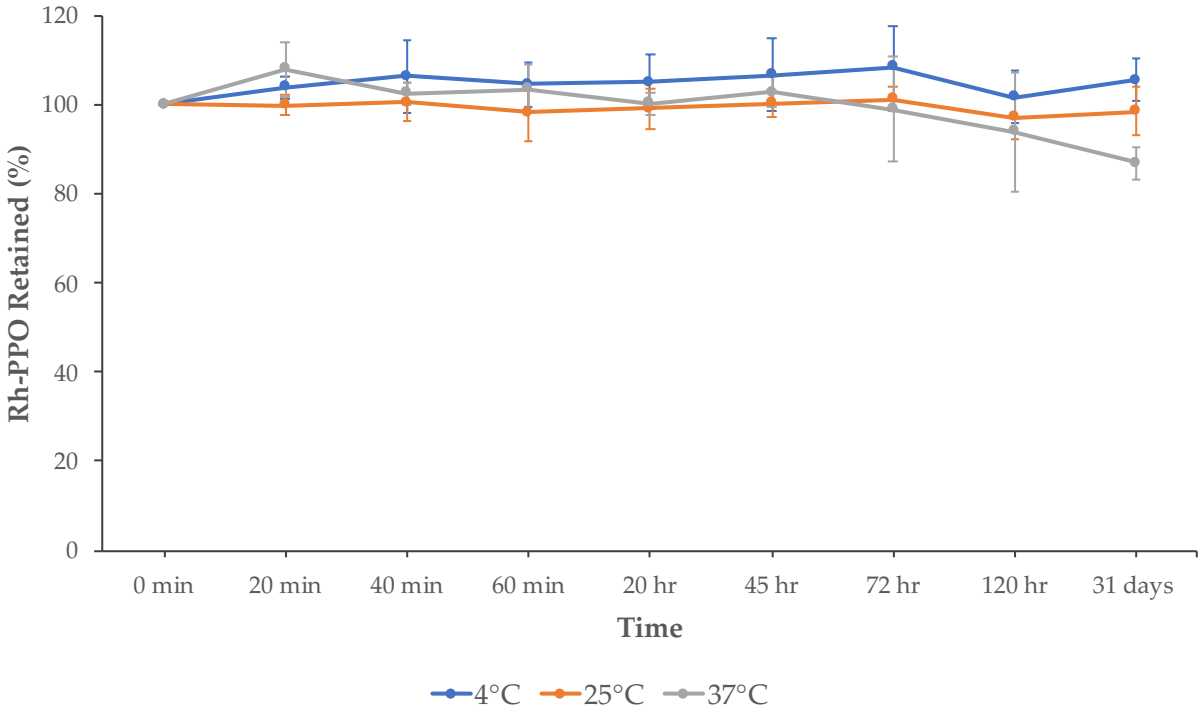

Figure 3.11 Stability of remote loaded Rh-PPO liposomes over time. Rh-PPO Lip R40 liposomes were diluted in cell culture media and incubated at 4°C, 25°C, and 37°C. The percent Rh-PPO retained in the liposomes was assessed over a 31-day time period. Samples were assessed for rhodium content using ICP-MS. Values represent the percent Rh-PPO retained in the liposome compared to the initial liposome solution. Error bars represent standard deviation calculated from three replicate experiments.

phosphorylation of histone H2AX and checkpoint protein kinase Chk1, which together indicates the formation of DNA double-strand breaks (DSBs) and activation of the DNA damage response (DDR) as a result of Rh-PPO treatment. Furthermore, the synthesis of a fluorescent Rh-PPO analogue (RhPPO-Cy3) has allowed for studies that revealed colocalization between RhPPO-Cy3 and DDR proteins, Rad51 and pH2AX, suggesting that DNA DSBs occur specifically at DNA mismatch sites and undergo initial resection.[6,24,25]

Preclinical assessment of the *in vivo* anti-cancer properties of Rh-O metalloinsertors, specifically Rh-PPO, in a subcutaneous, xenograft CRC model has shown that significant reductions in tumor growth rate occur in response to intraperitoneal Rh-PPO treatment at 0.5 and 1 mg/kg. Additionally, intratumoral Rh-PPO studies show that markedly higher reductions in tumor growth can be achieved when more metalloinsertor accumulates at the tumor site. However, these studies have also indicated that Rh-PPO is systemically toxic at higher concentrations, which limits the doses of metalloinsertor that can be administered. Therefore, the use of strategic delivery systems, such liposomal formulations, is a promising route for further development of these targeted chemotherapeutics.

Liposomal formulations of a number of cytotoxic compounds have been explored to reduce systemic toxicity and increase tumor cell targeting. Doxil and SCL-DOX are doxorubicin loaded liposomal formulations that have shown increased *in vivo* efficacy and tolerability compared to the free anthracycline.[11,26] Additionally, Lipoplatin and Lipoxal are FDA approved liposomes containing cisplatin and oxaliplatin, respectively.[9,27] While chemotherapeutic liposomes have proven to be a promising drug formulation approach, the development of these

drugs has also revealed the importance of lipid identity and composition, liposome stability and drug release, as well as liposome formation technique and encapsulation efficiency.

In order to increase the tolerability of the metalloinsertor and enhance the *in vivo* anti-cancer effects, Rh-PPO liposomes were generated. Multiple liposome synthesis techniques were explored to increase encapsulation efficiency of the metalloinsertor, while retaining the drug's potency and selectivity towards MMR-deficient cells *in cellulo*. Furthermore, protocols were developed to quantify Rh-PPO content within the liposomes and the stability of the nanoparticle over time. Overall, this investigation allowed for the exploration of a stable, novel metalloinsertor drug delivery system that has promise for future metalloinsertor therapeutic development.

3.4.1 Formation and Characterization of Chol:DSPE-PEG:DSPC Liposomes

The biological properties of liposomal drugs are significantly influenced by the identity and molar ratio of the lipids used to compose the nanoparticle, as well as the chemical properties of the drug encapsulated. Therefore, a comprehensive literature search was conducted in order to select the lipids used for the Rh-PPO metalloinsertor liposome. The acyl chain length, charge, and chemical functionality of each lipid significantly influence the stability of the liposomes, drug release mechanism, and encapsulation of the drug. DSPC, DSPE-PEG, and Cholesterol were each chosen to compose the Rh-PPO liposomes in order to achieve physical and chemical properties to enhance Rh-PPO's chemotherapeutic effects and tolerability. DSPC is a neutral, saturated phospholipid that is the main component of numerous therapeutic liposomal formulations, including DaunoXome and Onivyde. This high transition temperature lipid allows for liposomal stability and diminished reticuloendothelial system (RES) uptake.[12] DSPE-PEG is

expected to enhance the circulation time of the liposomes *in vivo* (Rh-PPO at 1 mpk currently has a half-life of 1.79 hr) and assist in faster lysolipid induced permeability once the liposome reaches the tumor cell site.[28] Lastly, cholesterol was incorporated to allow for modulation of membrane fluidity, elasticity, and permeability, which ultimately impacts complex encapsulation and drug release properties. These chosen lipids were used for all of the outlined Rh-PPO liposomal studies; however, different lipids could be explored in future studies.

3.4.2 Biological Activity of Rh-PPO Liposomes

Biological activity studies with DSPC, DSPE-PEG, and Cholesterol liposomes aimed to determine if the potency and selectivity of free Rh-PPO could be maintained with the liposomal formulation. Liposomes were assessed using MTT assays in two cell lines, HCT116N and HCT116O. The cell lines originate from the same HCT116 colorectal carcinoma cells; however, they differ in their MMR deficiency status. Specifically, HCT116N cells are MMR proficient and HCT116O cells are MMR deficient. As a result, HCT116O cells have a higher abundance of DNA base pair mismatches compared to the HCT116N cell line, which should make the HCT116O cells more sensitive to mismatch-targeting by metalloinsertors.[28]

Liposomes without Rh-PPO encapsulated (Chol:DSPE-PEG:DSPC liposomes; 40:5:55 mol%) were tested first to determine their physical properties and the cytotoxicity of the lipids composing the nanoparticle. Physical characterization of these liposomes revealed a mean diameter of 146.9 nm and polydispersity index of 0.277. These dynamic light scattering (DLS) measurements showed that passively loaded Chol:DSPE-PEG:DSPC liposomes have monodisperse size distribution and appropriate size for tumor site accumulation via the EPR effect. Furthermore, results from MTT studies indicate that millimolar concentrations of lipid

result in non-selective cytotoxicity within HCT116N and HCT116O cell lines (IC_{50} value of 1.44 mM and 1.55 mM, respectively). This finding suggests that efficient metalloinsertor encapsulation will be necessary to ensure that Rh-PPO cellular activity is the main mode of cell death.

Various liposomal drug encapsulation techniques, including passive loading, remote loading, and thin film formation, were explored to achieve stable, potent, and selective Rh-PPO liposomes. Each of these methods was used to produce liposomes with two lipid composition molar ratios: Chol:DSPE-PEG:DSPC at 40:5:55 mol% and 20:5:75 mol%. As described above, the ratio of Chol-to-DSPC greatly influences the membrane fluidity and permeability of the liposome, while DSPE-PEG is included consistently at 5% moles, a low molar ratio known to increase *in vivo* nanoparticle circulation by reducing antigenicity and immunogenicity in the recipient's immune system.[12] Note that 50% moles of cholesterol is the maximum amount reported to be incorporated into reconstituted bilayers.[14]

MTT cell viability studies with the described nanoparticles consistently showed that Rh-PPO liposomes with Chol:DSPE-PEG:DSPC at 40:5:55 mol% had the highest selectivity towards the HCT116O MMR-deficient cell line. For example, **Figure 3.8** displays that the passively loaded Rh-PPO Lip P40 has a maximum differential cytotoxicity (MDC) of 41.3 % at 1 μM, while free Rh-PPO metalloinsertor has a MDC of 12% at 1 μM and Rh-PPO Lip P20 displayed a MDC of 18.2% at 1 μM. Additionally, the potency for the two membrane compositions was very similar. In particular, IC_{50} values for remote loaded Rh-PPO Lip R20 and Rh-PPO Lip R40 based on **Figure 3.9** were approximately 200 nM and 400 nM, respectively. Importantly, the remote loading method allowed for the highest encapsulation efficiencies with

up to 80% of Rh-PPO becoming encapsulated and the resulting liposomes had the desired diameter and PDI values (ex. 155 nm and 0.24, respectively). Ultimately, due to the focus on increasing tolerability and potency, the remote loaded Rh-PPO Lip R40 was chosen as the focus for the remaining liposomal studies.

3.4.3 Characterization of Remote Loaded Rh-PPO Lip R40 Liposomes

The remote loaded Rh-PPO Lip R40 liposomes were further characterized to determine their suitability for *in vivo* studies. Stability assays in which supernatant samples were analyzed for rhodium content using ICP-MS showed that the liposomal drug formulation retained the metalloinsertor when incubated at 4°C and 25°C with 105.6 ± 4.7% and 98.5 ± 5.4% of drug retained, respectively, for up to 31 days (**Figure 3.11**). In addition to exhibiting that this liposomal formulation is sufficiently stable for *in vivo* investigation, these ICP-MS studies confirmed that premature release of the Rh-PPO metalloinsertor from the liposome was not responsible for the cytotoxicity observed in the detailed MTT cell viability assays. Liposomal Rh-PPO may have been internalized into the cells through endocytosis or membrane fusion.[29] Subsequently, studies to determine the drug-to-lipid ratio were conducted by comparing liposomal lipid and Rh-PPO concentrations. These experiments and calculations found a maximum Rh-PPO per lipid concentration of 0.0108 mM Rh-PPO/mg lipid * mL. Unfortunately, this limitation to the amount of Rh-PPO encapsulated into liposomes in addition to the toxicity of the empty liposomes did not allow for a maximum tolerable dose (MTD) study with Rh-PPO liposomes to be conducted (Rh-PPO liposome concentrations ranging from 1 mg Rh-PPO/kg to 10 mg Rh-PPO/kg would have been assessed in the MTD study). Note that a freeze-thaw drug encapsulation protocol was also attempted to increase the drug-to-lipid ratio; however, drug

encapsulation did not significantly change. While Rh-PPO liposomes have yet to be evaluated *in vivo*, this work serves as a basis for future metalloinsertor studies with nanoparticle delivery systems.

3.5 Conclusion and Implications for Future Drug Delivery Approaches

The Rh-PPO liposomal formulations described herein are the first attempts to utilize nanocarriers to increase the *in vivo* tolerability and anti-cancer efficacy of the metalloinsertor complex Rh-PPO. Various liposome formation techniques and lipid compositions were explored to produce stable, selective, and potent Rh-PPO liposomes. Ultimately, remote loaded Rh-PPO Lip R40 liposomes were found to have the best maximal differential cytotoxicity, minimal drug release over 31 days at various temperatures, and nanomolar potency. While this liposomal formulation showed much promise, the low drug-to-lipid ratio ultimately did not allow for an *in vivo* maximum tolerable dose study to be conducted. Cholesterol, DSPC, and DSPE-PEG were the lipids chosen for this study; however, the exploration of different lipid combinations may allow for the drug-to-lipid ratio to be increased. Future studies with nanoparticle delivery systems may focus on exploring different liposome membrane compositions, as well as active targeting of liposomes to tumors through the use of chemical functionalizations and targeting ligands, such as antibodies and peptides.[30]

3.6 References

(1) Gustavsson, B.; Carlsson, G.; MacHover, D.; Petrelli, N.; Roth, A.; Schmoll, H. J.; Tveit, K. M.; Gibson, F. A Review of the Evolution of Systemic Chemotherapy in the Management of Colorectal Cancer. *Clin. Colorectal Cancer* **2015**, *14* (1), 1–10. https://doi.org/10.1016/j.clcc.2014.11.002.

(2) Yoon, S. S.; Tanabe, K. K. Surgical Treatment and Other Regional Treatments for Colorectal Cancer Liver Metastases. *Oncologist* **1999**, *4* (3), 197–208. https://doi.org/10.1634/theoncologist.4-3-197.

(3) Zeglis, B. M.; Pierre, V. C.; Kaiser, J. T.; Barton, J. K. A Bulky Rhodium Complex Bound to an Adenosine-Adenosine DNA Mismatch: General Architecture of the Metalloinsertion Binding Mode. *Biochemistry* **2009**, *48* (20), 4247–4253. https://doi.org/10.1021/bi900194e.

(4) Arzimanoglou, I. I.; Gilbert, F.; Barber, H. R. Microsatellite Instability in Human Solid Tumors. *Cancer* **1998**, *82*, 1808–1820. https://doi.org/10.1016/S1357-4310(96)10055-1.

(5) Komor, A. C.; Barton, J. K. An Unusual Ligand Coordination Gives Rise to a New Family of Rhodium Metalloinsertors with Improved Selectivity and Potency. *J. Am. Chem. Soc.* **2014**, *136* (40), 14160–14172. https://doi.org/10.1021/ja5072064.

(6) Nano, A.; Bailis, J. M.; Mariano, N. F.; Pham, E. D.; Threatt, S. D.; Barton, J. K. Cell-Selective Cytotoxicity of a Fluorescent Rhodium Metalloinsertor Conjugate Results from Irreversible DNA Damage at Base Pair Mismatches. *Biochemistry* **2020**, *59*, acs.biochem.9b01037. https://doi.org/10.1021/ACS.BIOCHEM.9B01037.

(7) Jhaveri, A. M.; Torchilin, V. P. Multifunctional Polymeric Micelles for Delivery of Drugs and SiRNA. *Front. Pharmacol.* **2014**, *5 APR* (May).

https://doi.org/10.3389/fphar.2014.00077.

(8) Deshpande, P. P.; Biswas, S.; Torchilin, V. P. Current Trends in the Use of Liposomes for Tumor Targeting. *Nanomedicine (Lond)* **2013**, *8* (9), 1–32. https://doi.org/10.2217/nnm.13.118.Current.

(9) Zisman, N.; Dos Santos, N.; Johnstone, S.; Tsang, A.; Bermudes, D.; Mayer, L.; Tardi, P. Optimizing Liposomal Cisplatin Efficacy through Membrane Composition Manipulations. *Chemother. Res. Pract.* **2011**, *2011*, 1–7. https://doi.org/10.1155/2011/213848.

(10) Stathopoulos, G. P.; Boulikas, T. Lipoplatin Formulation Review Article. *J. Drug Deliv.* **2012**, *2012*, 1–10. https://doi.org/10.1155/2012/581363.

(11) Gabizon, a; Shmeeda, H.; Barenholz, Y. Pharmacokinetics of Pegylated Liposomal Doxorubicin: Review of Animal and Human Studies. *Clin.Pharmacokinet.* **2003**, *42* (5), 419–436. https://doi.org/10.2165/00003088-200342050-00002.

(12) Bulbake, U.; Doppalapudi, S.; Kommineni, N.; Khan, W. Liposomal Formulations in Clinical Use: An Updated Review. *Pharmaceutics* **2017**, *9* (2), 1–33. https://doi.org/10.3390/pharmaceutics9020012.

(13) Fritze, A.; Hens, F.; Kimpfler, A.; Schubert, R.; Peschka-Süss, R. Remote Loading of Doxorubicin into Liposomes Driven by a Transmembrane Phosphate Gradient. *Biochim. Biophys. Acta - Biomembr.* **2006**, *1758* (10), 1633–1640. https://doi.org/10.1016/j.bbamem.2006.05.028.

(14) Briuglia, M. L.; Rotella, C.; McFarlane, A.; Lamprou, D. A. Influence of Cholesterol on Liposome Stability and on in Vitro Drug Release. *Drug Deliv. Transl. Res.* **2015**, *5* (3), 231–242. https://doi.org/10.1007/s13346-015-0220-8.

(15) Selim, A.; Lila, A.; Ishida, T. Liposomal Delivery Systems: Design Optimization and

Current Applications. *Biol. Pharm. Bull* **2017**, *40* (40), 1–10. https://doi.org/10.1248/bpb.b16-00624.

(16) Najlah, M.; Suliman, A. S.; Tolaymat, I.; Kurusamy, S.; Kannappan, V.; Elhissi, A. M. A.; Wang, W. Development of Injectable PEGylated Liposome Encapsulating Disulfiram for Colorectal Cancer Treatment. *Pharmaceutics* **2019**, *11* (11), 1–16. https://doi.org/10.3390/pharmaceutics11110610.

(17) Jimah, J. R.; Schlesinger, P. H.; Tolia, N. H. Liposome Disruption Assay to Examine Lytic Properties of Biomolecules. *Bio. Protoc.* **2017**, *7* (15), 1–16. https://doi.org/10.1016/j.physbeh.2017.03.040.

(18) Huang, Z.; Jaafari, M. R.; Szoka, F. C. Disterolphospholipids: Non-Exchangeable Lipids and Their Application to Liposomal Drug Delivery. *Angew. Chem. Int. Ed. Engl.* **2009**, *48* (23), 4146–4149. https://doi.org/10.1038/jid.2014.371.

(19) Perry, B. J.; Balazs, R. E. ICP-MS Method for the Determination of Platinum in Suspensions of Cells Exposed to Cisplatin. *Anal. Proc. Incl. Anal. Commun.* **1994**, *31* (9), 269–271. https://doi.org/10.1039/AI9943100269.

(20) Shaloam, D.; Tchounwou, P. B. Cisplatin in Cancer Therapy: Molecular Mechanisms of Action. *Eur. J. Pharmacol.* **2014**, *0*, 364–378. https://doi.org/10.1016/j.ejphar.2014.07.025.Cisplatin.

(21) Longley, D. B.; Harkin, D. P.; Johnston, P. G. 5-Fluorouracil: Mechanisms of Action and Clinical Strategies. *Nat. Rev. Cancer* **2003**, *3* (5), 330–338. https://doi.org/10.1038/nrc1074.

(22) Boyle, K. M.; Barton, J. K. Targeting DNA Mismaches with Rhodium Metalloinsertors. *Inorganica Chim. Acta* **2016**, *452*, 3–11. https://doi.org/110.1016/j.bbi.2017.04.008.

(23) Song, H.; Kaiser, J. T.; Barton, J. K. Crystal Structure of Δ-Ru(Bpy)2 Dppz2+ Bound to Mismatched DNA Reveals Side-by-Side Metalloinsertion and Intercalation. *Nat Chem* **2013**, *4* (8), 615–620. https://doi.org/10.1038/jid.2014.371.

(24) Nano, A.; Bailis, J. M.; Mariano, N. F.; Pham, E. D.; Threatt, S. D.; Barton, J. K. Cell-Selective Cytotoxicity of a Fluorescent Rhodium Metalloinsertor Conjugate Results from Irreversible DNA Damage at Base Pair Mismatches. *Biochemistry* **2020**, *59*, 717–726. https://doi.org/10.1021/acs.biochem.9b01037.

(25) Bailis, J. M.; Weidmann, A. G.; Mariano, N. F.; Barton, J. K. Rhodium Metalloinsertor Binding Generates a Lesion with Selective Cytotoxicity for Mismatch. *Proc. Natl. Acad. Sci.* **2017**, *114* (27), 6948–6953. https://doi.org/10.1073/pnas.1706665114.

(26) Lin, J.; Yu, Y.; Shigdar, S.; Fang, D. Z.; Du, J. R.; Wei, M. Q.; Danks, A.; Liu, K.; Duan, W. Enhanced Antitumor Efficacy and Reduced Systemic Toxicity of Sulfatide-Containing Nanoliposomal Doxorubicin in a Xenograft Model of Colorectal Cancer. *PLoS One* **2012**, *7* (11), 1–10. https://doi.org/10.1371/journal.pone.0049277.

(27) Stathopoulos, G. P.; Boulikas, T.; Kourvetaris, A.; Stathopoulos, J. Liposomal Oxaliplatin in the Treatment of Advanced Cancer: A Phase I Study. *Anticancer Res.* **2006**, *26* (2 B), 1489–1493.

(28) Immordino, M. L.; Dosio, F.; Cattel, L. Stealth Liposomes: Review of the Basic Science, Rationale, and Clinical Applications, Existing and Potential. *Int. J. Nanomedicine* **2006**, *1* (3), 297–315.

(29) Kelly, C.; Jefferies, C.; Cryan, S.-A. Targeted Liposomal Drug Delivery to Monocytes and Macrophages. *J. Drug Deliv.* **2011**, *2011*, 1–11. https://doi.org/10.1155/2011/727241.

(30) Riaz, M. K.; Riaz, M. A.; Zhang, X.; Lin, C.; Wong, K. H.; Chen, X.; Zhang, G.; Lu, A.;

Yang, Z. Surface Functionalization and Targeting Strategies of Liposomes in Solid Tumor Therapy: A Review. *Int. J. Mol. Sci.* **2018**, *19* (195), 1–27. https://doi.org/10.3390/ijms19010195.

(31) Rosenblum, D.; Joshi, N.; Tao, W.; Karp, J. M.; Peer, D. Progress and Challenges towards Targeted Delivery of Cancer Therapeutics. *Nat. Commun.* **2018**, *9* (1). https://doi.org/10.1038/s41467-018-03705-y.

Chapter 4

DESIGN, SYNTHESIS, AND CHARACTERIZATION OF RH-O METALLOINSERTORS FUNCTIONALIZED FOR CONJUGATION TO ANTIBODIES

4.1 Introduction

Recent chemotherapeutic development efforts have focused on designing selective, as well as potent, drugs that have a specific biological target known to be characteristic of malignant cells.[1,2] Mismatch repair (MMR) deficiencies are a hallmark for 16% of all solid tumors and 80% of hereditary nonpolyposis colon cancers, and many patients with these types of malignancies are resistant to current oncology treatments. MMR repair is typically responsible for identifying and addressing the formation of mismatches and indels within newly synthesized DNA stands; however, when one or more of the MMR repair proteins does not function properly, DNA mismatches and eventually mutations result.[3]

A couple of strategies for selectively targeting these MMR-deficient cancers have been developed. First, therapeutics have been designed to take advantage of the neoantigens that result from the high mutation load of MMR-deficient cells. These mutated biomolecules are presented on the surface of malignant cells and recognized by immune regulatory T-cells. Within non-cancerous tissues, the identification of neoantigens on foreign or diseased cells results in the secretion of cytokines and activation of the immune response; however, many cancerous cells upregulate inhibitory ligands, such as PD-L1 and PD-L2, which bind the PD-1 on T-cells and prevent immune response activation.[4] Monoclonal antibodies that target the PD-1 receptor, such as the FDA-approved Pembrolizumab, have been developed and shown to block programed cell death ligand-receptor interactions, ultimately allowing for MMR-deficient tumors to be properly

identified and attacked by the immune system.[5] It should be noted that monoclonal antibodies have increasingly become chemotherapeutics of interest due to their enlistment of the natural immune system to fight cancers.[6,7]

Alternatively, small molecule therapeutics have been designed to target the DNA base pair mismatches that result from MMR-deficient cancers. In particular, our laboratory has worked to develop rhodium metalloinsertors, octahedral complexes able to specifically locate and bind mismatched DNA sites and ultimately induce cellular necrosis.[8] These transition metal complexes are capable of a unique binding mode known as metalloinsertion, in which the inserting ligand binds DNA via the minor groove resulting in ejection of the destabilized mismatched base pairs. Studies with first generation metalloinsertors, such as $[Rh(bpy)_2(chrysi)]^{3+}$ (**Figure 4.1**), revealed over 1000-fold selective binding to mismatches over well-matched sites, as well as an ability to target 80% of all DNA mismatches.[9,10] The most recent family of rhodium metalloinsertors contains an unexpected Rh-O axial coordination (**Figure 4.1**), and biological studies with Rh-O metalloinsertors display enhanced potency (IC_{50} value of 300 nM in HCT116O cells) and preferential cytotoxicity towards MMR-deficient CRC cells.[2,11]

In addition to showing enhanced potency and selectivity, these Rh-O metalloinsertors have displayed high functional group tolerance when functionalizing the N^O coordinating ligand. Chemical groups ranging from hydrophilic pyridines to hydrophobic hexyl chains have been incorporated into the N^O ligand, and the selective cytotoxic properties of these metalloinsertors has remained impressively intact. As a result, these metalloinsertors have been used as a scaffold for conjugate design. Previous conjugation efforts have focused on generating $[Rh(chrysi)(phen)(DPE\text{-}Pt(NH_3)_2Cl)]^{3+}$ (**Figure 4.1**), a bifunctional complex that aimed to

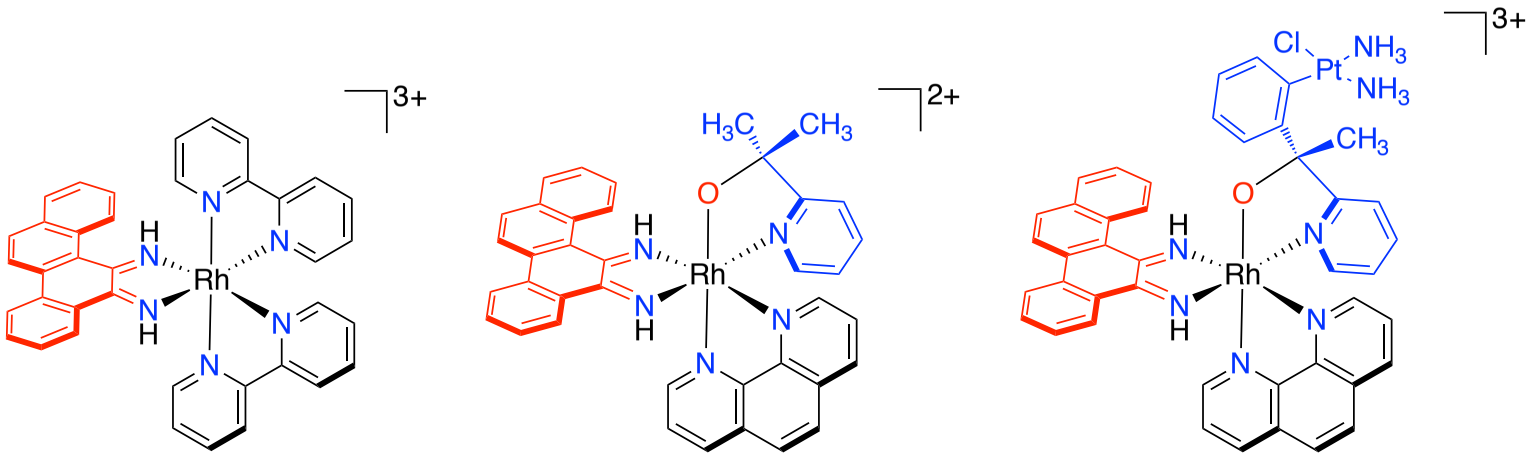

Figure 4.1 Chemical structures of metalloinsertor complexes relevant to this study. Chemical structure of (left) $[Rh(bpy)_2(chrysi)]^{3+}$, a first generation metalloinsertor, (middle) $[Rh(chrysi)(phen)(PPO)]^{2+}$ (Rh-PPO), a second generation Rh-O metalloinsertor, and (right) $[Rh(chrysi)(phen)(DPE\text{-}Pt(NH_3)_2Cl)]^{3+}$, a bifunctional conjugate containing a Rh-O metalloinsertor tethered to a cis-platinum (II) anticancer compound. The inserting chrysi ligand is shown in red and the axial oxygen-coordinating ligands are displayed in blue.

combine the DNA mismatch targeting capabilities of Rh-O metalloinsertors with the cytotoxic effects of a *cis*-platinum (II) anticancer compound. Biological studies with $[Rh(chrysi)(phen)(DPE\text{-}Pt(NH_3)_2Cl)]^{3+}$ showed enhanced potency compared to cisplatin; however, the selectivity of the complex for MMR-deficient cells was lost. We hypothesize that this nonselective activity was due to the platinum component dominating the cellular activity and inducing apoptotic cell death.

Current efforts to develop metalloinsertor drug conjugates have focused on utilizing the Rh-O metalloinsertor scaffold and monoclonal antibodies to achieve even greater cytotoxic selectivity for MMR deficient cancer cells. While Rh-O metalloinsertors, such as Rh-PPO, consistently display preferential killing of MMR-deficient cells at nanomolar and low micromolar ranges, at higher concentrations, the selectivity of these complexes greatly diminishes. This loss of selectivity became especially evident during *in vivo* mouse studies with Rh-PPO in which the complex displayed considerable systemic toxicity at concentrations greater than 1 mg/kg Rh-PPO. In order to target metalloinsertors to cancerous cells with still higher selectivity, we have explored the preparation of antibody drug conjugates (ADCs).[12–14] These drug carriers are capable of further discerning between healthy and malignant cells by targeting cytotoxic payloads to malignant cells using tumor-associated antibodies, as shown in **Figure 4.2**.

In the case of metalloinsertors, by attaching an antibody unique and specific to cancer-associated antigens and MMR deficiencies, our rhodium complexes may become even more specifically directed to induce cell death within diseased MMR-deficient cells. Herein, we describe the efforts to design and characterize metalloinsertor ADC drug linker scaffolds containing a Rh-O metalloinsertor complex and stabile maleimide ADC linkers with the

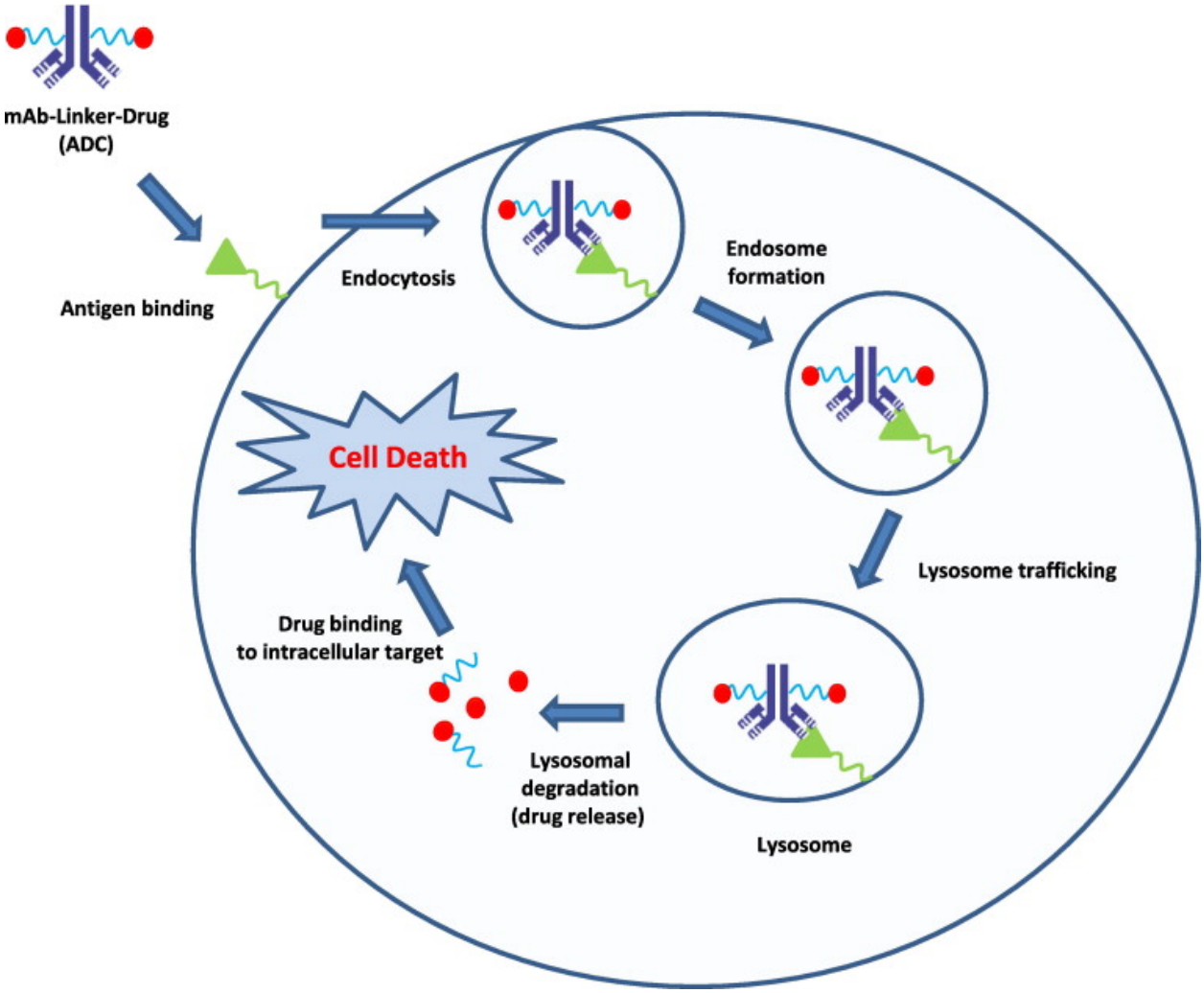

Figure 4.2 General pathway outlining the mechanism of action of antibody drug conjugates (ADCs). Briefly, the ADC will bind to surface-expressed, tumor-associated antigens. The complex is then taken into the cell via receptor-mediated endocytosis and the ADC drug component is released either due to changes in chemical environment once inside the cell or processing by endosomes and lysosomes. The freed, lethal drug cargo then acts independently within the cell. From Reference 15.[15]

ultimate goal of generating a metalloinsertor ADC that specifically targets MMR-deficient, cancerous tumors.

4.2 Experimental Methods

4.2.1 Materials

All chemicals, reagents, and solvents used for synthesis were commercially available, unless otherwise noted, and used as received. Organic reagents were purchased from Sigma Aldrich unless otherwise noted (St. Louis, MO). $RhCl_3$ reagent was purchased from Pressure Chemical Co. (Pittsburgh, PA). Water was purified using the Millipore Milli-Q system (Milford, MA, USA). HPLC-grade acetonitrile (ACN) and methanol were purchased from Fisher Scientific (Fair Lawn, NJ, USA). Sep-Pak C18 solid-phase extraction (SPE) cartridges were acquired from Waters Chemical Co. (Milford, MA). All HPLC metal complex purifications were carried out on a Hewlett-Packard 1100 HPLC. All UV-Visible spectroscopic experiments were performed on a Cary 100 spectrometer. Cell culture media and supplements were purchased from Life Technologies (Carlsbad, CA). Cell lines used in the experiment were purchased from ATCC (Manassas,VA). Tissue culture flasks and plates were obtained from Corning (Corning, NY). Colorimetric cell viability MTT assay kits were purchased from Roche Life Sciences (Penzberg, Upper Bavaria, Germany).

4.2.2 Ligand Synthesis

The ancillary ligands methyl 3-hydroxy-3-(pyridin-2-yl) butanoate (MHPB, **4b**), (*S*)-*N*-(2-(2,5-dioxo-2,5-dihydro-1*H*-pyrrol-1-yl)ethyl)-3-hydroxy-3-(pyridin-2-yl) butanamide ($L^{maleimide}$, **6**), and 2-(Pyridine-2-yl)propan-2-ol (PPO, **8**) were synthesized from 2-acetyl pyridine (**1**) according to **Scheme 1**. The ancillary ligand 4-((2,5-dioxo-2,5-dihydro-1*H*-pyrrol-1-yl)methyl)-*N*-(2-hydroxy-2-(pyridin-2-yl)propyl)cyclohexane-1-carboxamide (HMNPC, **13**) was

synthesized from 2-acetyl pyridine (**1**) according to **Scheme 2**. Ancillary ligands PPO-alkyne (**15**), 11-azido (**18a**), and 4-azido (**18b**) were synthesized from 2-acetyl pyridine (**1**) according to **Scheme 4.3**. Ancillary ligand N-(2-(2,5-dioxo-2,5-dihydro-1H-pyrrol-1-yl)ethyl)-4-(4-(1-hydroxy-1-(pyridin-2-yl)ethyl)-1H-1,2,3-triazol-1-yl)benzamide (NDDH, **20**) was synthesized from ligand 4-azido (**18b**) according to **Scheme 4.4**.

4.2.2.1 Synthesis and Characterization of 2-(pyridin-2-yl)pent-4-en-2-ol (3)

2-(pyridin-2-yl)pent-4-en-2-ol (**3**) was prepared according to a modified procedure originally established by Dr. Alexis Komor. 2-acetyl pyridine (**1**) (1.08 mg, 8.92 mmol, 1 equiv.) and 100 mL anhydrous diethyl ether were combined. The solution was degassed, and the flask cooled to -78°C using dry ice/acetone bath. Allyl magnesium bromide (**2**) (3.239 g, 22.3 mmol, 2.5 equiv.) was then added dropwise over ~15 min, and the reaction was stirred for 1 hr at -78°C. The reaction mixture was quenched using saturated NH_4Cl(aq) then extracted with ethyl acetate (3 x 50 mL). The EtOAc fractions were combined, washed with brine and dried over magnesium sulfate. Solvent was removed by rotary evaporation. The product was isolated using flash chromatography (SiO_2, 1:1 EtOAc:Hexanes/1%MeOH/1%NH_4OH) to give a clear-yellow oil. Yield: 1.02g (70%). ^{1}H NMR (300 MHz, Chloroform-*d*) δ 8.51 (ddd, *J* = 4.9, 1.8, 1.0 Hz, 1H), 7.73 – 7.64 (m, 1H), 7.34 (dt, *J* = 8.0, 1.1 Hz, 1H), 7.21 – 7.14 (m, 1H), 5.76 – 5.58 (m, 1H), 5.05 – 4.94 (m, 3H), 2.56 (ddt, *J* = 7.4, 2.4, 1.2 Hz, 2H), 1.52 (s, 3H). ESI-MS (cation): 164 m/z ($M + H^+$) obsd, 164.10 calcd.

4.2.2.2 Synthesis and Characterization of 3-hydroxy-3-(pyridin-2-yl)butanoic acid (L^{COOH}, 4a)

(3-hydroxy-3 (pyridin-2-yl)butanoic acid (**4a**) was prepared according to procedures adapted from Dr. Alyson Weidmann's procedures. 2-(pyridin-2-yl) pent-4-en-2-ol (**3)** (250 mg,

1.533 mmol, 1 equiv.), $NaIO_4$ (3.28 g, 15.33 mmol, 10 equiv.), and $RuCl_3.H_2O$ (47.6 mg. 0.2299 mmol, 0.15 equiv.) were suspended in a mixture of H_2O/MeOH/$CHCl_3$ (15 mL/ 10 mL/ 10mL) in a 50 mL RB flask. The flask was sealed and stirred for 16-18 hours at RT. Solids from the reaction were removed using filter paper and the organic and aqueous layers separated and dried *in vacuo*. Ether was added to the dried aqueous layer and the mixture was filtered through a medium course glass frit. The precipitate on the frit was washed with ethanol. The dark red filtrate that resulted was dried *in vacuo* and further purified using flash chromatography (SiO_2, equilibrated in DCM with 5% MeOH and eluting with DCM/13% MeOH/1% acetic acid) to give red solid. Yield: 220mg (80%). ^{1}H NMR (500 MHz, Deuterium Oxide) δ 8.52 (d, J = 5.1 Hz, 1H), 8.19 (t, J = 7.8 Hz, 1H), 7.84 (d, J = 8.0 Hz, 1H), 7.61 (t, J = 6.4 Hz, 1H), 2.98 – 2.71 (m, 2H), 1.56 (s, 3H). ESI-MS (cation): 182 m/z ($M + H^+$) obsd, 182.08 calcd.

4.2.2.3 Synthesis and Characterization of Methyl 3-hydroxy-3-(pyridin-2-yl)butanoate (MHPB, 4b)

3-hydroxy-3-(pyridin-2-yl)butanoic acid **(4a)** (300 mg, 1.65 mmol), ~30 mL methanol, and sulfuric acid (914 mg, 9.33 mmol) were combined, stirred, then refluxed at ~ 85°C for 1.5 hr. Heating was stopped and ~50 mL diethyl ether was added to the reaction. The resulting cloudy mixture was dried *in vacuo,* then 50 mL of anhydrous ether was added and 5% aqueous $NaHCO_3$ (3 x 50 ml) was used to extract the organic layer. Aqueous fractions were then extracted with dicholoromethane, dried with magnesium sulfate, and solvent removed using rotary evaporation. The product was isolated using flash chromatography (SiO_2, Hexanes: Ethyl Acetate = 9:1). Yield: 205 mg (65%). ^{1}H NMR (500 MHz, Chloroform-*d*) δ 8.53 (ddd, J = 4.9, 1.8, 1.0 Hz, 1H), 7.75 (ddd, J = 8.1, 7.4, 1.8 Hz, 1H), 7.65 (dt, J = 8.0, 1.1 Hz, 1H), 7.21 (ddd, J

= 7.4, 4.8, 1.2 Hz, 1H), 3.65 (s, 3H), 3.07 (dd, *J* = 189.0, 15.8 Hz, 2H), 1.60 (s, 3H). ESI-MS (cation): 196 m/z ($M + H^+$) obsd, 196.1 calcd.

4.2.2.4 Synthesis and Characterization of ((*S*)-*N*-(2-(2,5-dioxo-2,5-dihydro-1*H*-pyrrol-1-yl)ethyl)-3-hydroxy-3-(pyridin-2-yl)butanamide) ($L^{maleimide}$, 6)

Dried 3-hydroxy-3-(pyridin-2-yl)butanoic acid (**4a**) (135mg, 0.745 mmol, 1 equiv.) was added to a 100 mL Schlenk flask. N-Hydroxysuccinimide (90mg, 0.745 mmol, 1 equiv.) and N,N'-Dicyclohexylcarbodiimide (160mg, 0.745mmol, 1 equiv.) were put in the same flask with a stir bar. The flask was placed on ice and put under argon. 5 mL anhydrous DMF, then 3 mL dry DCM was added to the reaction. DIEA (130 µL, 0.82 mmol, 1.1 equiv.) was carefully added to the mixture under argon. The reaction was allowed to stir at 0°C for 1.5hr. 2-amino ethyl maleimide TFA salt (**5**) (200mg, 0.82 mmol, 1.1 equiv.) was then added to a separate Schlenk flask and put under argon. 2 mL anhydrous DMF was added to the flask under argon. The solution was then transferred to the reaction flask. The reaction was stirred on ice for additional 2 hr., then filtered using celite. The resulting solution was poured into 125 mL sep funnel. 20 mL water was added. The organic layer was collected and the water layer was extracted with DCM (3 x 30mL). The organic layers were pooled, dried with sodium sulfate, then dried using rotary evaporation. The crude product was isolated using flash chromatography (SiO_2, DCM with 2% MeOH). Yield: 60 mg (27%). ^{1}H NMR (300 MHz, Chloroform-*d*) δ 8.45 (ddt, *J* = 4.9, 1.8, 0.9 Hz, 1H), 7.69 (tdd, *J* = 7.4, 1.8, 0.8 Hz, 1H), 7.55 (dq, *J* = 8.0, 1.0 Hz, 1H), 7.16 (ddt, *J* = 7.2, 4.9, 1.0 Hz, 1H), 6.67 (d, *J* = 0.8 Hz, 3H), 3.60 – 3.51 (m, 2H), 3.45 – 3.23 (m, 2H), 2.92 – 2.60 (m, 2H), 1.47 (s, 3H). ESI-MS (cation): 304 m/z ($M + H^+$) obsd, 304.12 calcd.

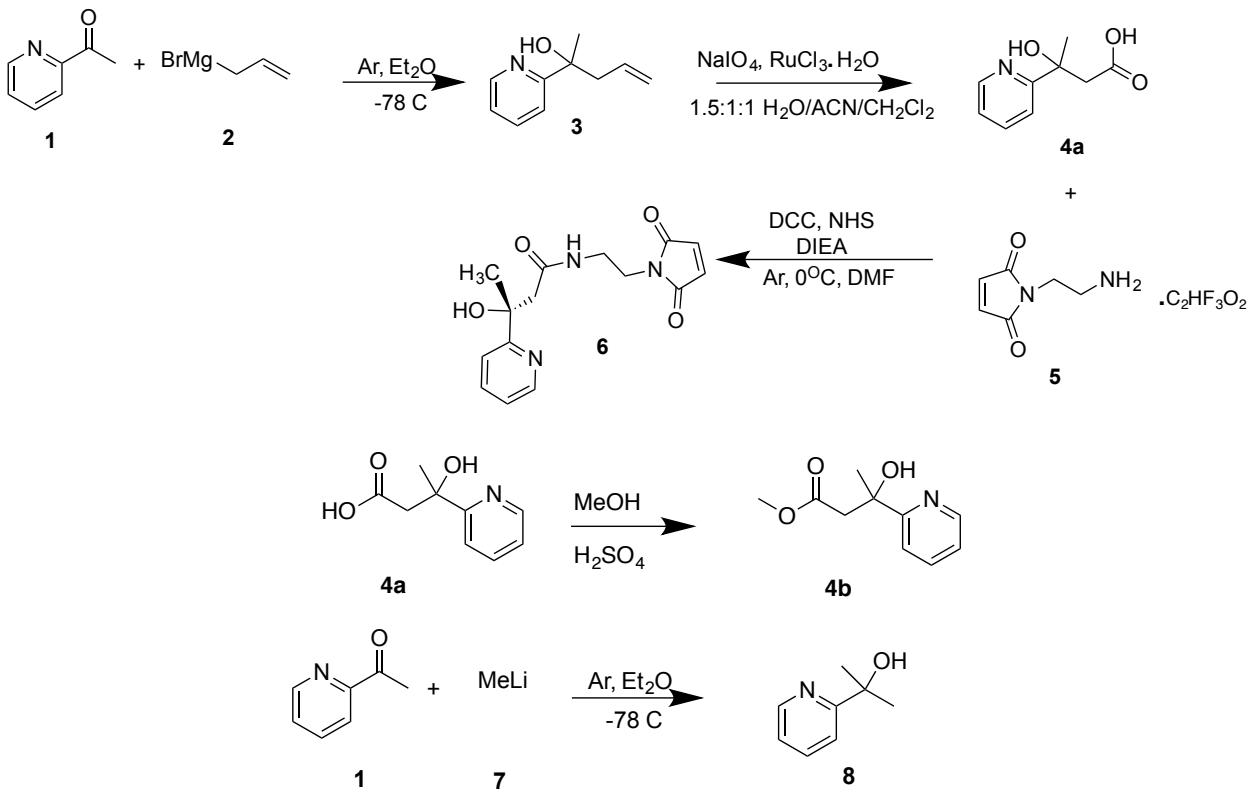

Scheme 4.1 Synthesis of ancillary ligands methyl 3-hydroxy-3-(pyridin-2-yl) butanoate (MHPB, **4b**), (*S*)-*N*-(2-(2,5-dioxo-2,5-dihydro-1*H*-pyrrol-1-yl)ethyl)-3-hydroxy-3-(pyridin-2-yl) butanamide ($L^{maleimide}$, **6**) and 2-(Pyridine-2-yl)propan-2-ol (PPO, **8**) from 2-acetyl pyridine (**1**).

4.2.2.5 Synthesis and Characterization of 2-(Pyridine-2-yl)propan-2-ol (PPO, 8)

2-(Pyridine-2-yl)propan-2-ol (**8**) was synthesized according to published procedures.[2] 2-acetyl pyridine (**1**) (1 mL, 8.9 mmol, 1 equiv.) was added to a dried 50 mL Schlenk flask. **1** was degassed, then 100 mL anhydrous diethyl ether was added under argon. The reaction was cooled to -78°C, then methyl lithium (**8**) (18 mL, 22.2 mmol, 2.5 equiv.) was added dropwise over 15 min. The reaction was stirred for 1 hr at 78°C, then warmed to room temperature. The reaction was quenched by adding saturated NH_4Cl(aq), then extracted with EtOAc (3 x 50 mL). The EtOAc fractions were combined, washed with brine, and dried over sodium sulfate. Solvent was removed *in vacuo*. The product was isolated using flash chromatography (SiO_2, 1:1 EtOAc:CH_2Cl_2) to give a yellow oil. Yield: 610 mg (50%) 1H NMR (CDCl3, 300 MHz): δ 8.52 (d of m, J = 4.8 Hz, 1 H); 7.71 (t of m, J = 7.8 Hz, 1 H); 7.38 (d of m, J = 8.1 Hz, 1H); 7.21 (t of m, J = 6.2 Hz, 1H); 5.08 (s, 1H); 1.54 (s, 6H). ESI-MS (cation): 138 m/z ($M + H^+$) obsd, 138.08 calcd.

4.2.2.6 Synthesis and Characterization of 1-nitro-2-(pyridin-2-yl)propan-2-ol (10)

Procedure was adapted from protocol published in Reference 16.[16] 20 mL 0.5 N NaOH was added to flask, then 2-acetyl pyridine (**1)** (3 g, 24.76 mmol, 1 equiv.) and nitromethane **(9)** (7.56 g, 123.8 mmol, 5 equiv.). The mixture was stirred at RT for 2 hr. Note that the reaction was yellow in color. The reaction was then saturated with NaCl and let stir for 10 min, then extracted gently with ethyl acetate (3 x 50 mL). Organic fractions were combined, washed with brine and, dried over magnesium sulfate. Solvent was removed by rotary evaporation. The product was isolated using flash chromatography (SiO_2, 1:9 EtoAc:Petroleum ether) resulting in a clear/beige

oil. ^{1}H NMR (300 MHz, Chloroform-*d*) δ 8.51 (ddt, *J* = 5.0, 1.7, 0.8 Hz, 1H), 7.85 – 7.62 (m, 1H), 7.54 (dq, *J* = 8.0, 0.9 Hz, 1H), 7.24 (ddt, *J* = 7.6, 4.9, 0.9 Hz, 1H), 4.83 (ddd, *J* = 74.4, 12.3, 0.6 Hz, 2H), 1.61 (d, *J* = 0.6 Hz, 3H). ESI-MS (cation): 181 m/z ($M + H^+$) obsd, 181.07 calcd.

4.2.2.7 Synthesis of 1-amino-2-(pyridin-2-yl)propan-2-ol (11)

1-nitro-2-(pyridin-2-yl)propan-2-ol **(10)** (120mg, 0.659 mmol, 2 equiv.) and nickel (II) chloride ($NiCl_2$-$6H_2O$, 78 mg, 0.329 mmol, 1 equiv.) were combined. Then, 10 mL anhydrous MeOH was added to the reaction and stirred for 10 min. Next, sodium borohydride (140 mg, 4 mmol, 12 equiv.) was added to the reaction and stirred on ice for 45 min. The reaction was then filtered using medium glass frit to afford the product. Compound was used without further purification.

4.2.2.8 Attempted Synthesis of 4-((2,5-dioxo-2,5-dihydro-1*H*-pyrrol-1-yl)methyl)-*N*-(2-hydroxy-2-(pyridin-2-yl)propyl)cyclohexane-1-carboxamide (HMNPC, 13)

1-amino-2-(pyridin-2-yl)propan-2-ol (**11**) (40 mg, 0.25 mmol, 2 equiv.) was dried in flask and put under argon. Then succinimidyl 4-(N-maleimidomethyl)cyclohexan-1-carboxylate (**12**) (SMCC, 43 mg, 0.129 mmol, 1 equiv.) was added to the reaction and placed into an ice bath. 3 mL dry DMF was used to solubilize the reactants. Reaction was stirred on ice for 2 hours, then extracted with EtOAc (3 x 50 mL). Organic fractions were combined, washed with brine, and dried over magnesium sulfate. Solvent was removed by rotary evaporation. The main product was isolated using flash chromatography (SiO_2, 1:9:1 EtoAc:Petroleum ether:MeOH) resulting in a brown oil. Product identity could not be confirmed using NMR or ESI-MS.

4.2.2.9 Synthesis and Characterization of 2-(pyridin-2-yl)but-3-yn-2-ol (PPO-alkyne, 15)

2-(pyridin-2-yl)but-3-yn-2-ol **(PPO-alkyne, 15)** was synthesized by adapting the PPO synthesis and purification. 2-acetyl pyridine (**1**) (2 mL, 17.84 mmol, 1 equiv.) was added to a dried 50 mL Schlenk flask. **1** was degassed, then 100 mL anhydrous diethyl ether was added under argon. The reaction was cooled to -78°C, then 0.5 M ethynylmagnesium bromide (**9)** (89 mL, 44.6 mmol, 2.5 equiv.) was added dropwise over 15 min. The reaction was stirred for 1.5 hr at 78°C, then warmed to room temperature. The reaction was quenched by adding saturated NH_4Cl(aq), then extracted with EtOAc (3 x 50 mL). The EtOAc fractions were combined, washed with brine, and dried over sodium sulfate. Solvent was removed by rotary evaporation. The product was isolated using flash chromatography (SiO_2, 3:1 Petroleum ether/ethyl acetate w/ 1% MeOH 1%NH4OH) to give an off-white powder. ^{1}H NMR (300 MHz, Chloroform-*d*) δ 8.52 (ddd, *J* = 4.9, 1.7, 1.0 Hz, 1H), 7.76 (ddd, *J* = 8.0, 7.4, 1.7 Hz, 1H), 7.61 (dt, *J* = 8.0, 1.1 Hz, 1H), 7.26 (ddd, *J* = 7.4, 4.9, 1.1 Hz, 1H), 5.50 (s, 1H), 2.54 (s, 1H), 1.78 (s, 4H). ESI-MS (cation): 148 m/z ($M + H^+$) obsd, 148.07 calcd.

4.2.2.10 Synthesis and Characterization of 1-(1-(2-(2-(2-(2-aminoethoxy)ethoxy)ethoxy)ethyl)-1*H*-1,2,3-triazol-4-yl)-1-(pyridin-2-yl)ethan-1-ol (11-azido, 18a)

2-(pyridin-2-yl)but-3-yn-2-ol **(PPO-alkyne, 15)** (300 mg, 2.04 mmol, 1 equiv.) and 11-azido-3,6,9-trioxaundecan-1-amine (**16**) (445 µL, 2.245 mmol, 1.1 equiv.) were dissolved in 14 mL of a 1:1 H_2O:CH_2Cl_2 solvent mixture. Then, $CuSO_4.5H_2O$ (26 mg, 0.102mmol, 0.05 equiv.) and sodium ascorbate (61 mg, 0.036 mmol, 0.02 equiv.) were added to the reaction. The reaction was stirred at RT for 3 hr. Solvent was removed from the reaction *in vacuo* and the product was

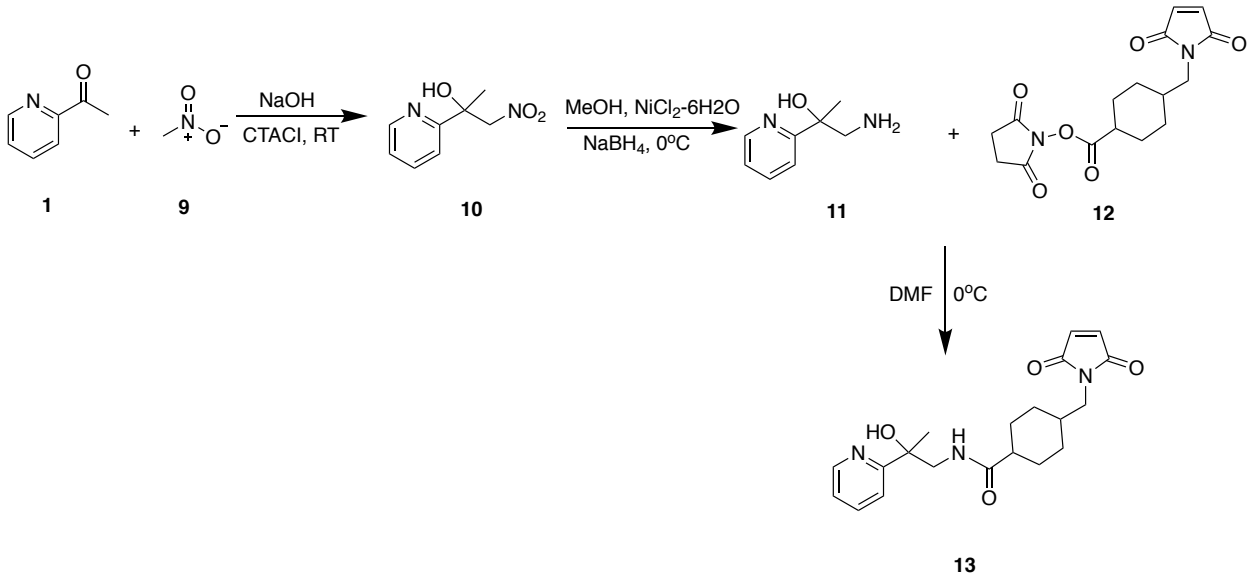

Scheme 4.2 Synthesis of ancillary ligand 4-((2,5-dioxo-2,5-dihydro-1*H*-pyrrol-1-yl)methyl)-*N*-(2-hydroxy-2-(pyridin-2-yl)propyl)cyclohexane-1-carboxamide (HMNPC, **13**) from 2-acetyl pyridine (**1**).

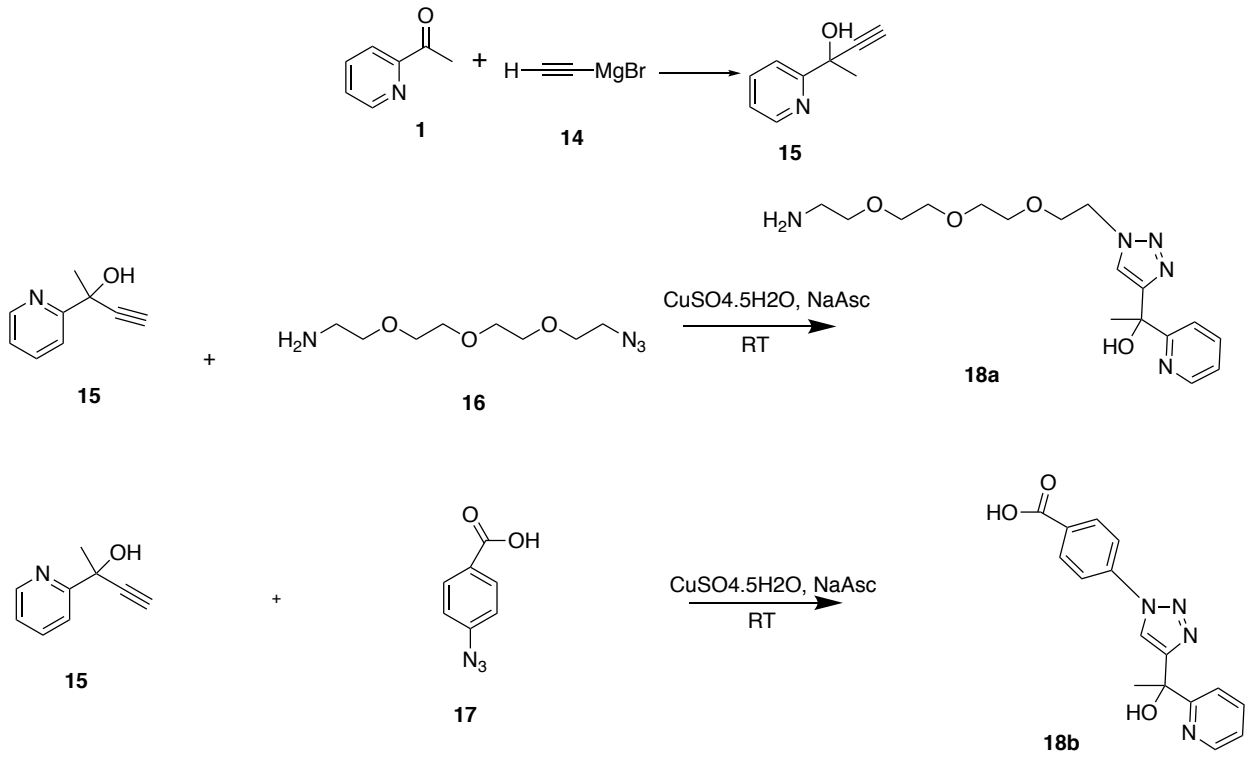

Scheme 4.3 Synthesis of ancillary ligands 2-(pyridin-2-yl)but-3-yn-2-ol (PPO-alkyne, **15**), 1-(1-(2-(2-(2-(2-aminoethoxy)ethoxy)ethoxy)ethyl)-1*H*-1,2,3-triazol-4-yl)-1-(pyridin-2-yl)ethan-1-ol (11-azido, **18a**), and 4-(4-(1-hydroxy-1-(pyridin-2-yl)ethyl)-1*H*-1,2,3-triazol-1-yl)benzoic acid (4-azido, **18b**) from 2-acetyl pyridine (**1**).

isolated using flash chromatography (SiO_2, ethyl acetate w/ 5% MeOH and 1%NH4OH/triethylamine). Product is an orange-brown oil. ^{1}H NMR (300 MHz, Methanol-d_4) δ 8.48 (ddd, J = 4.9, 1.8, 1.0 Hz, 1H), 7.89 – 7.67 (m, 3H), 7.29 (ddd, J = 7.4, 4.9, 1.3 Hz, 1H), 4.54 (dd, J = 5.5, 4.5 Hz, 2H), 3.93 – 3.80 (m, 2H), 3.71 – 3.62 (m, 2H), 3.61 – 3.48 (m, 8H), 3.38 – 3.23 (m, 5H), 1.95 (s, 4H). ESI-MS (cation): 366 m/z ($M + H^+$) obsd, 366.2 calcd.

4.2.2.11 Synthesis and Characterization of 4-(4-(1-hydroxy-1-(pyridin-2-yl)ethyl)-1*H*-1,2,3-triazol-1-yl)benzoic acid (4-azido, 18b)

2-(pyridin-2-yl)but-3-yn-2-ol **(PPO-alkyne, 15)** (105 mg, 0.71 mmol, 1 equiv.) and 4-azido benzoic acid (**17**) (130 mg, 0.78 mmol, 1.1 equiv.) were dissolved in 14 mL of a 1:1 H_2O:CH_2Cl_2 solvent mixture. Then $CuSO_4.5H_2O$ (9 mg, 0.036mmol) and sodium ascorbate (21 mg, 0.107 mmol) were added to the reaction. The reaction was stirred at RT for 4 hr. Solvent was removed from the reaction *in vacuo* and the product was isolated using flash chromatography (SiO_2, ethyl acetate w/ 10% MeOH). Yield ~27% Product is oil. ^{1}H NMR (300 MHz, Methanol-d_4) δ 8.49 (dt, J = 5.0, 1.1 Hz, 1H), 8.45 (s, 1H), 8.15 – 8.08 (m, 2H), 7.89 – 7.77 (m, 4H), 7.30 (ddd, J = 6.8, 4.9, 1.7 Hz, 1H), 2.02 (s, 3H). ESI-MS (cation): 311 m/z ($M + H^+$) obsd, 311.11 calcd.

4.2.2.12 Synthesis and Characterization of *N*-(2-(2,5-dioxo-2,5-dihydro-1*H*-pyrrol-1-yl)ethyl)-4-(4-(1-hydroxy-1-(pyridin-2-yl)ethyl)-1*H*-1,2,3-triazol-1-yl)benzamide (NDDH, 20)

4-(4-(1-hydroxy-1-(pyridin-2-yl)ethyl)-1*H*-1,2,3-triazol-1-yl)benzoic acid **(4-azido, 18b)** (90 mg, 0.29 mmol, 1 equiv.) and HBTU (143 mg, 0.377 mmol, 1.3 equiv.) were dried in the same RB flask. Then 2-amino ethyl maleimide TFA salt **(19)** (88 mg, 0.35 mmol, 1.2 equiv.) was

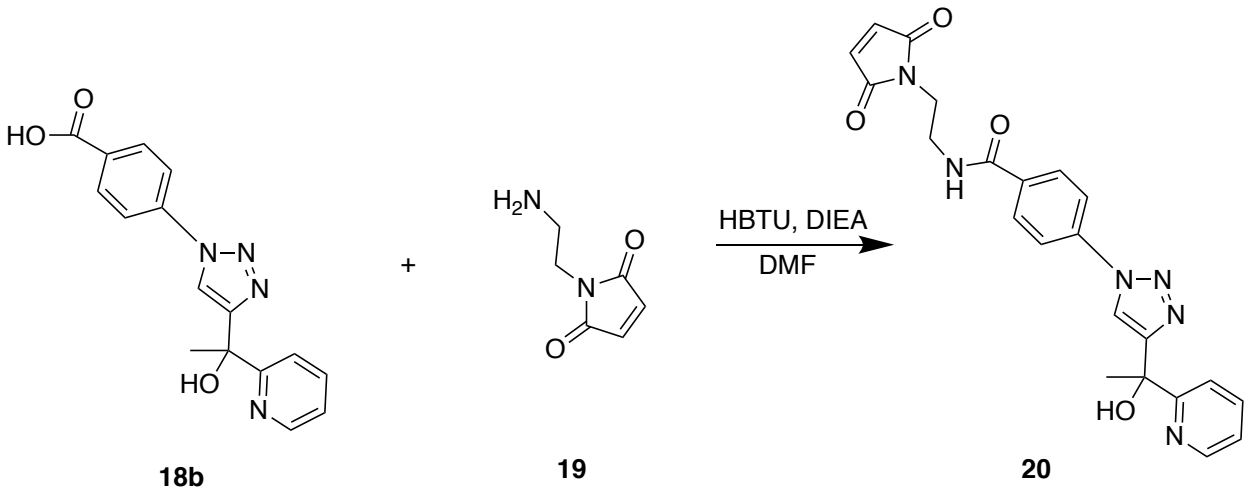

Scheme 4.4 Synthesis of ancillary ligand N-(2-(2,5-dioxo-2,5-dihydro-1H-pyrrol-1-yl)ethyl)-4-(4-(1-hydroxy-1-(pyridin-2-yl)ethyl)-1H-1,2,3-triazol-1-yl)benzamide (NDDH, **20**) from ligand 4-azido (**18b**).

added to a different flask and dried *in vacuo*. 3 mL dry DMF was used to solubilize reagents in both flasks then DIEA (60 µL, 0.66 mmol) was added to each flask. Reaction flask with **18b** was put on ice, then mixture from second flask was added to reaction. Reaction stirred on ice for 2 hr, then at RT for 1 hr. Reaction was diluted with EtOAc, washed once with water, twice with $NaHCO_3$ (aq), and once with brine. Then EtOAc layer was dried with sodium sulfate and solvent removed *in vacuo.* The product was isolated using flash chromatography (SiO_2, DCM w 5% MeOH and 1% acetic acid). ^{1}H NMR (300 MHz, Chloroform-*d*) δ 8.50 (ddt, *J* = 5.0, 1.7, 0.8 Hz, 1H), 8.05 (d, *J* = 0.7 Hz, 1H), 7.93 – 7.68 (m, 6H), 6.84 (d, *J* = 6.1 Hz, 1H), 6.75 (d, *J* = 0.7 Hz, 2H), 3.90 – 3.58 (m, 5H), 2.01 (s, 3H). ESI-MS (cation): 433 m/z ($M + H^+$) obsd, 433.15 calcd.

4.2.3 Metal Complex Synthesis

[Rh(chrysi)(phen)(2-(pyridine-2-yl)propan-2-ol]Cl_2 (Rh-PPO) and $[Rh(phen)(chrysi)(NH_3)_2]^{3+}$ were synthesized following published methodology.[2] Novel rhodium complexes were synthesized by adapting published procedures.[2,17,18] Full synthetic details for each complex, including specific amounts (masses, volumes, and moles), are described below, as well as in **Schemes 4.5** through **4.10**.

4.2.3.1 Synthesis and Characterization of $[Rh(phen)(chrysi)(L^{COOH})]^{2+}$ (22a)

$[Rh(phen)(chrysi)(NH_3)_2]TFA_3$ (**21**) (30mg, 0.0327 mmol, 1 equiv.) and 3-hydroxy-3-(pyridin-2-yl)butanoic acid (L^{COOH}**, 4a**) (12mg, 0.0655mmol, 2 equiv.) were added to a 100 mL RB flask. 40 mL of 12:1 mixture of EtOH:H_2O was added to the flask. The reaction was refluxed at 98°C for ~18 hours. Solvent was removed *in vacuo,* and the crude product was purified by HPLC, then ion exchanged for the chloride salt. ^{1}H NMR (300 MHz, Deuterium Oxide) δ 9.28 (d, *J* = 5.3 Hz, 0H), 8.90 – 8.47 (m, 6H), 8.28 – 7.25 (m, 23H), 3.24 – 3.16 (m, 1H), 3.13 (s, 1H),

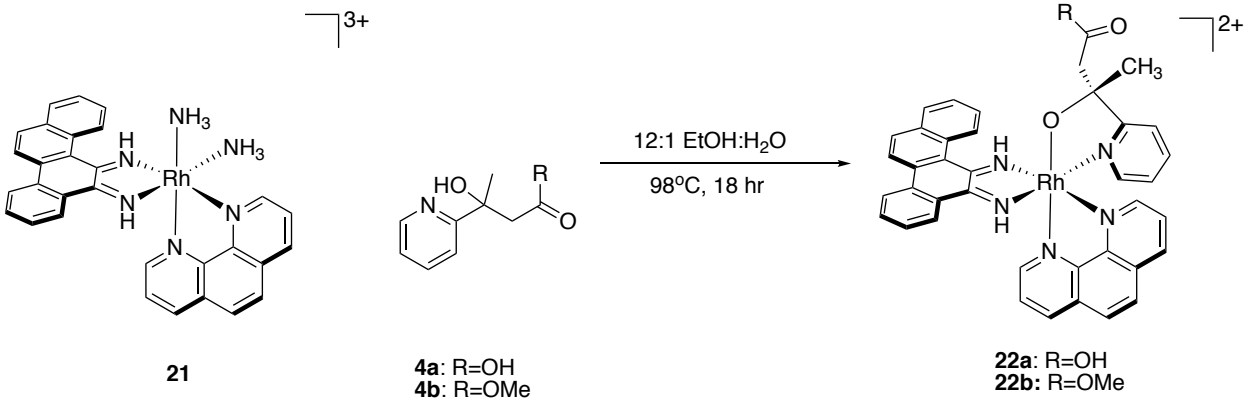

Scheme 4.5 Synthesis of *rac*-[Rh(chrysi)(phen)(L)]$^{2+}$, where L = 3-hydroxy-3-(pyridin-2-yl)butanoic acid (L^{COOH}, **4a**) or methyl 3-hydroxy-3-(pyridin-2-yl) butanoate (MHPB, **4b**).

2.95 (s, 1H), 2.92 – 2.75 (m, 1H), 2.72 – 2.53 (m, 1H), 1.82 (d, J = 26.9 Hz, 1H). ESI-MS (cation): 717.9 m/z ($M + H^+$) obsd, 718 calcd.

4.2.3.2 Synthesis and Characterization of $[Rh(phen)(chrysi)(MHPB)]^{2+}$ (22b)

$[Rh(phen)(chrysi)(NH_3)_2]TFA_3$ (**21**) (30mg, 0.0327 mmol, 1 equiv.) and methyl 3-hydroxy-3-(pyridin-2-yl)butanoate (MHPB, **4b**) (10mg, 0.0512mmol, 1.6 equiv.) were added to a 100 mL RB flask. 40 ml of 10:1 mixture of EtOH:H_2O was added to the flask. The reaction was refluxed at 98°C for ~18 hours. Solvent was removed *in vacuo,* and the crude product was purified by HPLC, then ion exchanged for the chloride salt. Note that limited product formation did not allow for NMR characterization of the complex. ESI-MS (cation): 732 m/z ($M + H^+$) obsd, 732.2 calcd.

4.2.3.3 Synthesis Route for $[Rh(phen)(chrysi)(L^{maleimide})]^{2+}$ (23) Procedure #1

$[Rh(phen)(chrysi)(L^{COOH})](TFA)_2$ (**22a**) (17.4 mg, 0.0242 mmol, 1 equiv.) was dried *in vacuo* in a 20 mL scintillation vial. N-Hydroxysuccinimide (3mg, 0.0242 mmol, 1 equiv.) and N,N'-Dicyclohexylcarbodiimide (5mg, 0.0242 mmol, 1 equiv.) were put in the same vial with a stir bar. The reaction vial was cooled to 0°C and placed under argon. 3 mL anhydrous DMF was added followed by one drop DIEA. The reaction was allowed to stir at 0°C for 1.5 hr. Then 2-amino ethyl maleimide TFA salt (**19**) in 250 µL dry DMF was added to the reaction under argon. The reaction was stirred for an addition 3 hours at 0°C, then the vial was allowed to reach room temperature and the solvent removed *in vacuo.* Note that limited product formation did not allow for NMR characterization of the complex; therefore, additional UV-Visible spectrum characterization was performed. ESI-MS (cation): 840.2 m/z ($M + H^+$) obsd, 840.19 calcd.

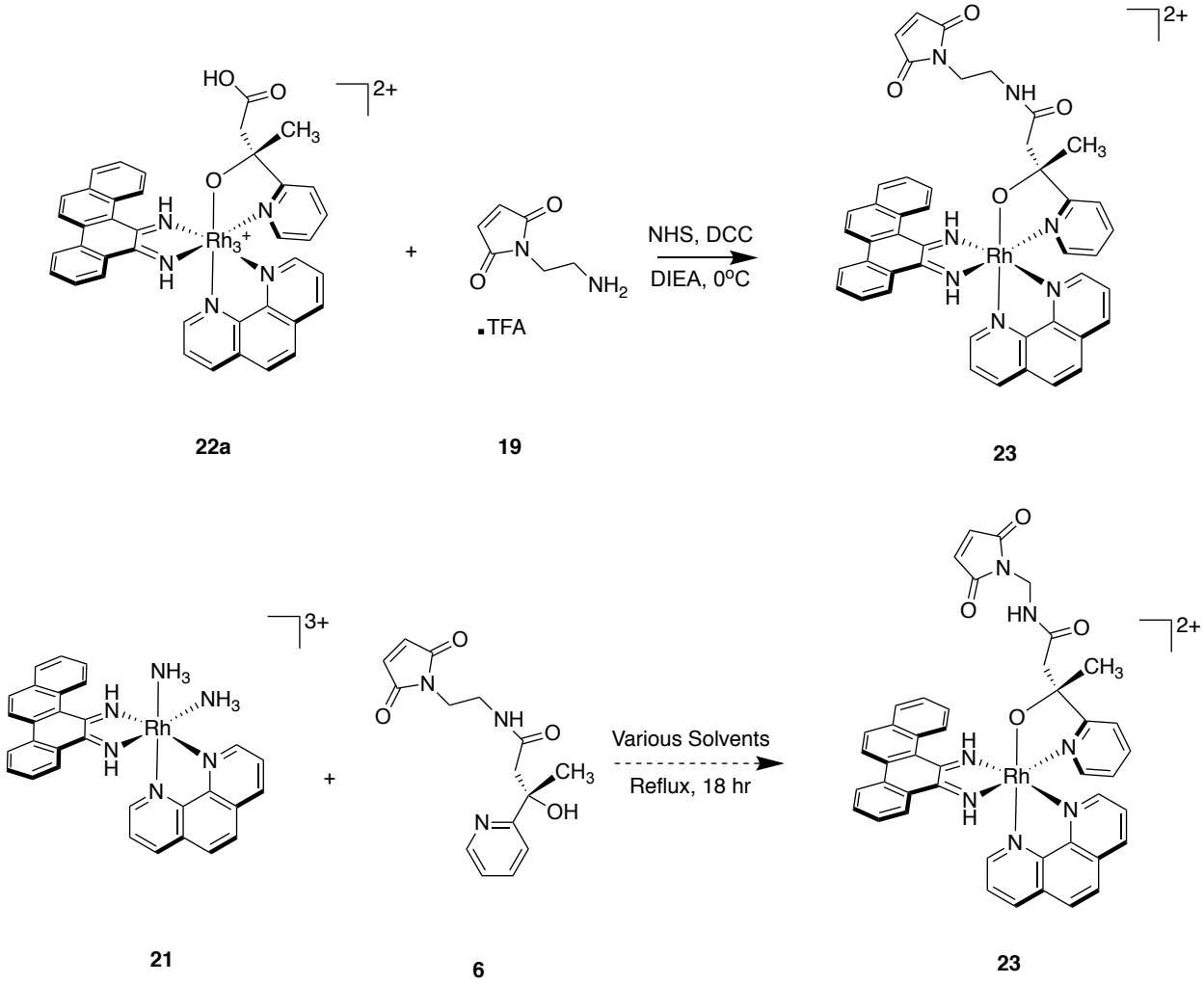

22a **19** **23**

21 **6** **23**

Scheme 4.6 Two attempted synthesis routes for metal complex $[Rh(phen)(chrysi)(L^{maleimide})]^{2+}$ **(23)** starting from 2-amino ethyl maleimide TFA salt **(19)** or $L^{maleimide}$ (**6**).

4.2.3.4 Synthesis Route for [Rh(phen)(chrysi)($L^{maleimide}$)]$^{2+}$ (23) Procedure #2

[Rh(phen)(chrysi)(NH_3)$_2$]TFA_2 (**21**) (30mg, 0.0327 mmol, 1 equiv.) and ((*S*)-*N*-(2-(2,5-dioxo-2,5-dihydro-1*H*-pyrrol-1-yl)ethyl)-3-hydroxy-3-(pyridin-2-yl)butanamide) ($L^{maleimide}$, **6**) (10mg, 0.0512mmol, 1.6 equiv.) were added to a 100 mL RB flask. 40 ml of 10:1 mixture of EtOH:H_2O was added to the flask. The reaction was refluxed at 98°C for ~18 hours. Solvent was removed *in vacuo* and the reaction analyzed by HPLC and ESI-MS. Note that this reaction was repeated with different solvents, including ACN, 1:1 ACN/H_2O, and 1:1 EtOH/H_2O. All reactions resulted in a product with a saturated maleimide double bond, as determined by mass spectrometry; therefore, product **23** was never isolated using the described reaction procedures. Note that limited product formation did not allow for NMR characterization of the reaction product. ESI-MS (cation): 842.2 m/z ($M + H^+$) obsd, 840.19 calcd.

4.2.3.5 Synthesis and Characterization of [Rh(phen)(chrysi)(PPO-alkyne)]$^{2+}$ (24)

[Rh(phen)(chrysi)(NH_3)$_2$]TFA_3 (**21**) (120mg, 0.131 mmol, 1 equiv.) and 2-(pyridin-2-yl)but-3-yn-2-ol (**15**) (30mg, 0.197mmol. 1.5 equiv.) were added to a 100 mL RB flask. 26 ml of 12:1 mixture of EtOH:H_2O was added to the flask. Then DIEA (34 μL, 0.197 mmol) was added to reaction and the reaction was refluxed at 98°C for 4 to 11 hours. Solvent was removed *in vacuo,* and the crude product was purified by HPLC. ^{1}H NMR (300 MHz, Methanol-d_4) δ 9.94 – 9.81 (m, 1H), 9.09 – 8.84 (m, 3H), 8.68 (dd, J = 19.4, 8.2 Hz, 1H), 8.56 – 8.21 (m, 7H), 8.18 – 7.70 (m, 7H), 7.61 – 7.50 (m, 2H), 7.38 – 7.18 (m, 2H), 2.05 – 1.85 (m, 5H), 1.65 (dd, J = 7.0, 0.9 Hz, 1H). ESI-MS (cation): 684.1m/z ($M + H^+$) obsd, 684 calcd.

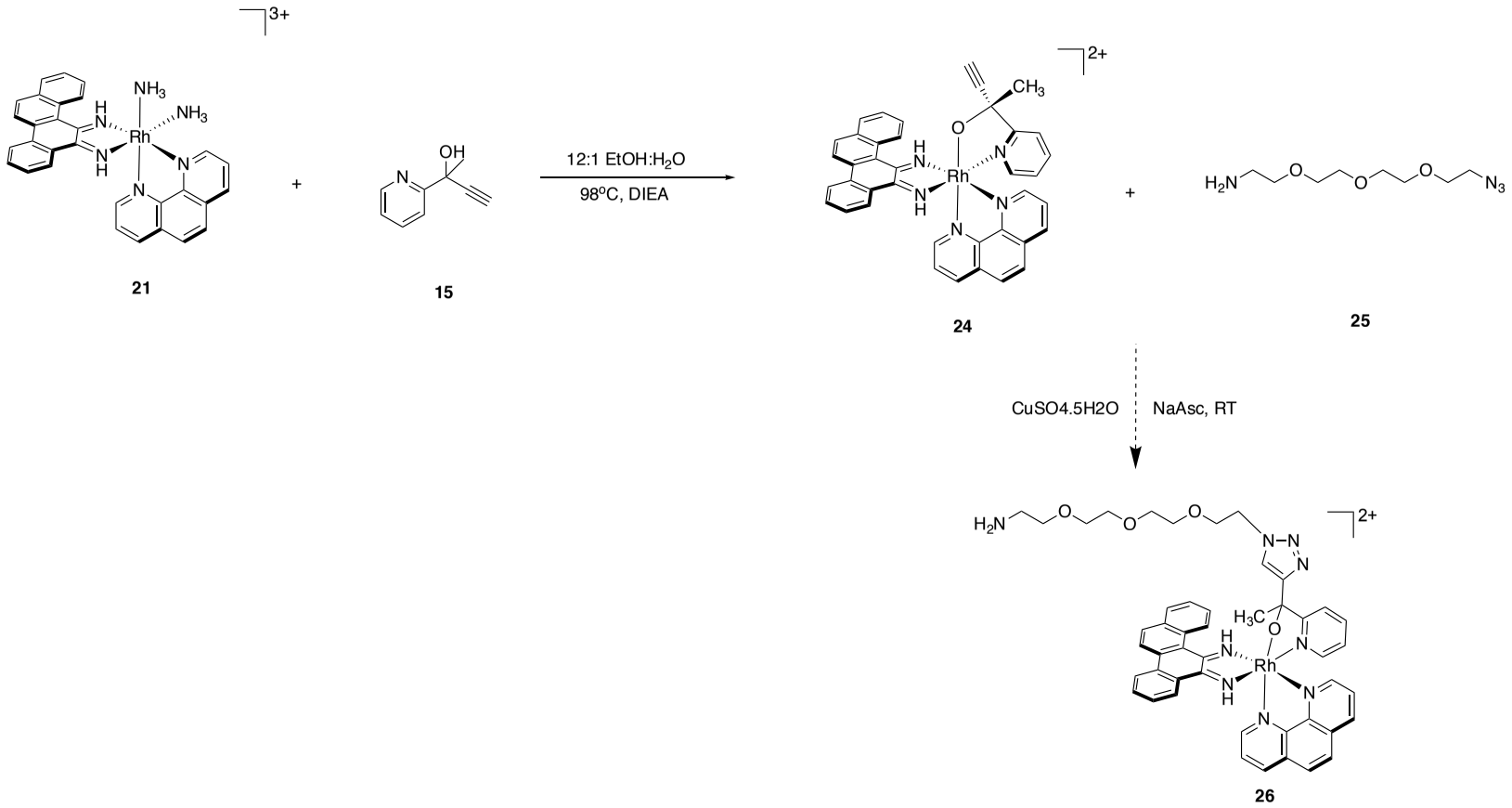

Scheme 4.7 Attempted synthesis route for metal complex $[Rh(phen)(chrysi)(11\text{-azido})]^{2+}$ (**26**) from $[Rh(phen)(chrysi)(NH_3)_2]TFA_3$ (**21**) and 2-(pyridin-2-yl)but-3-yn-2-ol (PPO-alkyne, **15**).

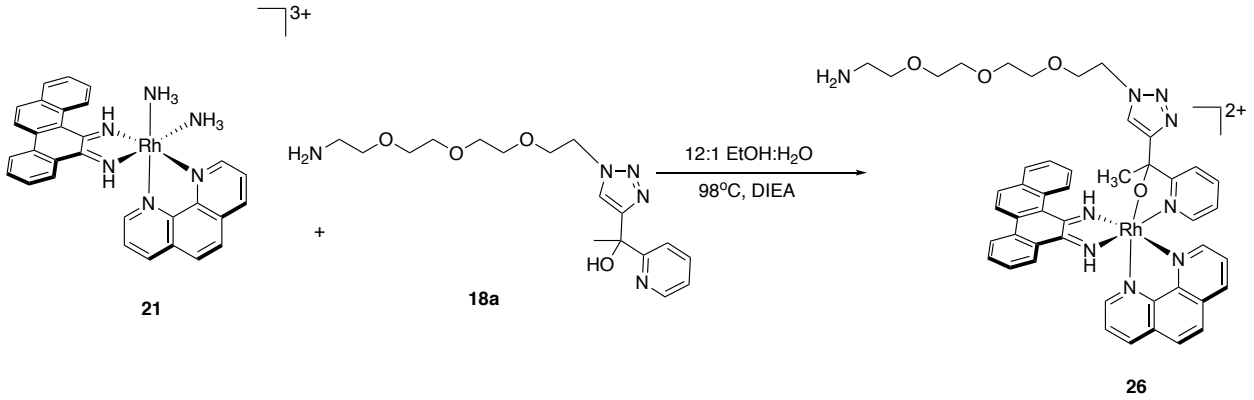

Scheme 4.8 Synthesis of metal complex [Rh(phen)(chrysi)(11-azido)]$^{2+}$ **(26)** from [Rh(phen)(chrysi)$(NH_3)_2$]TFA_3 (**21**) and 1-(1-(2-(2-(2-(2-aminoethoxy)ethoxy)ethoxy)ethyl)-1*H*-1,2,3-triazol-4-yl)-1-(pyridin-2-yl)ethan-1-ol (11-azido, **18a**).

4.2.3.6 Synthesis and Characterization of [Rh(phen)(chrysi)(11-azido)]$^{2+}$ (26)

Procedure #1

[Rh(phen)(chrysi)$(NH_3)_2$]TFA_3 (**21**) (24mg, 0.026 mmol, 1 equiv.) and 1-(1-(2-(2-(2-(2-aminoethoxy)ethoxy)ethoxy)ethyl)-1*H*-1,2,3-triazol-4-yl)-1-(pyridin-2-yl)ethan-1-ol (11-azido, **18a)** (12mg, 0.0329mmol, 1.26 equiv.) were added to a 50 mL RB flask. 13 ml of 12:1 mixture of EtOH:H_2O was added to the flask. Then DIEA (30 μL, .165 mmol) was added to reaction and the reaction was refluxed at 98°C for 1.75 hours. Solvent was removed *in vacuo,* and the crude product was purified by HPLC. ^{1}H NMR (300 MHz, Deuterium Oxide) δ 8.86 (ddd, *J* = 12.7, 7.1, 1.6 Hz, 3H), 8.67 – 8.57 (m, 1H), 8.47 (s, 1H), 8.35 – 8.05 (m, 7H), 8.01 – 7.90 (m, 2H), 7.88 – 7.48 (m, 4H), 7.36 (s, 1H), 4.51 (d, *J* = 2.3 Hz, 0H), 4.02 (t, *J* = 4.9 Hz, 2H), 3.62 – 2.79 (m, 13H), 2.55 (s, 0H), 2.34 (s, 4H). ESI-MS (cation): 902.1m/z (M + H^+) obsd, 902 calcd.

4.2.3.7 Synthesis and Characterization of [Rh(phen)(chrysi)(11-azido)]$^{2+}$ (26)

Procedure #2

[Rh(phen)(chrysi)(PPO-alkyne)]TFA_3 (**24**) (30 mg, 0.033 mmol, 1 equiv.) was dissolved in 1 mL of 2:1 t-BuOH/H_2O. Then 2-(2-(2-(2-azidoethoxy)ethoxy)ethoxy)ethan-1-amine (**25)** (8 μL, 0.0395 mmol, 1.2 equiv.) was added to a separate flask and dissolved in 1 mL of 1:1 H_2O/t-BuOH. Then **25** was moved to the reaction vial and $CuSO_4.5H_2O$ (1 mg, 0.0036mmol, 0.11 equiv.) and sodium ascorbate (2 mg, 0.01 mmol, 0.3 equiv.) were added to the reaction. Reaction was stirred at RT for 16 hr. No formation of product was detected.

4.2.3.8 Synthesis and Characterization of Rh(phen)(chrysi)(SMCC)]$^{2+}$ (27)

[Rh(phen)(chrysi)(11-azido)]TFA_2 **(26) (**3 mg, 0.0026 mmol, 1 equiv.) was thoroughly dried and 600 μL dry DMF was used to solubilize the complex. SMCC **(12)** (1.1 mg, 0.0033 mmol, 1.26 equiv.) was then added followed by DIEA (1 μL, 0.0053 mmol, 2 equiv.). Reaction

was stirred at RT for 4 hr. Solvent was removed using 5 g SepPak, and the crude product was purified by HPLC. ^{1}H NMR (300 MHz, Deuterium Oxide) δ 10.31 (d, *J* = 8.9 Hz, 1H), 8.90 (dtt, *J* = 40.5, 15.9, 8.4 Hz, 4H), 8.57 – 7.18 (m, 19H), 6.80 (s, 1H), 6.54 (s, 1H), 6.37 (s, 1H), 3.98 (s, 1H), 3.75 – 3.01 (m, 18H), 2.87 (s, 1H), 2.43 (s, 1H), 2.28 (s, 1H), 1.76 (s, 1H). ESI-MS (cation): 1121.1m/z (M + H^+) and 561 (M^{2+}) obsd, 1121 calcd.

4.2.3.9 Attempted Synthesis of [Rh(phen)(chrysi)(4-azido-maleimide)]$^{2+}$ (28)

[Rh(phen)(chrysi)(NH_3)$_2$]TFA_3 (**21**) (13mg, 0.0138 mmol, 1 equiv.) and *N*-(2-(2,5-dioxo-2,5-dihydro-1*H*-pyrrol-1-yl)ethyl)-4-(4-(1-hydroxy-1-(pyridin-2-yl)ethyl)-1*H*-1,2,3-triazol-1-yl)benzamide (NDDH, **20)** (9mg, 0.208mmol, 15 equiv.) were added to a 50 mL RB flask. 13 ml of 12:1 mixture of EtOH:H_2O was added to the flask. Then DIEA (3.6 μL, 0.21 mmol, 15 equiv.) was added to the reaction and the reaction was refluxed at 98°C for 6+ hours. No formation of product was detected.

4.2.3.10 Metal Complex Purification and Anion Exchange

The purification of [Rh(chrysi)(phen)(PPO]Cl_2 (Rh-PPO) was modified from the literature preparations as described in Chapter 2. All other rhodium complexes were purified using the following procedure: the crude reaction mixture of metalloinsertor was loaded onto a C18 SPE cartridge equilibrated with 15% acetonitrile in 0.1% TFA(aq). The concentration of acetonitrile was gradually increased and the complex eluted from the SPE cartridge with 25% to 30% acetonitrile in 0.1% TFA(aq), then dried *in vacuo*. The SPE purified complex was then dissolved in minimal acetonitrile before HPLC purification, and filtered. Complexes were further purified following either a gradient or isocratic HPLC method. The initial HPLC method tested involved a gradient elution from 85:15 to 5:95 H_2O + 0.1% TFA:ACN over 30 to 90 min. If this procedure did not result in sufficient separation between the products, isocratic methods ranging

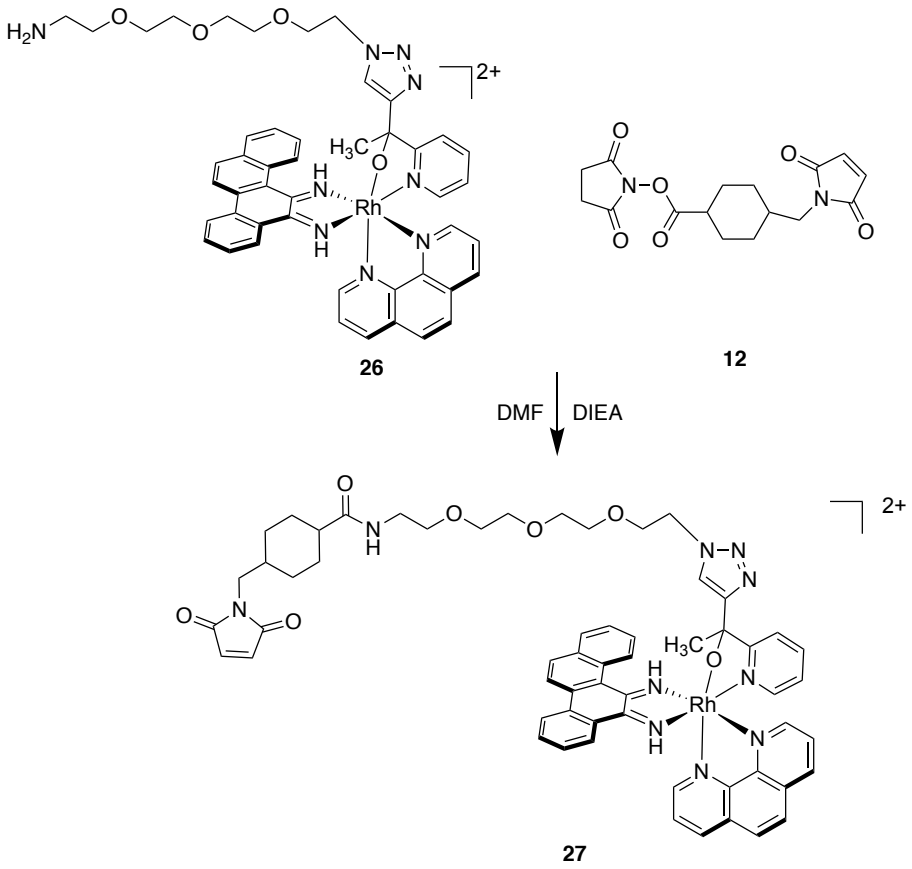

Scheme 4.9 Synthesis of metal complex $[Rh(phen)(chrysi)(SMCC)]^{2+}$ **(27)** from $Rh(phen)(chrysi)(11\text{-azido})]^{2+}$ (**26**) and succinimidyl 4-(N-maleimidomethyl)cyclohexan-1-carboxylate (SMCC, **12**).

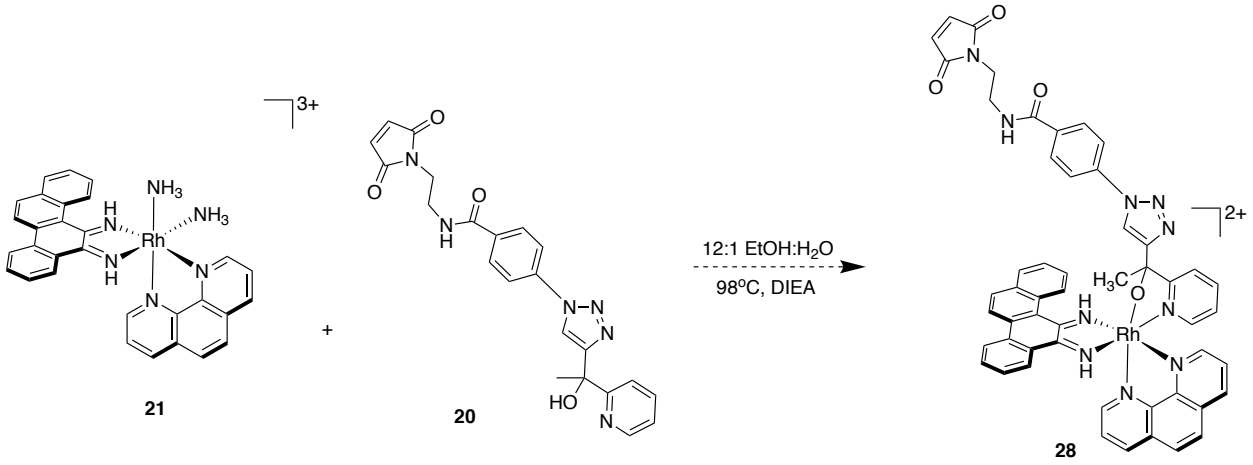

Scheme 4.10 Attempted synthesis of metal complex $[Rh(phen)(chrysi)(4\text{-azido-maleimide})]^{2+}$ **(28)** from NDDH **(20)**.

from 85:15 H_2O + 0.1% TFA:ACN to 65:35 H_2O + 0.1% TFA:ACN over 90 min were explored.

Peaks corresponding to the desired products were verified using ESI-MS and were collected using an automatic fraction collector or by hand. The chloride salts were obtained from a Sephadex QAE anion exchange column equilibrated with 0.1 M $MgCl_2$. Briefly, a Sephadex QAE column was prepped with 100mL 1M $MgCl_2$ (aq.) and washed with 1 L of H_2O to remove excess salts. Purified complex was dissolved in minimal water, loaded onto the column, and eluted with H_2O.

4.2.4 Concentration Determination of Rhodium Complexes

A stock solution of each Rh metalloinsertor was made in MilliQ water and a UV-Vis trace was recorded. The concentration of stock solution was then determined by using the Cary UV-Vis instrument, as well as molar absorptivity values from the literature.[2] The following molar absorptivity values were used to *estimate* the concentration of each complex synthesized: UV−vis (H_2O, pH 7): 270 nm (122,400 M^{-1} cm^{-1}), 300 nm (41,600 M^{-1} cm−1), 430 nm (12,300 M^{-1} cm^{-1}).

4.2.5 Cell Culture

The cells were incubated in tissue culture flasks at 37°C in a 5% CO_2 atmosphere. Standard procedures for entering and exiting cryostorage were followed, as well as methods for subculturing HCT116 cells. HCT116N and HCT116O cells were grown and maintained using RPMI (Roswell Park Memorial Institute) 1640 media supplemented with 10% FBS (fetal bovine serum), 2mM L-glutamine, 0.1 mM non- essential amino acids, 1 mM sodium pyruvate, 100 units/mL penicillin, streptomycin, and 100 μg/mL geneticin (G418).

4.2.5.1 MTT Cell Viability Assay

MTT experiments were performed in HCT116N and HCT116O cells as detailed in the literature.[2] Briefly, approximately 50,000 HCT116N or HCT116O cells in 100 μL of media were plated per well into a 96-well plate. 40 wells were filled with each cell line. Varying concentrations of free Rh-PPO or Rh-PPO liposome solutions (ex. 0-10 μM) were added to the wells and the cells were allowed to incubate at 37ºC for 72 hours. After incubation, MTT (2-(4,5-dimethylthiazol-2-yl)-2,5-diphenultatrazolium bromide) was added. Metabolically active cells were given 4 hours to convert the MTT reagent to insoluble formazan. The reaction was then stopped and solubilized using a solubilizing reagent. The quantity of formazan was determined colorimetrically by absorbance at 570 nm (background subtracted at 690 nm). Viability was determined by comparing absorbance for treated and untreated cells.

4.2.6 Literature Analysis to Determine Rh-O Metalloinsertor ADC Design

A literature search was conducted in order to determine the synthetic design of the three main components of the Rh-O metalloinsertor antibody drug conjugate (ADC): the drug, the linker, and the antibody. An antibody specific to tumor-associated antigens, as well as common in MMR-deficient cells, was thoroughly researched and selected for the ADC. Additionally, three Rh-O metalloinsertor drug-linkers were explored throughout this study: $[Rh(phen)(chrysi)(L^{maleimide})]^{2+}$, $[Rh(phen)(chrysi)(SMCC)]^{2+}$, and [Rh(phen)(chrysi)(4-azido-maleimide)]$^{2+}$, as described below.

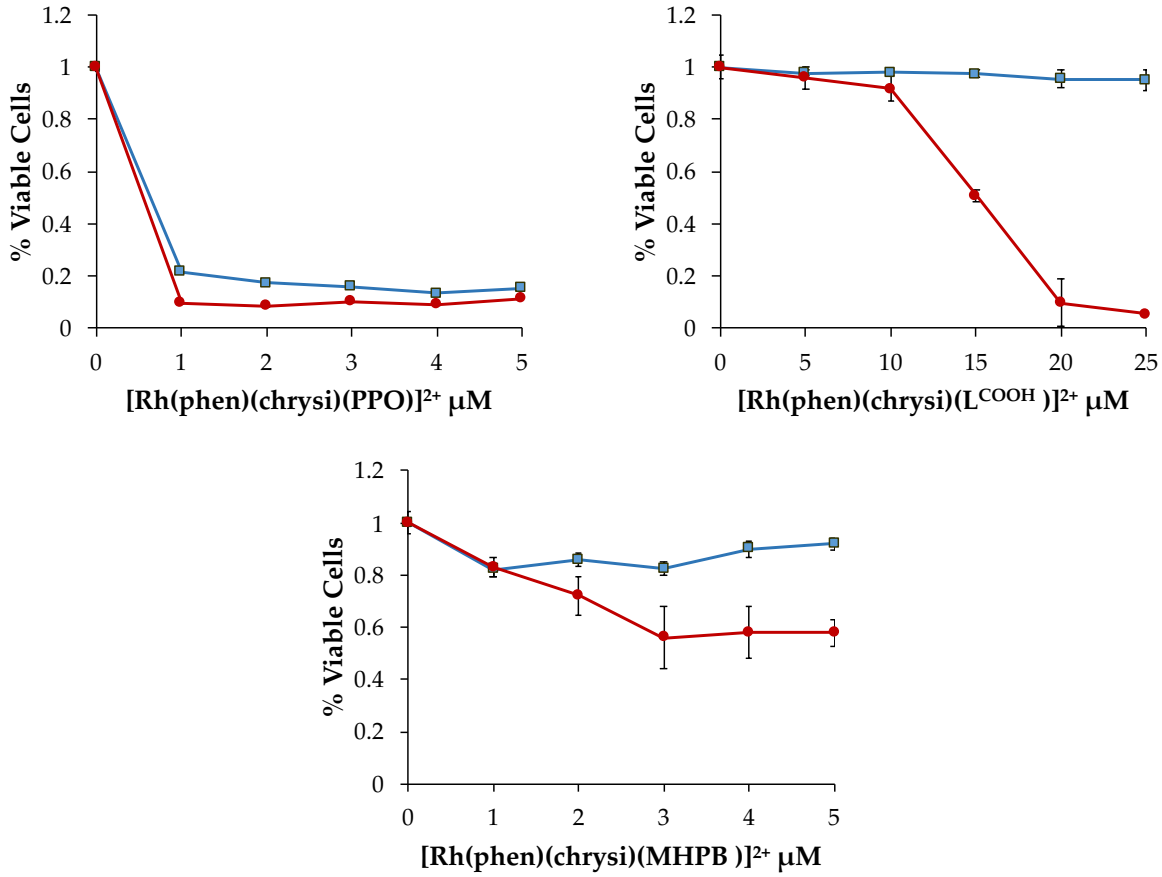

Figure 4.3 MTT cell viability assay comparing $[Rh(phen)(chrysi)(PPO)]^{2+}$, $[Rh(phen)(chrysi)(L^{COOH})]^{2+}$, and $[Rh(phen)(chrysi)(MHPB)]^{2+}$. HCT116N (MMR-proficient, blue squares) and HCT116O (MMR-deficient, red circles) cells were treated with Rh-O metalloinsertors (top left) $[Rh(phen)(chrysi)(PPO)]^{2+}$, (top right) $[Rh(phen)(chrysi)(L^{COOH})]^{2+}$, and (bottom middle) $[Rh(phen)(chrysi)(MHPB)]^{2+}$. Cells were incubated with each metalloinsertor solution at the concentrations indicated for 72 hr, then cells were treated with the MTT reagent for 4 hr. The resulting formazan crystals were solubilized with acidified SDS. Percent viable cells is defined as the percentage of formazan normalized to that of untreated cells. Error is shown as standard deviation calculated from 5 replicates.

4.3 Results

4.3.1 [Rh(phen)(chrysi)($L^{maleimide}$)]$^{2+}$ ADC Design, Synthesis, and Evaluation

4.3.1.1 Rh-O Metalloinsertor Initial Design Evaluation

A former labmate, Dr. Alyson Weidmann, previously synthesized and assessed the cell viability of Rh-O metalloinsertor [Rh(phen)(chrysi)(L^{COOH})]$^{2+}$ (**22a**). The carboxylic acid contained in this complex was viewed as a promising chemical group for potential functionalization. However, the MTT assay of [Rh(phen)(chrysi)(L^{COOH})]$^{2+}$ (Rh-L^{COOH}) revealed the complex to be significantly less potent than Rh-PPO, as shown in **Figure 4.3**, with an IC_{50} value of 15 μM in HCT116O cells; this is 50-fold less potent than Rh-PPO (IC_{50} value of 300 nM in HCT116O cells). One hypothesis for this decrease in cellular potency involved the anionic carboxylic acid group of the metalloinsertor interfering with DNA binding due to repulsion with the DNA backbone. To test this hypothesis, the methyl ester complex [Rh(phen)(chrysi)(MHPB)]$^{2+}$ (**22b**) was synthesized and evaluated. Cell viability studies showed that this complex has increased cellular potency (IC_{50} value of 3.3 μM in HCT116O cells) compared to Rh-L^{COOH} and retains preferential cytotoxicity towards MMR-deficient cells. These results supported the aforementioned hypothesis; therefore, ADC designs utilizing the L^{COOH} ligand were pursued. Note, complete cell death (0% Viable Cells) was not observed for [Rh(phen)(chrysi)(MHPB)]$^{2+}$ within the concentration range tested; a decrease in viability as low as 56% was observed.

4.3.1.2 Rh-O Metalloinsertor ADC Linker: Maleimide Functional Group

The literature analysis revealed that five of the eight FDA approved ADCs utilize maleimide groups to link the antibody and cytotoxic drug components of the ADC, including Trastuzumab deruxtecan and Brentuximab vedotin.[19,20] Furthermore, several ADCs undergoing

clinical development utilize this functional group. Cysteine residues within antibodies are used to form relatively stable and highly selective thiosuccinimide bonds to therapeutic compounds.[13,21,22] Additionally, thiol-maleimide reactions are particularly favorable for ADC linkers due to their rapid reaction kinetics and compatibility with aqueous reaction conditions, which are necessary for antibody stability.[23] ADCs that utilize maleimide linkers are reported to release drugs due to retro-Michael reactions with thiol containing molecules in the cell or degradation of the antibody itself if hydrolysis of the thiosuccinimide ring occurs.[24]

Due to the biological selectivity and potency of $[Rh(phen)(chrysi)(MHPB)]^{2+}$, a metalloinsertor ADC design using the L^{COOH} ligand to incorporate a maleimide functional group was pursued. Ultimately, two synthetic routes for synthesizing $[Rh(phen)(chrysi)(L^{maleimide})]^{2+}$ (**23**) were explored. The first approach involved the conjugation of 2-amino ethyl maleimide with $[Rh(phen)(chrysi)(L^{COOH})]^{2+}$ through peptide bond formation. Secondly, synthesis of $[Rh(phen)(chrysi)(L^{maleimide})]^{2+}$ was attempted by coordinating the $L^{maleimide}$ ligand with $[Rh(phen)(chrysi)(NH_3)_2]^{3+}$ (**Scheme 4.6**). Unfortunately, the high temperatures needed to coordinate the $L^{maleimide}$ ligand also resulted in saturation of the maleimide double bond, eliminating the functional group necessary to conjugate an antibody; therefore, the first synthetic approach was further investigated. Note, multiple reaction conditions, including solvent, temperature, and use of base, were varied for the reaction between $L^{maleimide}$ ligand and $[Rh(phen)(chrysi)(NH_3)_2]^{3+}$.

The peptide coupling reaction between $[Rh(phen)(chrysi)(L^{COOH})]^{2+}$ and 2-amino ethyl maleimide was purified by HPLC, as described; however, very low yields of the $[Rh(phen)(chrysi)(L^{maleimide})]^{2+}$ product were collected due to difficulty separating $[Rh(phen)(chrysi)(L^{COOH})]^{2+}$ and $[Rh(phen)(chrysi)(L^{maleimide})]^{2+}$ metalloinsertors. Note that a

number of gradient and isocratic HPLC methods were attempted. $[Rh(phen)(chrysi)(L^{maleimide})]^{2+}$ that was isolated was further characterized using UV-Visible spectrum data. As shown in **Figure 4.4**, $[Rh(phen)(chrysi)(L^{maleimide})]^{2+}$ has a UV-Vis spectra very similar to $[Rh(phen)(chrysi)(PPO)]^{2+}$ with a large peak at 270, a shoulder peak at 323, and a broad peak at 385 nm. The broad and shoulder peaks of $[Rh(phen)(chrysi)(L^{maleimide})]^{2+}$ are shifted compared to $[Rh(phen)(chrysi)(PPO)]^{2+}$ likely due to the compound being in more basic conditions (similar to $[Rh(phen)(chrysi)(DPE)]^{2+/1+}$ pH titration experiments).[2] Importantly, in addition to the listed peaks, $[Rh(phen)(chrysi)(L^{maleimide})]^{2+}$ has a more pronounced peak at 225 nm (20% higher) compared to $[Rh(phen)(chrysi)(PPO)]^{2+}$, which corresponds to the maleimide absorption wavelength, as seen in the 2-aminethyl maleimide TFA UV-Vis spectrum. These data provide further evidence of $[Rh(phen)(chrysi)(L^{maleimide})]^{2+}$ isolation.

As shown in **Figure 4.5**, the MTT cell viability assay with $[Rh(phen)(chrysi)(L^{maleimide})]^{2+}$ showed minimal cytotoxicity over a 10 μM concentration range (81.5% viable cells at 10 μM in HCT116O cells) with some selective cytotoxicity (maximal differential cytotoxicity of 22% at 2 μM). This low biological activity may be due to hydrolysis of the peptide bond and formation of $[Rh(phen)(chrysi)(L^{COOH})]^{2+}$; therefore, alternative Rh-O metalloinsertor ADC designs were explored.

4.3.2 $[Rh(phen)(chrysi)(SMCC)]^{2+}$ ADC Design, Synthesis, and Evaluation

4.3.2.1 Rh-O Metalloinsertor ADC Linker: SMCC Functional Group

Due to the limited activity and purification challenges of $[Rh(phen)(chrysi)(L^{maleimide})]^{2+}$, additional literature analyses was conducted. N- succinimidyl 4-(N-maleimidomethyl-cyclohexan-1-carboxylate (SMCC) is a hetero-bifunctional linker that contains a maleimide group and an N-hydroxysuccinimide (NHS) ester that allows for conjugation of thiol- and amine-

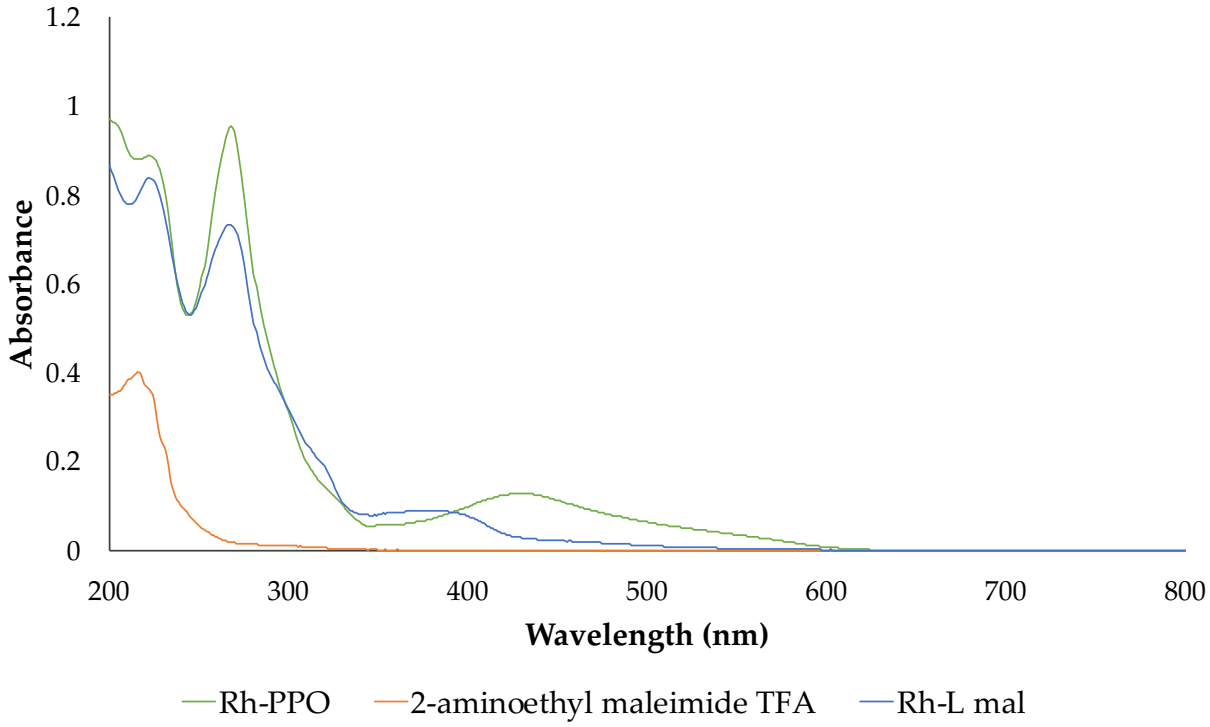

Figure 4.4 UV–Visible spectrum of $[Rh(chrysi)(phen)(PPO)]^{2+}$ (Rh-PPO), $[Rh(chrysi)(phen)(L^{maleimide})]^{2+}$ (Rh-L mal), and 2-aminoethyl maleimide TFA in H_2O.

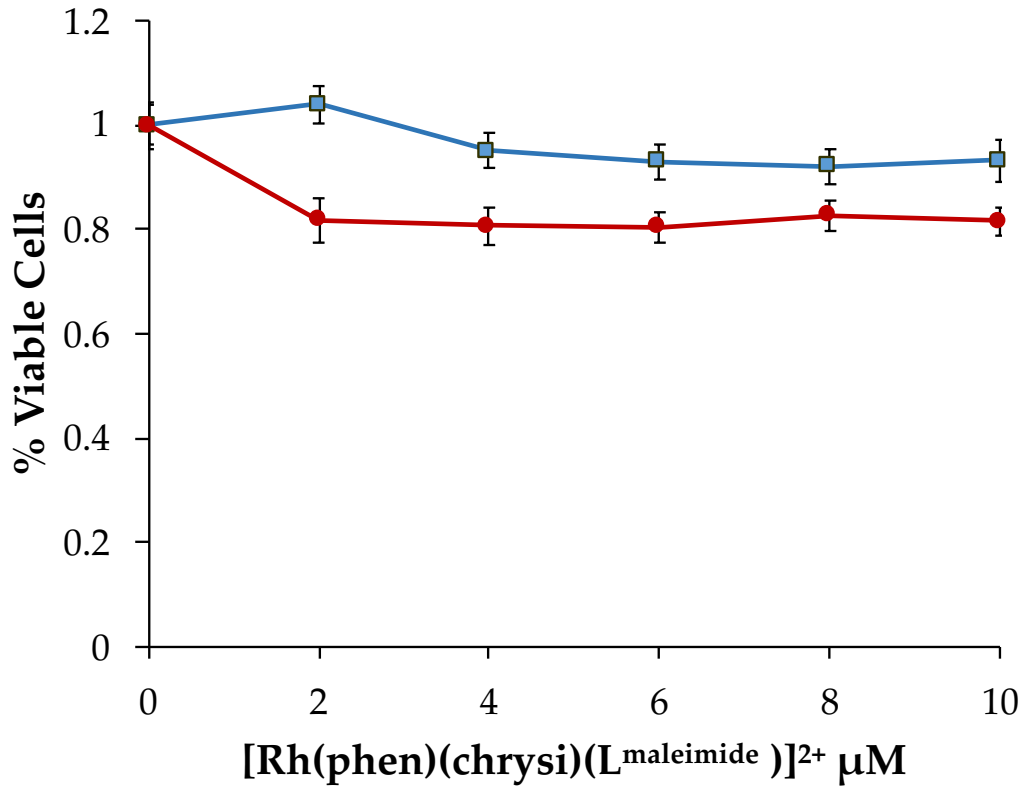

Figure 4.5 MTT cell viability assay for [Rh(phen)(chrysi)($L^{maleimide}$)]$^{2+}$. HCT116N (MMR-proficient, blue squares) and HCT116O (MMR-deficient, red circles) cells were treated with Rh-O metalloinsertor [Rh(phen)(chrysi)($L^{maleimide}$)]$^{2+}$. Cells were incubated with the metalloinsertor solution at the concentrations indicated for 72 hr, then cells were treated with the MTT reagent for 4 hr. The resulting formazan crystals were solubilized with acidified SDS. Percent viable cells is defined as the percentage of formazan normalized to that of untreated cells. Error is shown as standard deviation calculated from 5 replicates.

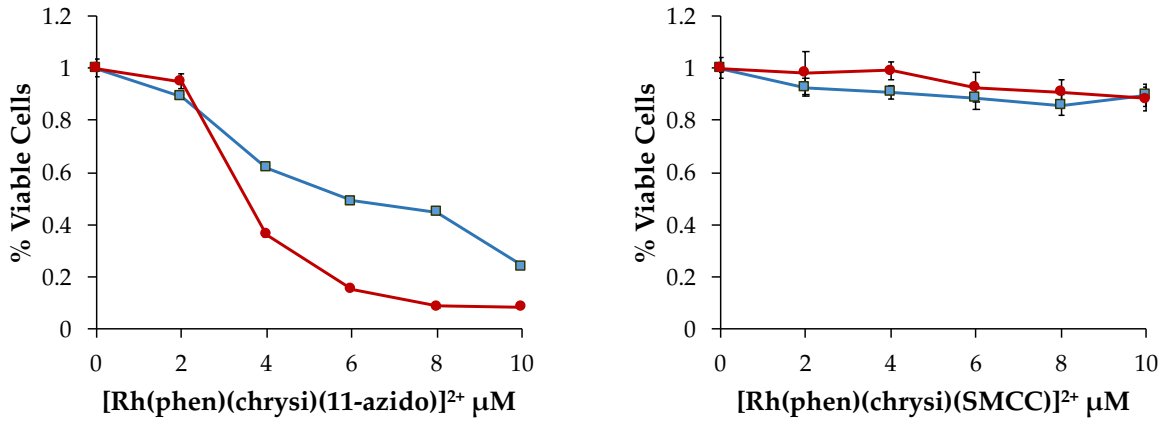

Figure 4.6 MTT cell viability assay for $[Rh(phen)(chrysi)(11\text{-azido})]^{2+}$ and $[Rh(phen)(chrysi)(SMCC)]^{2+}$. HCT116N (MMR-proficient, blue squares) and HCT116O (MMR-deficient, red circles) cells were treated with Rh-O metalloinsertor (left) $[Rh(phen)(chrysi)(11\text{-azido })]^{2+}$ and (right) $[Rh(phen)(chrysi)(SMCC)]^{2+}$. Cells were incubated with the metalloinsertor solution at the concentrations indicated for 72hr, then cells were treated with the MTT reagent for 4 hr. The resulting formazan crystals were solubilized with acidified SDS. Percent viable cells is defined as the percentage of formazan normalized to that of untreated cells. Error is shown as standard deviation calculated from 5 replicates.

containing compounds, respectively. This crosslinker has been used in the FDA approved ADC Trastuzumab emtansine in order to connect the cytotoxic drug DM1 with the anti-HER2 antibody trastuzumab through a non-cleavable, maleimidomethyl cyclohexane-1-carboxylate (MCC) thioether linker.[25]

A novel design for the Rh-O metalloinsertor linker was explored that utilized the SMCC compound to incorporate a maleimide functional group into the oxygen-coordinating ligand of the metalloinsertor. In order to react with the NHS ester of SMCC, a synthesis route that incorporated a stable primary amine was devised. In particular, the use of an azide alkyne Huisgen cycloaddition was employed (see **Scheme 4.3**). Specifically, 1-(1-(2-(2-(2-(2-aminoethoxy)ethoxy)ethoxy)ethyl)-1*H*-1,2,3-triazol-4-yl)-1-(pyridin-2-yl)ethan-1-ol (11-azido, **18a**) was synthesized, and a 1,2,3-triazole group was used in place of a peptide bond in order to afford a stable linker structure that would not be prone to hydrolysis. Additionally, a PEG chain was incorporated due to its hydrophilicity, low immunogenicity, and non-toxicity. PEGylated linkers are also reported to reduce aggregation and increase complex solutility.[13,26] In order to incorporate the maleimide group, the resulting metalloinsertor containing the 11-azido ligand, ([Rh(phen)(chrysi)(11-azido)]$^{2+}$), could then be reacted with SMCC to ultimately form [Rh(phen)(chrysi)(SMCC)]$^{2+}$ (**27**).

Two synthesis routes were explored to generate [Rh(phen)(chrysi)(11-azido)]$^{2+}$. In the first synthetic route, as shown in **Scheme 4.7**, PPO alkyne (**15**) was complexed with [Rh(phen)(chrysi)$(NH_3)_2$]$^{3+}$, then an azide alkyne Huisgen cycloaddition was attempted. Unfortunately, production of [Rh(phen)(chrysi)(11-azido)]$^{2+}$ was never detected by ESI-MS; therefore, a second approach involving the complexation of 11-azido (**18a**) with [Rh(phen)(chrysi)$(NH_3)_2$]$^{3+}$ (**Scheme 4.8**) was explored. This approach was successful, and after

isolation and purification of $[Rh(phen)(chrysi)(11\text{-azido})]^{2+}$, the complex was assessed in cell viability assays. These experiments revealed that the complex retained selective killing of MMR-deficient HCT116O cells and displayed decent potency (IC_{50} value of 3.5 μM in HCT116O cells; **Figure 4.6**).

Next, $[Rh(phen)(chrysi)(11\text{-azido})]^{2+}$ was reacted with SMCC to afford $[Rh(phen)(chrysi)(SMCC)]^{2+}$ (**Scheme 4.9**). Cell viability assays with the purified $[Rh(phen)(chrysi)(SMCC)]^{2+}$ compound were performed and showed very minimal cytotoxic activity (**Figure 4.6**). Specifically,10 μM $[Rh(phen)(chrysi)(SMCC)]^{2+}$ only caused a 11.7% reduction in cell viability. Note that an HPLC method using a gradient elution from 85:15 to 5:95 H_2O + 0.1% TFA:ACN over 50 minutes resulted in the desired purification of $[Rh(phen)(chrysi)(SMCC)]^{2+}$. Note that all MTT experiments were performed with the chloride salt of the isolated complexes.

4.4 Discussion

The mismatch repair (MMR) protein machinery is an essential pathway for identifying and repairing mismatched DNA base pairs and other types of DNA lesions. Mutations within the MMR pathway result in significant increases in mutation load, as well as microsatellite instability (MSI), which often leads to an increased cancer risk.[27,28] In particular, these MMR deficiencies can result in the development of Lynch syndrome and colorectal cancer (CRC). Unfortunately, patients with these malignancies are often less responsive to standard care therapeutics, such as cisplatin and 5-fluorouracil.[29] As a result, various alternative therapeutic approaches have been developed to treat MMR-deficient cancers.

Within recent years, the use of immunotherapeutics has become a promising chemotherapeutic strategy, especially for advanced, metastatic cancers. These monoclonal

antibody-based drugs have been shown to induce significant and impressively long-lasting responses, and due to the increased mutation rate and prevalence of neoantigens within MMR-deficient cancers, immunotherapies have proven to be especially effective for this patient population.[28] Pembrolizumab, a highly selective, humanized monoclonal antibody against the programmed cell death-1 (PD-1) receptor, has been approved for treating MMR-deficient and MSI-high solid tumors. Importantly, while MMR-deficient patients responsive to PD-1/PD-L1 inhibitors tend to have long-term, uniquely immunotherapy-related responses, these therapies only have overall response rates of 40%.[28]

An alternative approach for treating MMR-deficient cancers involves the use of molecules specifically targeted to the DNA lesions that result from MMR protein deficiencies. Rhodium metalloinsertors are octahedral complexes that bind specifically to DNA mismatches and other thermodynamically destabilized DNA sites.[8] This selective binding also corresponds to preferential cytotoxicity towards MMR-deficient cancer cells, and the most recent family of complexes, Rh-O metalloinsertors, displays high potency (ex. Rh-PPO IC_{50} value is 300 nM in HCT116O cells) and notable selective cellular toxicity.[2] However, as indicated in **Figure 4.3**, the range of cytotoxic selectivity within cells and *in vivo* is narrow for the most potent metalloinsertors (ex. Rh-PPO), which may hinder the development of these complexes as targeted chemotherapeutics.

In order to further increase the tumor selectivity and tolerable dose range of these complexes, metalloinsertor antibody drug conjugates (ADCs) were designed and explored. ADC's capitalize on the advancement of monoclonal antibody-based therapies in order to target cytotoxic payloads to tumor-associated antigen expressing cells.[22] Due to the reported functional group tolerability of the oxygen-coordinating, axial ligand, modifications to this ligand were

explored and various Rh-O metalloinsertors were designed and synthesized to incorporate maleimide functional groups. These complexes were assessed using MTT cell viability assays to determine their biological potency and selectivity with the ultimate aim of generating a stable, potent, and selective Rh-O metalloinsertor ADC.

4.4.1 Rh-O Metalloinsertor ADC Design, Synthesis, and Evaluation

4.4.1.1 Metalloinsertor ADC Design and Proposed Mechanism of Action

There are three main components of ADCs: the monoclonal antibody, the linker, and the drug. Selection of each ADC fragment is imperative to the generation of stable, selective, and effective ADC drugs. In the case of the metalloinsertor ADC, a Rh-O metalloinsertor was used as the cytotoxic agent due to the high potency (IC_{50} values ranging from 300 nM to 2 μM in HCT116O cells) and preferential toxicity toward MMR-deficient cells.[2,30] Furthermore, studies with the oxygen-containing ligand of the complex have displayed a tolerance to functionalization. The linker of the ADC was designed to incorporate a maleimide group because this chemical group has successfully been used to conjugate drugs to antibodies in numerous clinically-approved ADCs.[31–34] The free thiols generated from reducing disulfide bonds within the hinge region of antibodies can be reacted with the maleimide group within the drug to form stable succinimidyl thioether bonds.[34] Lastly, anti-mesothelin (MSLN) monoclonal antibodies were selected for the metalloinsertor ADC due to the high expression of MSLN in several MMR-deficient cell lines, including SKOV3 and HCT116 cells, and previous incorporation into successful ADCs.[35,36]

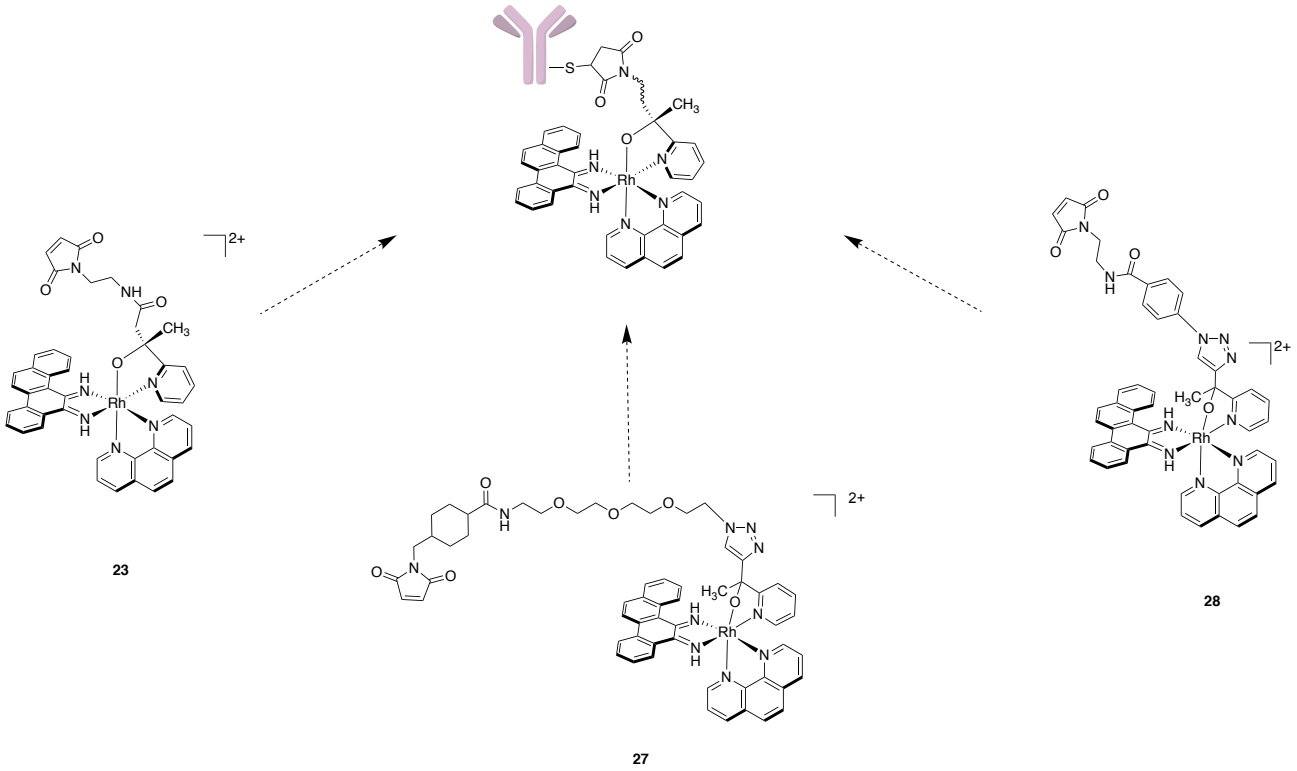

Figure 4.7 Chemical structures of ADC metalloinsertor drug-linker designs with maleimide groups incorporated on the oxygen-containing ligand. Chemical structure of (left) $[Rh(phen)(chrysi)(L^{maleimide})]^{2+}$, (bottom middle) $[Rh(phen)(chrysi)(SMCC)]^{2+}$, and (right) $[Rh(phen)(chrysi)(4\text{-azido-maleimide})]^{2+}$, as well as (top middle) the general structure for the full Rh-O metalloinsertor ADC design.

A successful metalloinsertor ADC would be expected to achieve selective cytotoxicity by first binding to the cell surface expressed mesothelin antigen and then entering the cell via endocytosis, upon which there will be an increase in glutathione levels, which should cause an exchange of thiols and release of the drug. Note that the succinimidyl thioether can also undergo hydrolysis, which results in irreversible ring opening and inhibits drug release; however, proteolytic degradation of the irreversibly bound metalloinsertor ADC can also result in drug release.[13]

4.4.1.2 Characterization of Maleimide Containing Rh-O Metalloinsertors

Three designs of Rh-O metalloinsertors with maleimide groups were explored synthetically, and the general schematic for generating the full metalloinsertor ADC is shown in **Figure 4.7**. In particular, $[Rh(phen)(chrysi)(L^{maleimide})]^{2+}$ and $[Rh(phen)(chrysi)(SMCC)]^{2+}$ were synthesized and evaluated for their biological activity. Unfortunately, $[Rh(phen)(chrysi)(4\text{-azido-maleimide})]^{2+}$ was never isolated.

In the case of $[Rh(phen)(chrysi)(L^{maleimide})]^{2+}$, initial experiments with the methyl ester $[Rh(phen)(chrysi)(MHPB)]^{2+}$ suggested that the L^{COOH} ligand was a suitable building block for incorporating a maleimide group through peptidic coupling reactions. Synthesis of a metalloinsertor containing $L^{maleimide}$ was explored due to the L^{COOH} ligand's previous use in amide coupling reactions, as well as the resulting compound's ($L^{maleimide}$) predicted stability due to the two carbon spacing between the maleimide group and the amide bond; these additional carbons were expected to reduce the electron-withdrawing effects of the peptide bond and therefore attenuate the rate of irreversible hydrolysis at the maleimide group.[24] However, separation of $[Rh(phen)(chrysi)(L^{maleimide})]^{2+}$ and $[Rh(phen)(chrysi)(L^{COOH})]^{2+}$ proved

significantly difficult, and ultimately $[Rh(phen)(chrysi)(L^{maleimide})]^{2+}$ displayed minimal potency (81.5% viable cells at 10 μM in HCT116O cells) and biological selectivity within MTT assays.

Therefore, synthesis of $[Rh(phen)(chrysi)(SMCC)]^{2+}$ was pursued. SMCC is a hetero-bifunctional compound containing a maleimide group and an NHS ester. The synthetic route explored for this complex involved the isolation of $Rh(phen)(chrysi)(11\text{-azido})]^{2+}$, which contains a primary amine attached to a PEG chain within the oxygen-containing ligand, followed by NHS ester crosslinking to incorporate the maleimide group from the SMCC compound. While $[Rh(phen)(chrysi)(11\text{-azido})]^{2+}$ displayed decent potency (IC_{50} value of 3.5 μM in HCT116O cells; **Figure 4.6**) and differential cytotoxicity, the final $[Rh(phen)(chrysi)(SMCC)]^{2+}$ complex showed very minimal potency with 89.3% of HCT116N and HCT116O cells still viable at 10 μM. The lack of cytotoxicity observed with the $[Rh(phen)(chrysi)(SMCC)]^{2+}$ complex may reflect lower uptake of the compound or decreased binding to DNA lesions; however, additional experiments would need to be conducted to clarify these results. Ultimately, none of the synthetic pathways for incorporating a maleimide functional group were successful, and these experiments revealed that the oxygen-containing ligand of Rh-O metalloinsertors may be less tolerant to modification than originally observed. Additionally, the reaction conditions (98ºC, 12:1 EtOH:H_2O, DIEA) necessary for successful complexation of oxygen-containing ligands with $Rh(phen)(chrysi)(NH_3)_2]^{2+}$ were not compatible with incorporation of antibody-reactive functional groups (ex. saturation of the maleimide double bond occurred under various $L^{maleimide}$ complexation reaction conditions); therefore, future metalloinsertor ADC studies should focus on functionalization of a different ancillary ligand.

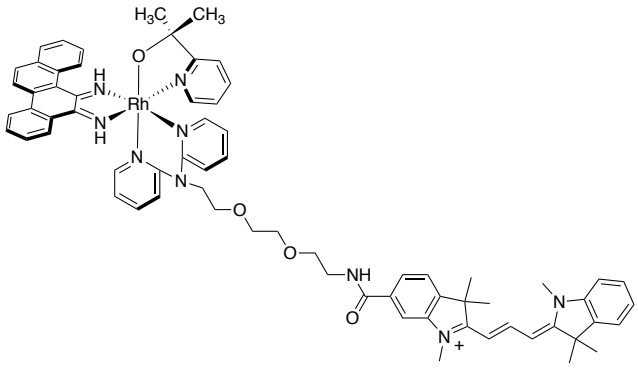

RhPPO-Cy3

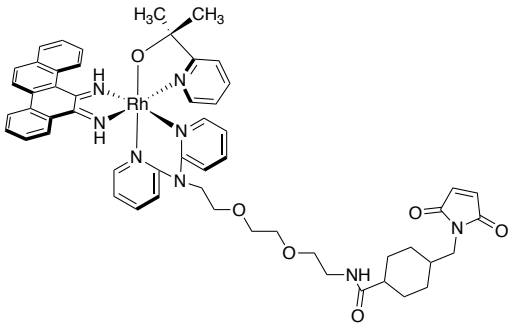

RhPPO-SMCC

Figure 4.8 Chemical structures relevant to potential ADC metalloinsertor designs. Chemical structure of (left) RhPPOCy-3, a fluorescent conjugate containing a Rh-O metalloinsertor and cyanine 3 fluorophore, and (right) RhPPO-SMCC, a Rh-O metalloinsertor containing an MCC linked maleimide on the HDPA ancillary ligand.

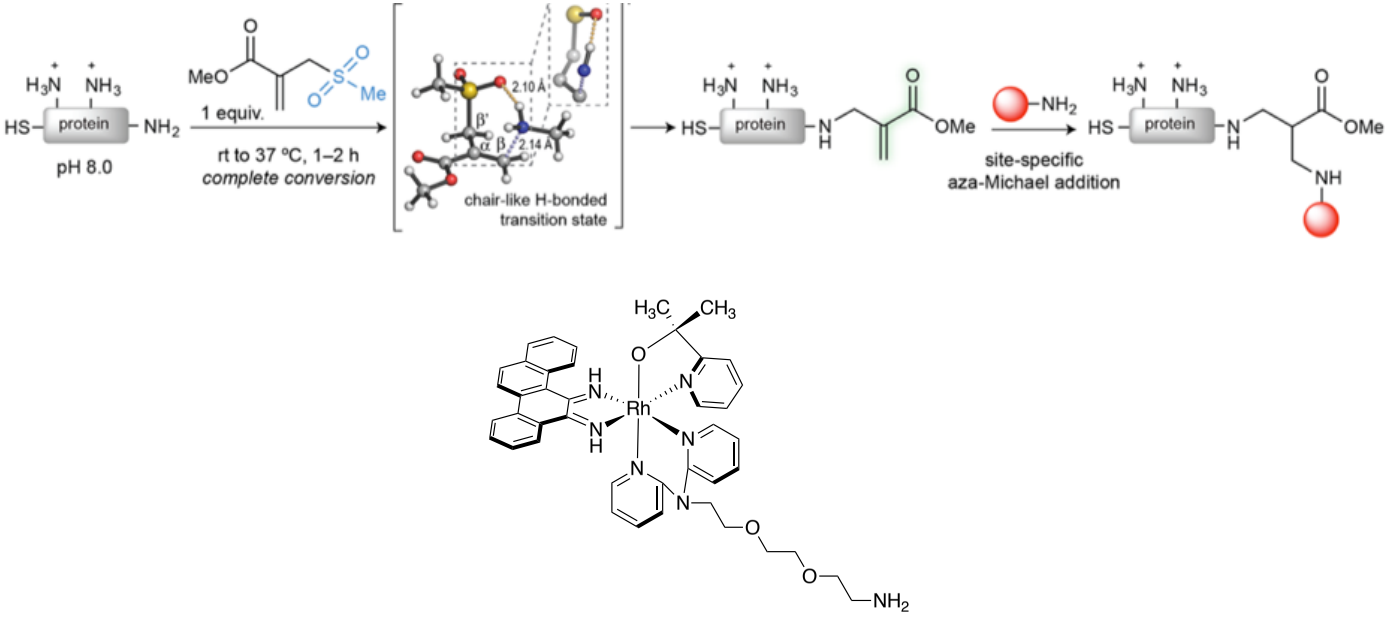

Figure 4.9 Metalloinsertor ADC design that could afford chemo- and regio-selective conjugation to antibodies. (Top) General schematic outlining the use of sulfonyl acrylate to modify lysines within proteins and ultimately conjugate amine-containing compounds through aza-michael additions. (Bottom) Design for Rh-O metalloinsertor containing a nucleophilic primary amine functionalized off the HDPA ligand. This ADC approach is currently being pursued by Dr. Adela Nano. Figure adapted from Reference 37.

4.4.1.3 Recommendations for Future Metalloinsertor ADC Studies

Various metalloinsertor ADC designs warrant exploration. In particular, the focus of these studies should be aimed towards using a different ancillary ligand to incorporate chemical groups that readily react with antibodies. Recently, a Rh-O metalloinsertor conjugated to a cyanine 3 fluorescent probe (RhPPO-Cy3) was synthesized and used to perform localization studies *in cellulo*.[18] Within the RhPPO-Cy3 complex, the 2,2′-dipyridylamine (HDPA) ancillary ligand was functionalized to contain the Cy3 fluorophore (**Figure 4.8**). Importantly, biological studies with RhPPO-Cy3 showed an IC_{50} value of 1 μM and preferential cytotoxicity within HCT116O cells.[18] Additionally, a metalloinsertor family of the form $[Rh(L)(chrysi)(PPO)]^{2+}$ was synthesized and each complex analyzed was found to exhibit selective cytotoxic activity toward the HCT116O MMR-deficient cells line.[17] Ultimately, these analyses indicate that functionalization of the HDPA ligand may allow for the synthesis of Rh-O metalloinsertors with ADC linkers that retain their potency and selectivity.

As such, RhPPO-SMCC, shown in **Figure 4.8**, was designed. Similar to $[Rh(phen)(chrysi)(SMCC)]^{2+}$, RhPPO-SMCC contains a maleimide group that can be used to conjugate the drug to a monoclonal antibody, ultimately with the potential of generating a stable and effective Rh-O metalloinsertor ADC.

A second suggested approach follows procedures outlined in Reference 37,[37] which reports achieving chemo- and regio-selective chemical conjugation of synthetic compounds to proteins using native lysines. This method involves the use of sulfonyl acrylate to modify the most reactive lysine within a given antibody. An aza-michael addition can then proceed between the type 2 alkene of the protein and a nucleophilic drug containing a primary amine, as outlined in **Figure 4.9**.[37] $[Rh(chrysi)(PPO)(HDPA\text{-}amine)]^{2+}$ was designed to evaluate this promising

ADC approach, and as shown in **Figure 4.9**, the metalloinsertor linker for this method uses functionalization of the HDPA ancillary ligand, which may allow the biological potency and selectivity of the complex to be maintained. Furthermore, conjugation of a metalloinsertor to the one, most reactive lysine in the protein would allow for the production of significantly more homogenous metalloinsertor ADCs. This is a very promising route for metalloinsertor ADC synthesis, and notably, Dr. Adela Nano has been pursuing the synthesis and characterization of $[Rh(chrysi)(PPO)(HDPA\text{-}amine)]^{2+}$-based metalloinsertor ADCs.

4.5 Conclusions

The development of Rh-O metalloinsertors has led to a family of DNA mismatch targeted complexes with significant potency and cytotoxic selectivity towards MMR-deficient cells. Uniquely, these metalloinsertors contain an oxygen-coordinating ligand,[2,17] and studies with these complexes have found that alterations to this ancillary ligand, including methyl (PPO), hexyl (PyOctanol), and pyridyl (DPE) group substitutions, have minimal effects on their biological activity.[2] This study outlines the use of Rh-O metalloinsertors as a scaffold to design a metalloinsertor ADC. Three synthetic designs were explored to incorporate thiol-reactive maleimide groups into the hydroxyl, ancillary ligand: $[Rh(phen)(chrysi)(L^{maleimide})]^{2+}$**,** $[Rh(phen)(chrysi)(SMCC)]^{2+}$, and $[Rh(phen)(chrysi)(4\text{-azido-maleimide})]^{2+}$. Unfortunately, all of the isolated and evaluated complexes displayed a loss of biological potency and selectivity. Future efforts to generate a Rh-O metalloinsertor ADC should focus on the functionalization of the HDPA ancillary ligand, similar to RhPPO-Cy3. The production of a successful metalloinsertor ADC would undoubtedly further increase the selectivity and tolerable dose range of metalloinsertor compounds, thereby advancing their development as DNA mismatch targeted chemotherapeutics.

4.6 References

(1) Longley, D. B.; Harkin, D. P.; Johnston, P. G. 5-Fluorouracil: Mechanisms of Action and Clinical Strategies. *Nat. Rev. Cancer* **2003**, *3* (5), 330–338. https://doi.org/10.1038/nrc1074.

(2) Komor, A. C.; Barton, J. K. An Unusual Ligand Coordination Gives Rise to a New Family of Rhodium Metalloinsertors with Improved Selectivity and Potency. *J. Am. Chem. Soc.* **2014**, *136* (40), 14160–14172. https://doi.org/10.1021/ja5072064.

(3) Li, Z.; Pearlman, A. H.; Hsieh, P. DNA Mismatch Repair and the DNA Damage Response. *DNA Repair (Amst).* **2016**, *38*, 94–101. https://doi.org/10.1111/mec.13536.Application.

(4) Alsaab, H. O.; Sau, S.; Alzhrani, R.; Tatiparti, K.; Bhise, K.; Kashaw, S. K.; Iyer, A. K. PD-1 and PD-L1 Checkpoint Signaling Inhibition for Cancer Immunotherapy: Mechanism, Combinations, and Clinical Outcome. *Front. Pharmacol.* **2017**, *8* (AUG), 1–15. https://doi.org/10.3389/fphar.2017.00561.

(5) McDermott, J; Jimeno, A. Pembrolizumab: PD-1 Inhibition as a Therapeutic Strategy in Cancer. *Drugs of Today* **2015**, *51* (1), 7–20.

(6) Weiner, L. M.; Surana, R.; Wang, S. Monoclonal Antibodies: Versatile Platforms for Cancer Immunotherapy. *Nat. Rev. Immunol.* **2010**, *10* (5), 317–327. https://doi.org/10.1038/nri2744.

(7) Weiner, G. J. Building Better Monoclonal Antibody-Based Therapeutics. *Nat. Rev. Cancer* **2015**, *15* (6), 361–370. https://doi.org/10.1038/nrc3930.

(8) Boyle, K. M.; Barton, J. K. Targeting DNA Mismaches with Rhodium Metalloinsertors. *Inorganica Chim. Acta* **2016**, *452*, 3–11. https://doi.org/110.1016/j.bbi.2017.04.008.

(9) Jackson, B. A.; Barton, J. K. Recognition of Base Mismatches in DNA by 5,6-Chrysenequinone Diimine Complexes of Rhodium(III): A Proposed Mechanism for Preferential Binding in Destabilized Regions of the Double Helix. *Biochemistry* **2000**, *39* (20), 6176–6182. https://doi.org/10.1021/bi9927033.

(10) Jackson, B. A.; Alekseyev, V. Y.; Barton, J. K. A Versatile Mismatch Recognition Agent: Specific Cleavage of a Plasmid DNA at a Single Base Mispair. *Biochemistry* **1999**, *38* (15), 4655–4662. https://doi.org/10.1021/bi990255t.

(11) Boyle, K. M.; Nano, A.; Day, C.; Barton, J. K. Cellular Target of a Rhodium Metalloinsertor Is the DNA Base Pair Mismatch. *Chem. Eur. J.* **2019**, *25*, 1–7. https://doi.org/10.1002/chem.201900042.

(12) Diamantis, N.; Banerji, U. Antibody-Drug Conjugates - An Emerging Class of Cancer Treatment. *Br. J. Cancer* **2016**, *114* (4), 362–367. https://doi.org/10.1038/bjc.2015.435.

(13) Kim, E. G.; Kim, K. M. Strategies and Advancement in Antibody-Drug Conjugate Optimization for Targeted Cancer Therapeutics. *Biomol. Ther.* **2015**, *23* (6), 493–509. https://doi.org/10.4062/biomolther.2015.116.

(14) Bailis, J. M.; Weidmann, A. G.; Mariano, N. F.; Barton, J. K. Rhodium Metalloinsertor Binding Generates a Lesion with Selective Cytotoxicity for Mismatch Repair-Deficient Cells. *Proc. Natl. Acad. Sci. U. S. A.* **2017**, *114* (27), 6948–6953. https://doi.org/10.1073/pnas.1706665114.

(15) Bouchard, H.; Viskov, C.; Garcia-Echeverria, C. Antibody-Drug Conjugates - A New Wave of Cancer Drugs. *Bioorganic Med. Chem. Lett.* **2014**, *24* (23), 5357–5363. https://doi.org/10.1016/j.bmcl.2014.10.021.

(16) Ballini, R.; Bosica, G. Nitroaldol Reaction in Aqueous Media: An Important Improvement

of the Henry Reaction. *J. Org. Chem.* **1997**, *62* (2), 425–427. https://doi.org/10.1021/jo961201h.

(17) Boyle, K. M.; Barton, J. K. A Family of Rhodium Complexes with Selective Toxicity toward Mismatch Repair-Deficient Cancers. *J. Am. Chem. Soc.* **2018**, *140* (16), 5612–5624. https://doi.org/10.1021/jacs.8b02271.

(18) Nano, A.; Bailis, J. M.; Mariano, N. F.; Pham, E. D.; Threatt, S. D.; Barton, J. K. Cell-Selective Cytotoxicity of a Fluorescent Rhodium Metalloinsertor Conjugate Results from Irreversible DNA Damage at Base Pair Mismatches. *Biochemistry* **2020**, *59*, 717–726. https://doi.org/10.1021/acs.biochem.9b01037.

(19) Modi, S.; Saura, C.; Yamashita, T.; Park, Y. H.; Kim, S. B.; Tamura, K.; Andre, F.; Iwata, H.; Ito, Y.; Tsurutani, J.; et al. Trastuzumab Deruxtecan in Previously Treated HER2-Positive Breast Cancer. *N. Engl. J. Med.* **2020**, *382* (7), 610–621. https://doi.org/10.1056/NEJMoa1914510.

(20) Younes, A.; Bartlett, N. L.; Leonard, J. P.; Kennedy, D. A.; Lynch, C. M.; Sievers, E. L.; Forero-Torres, A. Brentuximab Vedotin (SGN-35) for Relapsed CD30-Positive Lymphomas. *N. Engl. J. Med.* **2010**, *363* (19), 1812–1821. https://doi.org/10.1056/NEJMoa1002965.

(21) Zhao, P.; Zhang, Y.; Li, W.; Jeanty, C.; Xiang, G.; Dong, Y. Recent Advances of Antibody Drug Conjugates for Clinical Applications. *Acta Pharm. Sin. B* **2020**. https://doi.org/10.1016/j.apsb.2020.04.012.

(22) Nejadmoghaddam, M.; Minai-tehrani, A.; Ghahremanzadeh, R. Antibody-Drug Conjugates : Possibilities and Challenges. *Avicenna J. Med. Biotechnol.* **2019**, *11* (1), 3–23.

(23) Ponte, J. F.; Sun, X.; Yoder, N. C.; Fishkin, N.; Laleau, R.; Coccia, J.; Lanieri, L.; Bogalhas, M.; Wang, L.; Wilhelm, S.; et al. Understanding How the Stability of the Thiol-Maleimide Linkage Impacts the Pharmacokinetics of Lysine-Linked Antibody-Maytansinoid Conjugates. *Bioconjug. Chem.* **2016**, *27* (7), 1588–1598. https://doi.org/10.1021/acs.bioconjchem.6b00117.

(24) Lyon, R. P.; Setter, J. R.; Bovee, T. D.; Doronina, S. O.; Hunter, J. H.; Anderson, M. E.; Balasubramanian, C. L.; Duniho, S. M.; Leiske, C. I.; Li, F.; et al. Self-Hydrolyzing Maleimides Improve the Stability and Pharmacological Properties of Antibody-Drug Conjugates. *Nat. Biotechnol.* **2014**, *32* (10), 1059–1062. https://doi.org/10.1038/nbt.2968.

(25) Hunter, F. W.; Barker, H. R.; Lipert, B.; Rothé, F.; Gebhart, G.; Piccart-Gebhart, M. J.; Sotiriou, C.; Jamieson, S. M. F. Mechanisms of Resistance to Trastuzumab Emtansine (T-DM1) in HER2-Positive Breast Cancer. *Br. J. Cancer* **2020**, *122* (5), 603–612. https://doi.org/10.1038/s41416-019-0635-y.

(26) Feuillâtre, O.; Gély, C.; Huvelle, S.; Baltus, C. B.; Juen, L.; Joubert, N.; Desgranges, A.; Viaud-Massuard, M. C.; Martin, C. Impact of Maleimide Disubstitution on Chemical and Biological Characteristics of HER2 Antibody-Drug Conjugates. *ACS Omega* **2020**, *5* (3), 1557–1565. https://doi.org/10.1021/acsomega.9b03510.

(27) De Las Alas, M. M.; Aebi, S.; Fink, D.; Howell, S. B.; Los, G. Loss of DNA Mismatch Repair: Effects on the Rate of Mutation to Drug Resistance. *J. Natl. Cancer Inst.* **1997**, *89* (20), 1537–1541. https://doi.org/10.1093/jnci/89.20.1537.

(28) Zhao, P.; Li, L.; Jiang, X.; Li, Q. Mismatch Repair Deficiency/Microsatellite Instability-High as a Predictor for Anti-PD-1/PD-L1 Immunotherapy Efficacy. *J. Hematol. Oncol.* **2019**, *12* (1), 1–14. https://doi.org/10.1186/s13045-019-0738-1.

(29) Iwaizumi, M.; Tseng-Rogenski, S.; T. R.; Carethers, J. M. DNA Mismatch Repair Proficiency Executing 5-Fluorouracil Cytotoxicity in Colorectal Cancer Cells. *Cancer Biol. Ther.* **2011**, *12* (8), 756–764. https://doi.org/10.4161/cbt.12.8.17169.

(30) Boyle, K. M.; Nano, A.; Day, C.; Barton, J. K. Cellular Target of a Rhodium Metalloinsertor Is the DNA Base Pair Mismatch. *Chem. Eur. J.* **2019**, *25* (12), 3014–3019. https://doi.org/10.1002/chem.201900042.

(31) Ducry, L.; Stump, B. Antibody-Drug Conjugates: Linking Cytotoxic Payloads to Monoclonal Antibodies. *Bioconjug. Chem.* **2010**, *21* (1), 5–13. https://doi.org/10.1021/bc9002019.

(32) Agarwal, P.; Bertozzi, C. R. Site-Specific Antibody–Drug Conjugates: The Nexus of Bioorthogonal Chemistry, Protein Engineering, and Drug Development. *Bioconjug. Chem.* **2015**, 150130084838000. https://doi.org/10.1021/bc5004982.

(33) Sochaj, A. M.; Świderska, K. W.; Otlewski, J. Current Methods for the Synthesis of Homogeneous Antibody-Drug Conjugates. *Biotechnol. Adv.* **2015**, *33* (6), 775–784. https://doi.org/10.1016/j.biotechadv.2015.05.001.

(34) Fontaine, S. D.; Reid, R.; Robinson, L.; Ashley, G. W.; Santi, D. V; Bay, M.; South, B.; Francisco, S.; States, U. Long-Term Stabilization of Maleimide − Thiol Conjugates. *Bioconjug. Chem.* **2015**, *26*, 145–152. https://doi.org/10.1021/bc5005262.

(35) Golfier, S.; Kopitz, C.; Kahnert, A.; Heisler, I.; Schatz, C. A.; Stelte-Ludwig, B.; Mayer-Bartschmid, A.; Unterschemmann, K.; Bruder, S.; Linden, L.; et al. Anetumab Ravtansine: A Novel Mesothelin-Targeting Antibody–Drug Conjugate Cures Tumors with Heterogeneous Target Expression Favored by Bystander Effect. *Mol Cancer Ther* **2014**, *13* (6), 1537–1548. https://doi.org/10.1158/1535-7163.MCT-13-0926.

(36) Palmer, A. C.; Sorger, P. K.; Palmer, A. C.; Sorger, P. K. Combination Cancer Therapy Can Confer Benefit via Patient-to-Patient Variability without Drug Additivity or Synergy Theory Combination Cancer Therapy Can Confer Benefit via Patient-to-Patient Variability without Drug Additivity or Synergy. *Cell* **2017**, *171* (7), 1678-1682.e13. https://doi.org/10.1016/j.cell.2017.11.009.

(37) Matos, M. J.; Oliveira, B. L.; Martínez-Sáez, N.; Guerreiro, A.; Cal, P. M. S. D.; Bertoldo, J.; Maneiro, M.; Perkins, E.; Howard, J.; Deery, M. J.; et al. Chemo- and Regioselective Lysine Modification on Native Proteins. *J. Am. Chem. Soc.* **2018**, *140* (11), 4004–4017. https://doi.org/10.1021/jacs.7b12874.

Chapter 5

ATTEMPTS TO ELUCIDATE THE STRUCTURE OF RH-O METALLOINSERTORS BOUND TO A DNA MISMATCH*

5.1 Introduction

Numerous biological studies have been conducted with metalloinsertors to better understand their cellular activity and mechanism of action. Originally designed to bind to thermodynamically destabilized mismatch sites that result from mismatch repair (MMR) deficient cancers, metalloinsertors have planar, sterically expansive inserting ligands, such as chrysi (5,6-chrysenequinone diamine), that are slightly wider than well matched DNA base pairs.[1,2] Studies with first generation metalloinsertors, including $[Rh(NH_3)_4(chrysi)]^{3+}$ and $[Rh(bpy)_2(chrysi)]^{3+}$, found that these complexes selectively bind to DNA mismatches with high affinity ($[Rh(bpy)_2(chrysi)]^{3+}$ K_B (CC) = 3.4 x 10^7 M^{-1}). Furthermore, complex binding affinity (K_B) to mismatches and DNA lesions generally was found to correlate with thermodynamic destabilization, with the following relative binding affinities: abasic sites > mismatched base pair > single base bulge >> well matched base pair.[3–5]Additionally, these metalloinsertors, which contain an all N^N coordination environment, show preferential inhibition of cellular proliferation toward the MMR-deficient HCT116O cell line compared to the MMR-proficient HCT116N cells.[6]

In order to further understand the activity of first generation metalloinsertors, structural studies were conducted with these complexes. In particular, X-ray crystallography experiments involving $[Rh(bpy)_2(chrysi)]^{3+}$ and a 12 base pair oligomer containing two AA mismatches revealed that metalloinsertor complexes interact with DNA via a completely novel binding mode

---

* Most crystallography trays were set up with the assistance of Dr. Kelsey Boyle, and Dr. Jens Kaiser helped with screening samples sent to the SLAC beamline. All microED experiments were performed alongside Dr. Byung-Kuk Yoo, and microED data was solved by Dr. Kaiser and Dr. Yoo.

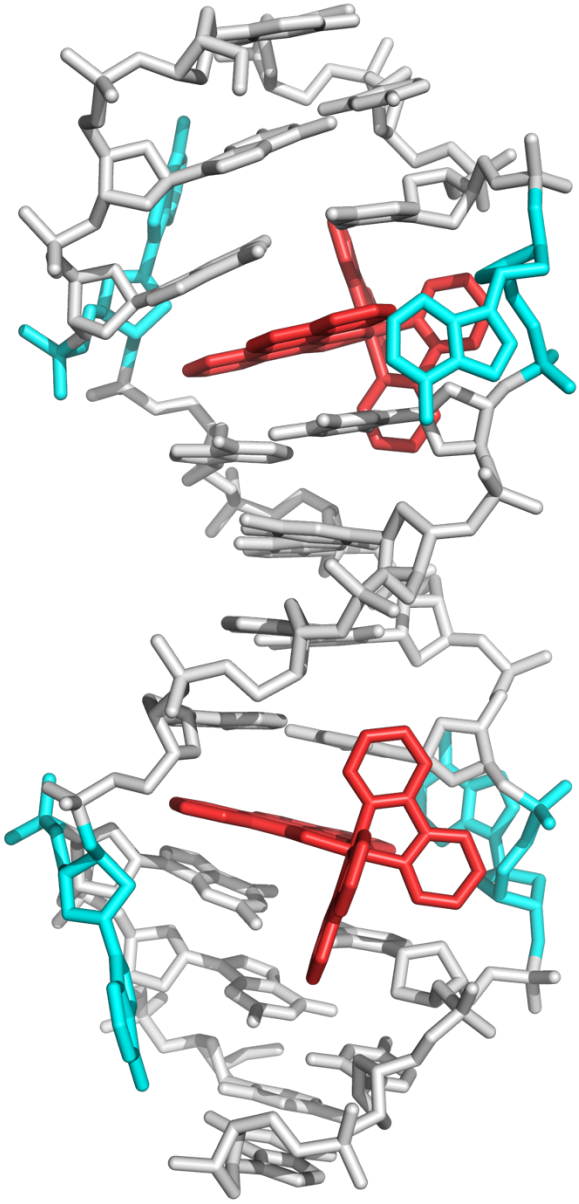

Figure 5.1 Crystal structure of first generation metalloinsertor bound to DNA mismatch. Structure of Δ-Rh(bpy)$_2$(chrysi)$^{3+}$ (red) bound via metalloinsertion to two AA mismatches (cyan) in the oligonucleotide 5′-CGGAAATTACCG-3′ (green), where the mismatch site is underlined. Importantly, the mismatched adenosines (cyan) are ejected from the DNA helix. Structure from Reference 7 and PDB 3GSK.[7]

termed metalloinsertion (**Figure 5.1**).[7] The metalloinsertor crystal structure shows the complex inserting into the mismatched DNA site from the minor grove side and ejecting the mismatched DNA base pairs from the helix.[7,8,9] This allows the inserting ligand of the metalloinsertor to form favorable pi stacking interactions within the helix. Structural changes to the DNA helix were localized to the binding site and no increase in base pair rise was observed, differing significantly from intercalation and covalent DNA binding modes.[,11] Importantly, only the Δ-$Rh(bpy)_2(chrysi)]^{3+}$ enantiomer was found to bind via metalloinsertion, which is consistent with other studies that show that DNA lesion recognition is enantiospecific for the right-handed isomer of this family of metalloinsertors.

The most recent family of Rh-O metalloinsertors, which includes $[Rh(chrysi)(phen)(PPO)]^{2+}$ (Rh-PPO) and $[Rh(chrysi)(phen)(DPE)]^{2+}$ (Rh-DPE), contains an unusual N^O coordination, which results in a number of unique chemical properties compared to first generation metalloinsertors (**Figure 5.2**). These complexes have an overall 2+ charge compared to the 3+ charge of the original metalloinsertor family (Rh-N metalloinsertors) at cellular pH. Additionally, the chrysi inserting ligand of these Rh-O metalloinsertors retains both immine protons when binding to mismatched DNA, while the first generation metalloinsertor $[Rh(HDPA)_2(chrysi)]^{3+}$ appears to bind with a mixture of protonated and deprotonated species. Binding competition titration studies with second generation metalloinsertors also revealed that these complexes do not photocleave DNA upon irradiation, and each of these complexes displays very similar binding affinities, varying from 2.6 to 5.5 × 10^6 M^{-1}.[11,12] Importantly, these results reflect the selective binding of racemic mixtures of Rh-O metalloinsertor complexes because both enantiomers have very similar affinities for mismatched DNA. For example, the Δ and Λ enantiomers of Rh-DPE have the following binding affinities to

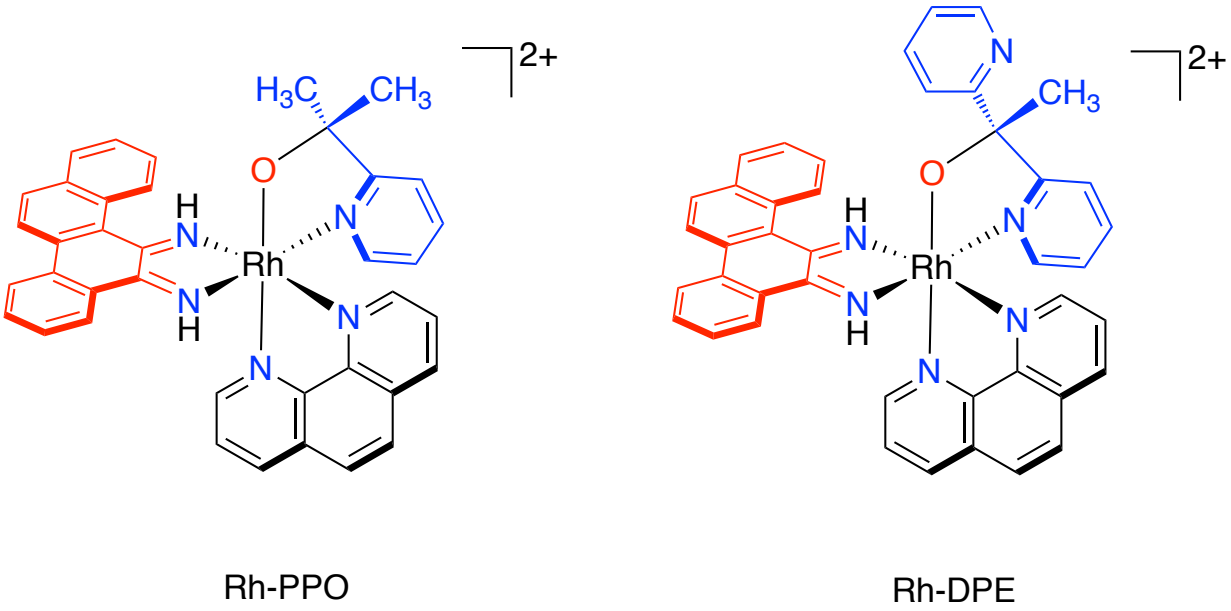

Figure 5.2 Chemical structures of compounds relevant to the Rh-O metalloinsertor structural studies. Chemical structure of second generation metalloinsertors (left) $[Rh(chrysi)(phen)(PPO)]^{2+}$ (Rh-PPO) and (right) $[Rh(chrysi)(phen)(DPE)]^{2+}$ (Rh-DPE). The inserting chrysi ligand is shown in red and the axial, oxygen-containing ligands, PPO and DPE, are displayed in blue.

CC mismatches: 6.0×10^6 and 5.7×10^6 M^{-1}, respectively.[11] Ultimately, these findings indicate that Rh-O metalloinsertors have distinct binding interactions with thermodynamically destabilized DNA sites compared to Rh-N metalloinsertors.

In addition to displaying various unique chemical properties, Rh-O metalloinsertors possess distinctively promising biological activity. Cell viability and proliferation studies show preferential cytotoxicity and inhibition of DNA replication towards the MMR-deficient HCT116O cell line to an even greater extent than Rh-N metalloinsertors. Furthermore, these complexes have increased cellular potency, with Rh-PPO having an IC_{50} value of 300 nM in HCT116O cells.[11,12] Also, colocalization studies with Rh-PPO and the fluorescent Rh-O metalloinsertor conjugate RhPPO-Cy3 that aimed to better understand these compound's mechanism of action found that these complexes activate the DNA damage response (DDR) and specifically target DNA mismatches within cells.[12,13] Most recently, *in vivo* studies with Rh-PPO revealed that the complex has significant anti-tumor effects; however, higher concentrations of the drug result in systemic toxicity, limiting the potential efficacy of these compounds.

Altogether, while Rh-O metalloinsertors have been thoroughly studied to better understand their unique chemical and biological properties, the exact nature of the DNA binding interactions that result in these characteristics remains elusive. Structural analyses with Rh-O metalloinsertors would further elucidate the unique cellular activity of these complexes, as well as potentially help direct future metalloinsertor development, as has been the case for numerous DNA targeting chemotherapeutic drugs.[14] Research within our group has continued to focus on crystallizing a Rh-O metalloinsertor, specifically Rh-PPO or Rh-DPE, bound to a DNA mismatch. Though a structure has yet to be obtained, this chapter outlines the recent efforts to

gain structural insights into the interactions between Rh-O metalloinsertors and mismatched DNA sites using X-ray crystallography and microcrystal electron diffraction (microED).

5.2 Experimental Methods

5.2.1 Materials

All chemicals, reagents, and solvents used were commercially available and used as received, unless otherwise noted. Organic reagents were purchased from Sigma Aldrich, unless otherwise noted (St. Louis, MO). Water was purified using the Millipore Milli-Q system (Milford, MA, USA). HPLC-grade acetonitrile (ACN) was purchased from Fisher Scientific (Fair Lawn, NJ, USA). Sep-Pak C18 solid-phase extraction (SPE) cartridges were acquired from Waters Chemical Co. (Milford, MA). All HPLC metal complex purifications were carried out on a Hewlett-Packard 1100 HPLC. Oligonucleotides were purchased from IDT DNA with standard desalting (Coralville, IA). Crystallography kits and reagents were purchased from Hampton Research (Aliso Viejo, CA). All UV-Visible experiments were performed on a Cary 100 spectrometer.

5.2.2 Purification of DNA Sequences

Twelve base pair DNA oligonucleotides containing AA and AC mismatches were purchased from IDT and ordered as 1 to 2 μmol quantities. The oligonucleotides were dissolved in 400 μL of MilliQ water, then purified using HPLC on a C18 reverse-phase column. The following gradient elution method was employed: 2:98 to 17:83 ACN:50 mM $NH_4CH_3CO_2$ (aq.) over 30 min. The purification efficiency of this method was initially assessed using analytical runs (<0.1 μmol) to determine the elution time of the desired oligonucleotide. After confirming efficiency of the HPLC purification method, preparatory runs were performed on the HPLC (0.2

to 0.5 μmol per run) and the middle of the desired peak was collected in 15 mL falcon tubes. The samples were then dried using a lyophilizer and desalted by ethanol precipitation, as outlined below.

5.2.2.1 Ethanol Precipitation of DNA for Structural Experiments

Pure EtOH, 3 M NaCl (aq.) and 70% EtOH (aq.) were cooled on dry ice (in a cold room) for one hour. Then, 200 μL of MilliQ water was added to the lyophilized DNA oligonucleotide samples (2 μmol). The samples were then vortexed to dissolve the DNA in the water and centrifuged. Next, 5 μL of each sample was removed for MALDI-TOF experiments and placed in PCR tubes. The remaining sample was transferred to 1.5mL eppendorf tubes (100 μL per tube) and 1 mL cold ethanol was added to each sample. The samples were then vortexed. Note that at this step, some cloudiness was visible in certain tubes. Next, 50 μL of cold 3M NaCl (aq.) was added to each sample and vortexed again. Samples were frozen for 30 minutes (-20°C freezer was used). Then, samples were centrifuged at 16,000 rcf for 30 minutes at 4ºC. Supernatant of the sample was carefully removed from the DNA pellet using pipette. Then, the DNA pellet was rinsed with 1 mL of cold 70% EtOH (aq.) and vortexed. The sample was centrifuged again at 16,000 rcf for 5 minutes at 4°C and the supernatant again removed. The resulting DNA samples were dried on the speedvac overnight (note that only 20 minutes on the speedvac is necessary). Dried samples were re-dissolved in a minimal amount of H_2O (~200 μL total) with 50 μL added at a time and mixing was achieved by pipetting and vortexing. Finally, a UV-Visible spectrum of the precipitated DNA sample was taken to quantify the concentration of DNA. Beer's law ($A = \varepsilon lc$) was used to perform these calculations, where ε is the extinction coefficient for the DNA (provided by IDT), A is the absorbance of the sample, and l is the path length of the solution. After concentrations were determined, DNA samples were either diluted (with MilliQ water) or

concentrated (by speedvac) and redissolved in MilliQ water in order to achieve the desired concentration (ex. 2 mM) of the detailed crystallographic and microcrystal electron diffraction studies.

5.2.3 Enantiomeric Separation of Metalloinsertors

5.2.3.1 Synthesis and Initial Purification of Metalloinsertors

[Rh(chrysi)(phen)(2-(pyridine-2-yl)propan-2-ol]$^{2+}$ (Rh-PPO) and [Rh(chrysi)(phen)(1,1-Di(pyridine-2-yl)ethan-1-ol))]$^{2+}$ (Rh-DPE) were synthesized following published methodology.[11] Note that DIEA (>2 equiv.) was added to promote the final reaction step (complexation of DPE or PPO to [Rh(phen)(chrysi)$(NH_3)_2$]$^{3+}$).

After synthesis of Rh-PPO and Rh-DPE, each complex underwent a SepPak purification followed by an initial HPLC purification using a C18 reverse-phase column. Rh-PPO was initially HPLC purified using the methods described in Chapter 2, while Rh-DPE was purified using methods developed by Dr. Kelsey Boyle. Briefly, the Rh-DPE method involved a gradient elution from 15:85 to 25:75 ACN:H_2O + 0.1% TFA over 5 min, then conditions were held at 25:75 for 5 min, subsequently increased to 50:50 over the next 40 min. This method was efficient at removing undesired impurities and separating the two diastereomers of Rh-DPE. Importantly, metalloinsertors are enantiomeric at the metal center and overall the complexes are diastereomers.

5.2.3.2 Enantiomeric and Diastereomeric Purification of Metalloinsertors

Enantiomeric separation studies were performed in collaboration with Dr. Kelsey Boyle, and an efficient method for separating the **Λ** and **Δ** enantiomers of each complex was

accomplished with the assistance of Dr. Scott Virgil.

In the case of Rh-PPO, HPLC purified [Rh(phen)(chrysi)(PPO)]TFA_2 was dissolved in 1:1 ethanol:water. This solution was purified on an Astec CYCLOBOND chiral column using an isocratic elution method of 60:40 KPF_6 (aq.) at 0.1M:ACN for 37 minutes. After each method, a 4-minute wash cycle of 60:40 H_2O:ACN was run to rinse the column of accumulating KPF_6, and after every fifth run a 30-minute wash sequence was performed in which the solvent was switched from 60:40 H_2O:ACN to 5:95 over 10 minutes, held for 10 minutes at 95% acetonitrile, and returned to 60:40 H_2O:ACN over the final 10 minutes. Additionally, an IC column with an isocratic method of 60:40 ACN:0.1M KPF_6 (aq.) was used for further purification of the enantiomers. The **Λ** and **Δ** enantiomers were collected separately and ion exchanged following the procedure described in Chapter 2.

For Rh-DPE, enantiomers were separated using methods developed by Dr. Kelsey Boyle. Briefly, the second eluted diastereomer of Rh-DPE (Rh-DPE-2) was purified using an Asec Cyclobond column. Specifically, an isocratic method of 42.5:57.5 ACN: 0.1 M KPF_6 (aq) was able to separate the enantiomers of Rh-DPE-2. The Rh-DPE-1 diastereomer was purified using a ChiralPak IC column with the following isocratic method: 50:50 ACN: 0.1 M KPF_6 (aq).

Purity of each enantiomer was confirmed using the ChiralPak IC column and circular dichroism experiments. The chloride salts of each complex were obtained from a Sephadex QAE anion exchange column equilibrated with 0.1 M $MgCl_2$ and used in the following crystallography experiments.

Table 5.1 Buffer conditions within the Hampton Research Nucleic Acid Mini Screen Kit used in crystallographic studies

Kit Buffer	Precipitant‡	Buffer§	Polyamine*	Monovalent Ion	Divalent Ion
1	10% MPD	40 mM NaCAC, pH 5.5	20 mM $[Co(NH_3)6]Cl_3$		20 mM $MgCl_2$
2	10% MPD	40 mM NaCAC, pH 5.5	20 mM $[Co(NH_3)6]Cl_3$	80 mM NaCl	20 mM $MgCl_2$
3	10% MPD	40 mM NaCAC, pH 5.5	20 mM $[Co(NH_3)6]Cl_3$	12 mM NaCl, 80 KCl	
4	10% MPD	40 mM NaCAC, pH 5.5	20 mM $[Co(NH_3)6]Cl_3$	40 mM LiCl	20 mM $MgCl_2$
5	10% MPD	40 mM NaCAC, pH 6	12 mM Spermine 4HCl	80 mM KCl	20 mM $MgCl_2$
6	10% MPD	40 mM NaCAC, pH 6	12 mM Spermine 4HCl	80 mM KCl	
7	10% MPD	40 mM NaCAC, pH 6	12 mM Spermine 4HCl	80 mM NaCl	20 mM $MgCl_2$
8	10% MPD	40 mM NaCAC, pH 6	12 mM Spermine 4HCl	80 mM NaCl	
9	10% MPD	40 mM NaCAC, pH 6	12 mM Spermine 4HCl	80 mM NaCl, 12 mM KCl	20 mM $MgCl_2$
10	10% MPD	40 mM NaCAC, pH 6	12 mM Spermine 4HCl	12 mM NaCl, 80 mMKCl	
11	10% MPD	40 mM NaCAC, pH 6	12 mM Spermine 4HCl	80 mM NaCl	20 mM $BaCl_2$
12	10% MPD	40 mM NaCAC, pH 6	12 mM Spermine 4HCl	80 mM KCl	20 mM $BaCl_2$
13	10% MPD	40 mM NaCAC, pH 6	12 mM Spermine 4HCl		80 mM $SrCl_2$
14	10% MPD	40 mM NaCAC, pH 7	12 mM Spermine 4HCl	80 mM KCl	20 mM $MgCl_2$
15	10% MPD	40 mM NaCAC, pH 7	12 mM Spermine 4HCl	80 mM KCl	
16	10% MPD	40 mM NaCAC, pH 7	12 mM Spermine 4HCl	80 mM NaCl	20 mM $MgCl_2$
17	10% MPD	40 mM NaCAC, pH 7	12 mM Spermine 4HCl	80 mM NaCl	
18	10% MPD	40 mM NaCAC, pH 7	12 mM Spermine 4HCl	80 mM NaCl, 12 mM KCl	20 mM $MgCl_2$
19	10% MPD	40 mM NaCAC, pH 7	12 mM Spermine 4HCl	12 mM NaCl, 12 mM KCl	
20	10% MPD	40 mM NaCAC, pH 7	12 mM Spermine 4HCl	80 mM NaCl	20 mM $BaCl_2$
21	10% MPD	40 mM NaCAC, pH 7	12 mM Spermine 4HCl	80 mM KCl	20 mM $BaCl_2$
22	10% MPD	40 mM NaCAC, pH 7	12 mM Spermine 4HCl	40 mM LiCl	80 mM $SrCl_2$, 20 mM $MgCl_2$
23	10% MPD	40 mM NaCAC, pH 7	12 mM Spermine 4HCl	40 mM LiCl	80 mM $SrCl_2$
24	10% MPD	40 mM NaCAC, pH 7	12 mM Spermine 4HCl		80 mM $SrCl_2$, 20 mM $MgCl_2$

‡MPD = (+/-)-2-Methyl-2,4-pentanediol

§ NaCAC = Sodium cacodylate trihydrate

* $MgCl_2$ derived from magnesium chloride hexahydrate

5.2.4 Crystallographic Methods

5.2.4.1 Setting Up Crystallography Trays

A 24-well plate format was used to set up crystal trays. The Hampton Research Mini Nucleic Acid Screen kit was used for these experiments. The kit contains 24 unique buffers with different properties, including various monovalent and divalent ions, pH ranges, and polyamines. See **Table 5.1** for details about each buffer. Crystallography experiments were set up by first adding 1 mL 35% MPD solution to the bottom well in each 24-well plate. Next, 2 μL kit buffer followed by 1 μL metalloinsertor and 1 μL DNA solution were combined on the sitting drop platform of each well. Note that no pipetting was performed to mix the final solution. Lastly, plates were sealed using clear packing tape and stored at room temperature in the dark. Crystallography plates were periodically checked for crystal growth using a light microscope.

5.2.4.2 Harvesting Crystals

In order to harvest promising, viable crystals that were identified with light microscopy, the following general procedure was followed. First, a razor blade was used to remove the clear packing tape (a circle was cut around the well of interest) and a piece of new tape that could easily be opened was placed over the well. Next, crystals were scooped out of the well using a crystal loop that was attached to a magnetic crystal wand. Note that loops of the appropriate size (ex. size 2 or 3) were used to ensure that the crystal was securely looped. Immediately after looping the crystal, it was plunged into liquid nitrogen and transferred to cryo-vials. These vials were placed into cryo-racks and stored in liquid nitrogen in the X-ray crystallography facility until beamtime on the SSRL became available. Once beamtime was acquired, the sample vials were transferred to SSRL large cassettes and screened using automated NoMachine software.

Crystal screenings were often done with the help of Dr. Jens Kaiser, and before looping and analyzing metalloinsertor samples, lysozyme crystals were grown in order to become familiarized with the sample collection and processing methods. Importantly, no additional cryo-protectant had to be added to metalloinsertor/DNA samples before freezing because of the presence of MPD in the buffers.

5.2.5 Microcrystal Electron Diffraction (MicroED) Experiments

5.2.5.1 Sample Selection

Initially samples with small dot patterns were chosen for microED experiments. Later experiments focused on samples with a few larger, uniform crystals, as well as crystal clusters and needles. Finally, we attempted to analyze samples from the crystal tray that produced the initial promising diffraction data.

5.2.5.2 Vitrobot Sample Preparation # 1

Quantifoil 200 or 300 mesh R2/2 copper EM grids (Electron Microscopy Services) were glow discharged for 1 minute (in some cases 30 seconds on each side) using the PELCO easiGlow Glow Discharge System (Ted Pella). Grid was placed into the Vitrobot instrument, then 3 μL of sample was applied to the secured grid. The EM grid was then blotted with filter paper before being immediately plunge-frozen using a Vitrobot Mark IV (Thermo Fisher). Different variations of this procedure were explored including: applying sample to the frontside and backside of the grid, as well as varying the blot force, blot time, vortexing and pipetting sample before applying to grid, and the volume of sample applied to the grid.

5.2.5.3 Vitrobot Sample Preparation # 2

Quantifoil 200 mesh R2/2 copper EM grids (Electron Microscopy Services) were glow discharged for 30 sec on each side using the PELCO easiGlow Glow Discharge System (Ted Pella). Grid was placed on PTFE polymer, then 3-5 μL of sample was applied to the grid, covered, and incubated (time varied). The grid was secured in the Vitrobot, then 1.5 μL of sample was applied to the backside of the secured grid. The EM grid was then blotted with filter paper and immediately plunge-frozen using a Vitrobot Mark IV (Thermo Fisher). Different variations of this procedure were explored including: applying sample to the frontside and backside of the grid, varying the blot force and blot time, vortexing and pipetting sample before applying to grid, sample incubation time (1 min to 3 hr), and the volume of sample applied to the grid.

5.2.5.4 Manual Sample Preparation #1

Lacey carbon, continuous carbon, 300 mesh, gold EM grids (Electron Microscopy Services) were glow discharged on both sides for 1 minute using the PELCO easiGlow Glow Discharge System (Ted Pella). Selected crystal sample was mixed by pipetting (5x), then added to grid (1-4 μL) on the gold side. The sample was incubated for 20 sec, then the grid was turned over and blotted on filter paper for 20-30 sec. Finally, the grid was clipped at room temperature, then transferred to LN2 right before putting in the EM cassette. Note that sample was taken from the edge of the well.

5.2.5.5 Manual Sample Preparation #2

Lacey carbon, continuous carbon, 300 mesh, gold EM grids (Electron Microscopy Services) were glow discharged on both sides for 1 minute using the PELCO easiGlow Glow

Discharge System (Ted Pella). Grid was stabilized on filter paper using tweezers (this allows sample to diffuse through grid and onto filter paper). Selected crystal sample was mixed by pipetting (5x), then added to grid (1 μL) on the gold side. Lastly, the grid was clipped at -196^{o}C (with clip set up covered to minimize ice contamination), then transferred to EM cassette or cryostorage.

5.2.5.6 Electron Microscopy Instrument Parameters

All data were collected on a Thermo-Fisher Talos Artica electron cryo-microscope operating at an acceleration voltage of 200keV, corresponding to a wavelength of ~0.025079 Å. Screening of MicroED data and collection was performed in rolling shutter using a Thermo-Fischer Ceta CMOS camera. Images were collected as a movie as the crystal was continuously rotated in the electron beam. Typical data collection was performed using a constant tilt rate of ~0.6 ° per sec over an angular wedge of ~60° between the minimum and maximum tilt ranges of -72° to +72° degrees, respectively. During continuous rotation, the camera integrated frames continuously at a rate of 1-3 sec per frame. The dose rate was calibrated to <0.03 e^{-} $Å^{-2}$ s^{-1}. Crystals selected for data collection were isolated by a selected area aperture to reduce the background noise contributions and calibrated to eucentric height to keep the crystal in the aperture over the entire tilt range.

Diffraction movies saved as SER files were converted to SMV format using in-house software developed by Dr. Byung-Kuk Yoo. Frames were indexed and integrated in XDS (http://xds.mpimf-heidelberg.mpg.de/html_doc/references.html). Note that all microED experiments were performed in collaboration with Dr. Byung-Kuk Yoo.

5.3. Results and Discussion

5.3.1 Attempts to Characterize the Structural Interaction Between Rh-O Metalloinsertors and Mismatched DNA

Detailed below are the X-ray crystallography and microcrystal electron diffraction (microED) experiments explored with Rh-O metalloinsertors and oligomers containing mismatched DNA. Attempts to optimize sample preparation, relevant takeaways, and suggestions for how to proceed with the project are discussed.

5.3.1.1 X-ray Crystallography Experiments

X-ray crystallography has long remained the primary method for resolving the three-dimensional structure of chemical and biological species of interest.[15] These structural determinations have been imperative to advancements in the drug discovery process, as well as understanding the mechanism of action of various therapeutics.[16] For instance, the crystal structure of cisplatin crosslinked to double-stranded DNA revealed the formation of notable adducts that unwind and bend the DNA duplex. These findings, alongside the atomic structure of cisplatin alone, assisted in the development of numerous platinum-based drugs, including oxaliplatin and carboplatin.[17] Additionally, X-ray crystallography studies elucidated important protein binding targets of platinum compounds, including the lysozyme protein.[17]

In order to continue the drug development of metalloinsertors and better understand their biological activity, the use of X-ray crystallography was explored to gain structural insights into the interaction between Rh-O metalloinsertors and their target DNA sites. Various approaches to crystallizing Rh-O metalloinsertors bound to DNA have been attempted since this family of complexes was developed. Before graduating, Dr. Kelsey Boyle focused on varying oligomer sequences and length, the ratio of DNA to metalloinsertor, and screening buffer conditions.

The crystallography trays set up in collaboration with Dr. Boyle involved the following self-complementary oligomeric sequences: 5'- CGG **A**AA TT**A** CCG -3' (contains two AA mismatches) and 5'- CGG **A**AA TT**C** CCG -3' (contains two AC mismatches), where the mismatch sites are bold and underlined. Trays contained a combination of precipitant buffer, DNA, and Rh-O metalloinsertor enantiomers. These DNA sequences were chosen because they were used in previously successful X-ray crystallography experiments with the Rh-N metalloinsertors $[Rh(bpy)_2(chrysi)]^{3+}$ and $[Ru(bpy)_2(dppz)]^{2+}$; [7,18,19] and these oligomers facilitated the formation of uniform, sizeable crystals. Furthermore, crystallography studies performed by Dr. Boyle found that DNA sequences containing two mismatches are more likely to form crystalline-type products. The described crystal trays, as well as all Rh-O metalloinsertor/DNA trays set up by previous lab members, were regularly examined for crystal formation.

5.3.1.1.1 Crystal Selection and Processing

Large, uniform crystals (typically >50 μm in length) are necessary for successful X-ray crystallography structural determination studies. Truly crystalline samples produce evenly spaced, regularly repeating diffraction spots of varying intensities that extend toward the edge of the diffraction pattern (spots further from the center indicate higher resolution data). Rh-O metalloinsertor samples with intriguing morphologies, including orange hexagons and red amorphous/rectangular crystals (**Figure 5.3**), were collected and analyzed using the synchrotron. Note that rhodium metalloinsertors are a vibrant red color; therefore, crystals that are orange or

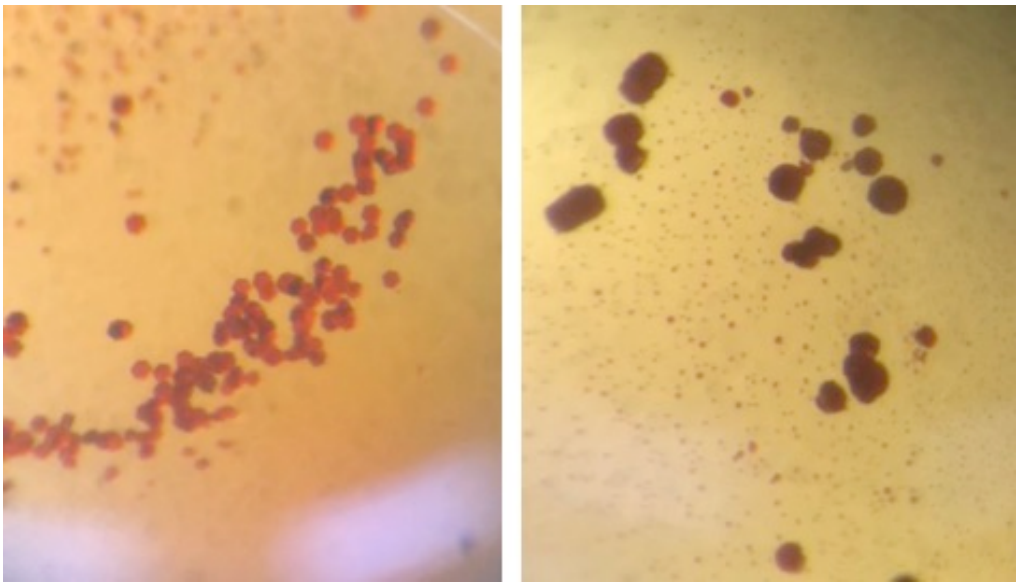

Figure 5.3 Representative morphologies observed and analyzed during crystallography experiments. Examples of (left) hexagon and (right) amorphous/rectangular crystal morphologies that were observed in Rh-O metalloinsertor crystallography trays. Note, various different crystalline samples were visualized during crystal tray analyses. While these samples were colored and appeared to have interesting, crystalline morphologies, suitable diffraction data could not be obtained.

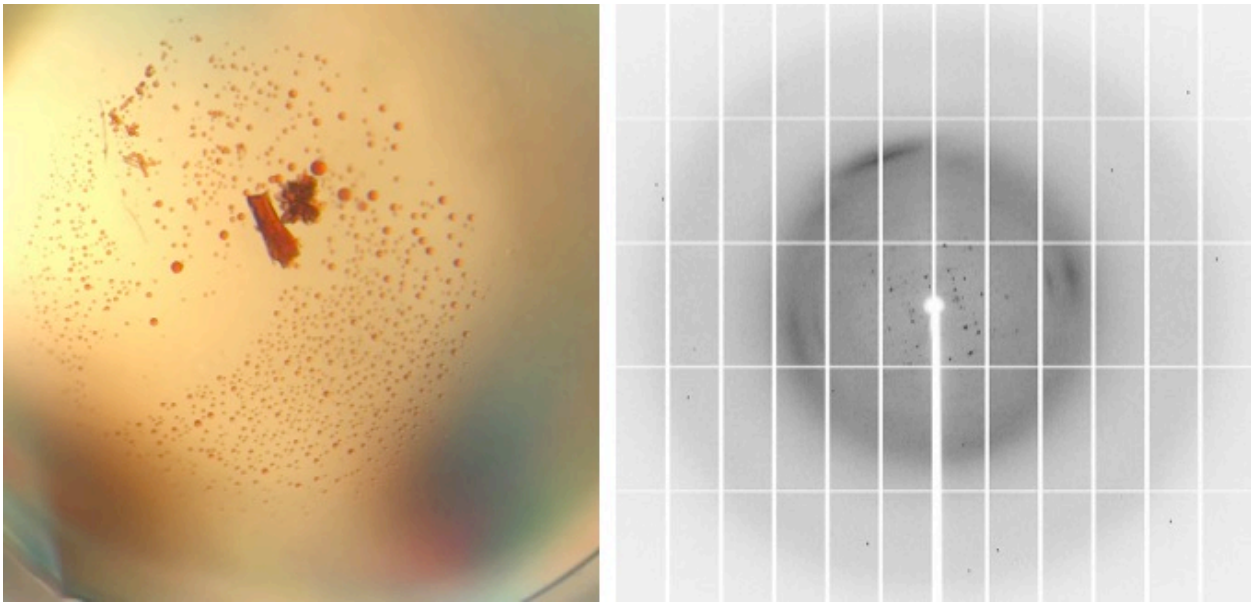

Figure 5.4 Example of a promising sample morphology and diffraction pattern that resulted from X-ray crystallography experiments. (Left) Light microscopy images of sample well with red clustered crystals and surrounding red oil-like dots. (Right) X-ray diffraction pattern that resulted from analysis of the sample. Sample was collected from Plate 2M Well D5 and contains a combination of the Rh-DPE 2.2 enantiomer, kit buffer 17, and the oligomer 5'- CGG **T**AA TT**C** CCG-3'.

red in color are hypothesized to be more likely to contain metalloinsertor complexes; though, the complex could be contained within solvent channels of the crystal or bound to DNA.

The most promising diffraction pattern observed resulted from the combination of Rh-DPE 2.2 enantiomer, kit buffer 17, and the TC mismatch containing oligomer 5'- CGG **T**AA TT**C** CCG-3' (Plate 2M Well D5), where the mismatch sites are bold and underlined. As shown in **Figure 5.4**, this crystal well contained red dots (perhaps oil) and clustered, red crystals based on light microscopy observations. Multiple samples from this well were looped, and the resulting diffraction pattern contained smeared diffraction spots with a slightly regular pattern. The smeared line in the top left may indicate base stacking of the DNA helix. Unfortunately, most of the patterns were not two-dimensional and the irregularities within the diffraction pattern indicate that the sample may contain multiple crystals that are diffracting simultaneously. Overall, these X-ray crystallography experiments did not produce promising diffraction patterns or structural data, and they may indicate that the Rh-O metalloinsertor/DNA interaction is incompatible with the crystallography conditions tested; however, it is possible that uniform microcrystals with Rh-PPO or Rh-DPE bound to mismatched DNA may be forming under the explored experimental conditions. As a result, microED structural studies with these samples were conducted.

5.3.1.2 Microcrystal Electron Diffraction (MicroED) Experiments

5.3.1.2.1 Use of MicroED for Rh-O Metalloinsertor Structural Studies

While X-ray crystallography is a seminal structural technique that has facilitated atomic resolution structural determinations of molecules ranging from DNA to the ribosome, large, well-ordered crystals (typically >50 μm in length) are imperative for accurate structural

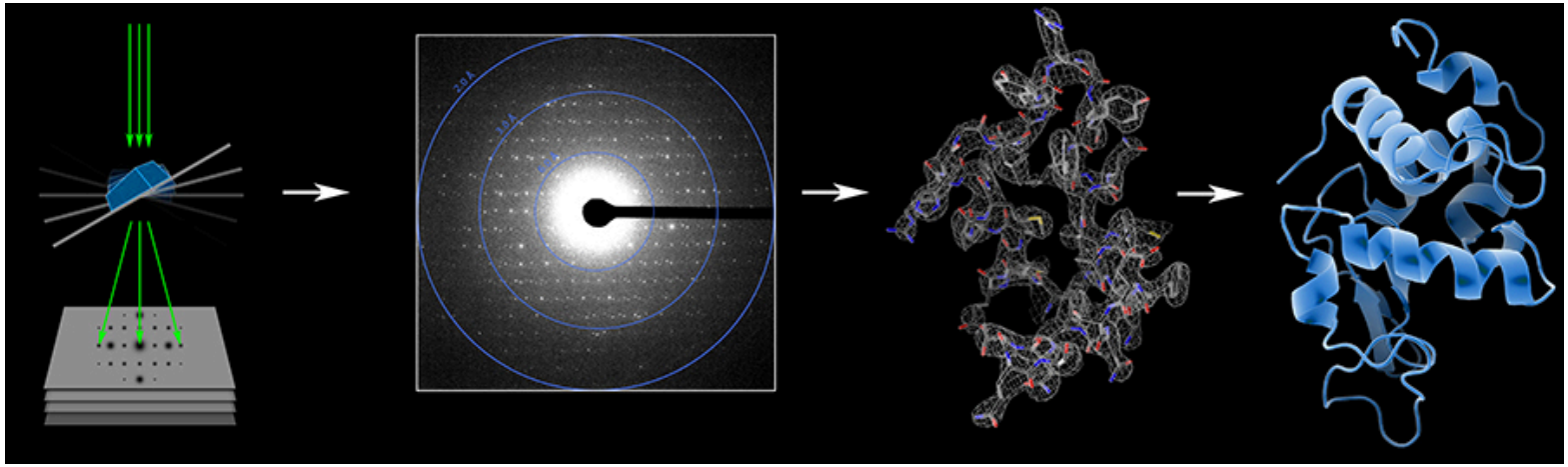

Figure 5.5 Schematic for microcrystal electron diffraction (microED) data collection and processing. Once a sample is identified, the crystal is centered and height adjusted such that a complete diffraction tilt series can be collected. This involves continuously rotating the crystal in the electron beam. These diffraction data are analyzed with data processing software to determine phases and generate an electron density map. Additional analysis is performed to fit the data and refine an atomic model for the sample. From Reference 21.[20]

determination; this is a major limitation that hinders the use of X-ray crystallography for particularly complex and difficult targets.[20] MicroED is a novel structural technique that involves collecting electron diffraction data from extremely small three-dimensional crystals (< 2 μm) in order to solve structures of biological and chemical samples.[20,21] Typically, microcrystals are frozen on an electron microscopy (EM) grid and then diffraction data is collected by continuously tilting the EM grid platform at angle increments of 0.1 – 1°. The electron diffraction data is then used for structural determination using processing techniques similar to those in X-ray crystallography. See **Figure 5.5** for a graphic representation outlining the microED data collection and analysis process. Note that data from multiple crystals are often needed to determine complete, high-resolution structures and crystals must be very thin due to the strong interaction between electrons and matter. Thus far, this technique has been used to solve mainly protein structures (ex. lysozyme and catalase);[22] however, this method has significant promise for samples that do not readily form large, uniform crystals.

5.3.1.2.2 MicroED Initial Sample Preparation and Analysis

Due to the lack of successful crystal formation with Rh-O metalloinsertors bound to DNA mismatches, microED was explored with samples originally intended for X-ray crystallography experiments. Samples from crystallography trays that displayed faint dot patterns were used in the initial microED experiments. The studies were carried out by following the standard Vitrobot procedure in which the crystal sample was pipetted onto a secured EM grid, blotted, and then plunged into liquid ethane. This vitrification process was enacted to preserve sample integrity by minimizing the formation of ice crystals.[23]

These initial studies allowed for the identification of one crystal with particularly promising diffraction data (~2 Å). As shown in **Figure 5.6**, the sample came from Plate 3A Well

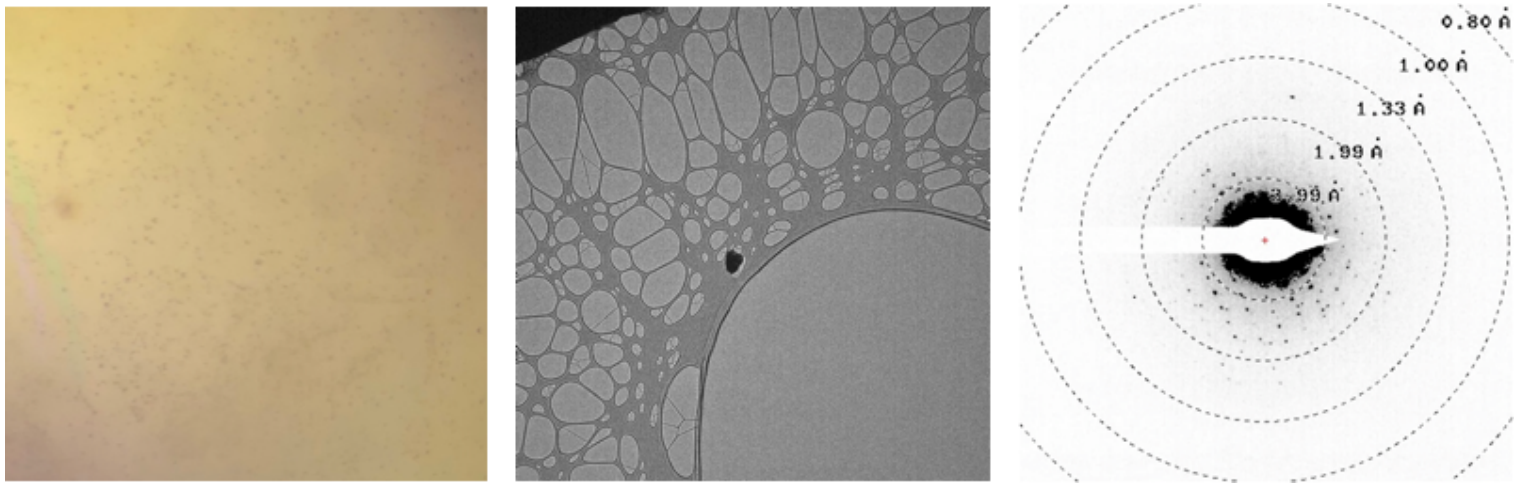

Figure 5.6 Microscopy images and diffraction pattern from promising Rh-O metalloinsertor/DNA microcrystal sample. (Left) Light microscope image of Plate 3A Well D2, which contained Rh-DPE and a 12-mer with two AA mismatches. Note the dot pattern in the well. (Middle) EM brightfield image of microcrystal from Plate 3A Well D2 that produced encouraging diffraction data. (Right) Representative EM diffraction pattern from microcrystal sample that ultimately produced 45% complete structural data.

D2. Light microscopy of the well revealed a faint dot pattern, and the promising microcrystal sample appeared as jagged and triangular in the brightfield EM image. Note that the EM sample was prepared on a 300 mesh, lacey carbon with continuous carbon, Cu grid using the standard Vitrobot procedure (5 sec blot time), and diffraction movies were collected from 0^o to 60^o at 0.03^o /sec. While the diffraction pattern produced was not ideal, processing of the collected diffraction movie was 45% complete and allowed for determination of unit cell parameters, including the following lengths of cell edges and angles between them: a = 41.265Å, b = 24.737Å, c = 20.991Å and $\alpha = 90.000°$, $\beta = 92.562°$, $\gamma = 90.000°$, respectively. Additionally, the space group was found to be C2 (analysis was performed by Dr. Jens Kaiser). These results indicate that there is one single strand of DNA in the asymmetric unit, and the full molecule would need to be resolved by using crystallographic symmetry. Furthermore, the R-merges were below 20% and no similar cells (a/b/c +/-10%, beta +/- 2.5^o) were found in the Protein Data Bank (PDB), indicating that it is likely a unique atomic structure. Importantly, this crystal sample originated from Plate 3A Well D2, which contained Rh-DPE and a 12 base pair DNA oligomer.

While the standard grid preparation process did result in thin films of sample on the EM grid and diffraction data from one particularly promising crystal, significant ice contamination (**Figure 5.7**) made it difficult to properly identify other promising crystals. Notably ice crystals often had spear-like morphologies with at least one straight side, which made distinguishing between ice and sample crystals based brightfield images quite challenging. Additionally, as shown in **Figure 5.8**, ice was found to contaminate promising crystal samples as well. Various parameters of the Vitrobot preparation, including blot time, blot force, humidity, and the side of the EM grid to which sample was applied, were altered to optimize sample crystal identification;

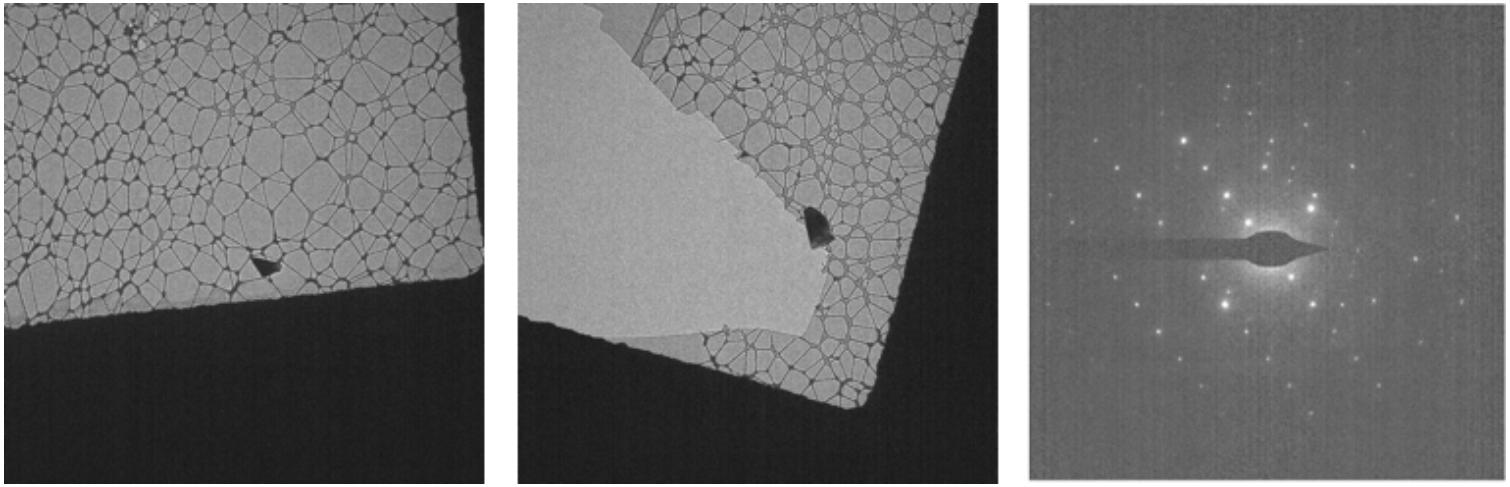

Figure 5.7 Representative examples of brightfield images and diffraction pattern that resulted from ice contamination on EM grids prepared using Vitrobot. (Left and middle) Representative brightfield images of ice crystals on EM grids. (Right) Representative diffraction pattern produced by ice crystals. Note that the diffraction pattern displays a bright lattice of equally spaced spots. Spots are relatively far apart which indicates that the molecule being analyzed (H_2O) is atomically small.

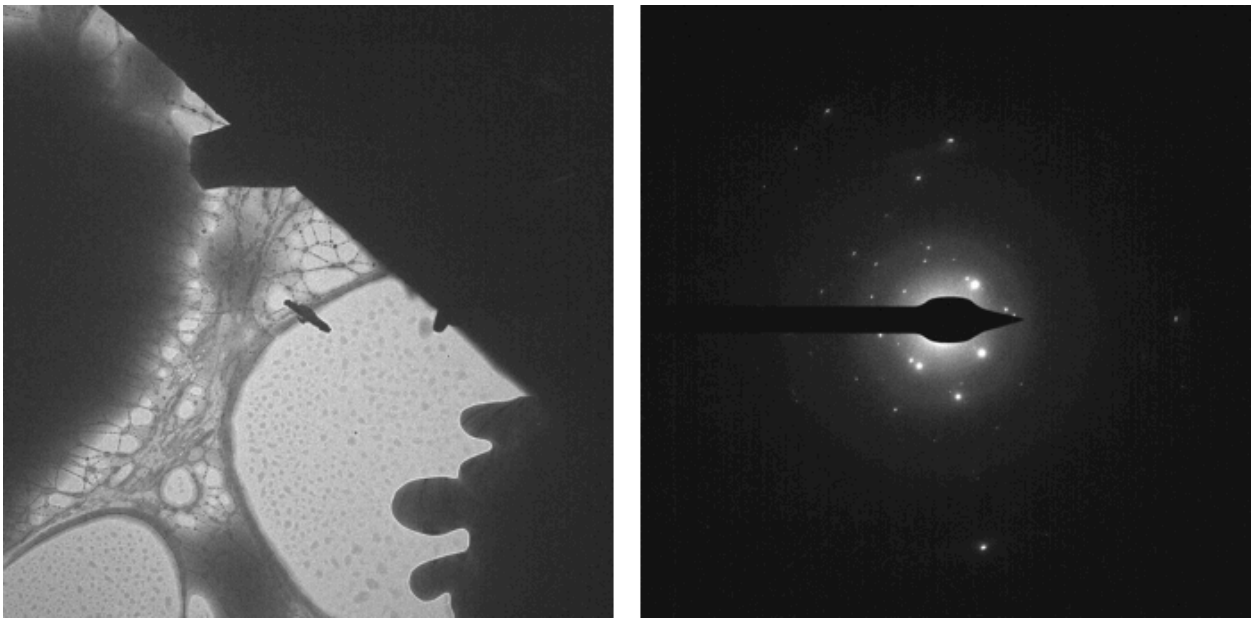

Figure 5.8 Example of brightfield image and diffraction pattern from potential Rh-O metalloinsertor/DNA sample contaminated with ice. (Left) Representative brightfield image of promising rod-like crystal that is contaminated with ice. (Right) Diffraction pattern that resulted from sample contaminated with ice. Importantly, brightest spots within the diffraction pattern correspond with ice contamination, while other spots may correspond to desired sample. Note that structures with mixtures of sample and ice cannot be resolved.

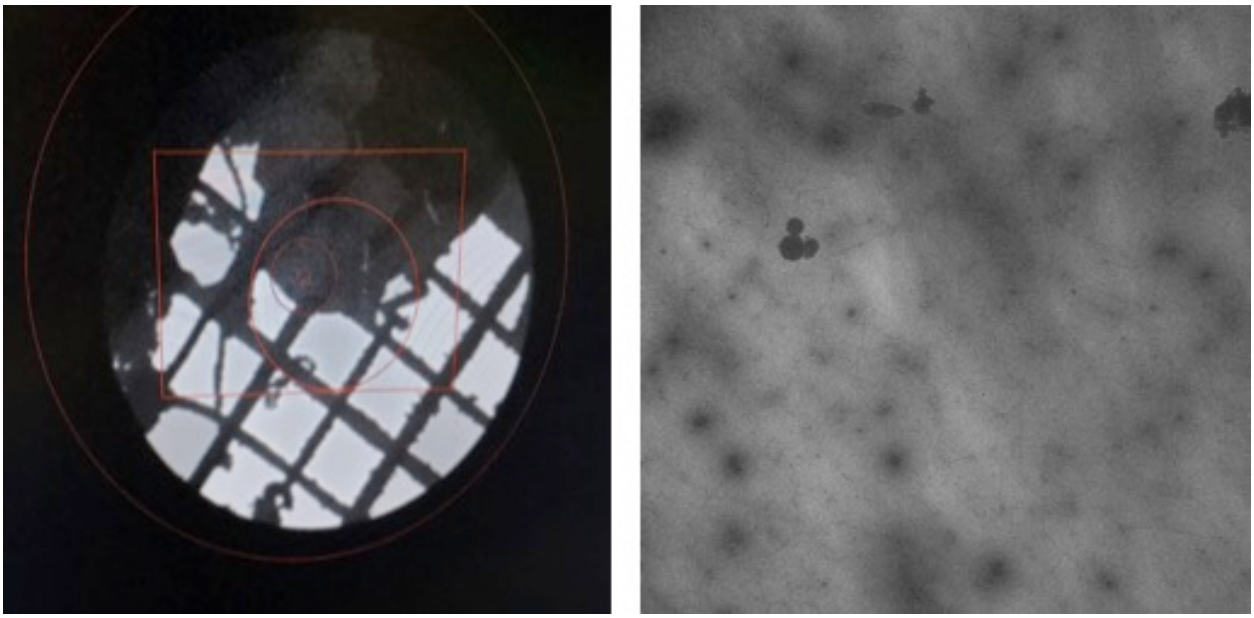

Figure 5.9 Example of brightfield images of Quantifoil EM grid after 3 hr incubation with metalloinsertor/DNA sample. (Left) Zoomed out image of degraded EM grid and (right) zoomed in brightfield image of sample on grid. Note the various shades of opaque gray on the image (right), which indicate the formation of uneven and thick ice.

however, the Vitrobot method consistently resulted in ice contaminated grids with very low sample density. As a result, alternative grid preparation protocols were explored.

5.3.1.2.3 MicroED Sample Preparation Optimization

Specifically, manual EM grid preparation methods were explored and factors such as sample incubation time and blotting method were varied. By preparing the grids manually, the sample could be incubated on the EM grid for different amounts of time with the goal of increasing sample concentration. By allowing time for the sample to diffuse onto the grid, we hypothesized that sample crystal density could be increased. In particular, crystal well samples were added to the frontside of EM grids (placed on PTFE polymer wells) and incubated for times ranging from 1 min to 3 hr, then frozen and prepared for electron microscopy using the Vitrobot technique. Importantly, the three-hour incubation time resulted in discoloration of the crystal solution (changed from orange to blue/green), as well as degradation of the carbon layer of the EM grid (**Figure 5.9**). Additionally, intact portions of the grid had thick and uneven deposition of sample, which complicates processing of any collected diffraction data. Results from these studies indicated that less than two minutes of sample incubation was necessary for maintaining the integrity of the EM grid and limiting thick ice formation. Ultimately, this method did not result in uniform deposition of sample.

Next, the blotting technique used for sample preparation was explored. In collaboration with Dr. Yoo, as shown in **Figure 5.10**, a novel procedure for blotting microED samples was developed. In order to both increase sample crystal density and create uniform, thin films of sample on EM grids, we explored the removal of excess solvent by allowing the liquid to diffuse through the grid and onto filter paper (secured together using tweezers). First, the grid was secured to a filter paper using tweezers. Then, sample was pipetted onto the copper or gold

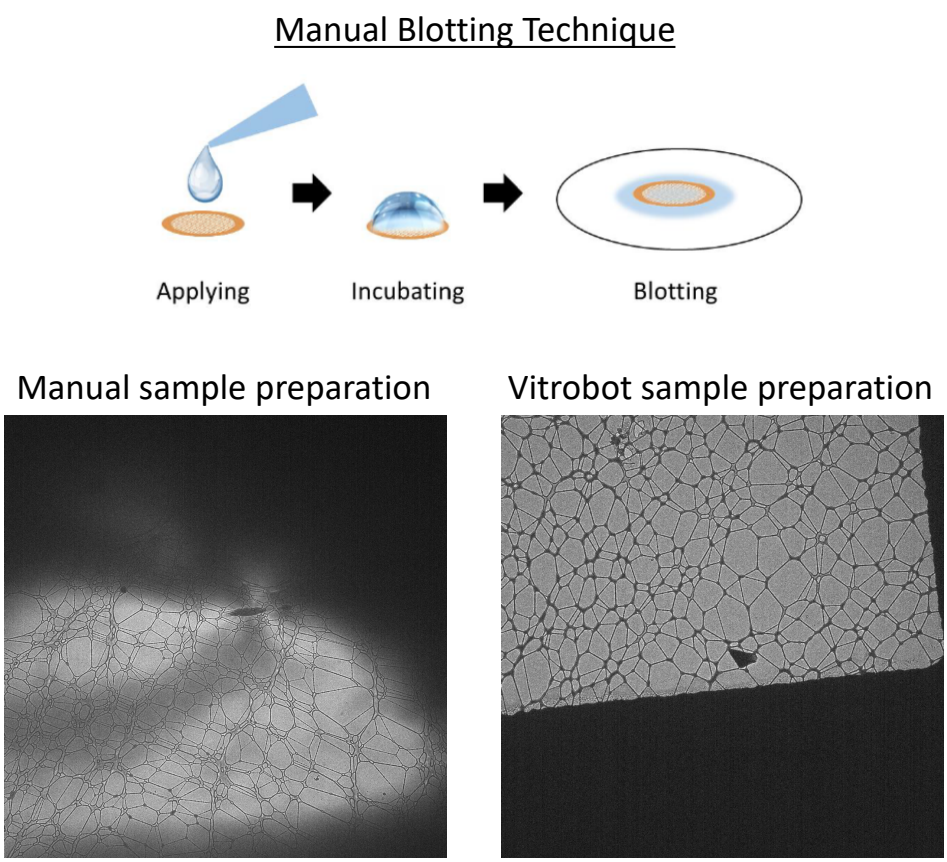

Figure 5.10 Manual blotting technique developed for microED studies with Rh-O metalloinsertors. (Top) Schematic outlining the manual blotting method where sample is applied to the EM grid, incubated for a short period of time, and then allowed to diffuse through the grid onto filter paper. (Bottom left) Representative brightfield image of EM grid and samples prepared using manual blotting technique compared to (right) image of EM grid prepared using Vitrobot method. Figure made with the assistance of Dr. Byung-Kuk Yoo.

(front) side of the EM grid. After a brief incubation (<10 sec), the solvent diffused through the grid and onto the filter paper. Then, the grid was prepared for EM experiments, as described above. While this novel technique did result in the detection of more promising samples, such as the rod-like sample shown in **Figure 5.10**, more uniform thin films were produced using the Vitrobot vitrification method. Notably, a variety of crystallography samples were used in the described sample preparations, and a range of crystal morphologies, including dots patterns, crystal clusters, and needle clusters, were examined.

Ultimately, a variety of sample wells and microED sample preparation procedures were investigated and developed; however, complete diffraction data from microcrystal samples was never collected and an atomic structure of Rh-O metalloinsertors bound to DNA mismatches was never resolved. MicroED remains a promising technique for probing the structural interactions between metalloinsertors and DNA that result in Rh-O metalloinsertors' unique chemical and biological properties. Given that a 45% complete structure with unique crystal properties was obtained, future studies should focus on setting up crystal trays with similar crystallization conditions in order to complete this structure.

5.5 Conclusions

X-ray crystallography and MicroED structural techniques were used to explore the unique atomic interaction between Rh-O metalloinsertors and mismatched DNA sites. The most promising results came from microED analysis of samples originally intended for X-ray crystallography. This study allowed for the development of novel microED sample preparation techniques that can be employed for future metalloinsertor studies, as well as other biological samples. Future experiments may aim to supplement the partial electron diffraction data discussed in order to obtain a complete atomic structure. This microED structure would be

especially exciting given that it would be the first DNA-drug interaction resolved using microED, and importantly, the results would increase our understanding of the uniquely potent and selective biological properties of the Rh-O metalloinsertor family.

5.6 References

(1) Junicke, H.; Hart, J. R.; Kisko, J.; Glebov, O.; Kirsch, I. R.; Barton, J. K. A Rhodium(III) Complex for High-Affinity DNA Base-Pair Mismatch Recognition. *Proc. Natl. Acad. Sci. U. S. A.* **2003**, *100* (7), 3737–3742. https://doi.org/10.1073/pnas.0537194100.

(2) Hart, J. R.; Glebov, O.; Ernst, R. J.; Kirsch, I. R.; Barton, J. K. DNA Mismatch-Specific Targeting and Hypersensitivity of Mismatch-Repair-Deficient Cells to Bulky Rhodium(III) Intercalators. *Proc. Natl. Acad. Sci. U. S. A.* **2006**, *103* (42), 15359–15363. https://doi.org/10.1073/pnas.0607576103.

(3) Zeglis, B. M.; Boland, J. A.; Barton, J. K. Targeting Abasic Sites and Single Base Bulges in DNA with Metalloinsertors. *J Am Chem Soc* **2008**, *130* (24), 7530–7531. https://doi.org/10.1038/jid.2014.371.

(4) Zeglis, B. M.; Boland, J. A.; Barton, J. K. Recognition of Abasic Sites and Single Base Bulges in DNA by a Metalloinsertor. *Biochemistry* **2009**, *48* (5), 839–849. https://doi.org/10.1038/jid.2014.371.

(5) Brunner, J.; Barton, J. K. Site-Specific DNA Photocleavage by Rhodium Intercalators Analyzed by MALDI-TOF Mass Spectrometry. *J. Am. Chem. Soc.* **2006**, *128* (21), 6772–6773. https://doi.org/10.1021/ja0612753.

(6) Ernst, R. J.; Song, H.; Barton, J. K. DNA Mismatch Binding and Antiproliferative Activity of Rhodium Metalloinsertors. *J. Am. Chem. Soc.* **2009**, *131* (6), 2359–2366. https://doi.org/10.1021/ja8081044.

(7) Zeglis, B. M.; Pierre, V. C.; Kaiser, J. T.; Barton, J. K. A Bulky Rhodium Complex Bound to an Adenosine-Adenosine DNA Mismatch: General Architecture of the Metalloinsertion Binding Mode. *Biochemistry* **2009**, *48* (20), 4247–4253.

https://doi.org/10.1021/bi900194e.A.

(8) Zeglis, B.; Pierrea, V.; Barton, J. K. Metallointercalators and Metalloinsertors. *Chem Commun* **2007**, *44*, 4565–4579. https://doi.org/10.1016/j.biotechadv.2011.08.021.Secreted.

(9) Cordier, C.; Pierre, C.; Barton, J. K. Insertion of a Bulky Rhodium Complex into a DNA Cytosine - Cytosine Mismatch : An NMR Solution Study. *J. Am. Chem. Soc.* **2007**, *129* (2), 12287–12295.

(10) Kellett, A.; Molphy, Z.; Slator, C.; McKee, V.; Farrell, N. P. Molecular Methods for Assessment of Non-Covalent Metallodrug-DNA Interactions. *Chem. Soc. Rev.* **2019**, *48* (4), 971–988. https://doi.org/10.1039/c8cs00157j.

(11) Komor, A. C.; Barton, J. K. An Unusual Ligand Coordination Gives Rise to a New Family of Rhodium Metalloinsertors with Improved Selectivity and Potency. *J. Am. Chem. Soc.* **2014**, *136* (40), 14160–14172. https://doi.org/10.1021/ja5072064.

(12) Boyle, K. M.; Barton, J. K. A Family of Rhodium Complexes with Selective Toxicity toward Mismatch Repair-Deficient Cancers. *J. Am. Chem. Soc.* **2018**, *140* (16), 5612–5624. https://doi.org/10.1021/jacs.8b02271.

(13) Nano, A.; Bailis, J. M.; Mariano, N. F.; Pham, E. D.; Threatt, S. D.; Barton, J. K. Cell-Selective Cytotoxicity of a Fluorescent Rhodium Metalloinsertor Conjugate Results from Irreversible DNA Damage at Base Pair Mismatches. *Biochemistry* **2020**, *59*, 717–726. https://doi.org/10.1021/acs.biochem.9b01037.

(14) Boer, D. R.; Canals, A.; Coll, M. DNA-Binding Drugs Caught in Action: The Latest 3D Pictures of Drug-DNA Complexes. *Dalt. Trans.* **2009**, No. 3, 399–414. https://doi.org/10.1039/b809873p.

(15) Zheng, H.; Handing, K. B.; Zimmerman, M. D.; Shabalan, I. G.; Almo, S. C.; Minor, M. X-Ray Crystallography over the Past Decade for Novel Drug Discovery – Where Are We Heading Next? *Expert Opin Drug Discov.* **2015**, *10* (9), 975–989. https://doi.org/10.1517/17460441.2015.1061991.X-ray.

(16) Blundell, T. L.; Patel, S. High-Throughput X-Ray Crystallography for Drug Discovery. *Curr. Opin. Pharmacol.* **2004**, *4* (5), 490–496. https://doi.org/10.1016/j.coph.2004.04.007.

(17) Messori, L.; Marzo, T.; Merlino, A. The X-Ray Structure of the Complex Formed in the Reaction between Oxaliplatin and Lysozyme. *Chem. Commun.* **2014**, *50* (61), 8360–8362. https://doi.org/10.1039/c4cc02254h.

(18) Pierre, C.; Kaiser, J. T.; Barton, J. K. Insights into Finding a Mismatch through the Structure of a Mispaired DNA Bound by a Rhodium Intercalator. *Proc. Natl. Acad. Sci.* **2007**, *104* (2), 429–434.

(19) Song, H.; Kaiser, J. T.; Barton, J. K. Crystal Structure of Δ-Ru(Bpy)2 Dppz2+ Bound to Mismatched DNA Reveals Side-by-Side Metalloinsertion and Intercalation. *Nat Chem* **2013**, *4* (8), 615–620. https://doi.org/10.1038/jid.2014.371.

(20) Hattne, J.; Reyes, F. E.; Nannenga, B. L.; Shi, D.; De La Cruz, M. J.; Leslie, A. G. W.; Gonen, T. MicroED Data Collection and Processing. *Acta Crystallogr. Sect. A Found. Adv.* **2015**, *71*, 353–360. https://doi.org/10.1107/S2053273315010669.

(21) Barringer, R. Illuminating the Secrets of Crystals: Microcrystal Electron Diffraction in Structural Biology. *Biosci. Horizons* **2018**, *11*, 1–12. https://doi.org/10.1093/biohorizons/hzy013.

(22) Nannenga, B. L.; Shi, D.; Hattne, J.; Reyes, F. E.; Gonen, T. Structure of Catalase Determined by MicroED. *Elife* **2014**, *3*, e03600. https://doi.org/10.7554/eLife.03600.

(23) Almgren, M.; Edwards, K.; Gustafsson, J. Cryotransmission Electron Microscopy of Thin Vitrified Samples. *Curr. Opin. Colloid Interface Sci.* **1996**, *1* (2), 270–278. https://doi.org/10.1016/s1359-0294(96)80015-x.

Chapter 6

CONCLUSIONS AND FUTHRE OUTLOOKS

Mismatch repair (MMR) deficient cancers continue to need novel therapeutic approaches due to their resistance to standard of care chemotherapeutic treatments. These cancers often result from deficiencies in MMR proteins, which cause DNA mismatches and indels to accumulate. An important strategy for treating these MMR-deficient cancers, including colorectal and breast cancers, involves the development of complexes that selectively target the DNA lesions that result from these MMR protein deficiencies. Specifically, over the last couple of decades, our laboratory has focused on developing rhodium metalloinsertors that selectively target and kill MMR-deficient cancer cells.

Metalloinsertor complexes are capable of selectively binding thermodynamically destabilized DNA lesions, including mismatches, indels, and abasic sites. These DNA binding interactions have been shown to result in the selective killing of MMR-deficient cancer cells. Our most recent family of Rh-O metallinsertors contains an N^O coordinating, axial ligand, and biological studies have revealed this family of metallinsertors displays nanomolar potency with highly selective toxicity towards MMR-deficient cancer cells. Within this thesis, efforts to explore the *in vivo* properties of the most potent Rh-O metalloinsertor, Rh-PPO, are described, as well as studies to further develop metalloinsertor drugs as targeted chemotherapeutics.

The *in vivo* studies presented here represent the first preclinical mouse evaluations of a rhodium metalloinsertor as a chemotherapeutic. Intraperitoneal studies with Rh-PPO revealed a notable increase in mouse survival compared to the FDA approved oxaliplatin, as well as significant decreases in mouse final tumor weights and tumor volumes. Together, these results

indicate that Rh-PPO has noteworthy anticancer activity within an HCT116 colorectal cancer xenograft tumor model. Notably, intratumoral studies with Rh-PPO showed that significantly enhanced anticancer effects can be achieved when the drug is administered specifically to the site of the tumor, suggesting that more selective delivery methods need to be explored in order for further development of metalloinsertors.

Liposomal and antibody drug conjugate (ADC) metalloinsertor drug formulations were explored in order to achieve increased targeting of MMR-deficient malignant cells. Within the liposomal studies, four distinct Rh-PPO liposome formulation methods were developed, and the resulting liposomes were analyzed for their cytotoxicity, encapsulation efficiency, and stability. Rh-PPO liposomes prepared with the remote loading procedure were found to show the most promising biological and chemical features; however, further development of this nanoparticle drug delivery approach is needed. The described metalloinsertor ADC studies involved the design of three ADC drug linkers that incorporate maleimide conjugation groups into the N^O coordinating metalloinsertor ligand. Each of these complexes was synthesized and characterized for their cytotoxic selectivity towards MMR-deficient cancer cells, as well as their cellular potency. Overall, these studies have been important attempts to develop novel drug formulations for rhodium metalloinsertors and further exploration is warranted.

The experiments outlined in this thesis showcase the promise of metalloinsertors as targeted therapeutics for MMR-deficient cancers. The presented *in vivo* studies show that the rhodium metalloinsertor Rh-PPO has significant anticancer activity that has potential for further optimization. The exact reason for the observed *in vivo* potency of metalloinsertors remains unknown; therefore, structural studies involving X-ray crystallography and microcrystal electron diffraction remain underway. Additionally, the use of drug delivery strategies, such as ADCs and

liposomal formulations, will likely be crucial to the further development of metalloinsertors as therapeutics. Ultimately, our group will use the results of these studies to continue progressing metalloinsertors towards clinical relevance.